AFOSR-TR- 93 0076

FINAL REPORT

on

FAILURE CONSIDERATIONS IN COMPOSITE SYSTEMS BASED ON 3D MICROMECHANICAL STRESS FIELDS : PART A

by

E.S. Folias

Submitted to

AIR FORCE OFFICE OF SCIENTIFIC RESEARCH

Department of Mathematics
University of Utah
Salt Lake City, Utah 84112

December 31, 1992

1. Introduction

It is well recognized that laminated composite plates exhibit extraordinary strength per weight ratio characteristics. Consequently, their use in aerospace structures is the way of the future. However, in order to be able to predict their failing characteristics particularly in the neighborhood of free surfaces such as straight edges, holes edges, cracks etc., it is necessary to know the local stress behavior particularly from a 3D point of view. Thus, if rational designs using fiber reinforced-resin matrix composite laminates are to be made, their performance under static, dynamic and fatigue loads need to be predictable. The first step towards this goal is the realization that the ultimate failure, as well as many other aspects of the composite behavior, is the result of the growth and accumulation of micro-damage to the fibers, matrix and their interfaces. Thus, it appears that any generally successful model of performance and failure must incorporate the effects of this local damage in some way. This certainly represents a challenge.

In this investigation, a systematic , 3D, micromechanics approach is used where the fibers are assumed to be cylindrical inclusions which are embedded into a matrix plate. A three dimensional analysis is used in order to capture any edge effects which may be present. A set of fundamental key problems is identified and their respective solutions are then used in order to provide some answers to the following fundamental questions:

(i) UNIDIRECTIONAL COMPOSITE PLATE:

- transverse strength
- edge delamination
- modeling of fiber matrix interface
- longitudinal strength
- residual stresses due to thermal expansion mismatch

The approach consists of first solving for the 3D stress field of one fiber only. The solution is then extended to the case of a periodic array of fibers. The 3D results are then used to first identify critical locations where failure, due to fracture, is most likely to initiate and second to derive fracture criteria for crack initiation at the local level. The criteria reveal the dependance of the transverse strength on the material properties, the local geometry and the applied loads. Ultimately, a general criterion will be derived which incorporates all of the above effects. In this phase of the research we are focusing on the process of crack initiation and, as a result, the criteria will be valid only for crack lengths up to 30% or 40%

of the fiber radius. This is because the present analysis does not account for the interactions between cracks and periodic fibers. It may be noted, however, that it is now possible to indeed take into account such interactions at the local level, a subject which will be investigated in the near future. Be that as it may, the identification of the critical areas for possible failure and the prediction of the critical stress for crack initiation are of great interest to the desingners.

(ii) BRIDGING THE GAP BETWEEN MICRO AND MACROMECHANICS

Our investigation shows that it is now possible to relate results based on macromechanical considerations with results based on micromechanical considerations via certain correlation functions which are obtained in part (i). As a practical matter , once these correlation functions have been established, then results based on macromechanical considerations (eg. finite ellements etc.) may then be used to also answer questions of damage at the local level. Thus, one of the important findings in part (i) is the identification of the regions of applicability of the results which are based on macromechanical considerations.

(iii) LAMINATED COMPOSITE PLATE BASED ON MICROMECHANICS

The above work will next be extended to the more general case of a laminated composite plate of different ply orientations. The cylindrical fibers in this case have two different fiber orientations , thus modeling from a micromechanics point of view the consept of an interface.

2a. Effects of Transverse Load on a Fiber/Matrix Interface Failure

The low transverse tensile strength of unidirectional laminae presents a major problem in the design of composite laminate structures. Although the fibers can be oriented so that they are parallel to the external loads, it is almost impossible to avoid transverse stresses which may lead to premature failure of the laminate. An excellent example of this is in the design of a filament wound pipe or pressure vessel .

There is no simple relation for predicting the transverse strength. Unlike the longitudinal tensile strength which is determined almost entirely by a single factor, i.e. the fiber strength, the transverse strength is governed by many factors including the properties

of the fiber and matrix, the interface bond strength, the presence and distribution of voids, and the internal stress and strain distribution due to the interactions between fibers, voids etc.

Recently, we were able to investigate what effect if any does a transverse load have on the failure characteristics of a fiber/matrix interface. To establish this, we carried out an analysis based on 3D analytical considerations . (For more details see Part I). The analysis shows the stresses σ_{rr} and $\sigma_{\theta\theta}$ for ratios of (a/h) $\leq$ 0.05, to be almost constant in the interior of the laminate and that as one approaches the free edges of the laminate, i.e. the region where the fiber intersects the free surface, a boundary layer effect is shown to prevail. A separate local asymptotic analysis carried out by the author shows that the stress field there is indeed singular. For example, for a glass fiber/ epoxy matrix the stress singularity is 0.25 (Folias 1989), while for the case of a carbon fiber/epoxy matrix it is 0.31 (for more details see Part II) .This neighborhood, therefore, is an area with potential for a fiber/matrix interface failure due to the relatively high stress levels which are present. It may, furthermore, be noted that for ratios of (a/h) > 0.3 the stress profiles along the fiber length is very much non uniform. The model, however, is still applicable and it does provide us with accurate results.

The results may now be used to derive failure criteria based on micromechanical considerations. For example, such a criterion due to the presence of an interface crack has been derived and the details may be found in PART III (see eq.34 and fig 12). Similarly a failure criterion due to the presence of a θ - type of crack has also been derived.

Finally, in the limit , if one allows all the fibers to debond completely one arrives at a local lower bound for the overall matrix strength of the material system..

2b. Effect of Fiber Coating on the Strength Characteristics

The properties of fiber reinforced composites are very much dependendent upon the interfacial region between the matrix and the fiber. This is because the primary function of this interface region is to transmit a portion of the load from the matrix to the reinforcing fibers and vise versa. This ability to transmit stress across the phase boundary must, ultimately, depend upon the mechanical properties of the matrix, the load bearing capacity of the fibers as well as the strength of the fiber matrix interface. It is natural, therefore, to seek the relationship between the overall composite strength and the above variables.

Based on 3D considerations the subject was recently investigated by Folias and Liu (see PART IV) for transverse loads and by Zhong and Folias (see PART VI) for axial loads.

In the case of a glass fiber/ epoxy matrix the effect of a fiber coating is shown to have a minimal effect on the stress field. For other type of material systems, however, this effect can be substantial. Our 3D model does provide us with accurate results. For more details see PART IV. Finaly, as a practical matter, if one has a functionally gradient property matrix then the singular stress at the fiber edge may also be eliminated.

3. The Effect of Thermal Stresses and Curing Stresses

Shrinkage stresses during cure and thermal stresses due to differences between the thermal expansion coefficients of the matrix and fiber may have a major effect on the microstresses within a composite material and as a result their contributions should be added to the stresses introduced by the mechanical loads. It may also be noted that these microstresses are often sufficient to produce microcracking even in the absence of external loads.

As it was noted previously, the stress field in the neighborhood where a fiber meets a free surface is singular. Thus, all things being equal, small cracks are more likely to develop at such neighborhoods and subsequently propagate into the interior of the matrix. The condition, as expected, is further aggravated when a temperature change takes place because of the difference in the thermal expansion coefficients between matrix and fibers. The problem is of particular concern to ceramic type of composites.

The objective of this investigation was to study the 3D stress field of a periodic array of fibers embedded into a matrix plate and subjected to a temperature change $\mathcal{D}T$, e.g. during the curing process. Particular emphasis is placed in the neighborhood of the free surface as well in the interior of the fiber length. The analysis reveals the influence that each individual ratio, fiber radius to fiber length , fiber volume fraction, material properties Gf/Gm, cooling temperature, and thermal expansion coefficients have on the residual stresses field which is induced within the material system during the process of manufacturing for example. The model identifies the critical locations where possible failures are most likely to initiate. In general, the location dependents on the material properties as well as the other ratios previously mentioned. For more details, see PART V. Fracture criteria for crack initiation have also been derived and the results will be reported

soon. It may be noted that the model is applicable to intermetalic, ceramic and organic composites. The applications are numerous, e.g. jet engine technology, automobile engines, thermal fatigue for high performance aircraft, etc.

4. Zone of Influence of a Break in one Fiber

Unidirectional fiber composites are important structural elements of many modern composite materials. Their tensile strength frequently determines the possibility of using them in various structures. Due to various technological reasons, breakage of individual fibers long before fracture of the entire specimen is absolutely unavoidable. For example, in glass-reinforced plastics, some individual fibers break at loads of only one-tenth of the maximum load for the material. Actually, all fibers used in composites usually have high mean statistical strength, but an extremely low fracture toughness, and as a result, they are quite sensitive to tiny cracks, which unavoidably arise in the process of manufacture of the fibers. Therefore, a certain number of these fibers always break at extremely low tensile loads.

In view of the above, the following questions come to mind: (i) Is there an optimal placement of fibers in a matrix and (ii) is there a lower limit of the volumetric fraction of fibers for which the failure of a composite will be ideally ductile so that the influence of the breakage of individual fibers may be ignored? In order to give a partial answer to these important questions, we investigated the following problem.

We consider a cylindrical fiber which is embedded into a matrix binder. Both fiber and matrix materials were assumed to be homogeneous and isotropic but of different material constants. As to loading, the fiber and matrix were subjected to uniform loads σ_0 and σ_1 respectively (for more details see PART VI). The analysis revealed the load transfer characteristics from the matrix to the fiber and vise versa. The analysis was subsequently extended to the periodic case and the results may be found in PART VII. Suppose now at a certain moment in time, because of the applied loads, a plane crack perpendicular to the axis of the cylinder is formed. It is now possible to estimate the 3D stress field due to the presence of the crack (static considerations) and thus establish the zone of influence of a break in one fiber. These results can then be extended to also include an infinite periodic array of fibers. The results are presently being used to study the effect of bridging in cracked composite systems.

5. Adhesive Butt Joints.

Finally, the problem of an adhesive butt joint has been investigated and the results are given in PART VIII.

6. Generalized Failure Criteria

The results may now be combined in order to derive failure criteria for crack initiation applicable to unidirectional composite systems based on 3D micromechanical considerations. Much of this work has already been carried out and the results will be reported in a separate report. But most importantly the results are essential for a better understanding of the damage evolution process in critical neighborhoods such as holes, cracks, joints, edges etc.

For example, the results of parts I , II, III, IV, V, VI, and VII may now be used to address the phenomenon of bridging in ceramic and intermetalic composites and thus develop a relationship between fracture toughness, fiber volume fraction and combined mechanical thermal loads.

PART I

ON THE THREE-DIMENSIONAL STRESS FIELD OF A PERIODIC ARRAY OF FIBERS EMBEDDED INTO A PLATE MATRIX

by
E.S. Folias and J.H. Liu

Department of Mathematics
University of Utah
Salt Lake City, Utah 84112

Abstract

A 3D micromechanical model has been developed to represent a undirectional composite plate which is subjected to a uniform transverse load σ_o. The model assumes the fibers to be cylindrical inclusions which are periodically embedded into an epoxy matrix. The materials of both fibers and matrix are assumed to be linear, elastic, and isotropic. The analytical solution shows the radial stress σ_{rr} to decrease as the fiber volume fraction V_f increases. The stress profile along a fiber length is shown to be constant except in the neighborhood of the fiber edge where a boundary layer is shown to prevail. In this region, the analytical solution shows the stress field to be singular which is a departure from the results given by macromechanical theories.

In the limit, as $G_f \rightarrow 0^+$ the 3D stress field of a plate weakened by a periodic array of holes is recovered.

1 INTRODUCTION

It is well recognized that fiber composite materials are very attractive for use in aerospace, automotive and other applications. These composites consist of relatively stiff fibers which are embedded into a lower stiffness matrix. Although in most designs the fibers are aligned so that they are parallel to the direction of the external loads, it is almost impossible to avoid induced transverse stresses which may lead to premature failure of the laminate. An excellent example of this is the case of a filament wound pressure vessel in which the presence of curvature induces bending as well as transverse stresses (Folias, 1965). However, in order to be able to predict their failing characteristics, particularly in the neighborhood of free surfaces such as holes, edges etc., it is necessary to know the local stress behavior from a 3D point of view.

An overall summary of some of the results, which are based on 2D elasticity considerations can be found in the books by Hull (1981) and by Chamis (1975). In their pioneering work, Adams and Doner (1967) used finite differences to solve the problem of a doubly periodic array of elastic fibers contained in an elastic matrix and subjected to a transverse load. Their results reveal the dependence of the maximum principal stress versus the constituent stiffness ratio (E_f/E_m) for various fiber volume ratios. A

few years later, Yu and Sendeckyj (1974) used a complex variable approach to solve the problem of multiple inclusions embedded into an infinite matrix. Their results were subsequently specialized to cases of two and three inclusions thus providing us with further insight into the strength of the composite.

In this paper, we will construct an analytical solution for the 3D stress field of a matrix which has been reinforced in one of the directions with cylindrical fibers.

2 Formulation of the problem

Consider the equilibrium of a body which occupies the space $|x| < \infty, |y| < \infty, |z| \leq h$ and contains a periodic array of cylindrical inclusions of radius a, whose generators are parallel to the z-axis (see Fig. 1). The physical situation depicted here is that of a uniderectional composite plate that consists of a matrix where fibers are embedded into. For convenience, all quanties with the script (m) will refer to the matrix while quanties the with script f will refer to the fibers. The materials of both matrix and fibers will be assumed to be homogeneous, isotropic and linear elastic. At the interface, i.e. at $r = a$, perfect bonding will be assumed to prevail. As to loading, a uniform tensile stress σ_o is applied on the composite plate (see Fig. 1) which is in a direction perpendicular to the axis of the fibers. Furthermore, the surface $|z| = h$, for both regions, matrix and inclusion, will be assumed to be free of stress and constraints.

In the absence of body forces, the coupled differential equations governing the displacement functions $u_i^{(j)}$ are :

$$\frac{1}{1-2\nu_j}\frac{\partial e^{(j)}}{\partial x_i} + \nabla^2 u_i^{(j)} = 0; \quad i = 1,2,3; \; j = m, f \tag{1}$$

where ∇^2 is the Laplacian operator, ν_j is Poisson's ratio, $u_i^{(m)}$ and $u_i^{(f)}$ represent the displacement functions in the matrix and fibers respectively, and

$$e^{(j)} = \frac{\partial u_i^{(j)}}{\partial x_i} \; ; \; i = 1,2,3 \; ; \; j = m, f. \tag{2}$$

The stress-displacement relations are given by Hooke's law as

$$\sigma_{ik}^{(j)} = \lambda_j e_{ll}^{(j)} \delta_{ik} + 2G_j e_{ik}^{(j)} \tag{3}$$

where λ_j and G_j are the Lame constants describing the material properties of the matrix and of the inclusions.

As to boundary conditions, one must require that (see Fig. 2 for cell configuration)

$$at \qquad |z| = h: \qquad \sigma_{zz}^{(j)} = \tau_{xz}^{(j)} = \tau_{yz}^{(j)} = 0; \quad j = m, f. \tag{4}$$

$$at \qquad r = a: \quad u_r^{(m)} - u_r^{(f)} = u_\theta^{(m)} - u_\theta^{(f)} = u_z^{(m)} - u_z^{(f)} = 0. \tag{5}$$

$$\sigma_{rr}^{(m)} - \sigma_{rr}^{(f)} = \tau_{r\theta}^{(m)} - \tau_{r\theta}^{(f)} = \tau_{rz}^{(m)} - \tau_{rz}^{(f)} = 0 \tag{6}$$

Moreover, at $r = 0$ we require that all stresses and displacements be finite. the cell configuration boundaries AB and CD will be taken as planes of symmetry, thus satisfying the respective boundary conditions automatically. It remains, therefore, for us to satisfy only the continuity boundary conditions along the segment BC, i.e.

$$u_x^{(m)}(\theta) - u_x^{(m)}(\frac{\pi}{4}) = -u_x^{(m)}(\frac{\pi}{2} - \theta) + u_x^{(m)}(\frac{\pi}{4}) \tag{7}$$

$$u_y^{(m)}(\theta) - u_y^{(m)}(\frac{\pi}{4}) = -u_y^{(m)}(\frac{\pi}{2} - \theta) + u_y^{(m)}(\frac{\pi}{4}) \tag{8}$$

$$F_x^{(m)}(\theta) = F_x^{(m)}(\frac{\pi}{2} - \theta) \tag{9}$$

$$F_y^{(m)}(\theta) = F_y^{(m)}(\frac{\pi}{2} - \theta). \tag{10}$$

Fianlly, in order to complete the formulation of the problem, one must also require the resultant forces

$$\int_{BC} F_x ds = 0 \tag{11}$$

$$\int_{BC} F_y ds = b\sigma_o. \tag{12}$$

It is found convenient at this stage to seek the solution to equation (1) in the form:

$$u_i^{(j)} = u_i^{(p)(j)} + u_i^{(c)(j)} \; ; \; i = 1,2,3; \; j = m, f \tag{13}$$

where the first term represents the particular solution and the second term the complementary solution.

3 Method of Solution

A generalized analytical solution to a class of three-dimensional problems which arise in elastostatics has been constructed by Folias (1975 , 1990a). The solution was subsequently used, Folias and Wang (1990b), to solve for the 3D stress field in a plate which has been weakened by a hole. This work was later extended to the solution of an isotropic inclusion embedded into a matrix, Penado and Folias (1989). On the bases of these results, one may now assume the solution to system (1), which automatically satisfies the boundary conditions at the plate faces eq. (4), in the form [2] :

$$\begin{aligned} u^{(c)(j)} = & \frac{1}{m_j - 2} \sum_{\nu=1}^{\infty} \frac{\partial^2 H_\nu^{(j)}}{\partial x^2} \{2(m_j - 1) f_1(\beta_\nu z) + m_j f_2(\beta_\nu z)\} \\ & + \sum_{n=1}^{\infty} \left\{ -\frac{\partial^2 H_n^{(j)}}{\partial x^2} + \alpha_n^2 H_n^{(j)} \right\} cos\,(\alpha_n h)\, cos\,(\alpha_n z) \\ & + \lambda_1^{(j)} - y \frac{\partial \lambda_3^{(j)}}{\partial x} + \frac{1}{m_j + 1} z^2 \frac{\partial^2 \lambda_3^{(j)}}{\partial x \partial y} \end{aligned} \tag{14}$$

$$v^{(c)(j)} = \frac{1}{m_j - 2} \sum_{\nu=1}^{\infty} \frac{\partial^2 H_\nu^{(j)}}{\partial x \partial y} \{2(m_j - 1) f_1(\beta_\nu z) + m_j f_2(\beta_\nu z)\}$$

[2] Note that because of symmetry in the present problem, one needs only to consider the region $0 \leq \theta \leq \pi/2$.

$$-\sum_{n=1}^{\infty}\frac{\partial^2 H_n^{(j)}}{\partial x\partial y}\cos(\alpha_n h)\cos(\alpha_n z) \tag{15}$$

$$+\frac{3m_j-1}{m_j+1}\lambda_3^{(j)}+\lambda_2^{(j)}-y\frac{\partial\lambda_3^{(j)}}{\partial y}-\frac{1}{m_j+1}z^2\frac{\partial^2\lambda_3^{(j)}}{\partial x^2}$$

$$w^{(c)(i)}=\frac{1}{m_j-2}\sum_{\nu=1}^{\infty}\frac{\partial H_\nu^{(j)}}{\partial x}\beta_\nu\{(m_j-2)f_3(\beta_\nu z)-m_j f_4(\beta_\nu z)\}-\frac{1}{m_j+1}z\frac{\partial\lambda_3^{(j)}}{\partial y} \tag{16}$$

From which the stresses can easily be obtained as:

$$\frac{1}{2G_j}\sigma_{xx}^{(c)(j)}=\frac{1}{m_j-2}\sum_{\nu=1}^{\infty}\left\{2\beta_\nu^2\frac{\partial H_\nu^{(j)}}{\partial x}f_1(\beta_\nu z)\right.$$

$$\left.+\frac{\partial^3 H_\nu^{(j)}}{\partial x^3}[2(m_j-1)f_1(\beta_\nu z)+m_j f_2(\beta_\nu z)]\right\} \tag{17}$$

$$+\sum_{n=1}^{\infty}\left\{-\frac{\partial^3 H_n^{(j)}}{\partial x^3}+\alpha_n^2\frac{\partial H_n^{(j)}}{\partial x}\right\}\cos(\alpha_n h)\cos(\alpha_n z)$$

$$+\frac{\partial\lambda_1^{(j)}}{\partial x}-y\frac{\partial^2\lambda_3^{(j)}}{\partial x^2}+\frac{2}{m_j+1}\frac{\partial\lambda_3^{(j)}}{\partial y}+\frac{1}{m_j+1}z^2\frac{\partial^3\lambda_3^{(j)}}{\partial x^2\partial y}$$

$$\frac{1}{2G_j}\sigma_{yy}^{(c)(j)}=\frac{1}{m_j-2}\sum_{\nu=1}^{\infty}\left\{2\beta_\nu^2\frac{\partial H_\nu^{(j)}}{\partial x}f_1(\beta_\nu z)\right.$$

$$\left.-(\frac{\partial^3 H_\nu^{(j)}}{\partial x^3}-\beta_\nu^2\frac{\partial H_\nu^{(j)}}{\partial x})[2(m_j-1)f_1(\beta_\nu z)+m_j f_2(\beta_\nu z)]\right\} \tag{18}$$

$$+\sum_{n=1}^{\infty}\left\{\frac{\partial^3 H_n^{(j)}}{\partial x^3}-\alpha_n^2\frac{\partial H_n^{(j)}}{\partial x}\right\}\cos(\alpha_n h)\cos(\alpha_n z)$$

$$+\frac{2m_j}{m_j+1}\frac{\partial\lambda_3^{(j)}}{\partial y}-\frac{\partial\lambda_1^{(j)}}{\partial x}+y\frac{\partial^2\lambda_3^{(j)}}{\partial x^2}-\frac{1}{m_j+1}z^2\frac{\partial^3\lambda_3^{(j)}}{\partial x^2\partial y}$$

$$\frac{1}{2G_j}\sigma_{zz}^{(c)(j)} = -\frac{m_j}{m_j-2}\sum_{\nu=1}^{\infty}\frac{\partial H_\nu^{(j)}}{\partial x}\beta_\nu^2 f_2(\beta_\nu z) \tag{19}$$

$$\frac{1}{2G_j}\tau_{xy}^{(c)(j)} = \frac{1}{m_j-2}\sum_{\nu=1}^{\infty}\frac{\partial^3 H_\nu^{(j)}}{\partial x^2\partial y}\{2(m_j-1)f_1(\beta_\nu z)+m_j f_2(\beta_\nu z)\}$$

$$-\sum_{n=1}^{\infty}\left\{\frac{\partial^3 H_n^{(j)}}{\partial x^2\partial y}-\frac{1}{2}\alpha_n^2\frac{\partial H_n^{(j)}}{\partial y}\right\}\cos(\alpha_n h)\cos(\alpha_n z) \tag{20}$$

$$+\frac{m_j-1}{m_j+1}\frac{\partial\lambda_3^{(j)}}{\partial x}+\frac{\partial\lambda_2^{(j)}}{\partial x}-y\frac{\partial^2\lambda_3^{(j)}}{\partial x\partial y}-\frac{1}{m_j+1}z^2\frac{\partial^3\lambda_3^{(j)}}{\partial x^3}$$

$$\frac{1}{2G_j}\tau_{yz}^{(c)(j)} = -\frac{m_j}{m_j-2}\sum_{\nu=1}^{\infty}\frac{\partial^2 H_\nu^{(j)}}{\partial x\partial y}\beta_\nu\{f_3(\beta_\nu z)+f_4(\beta_\nu z)\}$$

$$+\frac{1}{2}\sum_{n=1}^{\infty}\alpha_n\frac{\partial^2 H_n^{(j)}}{\partial x\partial y}\cos(\alpha_n h)\sin(\alpha_n z) \tag{21}$$

$$\frac{1}{2G_j}\tau_{xz}^{(c)(j)} = -\frac{m_j}{m_j-1}\sum_{n=1}^{\infty}\frac{\partial^2 H_\nu^{(j)}}{\partial x^2}\beta_\nu\{f_3(\beta_\nu z)+f_4(\beta_\nu z)\}$$

$$+\frac{1}{2}\sum_{n=1}^{\infty}[\frac{\partial^2 H_n^{(j)}}{\partial x^2}-\alpha_n^2 H_n^{(j)}]\alpha_n\cos(\alpha_n h)\sin(\alpha_n z), \tag{22}$$

where

$$\alpha_n = \frac{n\pi}{h}, n = 1,2,3,\ldots, \tag{23}$$

β_ν are the roots of the equation

$$\sin(2\beta_\nu h) = -(2\beta_\nu h), \tag{24}$$

$H_\nu^{(j)}$ and $H_n^{(j)}$ are functions of x and y which satisfy the reduced wave equation:

$$(\frac{\partial^2}{\partial x^2}+\frac{\partial^2}{\partial y^2}-\beta_\nu^2)\frac{\partial H_\nu^{(j)}}{\partial x} = 0 \tag{25}$$

$$(\frac{\partial^2}{\partial x^2} + \frac{\partial^2}{\partial y^2} - \alpha_n^2)\frac{\partial H_n^{(j)}}{\partial y} = 0 \tag{26}$$

$\lambda_1^{(j)}, \lambda_2^{(j)}$ and $\lambda_3^{(j)}$ are two dimensional harmonic functions, and

$$f_1(\beta_\nu z) \equiv \cos(\beta_\nu h)\cos(\beta_\nu z) \tag{27}$$

$$f_2(\beta z) \equiv \beta_\nu h \sin(\beta_\nu h)\cos(\beta_\nu z) - \beta_\nu z \cos(\beta_\nu h)\sin(\beta_\nu z) \tag{28}$$

$$f_3(\beta_\nu z) \equiv \cos(\beta_\nu h)\sin(\beta_\nu z) \tag{29}$$

$$f_4(\beta_\nu z) \equiv \beta_\nu h \sin(\beta_\nu h)\sin(\beta_\nu z) + \beta_\nu z \cos(\beta_\nu h)\cos(\beta_\nu z). \tag{30}$$

Examining the nature of the boundary conditions, we furthermore construct the solution to equations (25) and (26) in the form:

$$H_\nu^{(m)} = \sum_{k=0}^{\infty} a_k K_k(\beta_\nu r)\cos(2k\theta) \tag{31}$$

$$H_\nu^{(m)} = \sum_{k=0}^{\infty} \{a_k K_{2k}(\beta_\nu r) + \tilde{a}_k I_{2k}(\beta_\nu r)\}\cos(2k\theta) \tag{31}$$

$$H_\nu^{(f)} = \sum_{k=0}^{\infty} b_k I_{2k}(\beta_\nu r)\cos(2k\theta) \tag{32}$$

$$H_n^{(m)} = \sum_{k=0}^{\infty} \{c_k K_{2k}(\alpha_n r) + \tilde{c}_k I_{2k}(\alpha_n r)\}\sin(2k\theta) \tag{33}$$

$$H_n^{(f)} = \sum_{k=0}^{\infty} d_k I_{2k}(\alpha_n r)\sin(2k\theta). \tag{34}$$

$$\lambda_1^{(m)} = \sum_{k=0}^{\infty} \left\{\frac{A_k}{r^{2k+1}} + \tilde{A}_k r^{2k+1}\right\}\sin(2k+1)\theta \tag{35}$$

$$\lambda_2^{(m)} = \sum_{k=0}^{\infty} \left\{\frac{A_k}{r^{2k+1}} + \tilde{A}_k r^{2k+1}\right\}\cos(2k+1)\theta \tag{36}$$

$$\lambda_3^{(m)} = \sum_{k=0}^{\infty} \left\{\frac{B_k}{r^{2k+1}} + \tilde{B}_k r^{2k+1}\right\}\cos(2k+1)\theta \tag{37}$$

$$\lambda_1^{(f)} = \sum_{k=0}^{\infty} (-1)^k E_k r \; sin \; (2k+1)\theta \tag{38}$$

$$\lambda_2^{(f)} = \sum_{k=0}^{\infty} (-1)^k E_k r \; cos \; (2k+1)\theta \tag{39}$$

$$\lambda_3^{(f)} = \sum_{k=0}^{\infty} (-1)^k G_k r \; cos \; (2k+1)\theta \tag{40}$$

where $I_k(\beta r)$ and $K_k(\beta r)$represent the modified Bessel functions of the first and second kind and $a_k, b_k, c_k, d_k, A_k, B_k, E_k$ and G_k etc. are arbitrary constants to be determined from the remaining boundary conditions (5) - (12). Upon substitution of equations (14) - (40) into equations (5) - (12) one arrives at a system of twelve equations involving series in z. The system may then be solved numerically for the unknown coefficients. Perhaps it may be worth noting that in our numerical analysis we satisfied first the boundary conditions at $r = a$ by using well over 200 roots. The method of solution, as well as the rate of convergence of these series, is similar to that found by Penado and Folias (1989, see reference for details). The system is sensitive to small changes and for this reason double precision was used throughout the numerical analysis.

4 Numerical results

Once the coefficients have numerically been determined, the stresses and displacements may then be calculated at any point in the body. Avoiding the long and tedious numerical details, the behavior of the stresses σ_{rr} and $\sigma_{\theta\theta}$ versus (z/h) and at $r = a$ and $\theta = 0$ are given by figures 3 and 4 respectively. It is noted that the stresses along the interior length of the fiber are essentially constant and that as one approaches the edge of the fiber length, a boundary layer is shown to exist. This sudden change suggests, therefore, the presence of a stress singularity at such regions. Indeed, a separate asymptotic analysis for the investigation of the local stress field, at such neighborhoods, shows the stresses to be proportional to $\rho^{-\alpha}$, where $\alpha = 0.249$ for a glass fiber/epoxy matrix interface (Folias 1989) and $\alpha = 0.318$ for a carbon fiber [3]/ epoxy matrix interface (Li and Folias 1990). It may also be noted that Figs 3 and 4 provide us with important information concerning the regions of applicability of macromechanical theories. The reader may recall that such theories predict the stress values at edges to be finite, except in the vicinity of an interface where the singularity strength is shown to be very weak (Wang and Choi, 1982; Folias, 1991). Thus, they tend to underestimate the actual stress levels at such edges, e.g. surface of a hole, surface of a crack etc. But, if one is to study damage evolution at such regions, the knowledge of the local stress field is essential. Be that as it may, a closer examination of Figs 3 and 4 shows the boundary layer region, for a transverse applied load, to be restricted to a distance of one fiber diameter away from the fiber edge. On the other hand, if the applied load is in the direction of the fiber axis, the boundary layer is then spread out to a distance of six fiber diameters away from the edge (Zhong and Folias 1991). Thus coupling between the macromechanical and micromechanical results may be desirable in predicting local damage due to fracture.

Returning to the stress profiles σ_{rr} and $\sigma_{\theta\theta}$ (Fig. 3 and 4) we note that the magnitude of the stresses decreases as the fiber volume fraction, V_f, increases. The decrease, however, is only noticed when the spacing of the fibers becomes less than four fiber diameters center to center. Figs 5 and 6 show typical stress profiles for σ_{rr} and $\sigma_{\theta\theta}$ as a function of G_f/G_m. It

[3] In this analysis the material of the carbon fiber is assumed to be transversely isotropic.

is interesting to note that the circumferencial stress $\sigma_{\theta\theta}$ decreases rapidly as the ratio (G_f/G_m) increases. For glass fiber/epoxy matrix $(G_f/G_m) = 16.67$, which implies that the $\sigma_{\theta\theta}$ stress is approximately zero. Thus, all things being equal, the controlling stress for possible crack failure is the radial stress σ_{rr} at the particular location of $\theta = 0$. For large (G_f/G_m) ratios, the radial stress reaches an asymptotic value. A similar result was also obtained by other researchers based on 2D considerations (e.g. Adams and Donen 1967). In Fig. 7, a plot of the radial stress on the interface boundary is shown to decrease as the angle θ increases. On the other hand, the shear stress $\tau_{r\theta}$ (See Fig. 8) vanishes at the two positions $\theta = 0°$ and 90° and attains its maximum value at $\theta \approx 45°$. The location of this maximum shifts slightly to the right as the ratio of (a/b) increases. Similar stress profiles also appear as one moves towards the free surface. At the free surface, the question arises as to whether the strength of the stress singularity is affected as the separation distance between fibers becomes smaller and smaller. While initially the authors believed that this may be the case, lately they believe that the singularity strength will not be altered but that the function multiplying the singular term is expected to change. Be that as it may, the subject is under further investigation.

5 Conclusions

A 3D micromechanical model has been developed to represent the response of a unidirectional composite plate subject to a transverse load. In this model, the fibers are considered to be cylindrical inclusions which are periodically embedded into the matrix. The material of both fibers and matrix is assumed to be linear, elastic and isotropic. The analysis has shown that, as the fiber volume fraction V_f increases, the radial stress σ_{rr} decreases by 30 to 40 percent. On the other hand, the circumferential stress $\sigma_{\theta\theta}$ is almost negligible. The stress profiles across the fiber length are almost constant except in the neighborhood of the fiber edge, where a boundary layer is shown to prevail. In this region, the stress field possesses a weak stress singularity which for a glass fiber/epoxy matrix composite is of the order 0.25. This result represents a departure from the results predicted by a macromechanical theory. This inconsistency is attributed to the fact that macromechanical theories tend to average the local effects throughout each

layer thickness, and as a result all stresses at the edge are predicted to be finite. Thus, the present analysis also provides us with important information regarding the regions of applicability of macromechanical theories.

A closer examination of the stress field reveals that, in the presence of a crack, the damaging stress for possible failure is the radial stress σ_{rr}, particularly at the location $\theta = 0$. Two types of failure immediately come to mind: a fiber/matrix interface crack and a radial matrix crack. In conjunction with this work, the former was recently considered by Folias (1991) and the latter by Folias and Liu (1991).

It is well recognized that void nucleation occurs more readily in a triaxial tensile stress field, a result which is consistent with experimental observations. Such a model for estimating the void nucleation stress may now be obtained, if in our previous analysis we let $G_f \to 0^+$. The physical situation depicted here is that of a matrix which has been weakened by a uniformly distributed periodic array of cylindrical voids or holes. Such an estimate may then serve as a lower bound for the transverse strength of a unidirectional composite plate. Without going into the numerical details, we plot in Fig. 9 the stress concentration factor $\sigma_{\theta\theta}$ through the thickness (z/h) and for a typical ratio of $(a/b) = 0.3$. It is noted that the s.c.f. is relatively constant throughout the interior and that it rises slightly as it reaches the vicinity of the free surface whereby it begins to drop rather abruptly. The characteristic stress profile is in agreement with that found by Folias and Wang (1990) for the case of one hole. the variation of the s.c.f. as a function of the ratio (a/b) is given by Fig. 10, where it may be noted that the void volume fraction in the matrix is given by

$$V_h = (\frac{\pi}{2})(\frac{a}{b})^2. \tag{41}$$

It is clear from this Fig. that the s.c.f. increases rather rapidly as the void volume fraction ratio increases. The result is in agreement with our physical expectations. A similar stress profile is also observed throughout the thickness including the plane [4] $z = h$. (see Fig. 11). Finally, in Figs. 12a and 12b we plot the variation of the s.c.f. on the planes $z = 0$ and $z = h$ as a function of the position angle θ and for different (a/b) ratios.

[4]Folias (1987) has shown that no stress singularity is present in the vicinity of the intersection of the hole surface and the free of stress plane.

It is noted that in the region $70° < \theta < 90°$ the s.c.f. is relatively flat. This is the region where a crack is most likely to initiate and subsequently propagate.

In closing, it may be appropriate here to note that the analysis may now be extended to also include row of fibers with different fiber orientations, which points to the concept of a laminated composite plate. This defines the subject of a subsequent paper.

References

Adams, D.F. and Doner, D.R., 1967, "Transverse Normal Loading of a Unidirectional Composite", J. of Composite Mateirals, Vol. 1, pp.152-164.

Chamis, C.C., 1975, Edited, "Composite Materials", Academic Press, Vol. 1-8.

Folias, E.S., 1989, "The 3D Stress Singularities at the Intersection of a Cylindrical Inclusion and a Free Surface", International Journal of Fracture, Vol. 39, pp. 25-34

Folias, E.S., 1987, "The 3D Stress Field at the Intersection of a Hole and a Free Surface", International Journal of Fracture, Vol. 35, No. 3, pp. 187-194.

Foilias, E.S., "A 3D Griffith Criterion for the Prediction of Failures in Plates Weakened by a Hole" under review, Journal of Applied Mechanics.

Folias, E.S. and Liu, J., 1990, "The 3D Stress Field of a Cylindrical Fiber Embedded into a Matrix with a Layer of Modified Matrix Around the Fiber" under review.

Folias, E.S. and Reuter, W., 1990, "A General 3D Analytical Solution for the Equilibrium of Linear Elastic Plates" International Journal of Computational Mechanics, Vol. 5, pp. 459-468.

Folias, E.S. and Wang, J.J., 1990, "On the Three-Dimensional Stress Field Around a Circular Hole in a Plate of an Arbitrary Thickness", Computational Mechanics, Vol. 6, No. 5.

Hull, D., 1981, "An Introduction to Composite Materials", Cambridge University Press.

Li, P.C. and Folias, E.S., "The 3D Stress Field of a Carbon Fiber Intersecting a Free Surface and Under the Action of a Uniform Transverse Load", in press, International Journal of Mechanics of Materials.

Penado, F.E., Folias, E.S., 1989, "The Three-Dimensional Stress Field Around a Cylindrical Inclusion in a Plate of Arbitrary Thickness", International Journal of Fracture, Vol. 39, pp. 129-146.

Yu, I.W. and Sendeckyj, G.P., 1974, "Multiple Circular Inclusion Problems in Plane Elastostatics," pp. 215-220.

Zhong, F.H. and Folias, E.S., "The 3D Stress Field of a Fiber Embedded into a Matrix and Subjected to an Axial Load", under review International Journal of Computational Mechanics.

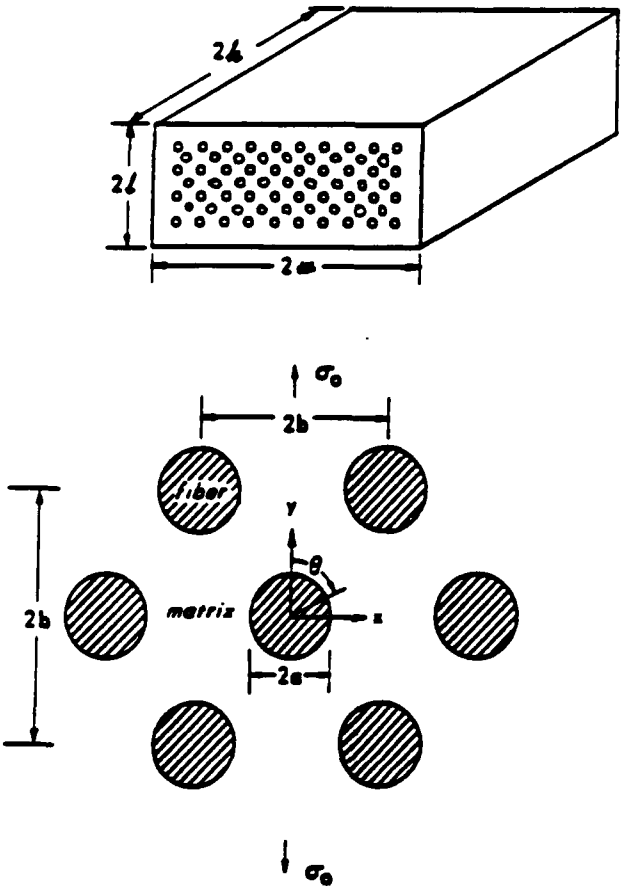

Fig. 1. Geometrical configuration

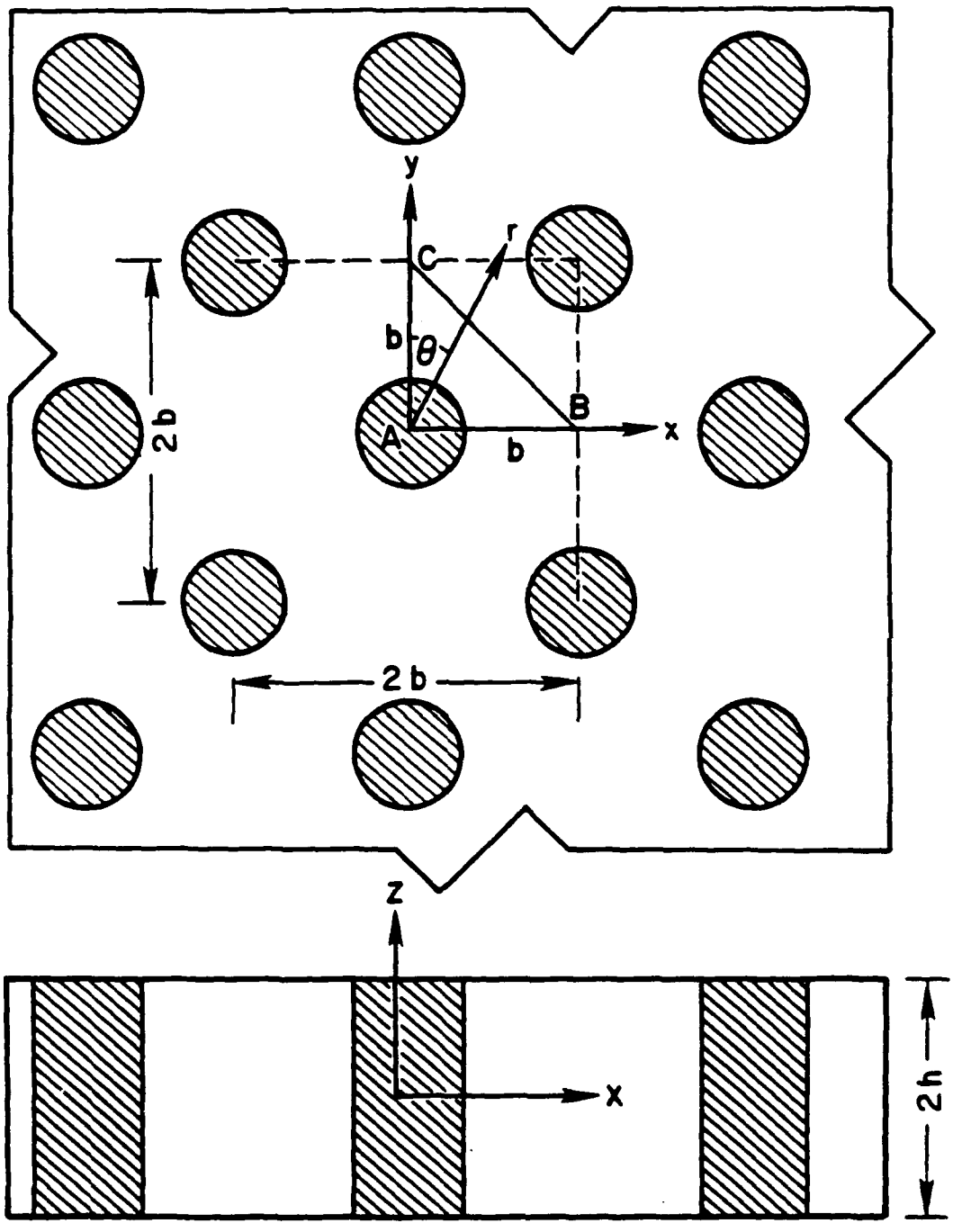

Fig. 2. Local geometrical configuration

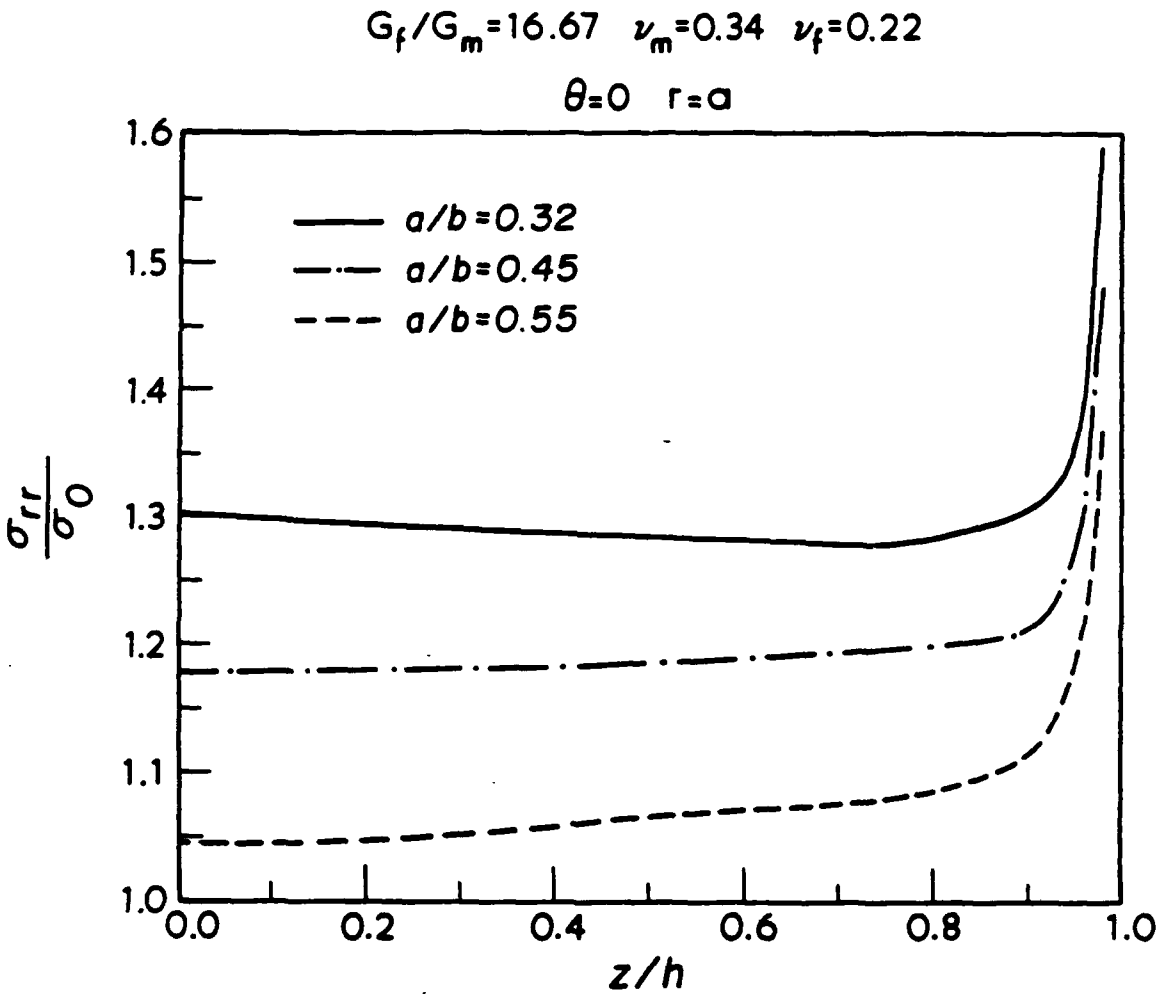

Fig. 3. Radial stress σ_{rr} versus thickness (z/h) at the position $r = a$ and $\theta = 0$.

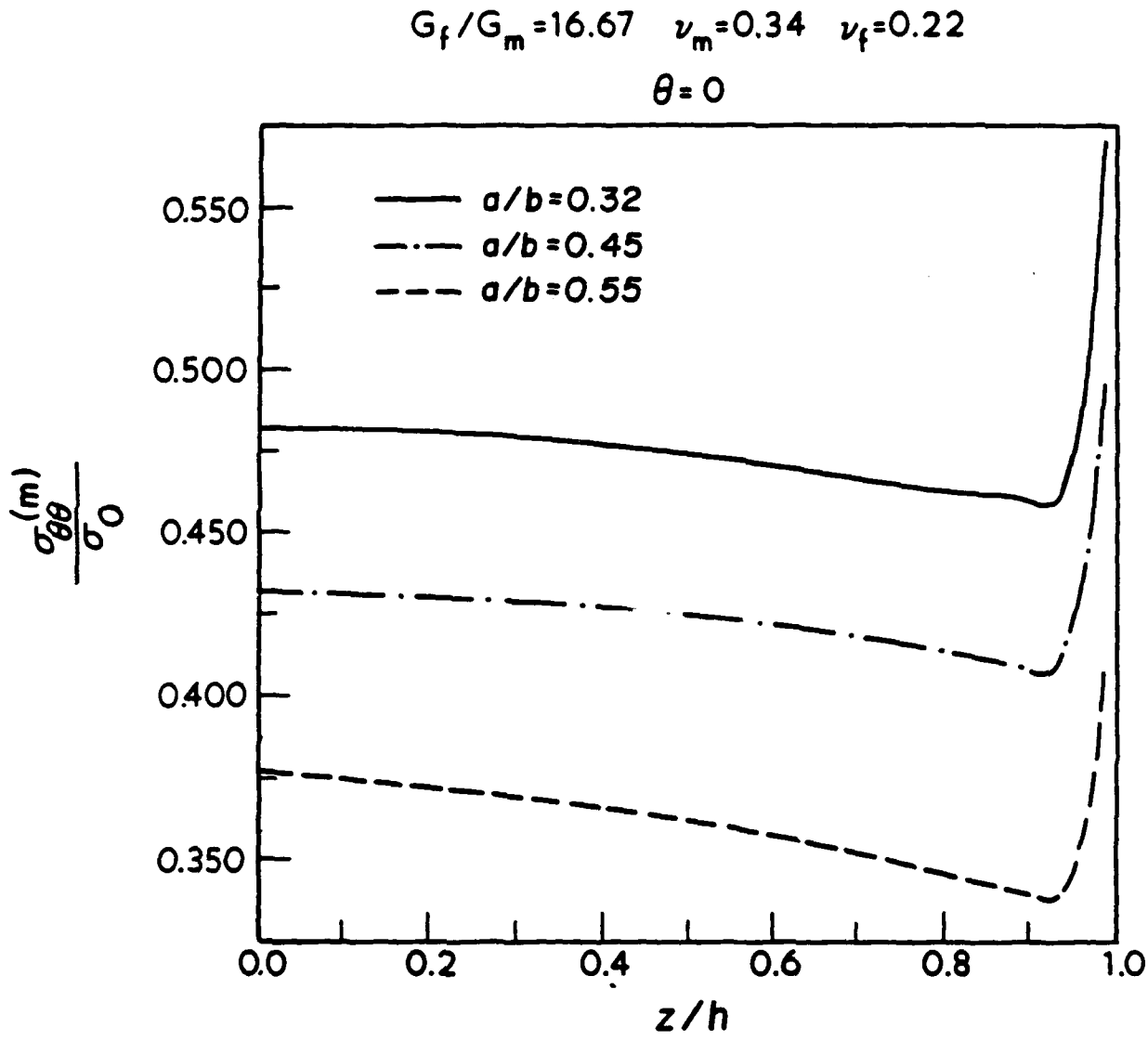

Fig. 4. Circumferential stress $\sigma_{\theta\theta}$ versus thickness (z/h), athe position $r = a$

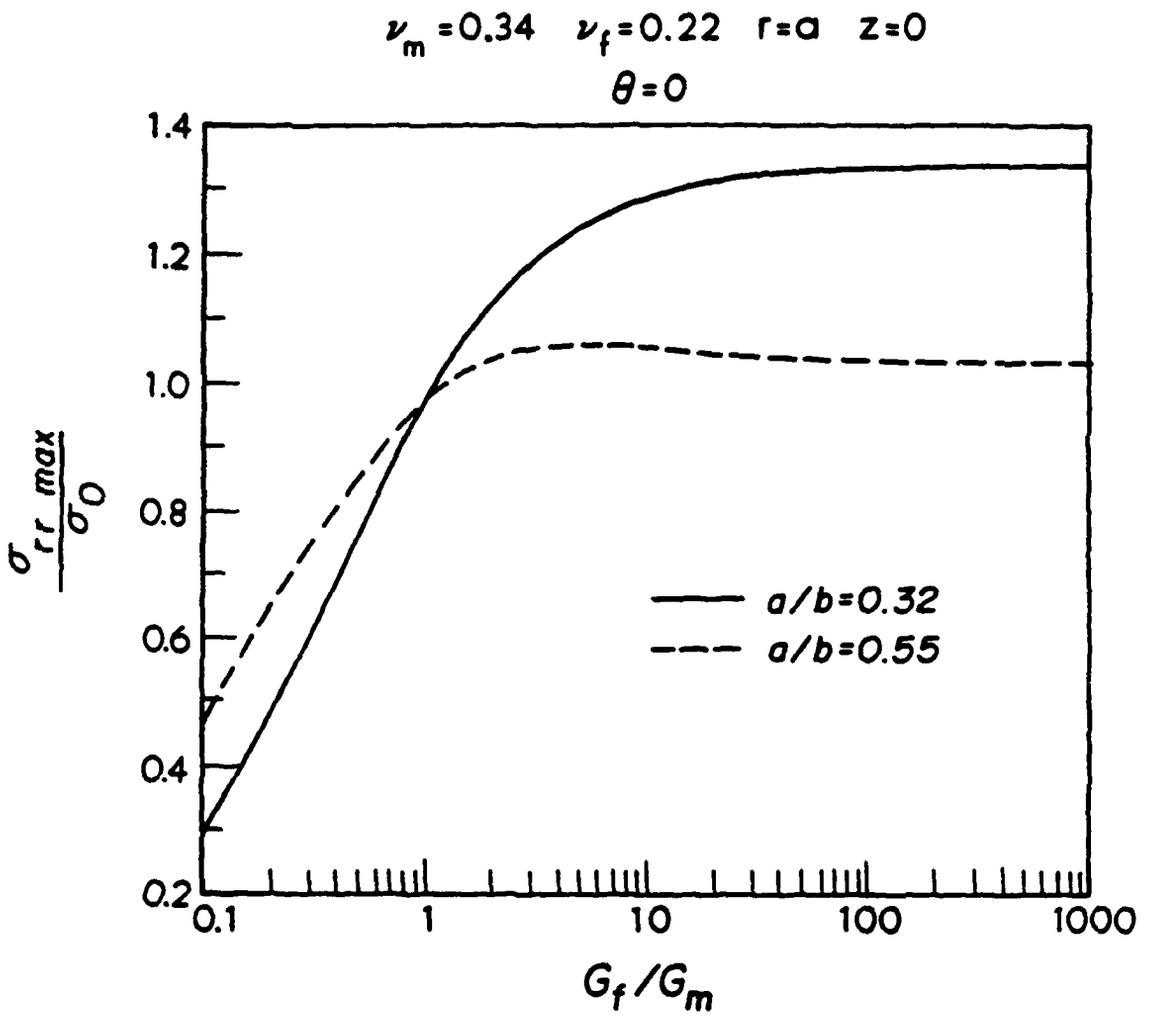

Fig. 5. Radial stress versus the ratio G_f/G_m

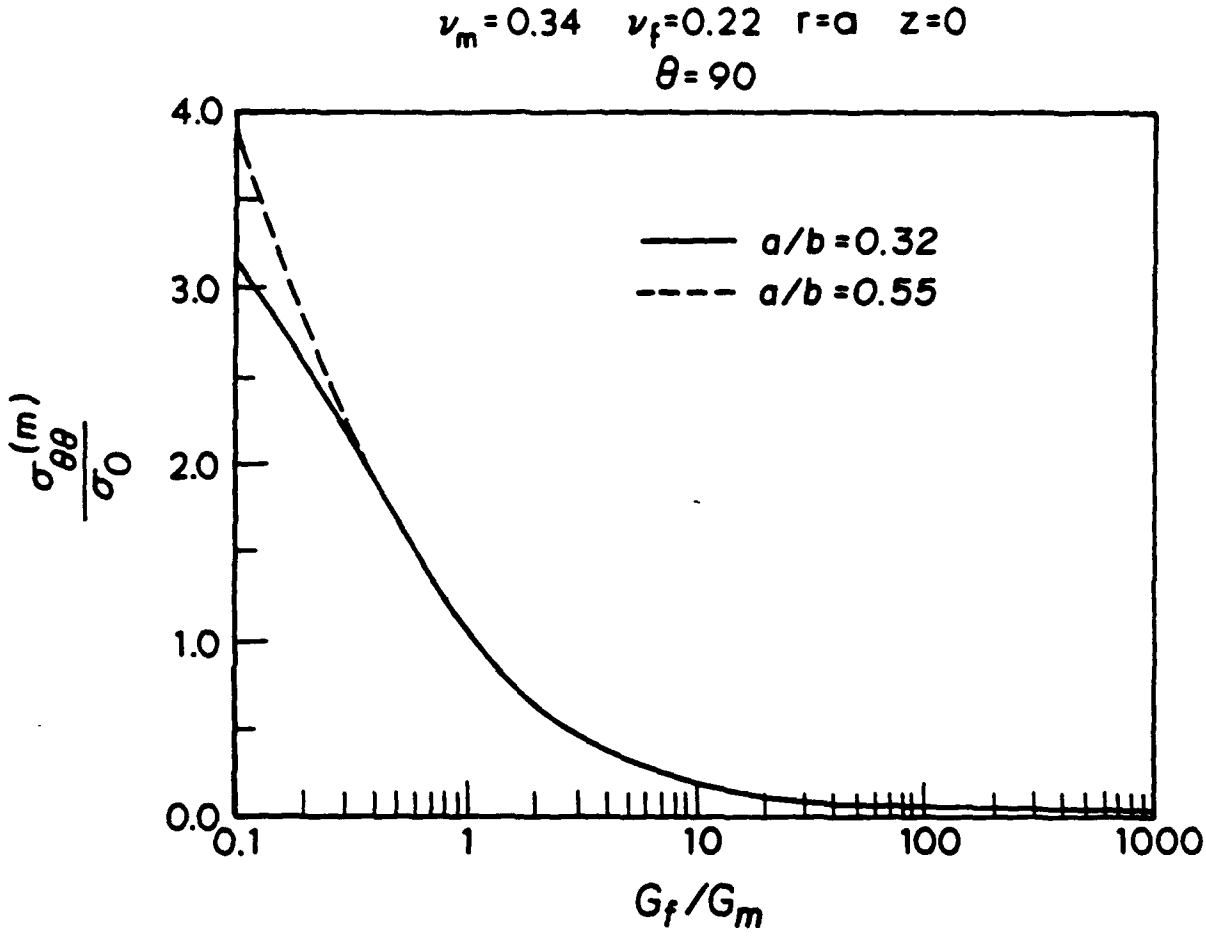

Fig. 6. Circumferential stress versus the ratio G_f/G_m.

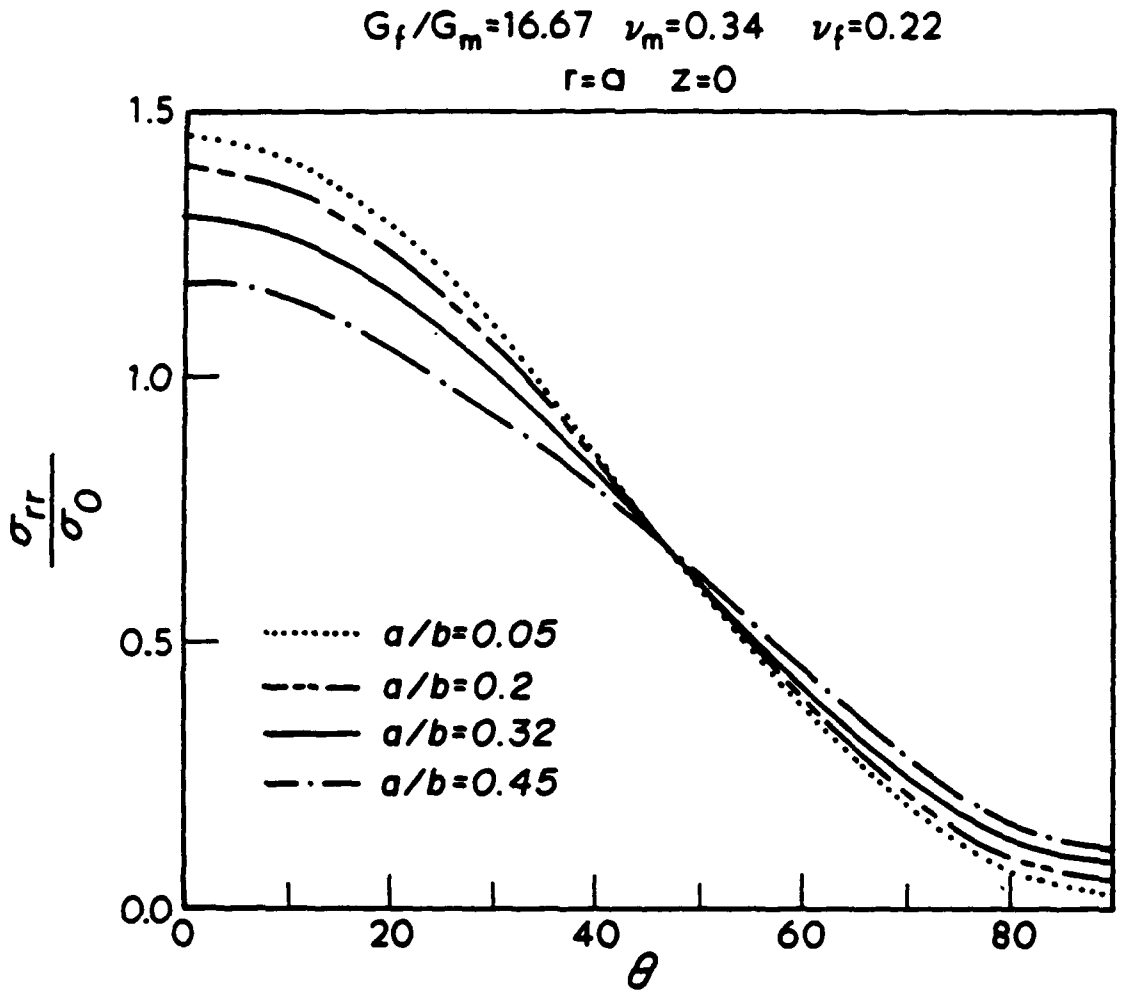

Fig. 7. Radial stress versus θ, at $r = a$.

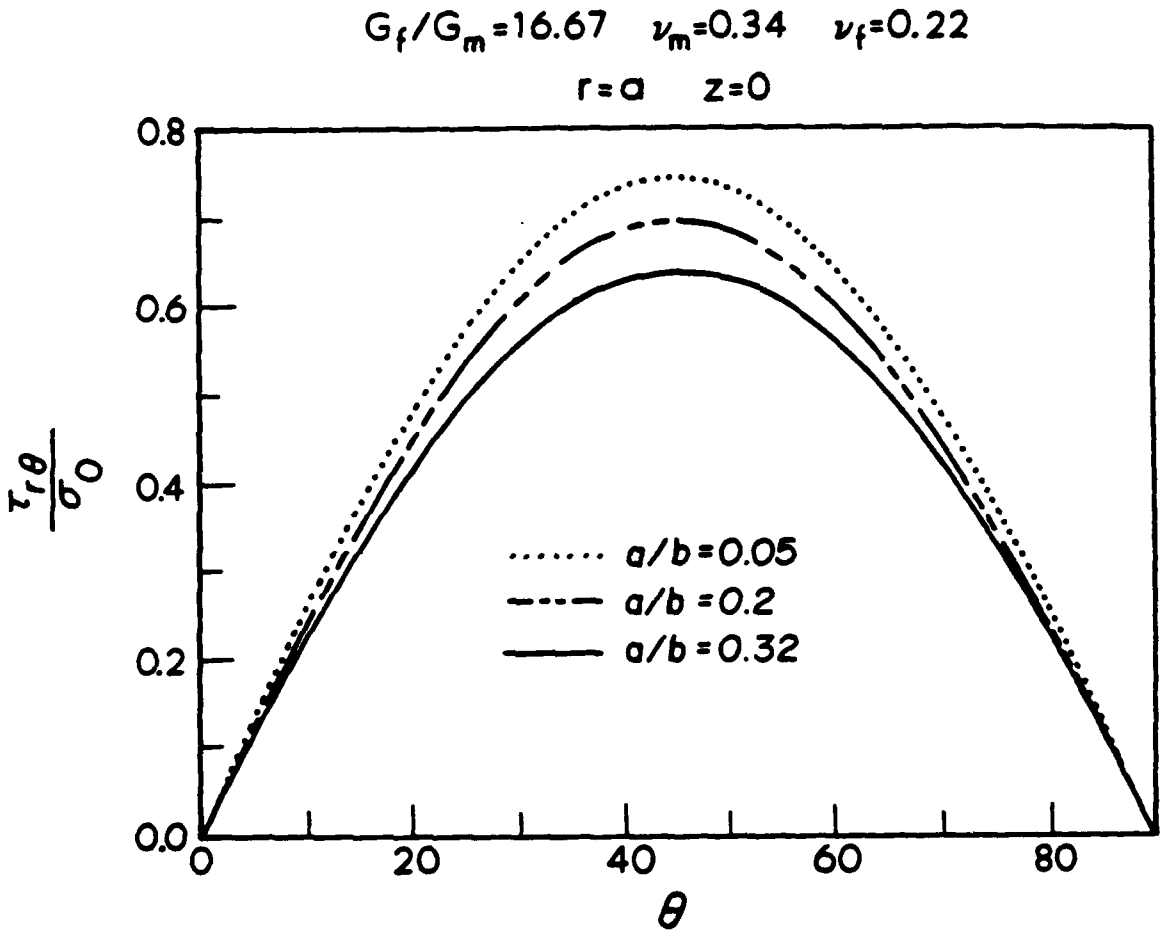

Fig. 8. Shear stress $\tau_{r\theta}$ versus θ, at $r = a$.

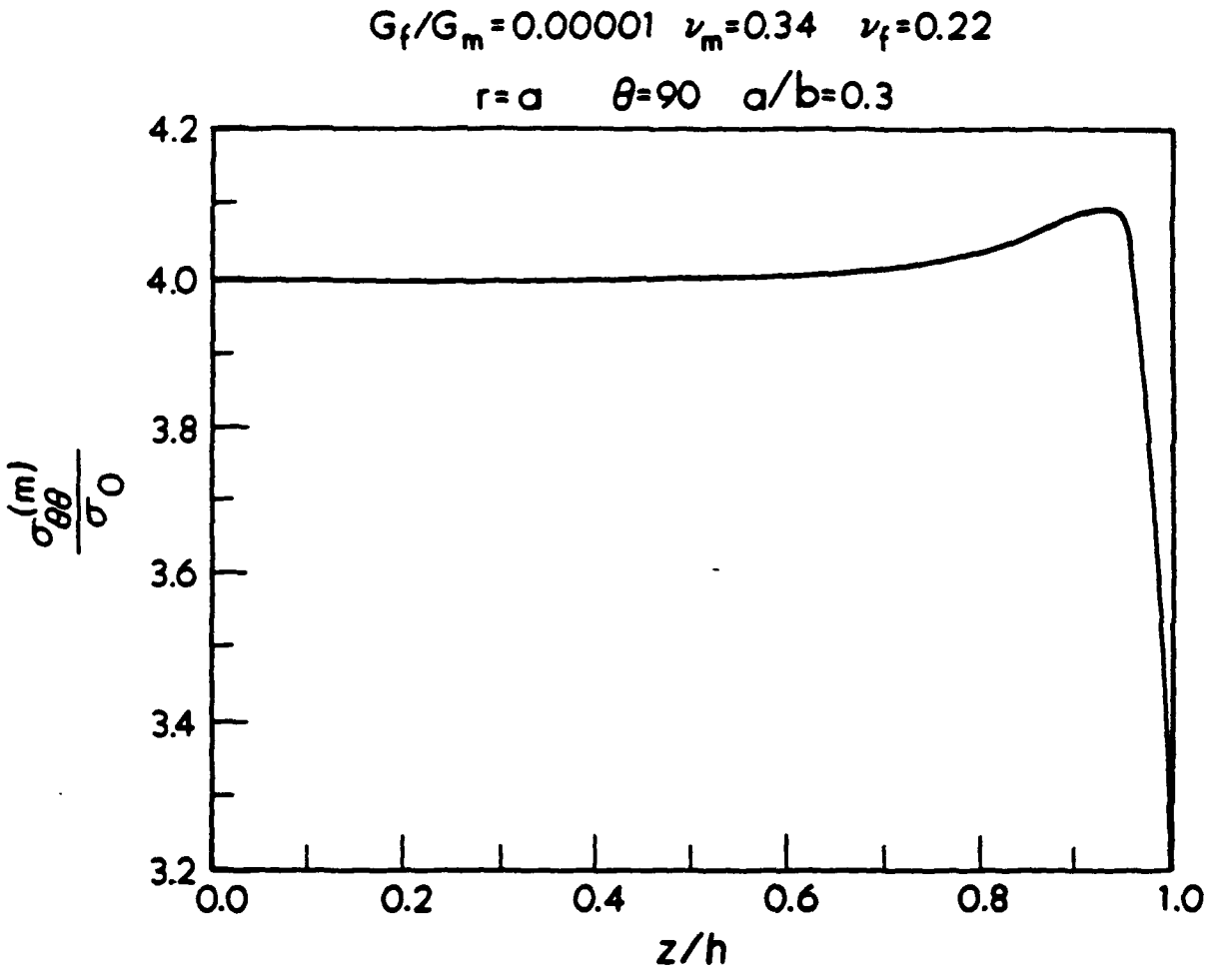

Fig. 9. The stress concentration factor versus the thickness (z/h) for a periodic array of holes.

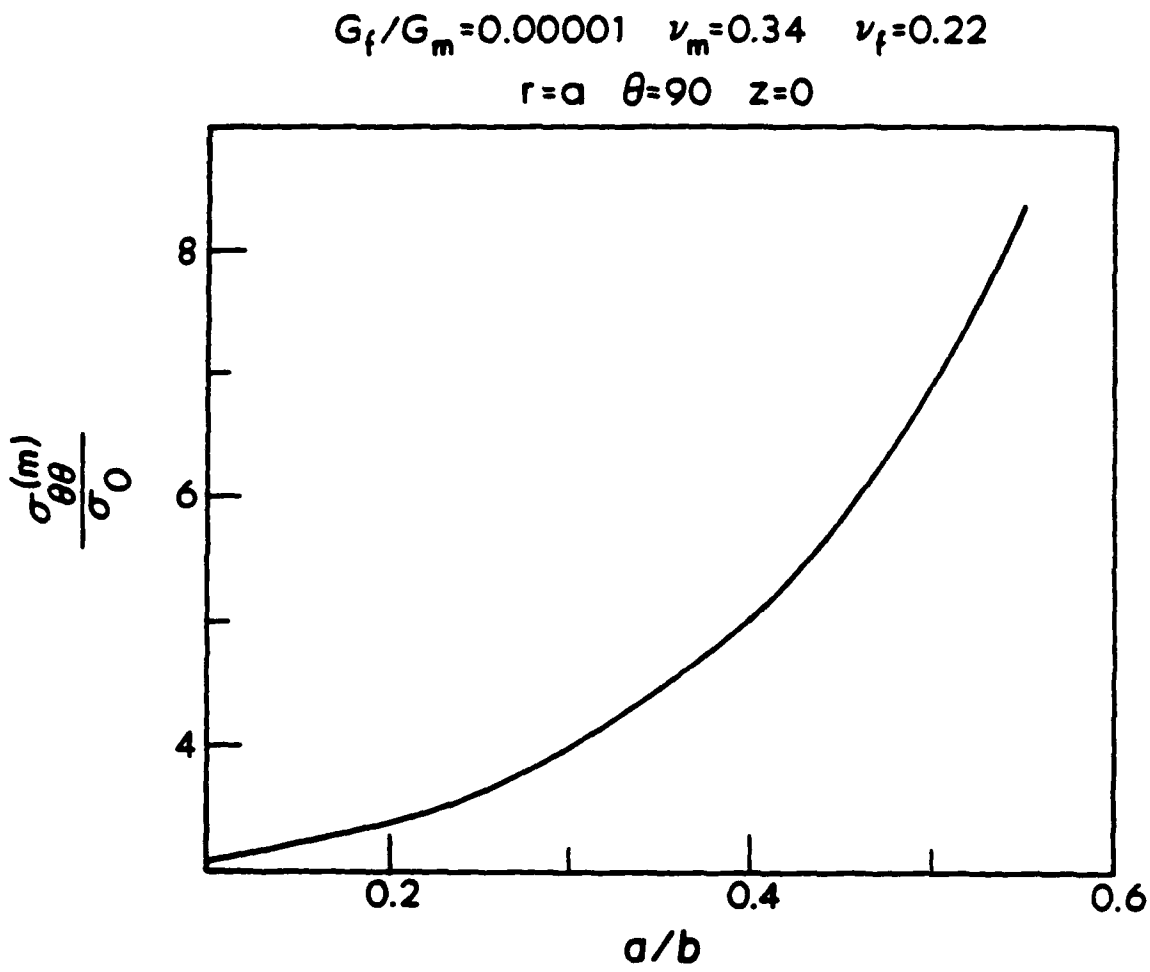

Fig. 10. The stress concentration factor versus the ratio a/b, at $z = 0$.

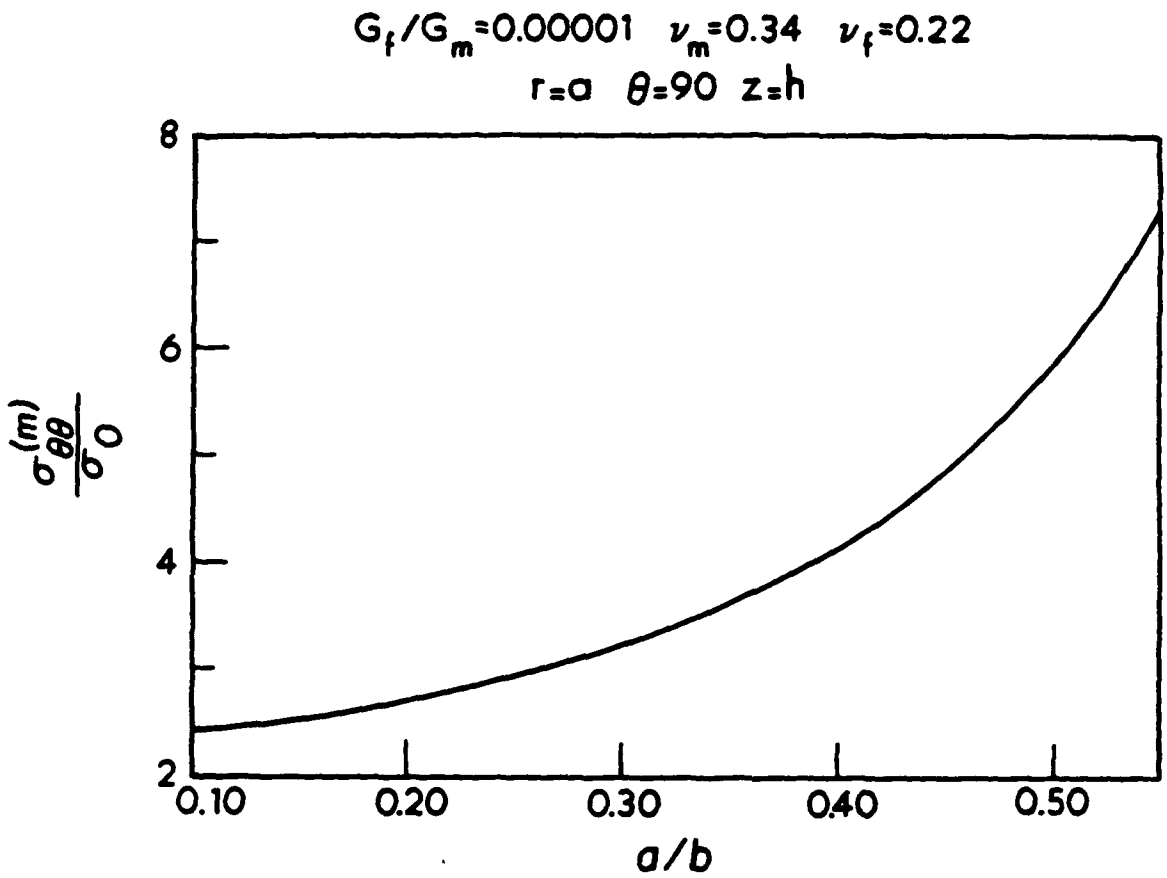

Fig. 11. The stress concentration factor versus the ratio a/b, at $z = h$.

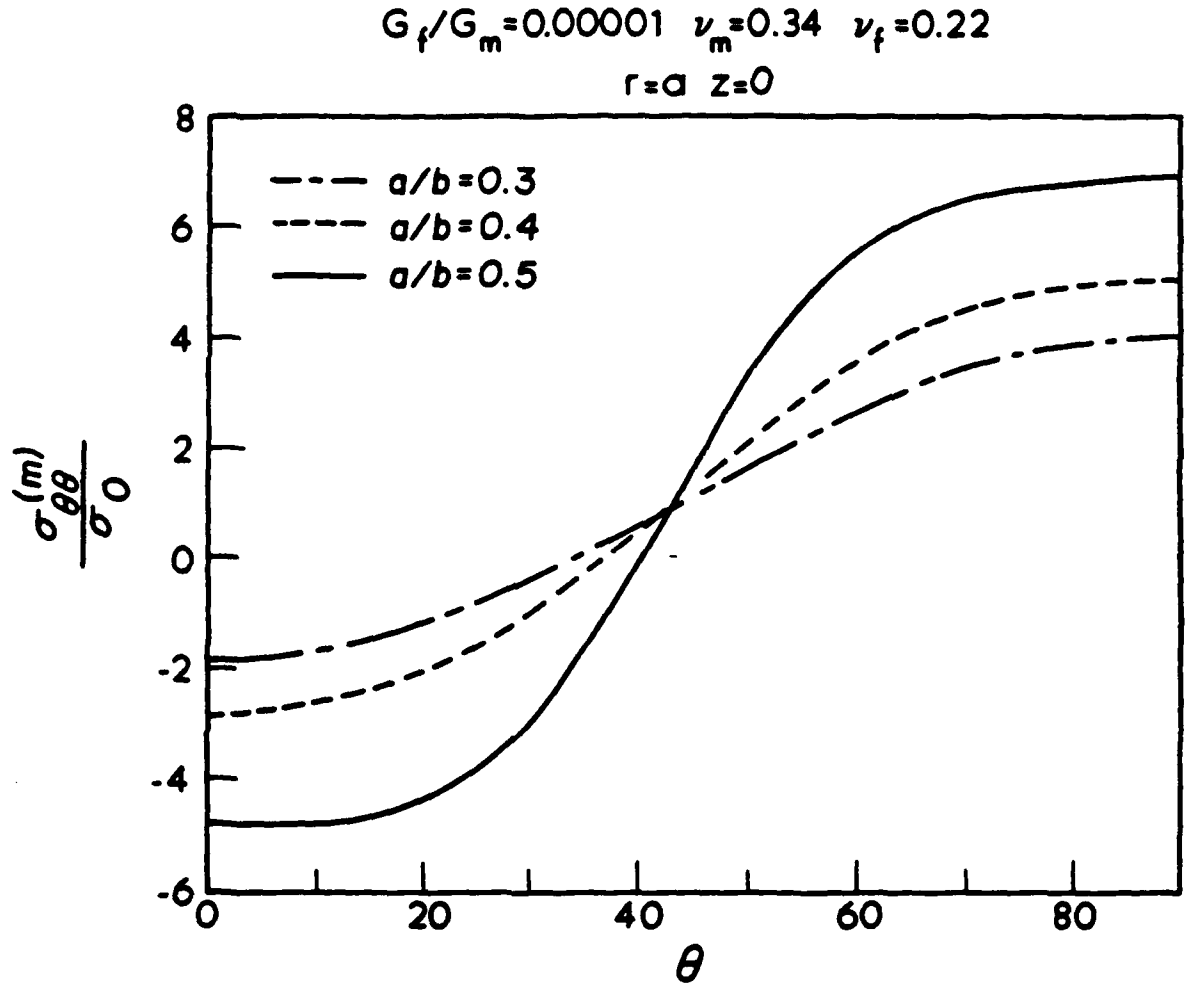

Fig. 12a. The stress concentration factor versus θ, at $z = 0$.

PART II

EDGE EFFECT OF A CARBON FIBER MEETING A SURFACE

by

C. C. Li* and E. S. Folias**

Department of Mechanical Engineering
University of Utah
Salt Lake City, Utah 84112

* Graduate Student
** Professor

Abstract

This paper investigates the free edge effect on the stress field of a carbon fiber, which is embedded into an epoxy matrix. The fiber is assumed to possess cylindrical symmetry and to be transversely isotropic. The matrix is assumed to be of an isotropic material. The stress field is induced by a uniform tension applied on the matrix at points far away from the fiber surface.

The displacement and stress fields are explicitly derived and a stress singularity is shown to prevail. The singularity strength is shown to be a function of the material constants of the fiber as well as those of the matrix. Finally, the displacement and stress profiles are plotted as a function of the angle ϕ which is measured from the free surface.

1. Introduction

Quite often in engineering practice, structures are composed of two elastic materials with different properties which are bonded together over some surface. Such type of problem has been investigated from a 2D point of view by many researchers and the results can be found in the literature. For example, Knein (1927) considered the plane strain problem of an orthogonal elastic wedge bonded to a rigid base. Rongved (1955) investigated the problem of two bonded elastic half-spaces subjected to a concentrated force in the interior. Subsequently, Williams (1959) studied the stress field around a fault or a crack in dissimilar media. The work was then generalized by Rice and Sih (1965) to also include arbitrary angles.

It was not until 1968 that Bogy (1968) considered the general problem of two bonded quarter-planes of dissimilar isotropic, elastic materials subjected to arbitrary boundary tractions. The problem was solved by an application of the Mellin transform in conjunction with the Airy stress function. The same author (1971) extended his work to also include dissimilar wedges of arbitrary angles. Shortly thereafter, Hein and Erdogan (1971), using the same method of solution, independently reproduced the results by Bogy. Finally, Westmann (1975) studied the case of a wedge of an arbitrary angle which was bonded along a finite length to a half-space. His analysis showed the presence of two singularities close to each other. Thus, elimination of the first singular term does not lead to a bounded stress field since the second singularity is still present.

Based on 3D consideration, Luk and Keer (1979) investigated the stress field in an elastic half-space containing a partially embedded axially-loaded, rigid cylindrical rod. The problem was formulated in terms of Hankel integral transforms and was finally cast into a system of coupled singular integral equations the solution of which was sought numerically. The authors were able, however, to extract in the limit from the integral equations the characteristic equation governing the singular behavior at the intersection of the free surface and that of the rigid inclusion. Their result was in agreement with that obtained by Williams (1952) for a right-angle corner with fixed-free boundary conditions.

Haritos and Keer (1979) investigated the stress field in a half-space containing an embedded rigid block under conditions of plane strain. The problem was formulated by cleverly superimposing the solutions to the problem of horizontal and vertical line inclusions beneath an elastic half-space. By isolating the pertinent terms, the authors were

able to extract directly from the integral equations the order of the stress singularity at both corners. Both results are in agreement with the Williams solution. Moreover, the authors point out the importance of the second singularity to the results of the load transfer problems.

With the advancement of composites and their extensive use in the aerospace industry, problems for the determination of the stress and displacement fields around inclusions have drawn considerable attention. For instance, Goodier (1933) investigated the disturbing effect of small spherical and cylindrical inclusions on an otherwise uniform stress distribution plate. Numerical results were presented for flaws, perfectly-bonded rigid inclusions and slag globules cases. Hardiman (1952) used the complex variable method to treat the elliptic inclusion problem, he was the first to find that a uniform applied load at infinity induces a constant state of stress within an elliptic inclusion. The work was later generalized by Sendeckyj (1970) to include the solutions of the elastic curvilinear inclusion problems. It was not until 1979 that Tirosh, Katz and Lifschuetz (1979) studied the stress interaction of a single fiber, embedded in an elastic matrix, with a micro-crack situated along or near the interface. They found that the radial tensile stress component σ_{rr} is higher than the tangential component $\sigma_{\theta\theta}$, and the location r at which the maximum stress takes place is not on the interface but at a small distance ahead, depending on the Poisson's ratio of the matrix. Dundurs(1989) noticed that the stresses in a body that contains rigid inclusions and is subjected to a specified surface traction depend on the Poisson's ratio of the materials. If the Poisson's ratio is set equal to one we recover the case of plane strain while if it is set equal to infinity we recover the case of plane stress.

In the area of multiple or periodical inclusions problems, Adams and Doner (1967) obtained a 2D numerical solution by a systematic overrelaxation procedure for a plate containing a rectangular array of inclusions embedded in an elastic matrix and subjected to a uniform normal transverse stress at infinity. At the same time, Goree (1967) presented a solution for the stress and displacement distributions in an infinite elastic matrix containing two perfectly-bonded rigid cylindrical inclusions of different radii. Subsequently, Haener and Ashbaugh (1967) used the displacement potentials method to express the stress distributions in a unidirectional multiple fibers composite plate under external and residual loads. Marloff and Daniel (1969) used a standard stress-freezing technique to determine the 3D stress distribution in the matrix of a unidirectional composite plate subjected to matrix shrinkage and normal transverse load. Based on Sendeckj's previous work, Yu and Sendeckj (1974) extended their study by means of the Schwarz alternating method to the

case of an infinite elastic matrix containing random number of elastic inclusions. Moreover, Adams and Crane (1984) studied a microscopic region of a unidirectional composite plate by the finite element micromechanical analysis using a generalized plane strain formulation. Finally, Keer, Dundurs and Kiattikomol (1973) studied the phenomena of the separation of a smooth circular inclusion from a matrix which is subjected to an uniform load. Using finite integral transforms, the problem of finding the extension of separation and the contact pressure is reduced to the solution of a Fredholm integral equation with a weakly singular Kernel.

Recently, Folias (1989) examined the local stress field in the neighborhood where a fiber embeddded into an epoxy matrix meets a free surface. In this analysis, Folias assumed the fiber and the matrix to be isotropic but of different material constants. The analysis showed that the stress field in this vicinity to be singular. Moreover, the 3D analysis showed that for the case of a cylindrical inclusion, the order of the singularity strength is precisely that which was reported by Bogy (1968) based on 2D consideration. In the present paper the analysis is extended to also include a transversely isotropic fiber, e.g. carbon fiber, and the explicit 3D displacement and stress fields are recovered.

2. Formulation of the problem

Consider the equilibrium of a cylindrical carbon fiber of radius a which is embedded into a homogeneous, isotropic and linear elastic matrix that occupies the space $|x| < \infty$, $|y| < \infty$ and $|z| \le h$. The fiber is assumed to be of a transversely isotropic material with different material properties than those of the matrix. Moreover, the axis of the fiber is assumed to intersect the bounding plane $z = \pm h$ perpendicularly and that the matrix is subjected to a uniform tensile load σ_0 in the direction of the y-axis and parallel to the xy-plane (see Fig. 1). Perfect bonding at the interface is assumed to prevail.

In the absence of body forces, the equilibrium equations, in terms of the stresses σ_{ij}, are:

$$\frac{\partial \sigma_{rr}^{(m)}}{\partial r} + \frac{1}{r}\frac{\partial \tau_{r\theta}^{(m)}}{\partial \theta} + \frac{\partial \tau_{rz}^{(m)}}{\partial z} + \frac{\sigma_{rr}^{(m)} - \sigma_{\theta\theta}^{(m)}}{r} = 0 \qquad (1)$$

$$\frac{\partial \tau_{r\theta}^{(m)}}{\partial r} + \frac{1}{r}\frac{\partial \sigma_{\theta\theta}^{(m)}}{\partial \theta} + \frac{\partial \tau_{\theta z}^{(m)}}{\partial z} + \frac{2\tau_{r\theta}^{(m)}}{r} = 0 \qquad (2)$$

$$\frac{\partial \tau_{rz}^{(m)}}{\partial r} + \frac{1}{r}\frac{\partial \tau_{\theta z}^{(m)}}{\partial \theta} + \frac{\partial \sigma_{zz}^{(m)}}{\partial z} + \frac{\tau_{rz}^{(m)}}{r} = 0 \qquad (3)$$

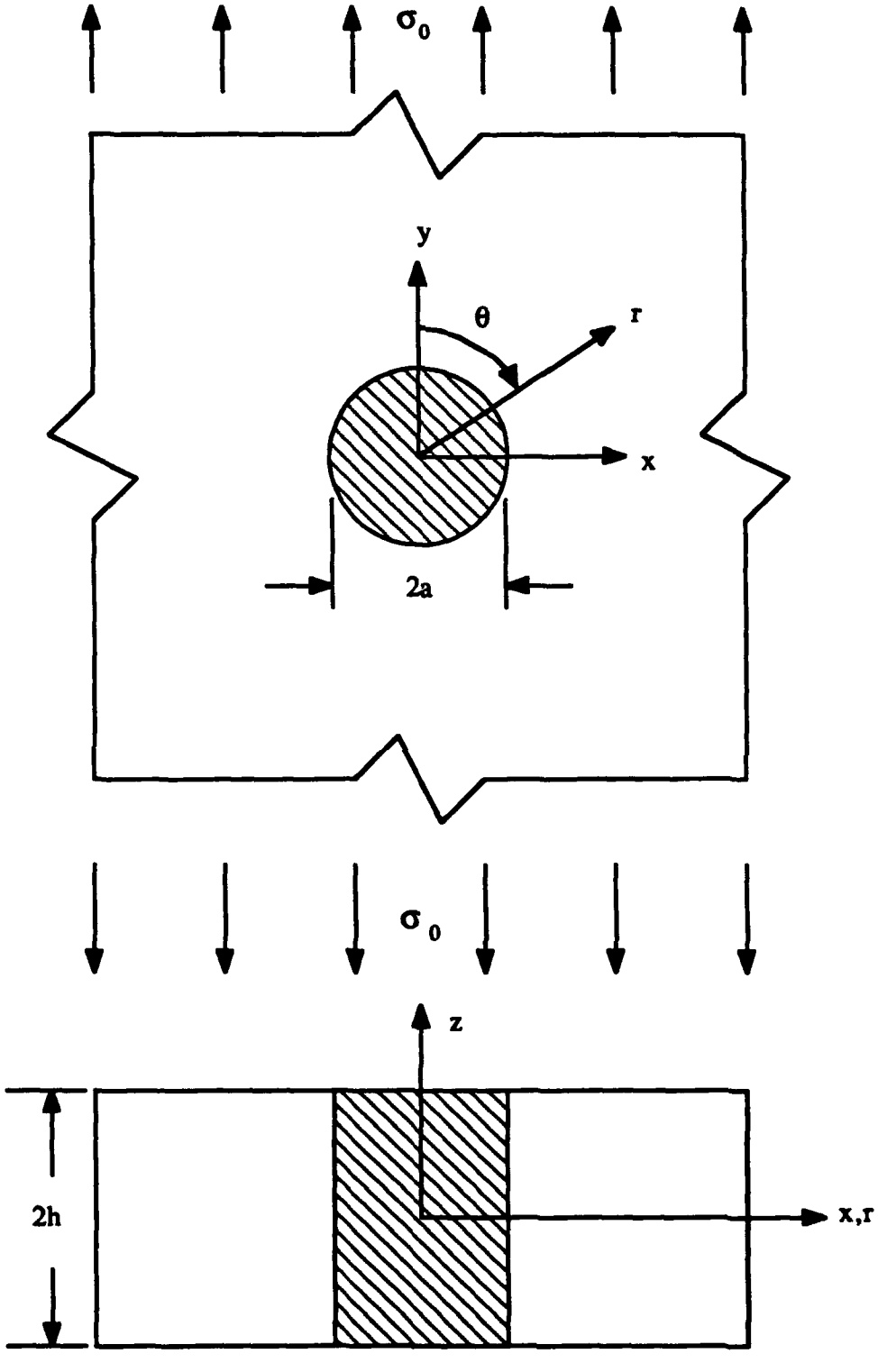

Fig. 1 Infinite plate of arbitrary thickness with cylindrical inclusion

where superscript m=1 represents the material of the matrix and m=2 represents the material of the fiber.

The stress-strain relations for a transversely isotropic[1] , as well as an isotropic, material are given by the constitutive relations

$$\begin{bmatrix} \sigma_{rr}^{(m)} \\ \sigma_{\theta\theta}^{(m)} \\ \sigma_{zz}^{(m)} \\ \tau_{\theta z}^{(m)} \\ \tau_{rz}^{(m)} \\ \tau_{r\theta}^{(m)} \end{bmatrix} = \begin{bmatrix} C_{11}^{(m)} & C_{12}^{(m)} & C_{13}^{(m)} & 0 & 0 & 0 \\ C_{12}^{(m)} & C_{11}^{(m)} & C_{13}^{(m)} & 0 & 0 & 0 \\ C_{13}^{(m)} & C_{13}^{(m)} & C_{33}^{(m)} & 0 & 0 & 0 \\ 0 & 0 & 0 & C_{44}^{(m)} & 0 & 0 \\ 0 & 0 & 0 & 0 & C_{44}^{(m)} & 0 \\ 0 & 0 & 0 & 0 & 0 & \frac{C_{11}^{(m)} - C_{12}^{(m)}}{2} \end{bmatrix} \begin{bmatrix} \varepsilon_{rr}^{(m)} \\ \varepsilon_{\theta\theta}^{(m)} \\ \varepsilon_{zz}^{(m)} \\ \gamma_{\theta z}^{(m)} \\ \gamma_{rz}^{(m)} \\ \gamma_{r\theta}^{(m)} \end{bmatrix} \tag{4}$$

where the $C_{ij}^{(m)}$ represent the respective material constants.

As to boundary conditions, we require that (i) the stresses on the planes $z = \pm h$ must vanish and (ii) that the displacements and stresses of the two materials must match at the interface, i.e. at r=a.

3. Method of solution

The primary objective of this analysis is to derive an asymptotic solution which is valid in the immediate vicinity of the corner points, i.e. the points where the interface meets the free surface of the matrix. Thus following the same method of solution as that of Folias (1989), one may write the equilibrium equations (1)-(3) in terms of the displacements $u_{ij}^{(m)}$ as[2]

$$C_{11}^{(m)} \frac{\partial^2 u_r^{(m)}}{\partial (r-a)^2} + \left(C_{13}^{(m)} + C_{44}^{(m)}\right) \frac{\partial^2 w^{(m)}}{\partial (r-a) \partial z} + C_{44}^{(m)} \frac{\partial^2 u_r^{(m)}}{\partial z^2} = 0 \tag{5}$$

$$\left(\frac{C_{11}^{(m)} - C_{12}^{(m)}}{2}\right) \frac{\partial^2 u_\theta^{(m)}}{\partial (r-a)^2} + C_{44}^{(m)} \frac{\partial^2 u_\theta^{(m)}}{\partial z^2} = 0 \tag{6}$$

$$C_{44}^{(m)} \frac{\partial^2 w^{(m)}}{\partial (r-a)^2} + \left(C_{44}^{(m)} + C_{13}^{(m)}\right) \frac{\partial^2 u_r^{(m)}}{\partial (r-a) \partial z} + C_{33}^{(m)} \frac{\partial^2 w^{(m)}}{\partial z^2} = 0 \tag{7}$$

---

[1] The material of the fiber is assumed to possess a cylindrical symmetry.

[2] In writing the following equations, we assumed that (r-a) << a.

It is interesting to note that the stress field, at the vicinity of the fiber interface, leads to two coupled equations (5) and (7) for the displacements $u_r^{(m)}$ and $w^{(m)}$ and an additional equation (6) for the displacement $u_\theta^{(m)}$.

Without going into the mathematical details, by direct substitution, one can show that the following displacement field satisfies the governing equations (5)-(7):

$$u_r^{(m)} = -\left\{C_{13}^{(m)} + C_{44}^{(m)}\right\}\frac{\partial^2 H^{(m)}}{\partial(r-a)\partial z} \tag{8}$$

$$w^{(m)} = \left\{C_{11}^{(m)}\frac{\partial^2}{\partial(r-a)^2} + C_{44}^{(m)}\frac{\partial^2}{\partial z^2}\right\}H^{(m)} \tag{9}$$

$$u_\theta^{(m)} = \tilde{H}^{(m)} \tag{10}$$

where the psudo-harmonic functions $H^{(m)}$ and $\tilde{H}^{(m)}$ satisfy the equations:

$$\left\{\frac{\partial^2}{\partial(r-a)^2} + \varepsilon_1^{(m)}\frac{\partial^2}{\partial z^2}\right\}\left\{\frac{\partial^{(m)}}{\partial(r-a)^2} + \varepsilon_2^{(m)}\frac{\partial^2}{\partial z^2}\right\}H^{(m)} = 0 \tag{11}$$

and

$$\left\{\frac{\partial^2}{\partial(r-a)^2} + \tilde{\varepsilon}_1^{(m)}\frac{\partial^2}{\partial z^2}\right\}\tilde{H}^{(m)} = 0 \tag{12}$$

with

$$\varepsilon_{1,2}^{(m)} = \frac{c_m}{2} \pm \frac{\sqrt{c_m^{\,2} - 4d_m}}{2} \tag{13}$$

$$\tilde{\varepsilon}_1^{(m)} = \frac{2C_{44}^{(m)}}{\left(C_{11}^{(m)} - C_{12}^{(m)}\right)} \tag{14}$$

$$d_m = \frac{C_{33}^{(m)}}{C_{11}^{(m)}} \tag{15}$$

$$c_m = \frac{C_{33}^{(m)}}{C_{44}^{(m)}} - \frac{C_{13}^{(m)^2}}{C_{11}^{(m)}C_{44}^{(m)}} - \frac{2C_{13}^{(m)}}{C_{11}^{(m)}} \tag{16}$$

It is found convenient at this stage to introduce the local coordinate system (see Fig. 2),

$$r - a = \rho\cos\phi \tag{17}$$

$$h - z = \rho\sin\phi \tag{18}$$

and to adopt the following definitions:

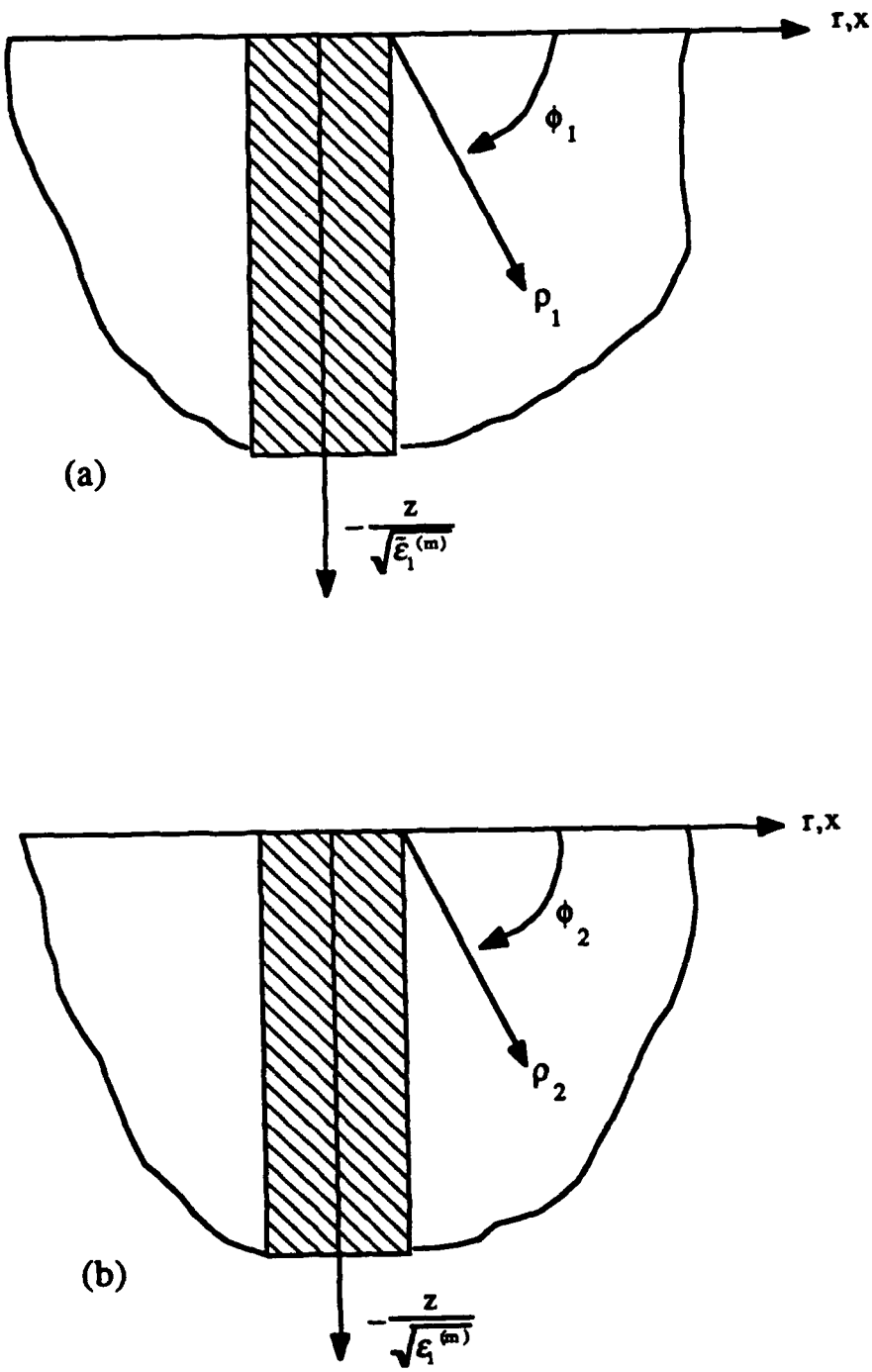

Fig. 2 Definition of two local coordinate systems (a) and (b) at the corner

$$\rho_1 = \rho\sqrt{\cos^2\phi + \frac{\sin^2\phi}{\tilde{\varepsilon}_1^{(m)}}} \tag{19}$$

$$\rho_2 = \rho\sqrt{\cos^2\phi + \frac{\sin^2\phi}{\varepsilon_1^{(m)}}} \tag{20}$$

$$\phi_1 = \tan^{-1}\left\{\frac{\tan\phi}{\sqrt{\tilde{\varepsilon}_1^{(m)}}}\right\} \tag{21}$$

$$\phi_2 = \tan^{-1}\left\{\frac{\tan\phi}{\sqrt{\varepsilon_1^{(m)}}}\right\} \tag{22}$$

in view of which, one may now construct asymptotic solutions for the functions $H^{(m)}$ and $\tilde{H}^{(m)}$ in ascending powers of ρ, i.e.

$$H^{(m)} = \rho_2^{\alpha+1}\cos(\beta\theta)\left\{A_2^{(m)}\cos[(\alpha+1)\phi_2] + B_2^{(m)}\sin[(\alpha+1)\phi_2] + \frac{1}{(\alpha+1)}\int_0^{\phi_2}\psi^{(m)}(\zeta)\sin[(\alpha+1)(\phi_2-\zeta)]d\zeta\right\} + O(\rho_2^{\alpha+2}) \tag{23}$$

and

$$\tilde{H}^{(m)} = \rho_1^{\alpha+1}\cos(\beta\theta)\left\{A_1^{(m)}\cos[(\alpha+1)\phi_1] + B_1^{(m)}\sin[(\alpha+1)\phi_1]\right\} + O(\rho_1^{\alpha+2}) \tag{24}$$

where

$$\psi^{(m)}(\xi) = \left\{A_3^{(m)}\cos\left[(\alpha-1)\tan^{-1}\left(\sqrt{\frac{\varepsilon_1^{(m)}}{\varepsilon_2^{(m)}}}\tan\xi\right)\right] + B_3^{(m)}\sin\left[(\alpha-1)\tan^{-1}\left(\sqrt{\frac{\varepsilon_1^{(m)}}{\varepsilon_2^{(m)}}}\tan\xi\right)\right]\right\}\left\{\frac{1+\frac{\varepsilon_1^{(m)}}{\varepsilon_2^{(m)}}\tan^2\xi}{1+\tan^2\xi}\right\}^{\frac{\alpha}{2}-1} \tag{25}$$

and α, $A_1^{(m)}$, $B_1^{(m)}$, $A_2^{(m)}$, $B_2^{(m)}$, $A_3^{(m)}$ and $B_3^{(m)}$ are unknown constants to be determined from the following boundary conditions:

$$\text{at } \phi = 0 \quad : \quad \sigma_{zz}^{(1)} = \tau_{rz}^{(1)} = \tau_{\theta z}^{(1)} = 0 \tag{26}$$

$$\text{at } \phi = \pi \quad : \quad \sigma_{zz}^{(2)} = \tau_{rz}^{(2)} = \tau_{\theta z}^{(2)} = 0 \tag{27}$$

$$\text{at } \phi = \frac{\pi}{2} \quad : \quad u_r^{(1)} = u_r^{(2)}, u_\theta^{(1)} = u_\theta^{(2)}, w^{(1)} = w^{(2)} \tag{28}$$

$$\sigma_{rr}^{(1)} = \sigma_{rr}^{(2)}, \tau_{r\theta}^{(1)} = \tau_{r\theta}^{(2)}, \tau_{rz}^{(1)} = \tau_{rz}^{(2)} \tag{29}$$

Substituting the previously constructed displacement field into the boundary conditions (26)-(29), we arrive at a system of twelve algebraic equations, the determinant of which must vanish. This latter condition leads to a transcendental equation for the characteristic value α.

Without going into the mathematical details, these characteristic values α may easily be determined with the aid of a computer. Although the transcendental equation has an infinite number of real roots, only those values which lie in the interval $1< \alpha < 2$ are of practical interest. Furthermore, in this interval there are no complex roots present. In general α depends on the respective material properties of the matrix as well as of the fiber.

The displacement and stress fields may now be computed in terms of one unknown constant which in turn is to be determined from the loading conditions far away from the fiber-matrix interface. Without going into the mathematical details, the explicit displacement and stress fields are found to be:

(i) displacement field:

$$u_r^{(m)} = \frac{1}{\sqrt{\varepsilon_1^{(m)}}}\left(C_{13}^{(m)} + C_{44}^{(m)}\right)\alpha(\alpha+1)\rho_2^{\alpha-1}\cos(\beta\theta)$$
$$\left\{-A_2^{(m)}\sin[(\alpha-1)\phi_2] + B_2^{(m)}\cos[(\alpha-1)\phi_2] + \frac{1}{(\alpha+1)}\int_0^{\phi_2}\psi^{(m)}(\zeta)\right.$$
$$\left.\cos[(\alpha-1)\phi_2 - (\alpha+1)\zeta]d\zeta - \frac{\cos\phi_2\sin\phi_2}{\alpha(\alpha+1)}\psi^{(m)}(\phi_2)\right\} + O(\rho_2^{\alpha}) \qquad (30)$$

$$w^{(m)} = \alpha(\alpha+1)\rho_2^{\alpha-1}\cos(\beta\theta)$$
$$\left\{\left(C_{11}^{(m)} - \frac{C_{44}^{(m)}}{\varepsilon_1^{(m)}}\right)\left\{A_2^{(m)}\cos[(\alpha-1)\phi_2] + B_2^{(m)}\sin[(\alpha-1)\phi_2]\right.\right.$$
$$\left.+\frac{1}{(\alpha+1)}\int_0^{\phi_2}\psi^{(m)}(\zeta)\sin[(\alpha-1)\phi_2 - (\alpha+1)\zeta]d\zeta\right\} + \left[C_{11}^{(m)}\frac{\sin^2\phi_2}{\alpha(\alpha+1)}\right.$$
$$\left.\left.+\frac{C_{44}^{(m)}}{\varepsilon_1^{(m)}}\frac{\cos^2\phi_2}{\alpha(\alpha+1)}\right]\psi^{(m)}(\phi_2)\right\} + O(\rho_2^{\alpha}) \qquad (31)$$

$$u_\theta^{(m)} = \alpha(\alpha+1)\rho_1^{\alpha-1}\cos(\beta\theta)$$
$$\left\{A_1^{(m)}\cos[(\alpha-1)\phi_1] + B_1^{(m)}\sin[(\alpha-1)\phi_1]\right\} + O(\rho_1^{\alpha}) \tag{32}$$

(ii) stress field:

$$\sigma_{rr}^{(m)} = -\frac{1}{\sqrt{\varepsilon_1^{(m)}}}C_{44}^{(m)}(\alpha-1)\alpha(\alpha+1)\rho_2^{\alpha-2}\cos(\beta\theta)$$
$$\left\{\left(C_{11}^{(m)} + \frac{C_{13}^{(m)}}{\varepsilon_1^{(m)}}\right)\left\{A_2^{(m)}\sin[(\alpha-2)\phi_2] - B_2^{(m)}\cos[(\alpha-2)\phi_2]\right.\right.$$
$$\left.\left.\frac{1}{(\alpha+1)}\int_0^{\phi_2}\psi^{(m)}(\zeta)\cos[(\alpha-2)\phi_2-(\alpha+1)\zeta]d\zeta\right\} + \left[\left(C_{11}^{(m)}\right.\right.\right.$$
$$\left.\left.\left.+\frac{C_{13}^{(m)}}{\varepsilon_1^{(m)}}\right)\frac{\sin 2\phi_2\cos\phi_2}{\alpha(\alpha+1)} - C_{11}^{(m)}\frac{\sin^3\phi_2}{\alpha(\alpha+1)} + \frac{C_{13}^{(m)}}{\varepsilon_1^{(m)}}\frac{\cos^2\phi_2\sin\phi_2}{\alpha(\alpha+1)}\right]\right.$$
$$\psi^{(m)}(\phi_2) + \left[-C_{11}^{(m)}\frac{\sin^2\phi_2\cos\phi_2}{(\alpha-1)\alpha(\alpha+1)} + \frac{C_{13}^{(m)}}{\varepsilon_1^{(m)}}\frac{\cos^3\phi_2}{(\alpha-1)\alpha(\alpha+1)}\right]$$
$$\left.\psi^{(m)'}(\phi_2)\right\} + O(\rho_2^{\alpha-1}) \tag{33}$$

$$\sigma_{\theta\theta}^{(m)} = -\frac{1}{\sqrt{\varepsilon_1^{(m)}}}(\alpha-1)\alpha(\alpha+1)\rho_2^{\alpha-2}\cos(\beta\theta)$$
$$\left\{\left[C_{12}^{(m)}\left(C_{13}^{(m)}+C_{44}^{(m)}\right) - C_{13}^{(m)}\left(C_{11}^{(m)} - \frac{C_{44}^{(m)}}{\varepsilon_1^{(m)}}\right)\right]\left\{A_2^{(m)}\right.\right.$$
$$\sin[(\alpha-2)\phi_2] - B_2^{(m)}\cos[(\alpha-2)\phi_2] - \frac{1}{(\alpha+1)}\int_0^{\phi_2}\psi^{(m)}(\zeta)$$
$$\left.\cos[(\alpha-2)\phi_2-(\alpha+1)\zeta]d\zeta\right\} + \left\{C_{12}^{(m)}(C_{13}^{(m)}+C_{44}^{(m)}) - C_{13}^{(m)}\right.$$
$$\left.\left(C_{11}^{(m)} - \frac{C_{44}^{(m)}}{\varepsilon_1^{(m)}}\right)\right]\frac{\sin 2\phi_2\cos\phi_2}{\alpha(\alpha+1)} + \left[-C_{12}^{(m)}(C_{13}^{(m)}+C_{44}^{(m)})\right.$$
$$\left.+C_{13}^{(m)}C_{11}^{(m)}\right]\frac{\sin^3\phi_2}{\alpha(\alpha+1)} + \frac{C_{13}^{(m)}C_{44}^{(m)}}{\varepsilon_1^{(m)}}\frac{\cos^2\phi_2\sin\phi_2}{\alpha(\alpha+1)}\Big\}\psi^{(m)}(\phi_2)$$
$$+\left\{\left[-C_{12}^{(m)}\left(C_{13}^{(m)}+C_{44}^{(m)}\right) + C_{13}^{(m)}C_{11}^{(m)}\right]\frac{\sin^2\phi_2\cos\phi_2}{(\alpha-1)\alpha(\alpha+1)}\right.$$
$$\left.\left.+\frac{C_{13}^{(m)}C_{44}^{(m)}}{\varepsilon_1^{(m)}}\frac{\cos^3\phi_2}{(\alpha-1)\alpha(\alpha+1)}\right\}\psi^{(m)'}(\phi_2)\right\} + O(\rho_2^{\alpha-1}) \tag{34}$$

$$\sigma_{zz}^{(m)} = -\frac{1}{\sqrt{\varepsilon_1^{(m)}}}(\alpha-1)\alpha(\alpha+1)\rho_2^{\alpha-2}\cos(\beta\theta)$$

$$\left\{\left[C_{13}^{(m)}\left(C_{13}^{(m)}+C_{44}^{(m)}\right)-C_{33}^{(m)}\left(C_{11}^{(m)}-\frac{C_{44}^{(m)}}{\varepsilon_1^{(m)}}\right)\right]\{A_2^{(m)}\right.$$

$$\sin[(\alpha-2)\phi_2]-B_2^{(m)}\cos[(\alpha-2)\phi_2]-\frac{1}{(\alpha+1)}\int_0^{\phi_2}\psi^{(m)}(\zeta)$$

$$\cos[(\alpha-2)\phi_2-(\alpha+1)\zeta]d\zeta\}+\left\{\left[C_{13}^{(m)}\left(C_{13}^{(m)}+C_{44}^{(m)}\right)-C_{33}^{(m)}\right.\right.$$

$$\left.\left(C_{11}^{(m)}-\frac{C_{44}^{(m)}}{\varepsilon_1^{(m)}}\right)\right]\frac{\sin 2\phi_2\cos\phi_2}{\alpha(\alpha+1)}+[-C_{13}^{(m)}(C_{13}^{(m)}+C_{44}^{(m)})+$$

$$C_{33}^{(m)}C_{11}^{(m)}]\frac{\sin^3\phi_2}{\alpha(\alpha+1)}+\frac{C_{33}^{(m)}C_{44}^{(m)}}{\varepsilon_1^{(m)}}\frac{\cos^2\phi_2\sin\phi_2}{\alpha(\alpha+1)}\Big\}\psi^{(m)}(\phi_2)$$

$$+\left\{\left[-C_{13}^{(m)}(C_{13}^{(m)}+C_{44}^{(m)})+C_{33}^{(m)}C_{11}^{(m)}\right]\frac{\sin^2\phi_2\cos\phi_2}{(\alpha-1)\alpha(\alpha+1)}\right.$$

$$\left.+\frac{C_{33}^{(m)}C_{44}^{(m)}}{\varepsilon_1^{(m)}}\frac{\cos^3\phi_2}{(\alpha-1)\alpha(\alpha+1)}\right\}\psi^{(m)'}(\phi_2)\}+O(\rho_2^{\alpha-1}) \qquad (35)$$

$$\tau_{rz}^{(m)} = C_{44}^{(m)}(\alpha-1)\alpha(\alpha+1)\rho_2^{\alpha-2}\cos(\beta\theta)$$

$$\left\{\left(C_{11}^{(m)}+\frac{C_{13}^{(m)}}{\varepsilon_1^{(m)}}\right)\{A_2^{(m)}\cos[(\alpha-2)\phi_2]+B_2^{(m)}\sin[(\alpha-2)\phi_2]\right.$$

$$\left.+\frac{1}{(\alpha+1)}\int_0^{\phi_2}\psi^{(m)}(\zeta)\sin[(\alpha-2)\phi_2-(\alpha+1)\zeta]d\zeta\right\}$$

$$+\left[\left(C_{11}^{(m)}+\frac{C_{13}^{(m)}}{\varepsilon_1^{(m)}}\right)\frac{\sin 2\phi_2\sin\phi_2}{\alpha(\alpha+1)}-\frac{C_{13}^{(m)}}{\varepsilon_1^{(m)}}\frac{\cos^3\phi_2}{\alpha(\alpha+1)}\right.$$

$$\left.+C_{11}^{(m)}\frac{\sin^2\phi_2\cos\phi_2}{\alpha(\alpha+1)}\right]\psi^{(m)}(\phi_2)+\left[-C_{11}^{(m)}\frac{\sin^3\phi_2}{(\alpha-1)\alpha(\alpha+1)}\right.$$

$$\left.+\frac{C_{13}^{(m)}}{\varepsilon_1^{(m)}}\frac{\cos^2\phi_2\sin\phi_2}{(\alpha-1)\alpha(\alpha+1)}\right]\psi^{(m)'}(\phi_2)\Big\}+O(\rho_2^{\alpha-1}) \qquad (36)$$

$$\tau_{\theta z}^{(m)} = -\frac{1}{\sqrt{\tilde{\varepsilon}_1^{(m)}}}C_{44}^{(m)}(\alpha-1)\alpha(\alpha+1)\rho_1^{\alpha-2}\cos(\beta\theta)$$

$$\{-A_1^{(m)}\sin[(\alpha-1)\phi_1]+B_1^{(m)}\cos[(\alpha-1)\phi_1]\}+O(\rho_1^{\alpha-1}) \qquad (37)$$

$$\tau_{r\theta}^{(m)} = \frac{C_{11}^{(m)} - C_{12}^{(m)}}{2}(\alpha-1)\alpha(\alpha+1)\rho_1^{\alpha-2}\cos(\beta\theta)$$
$$\left\{A_1^{(m)}\cos[(\alpha-1)\phi_1] + B_1^{(m)}\sin[(\alpha-1)\phi_1]\right\} + O(\rho_1^{\alpha-1}) \qquad (38)$$

4. Discussion

As a practical matter, two different types of fibers embedded into an epoxy matrix were considered, a carbon fiber and a glass fiber defined by the following elastic properties (see Table 1.):

Table 1. The Material Properties for Carbon Fiber, Glass Fiber and Epoxy Matrix

Carbon Fiber	Glass Fiber	Epoxy Matrix
C_{11}=20.40 MPa	C_{11}= 99.19 MPa	C_{11}= 6.62 MPa
C_{12}= 9.40 MPa	C_{12}= 27.69 MPa	C_{12}= 3.41 MPa
C_{13}=10.50 MPa		
C_{33}=240.00 MPa		
C_{44}= 24.00 MPa		

Omitting the long and tedious numerical details, the characteristic values of α were found to be α=1.693 and α=1.737, respectively[3]. The analysis suggests that the presence of a carbon fiber induces a slightly higher singular stress field than that of a glass fiber and consequently is more prone to failure. Moreover, in the limit, one recovers precisely the corresponding isotropic solution derived by Folias (1989). In Figs. 3-6, the behaviors of the local displacement and stress fields as a function of angular distribution ϕ are depicted for both fibers considered above. The reader may note that for simplicity we have adopted the definition:

$$C(\theta) = A_2^{(2)}\alpha(\alpha+1)\cos(\beta\theta) \qquad (39)$$

which in the limit, as the material constants

$$C_{ij} \rightarrow C_{ij\ \text{isotropic}}, \qquad (40)$$

[3] It may be noted that a second real root exists within this interval, however it leads to a slightly weaker stress singularity (see Westmann, 1975).

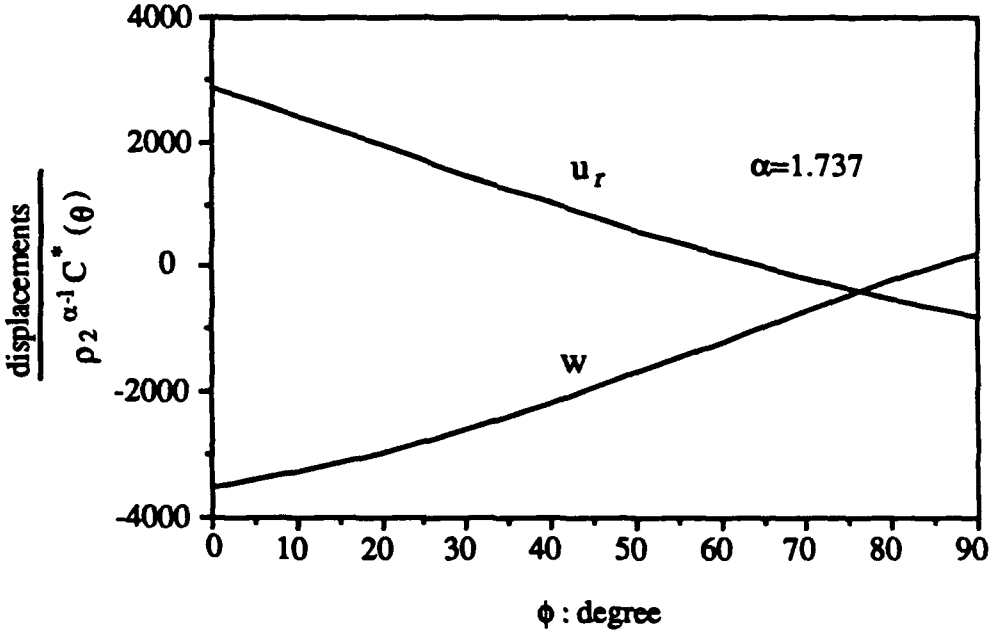

Fig. 3 Displacements versus ϕ for isotropic case

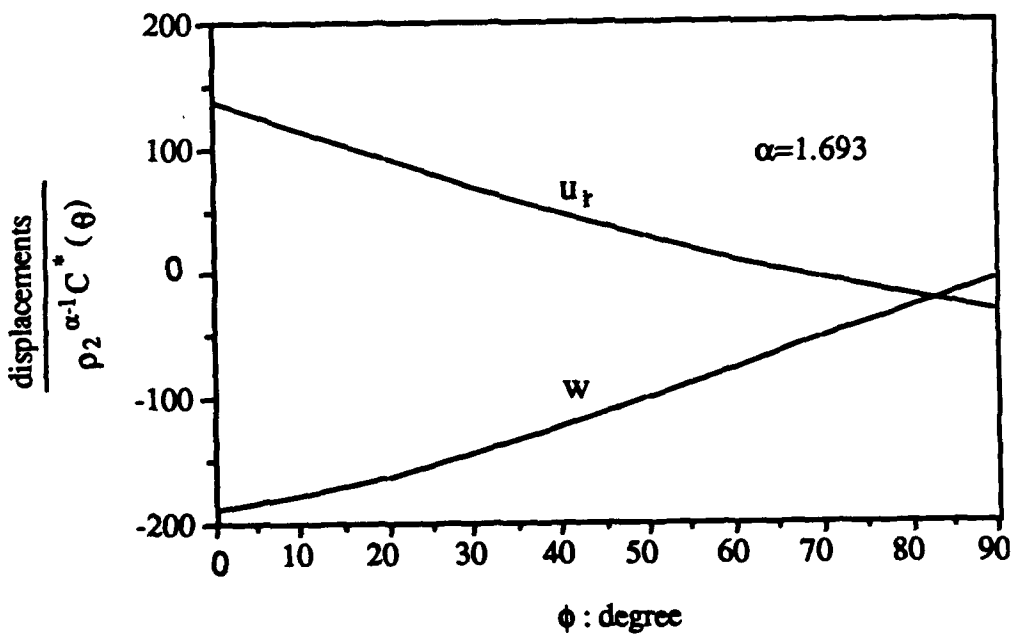

Fig. 4 Displacements versus ϕ for transversely isotropic case

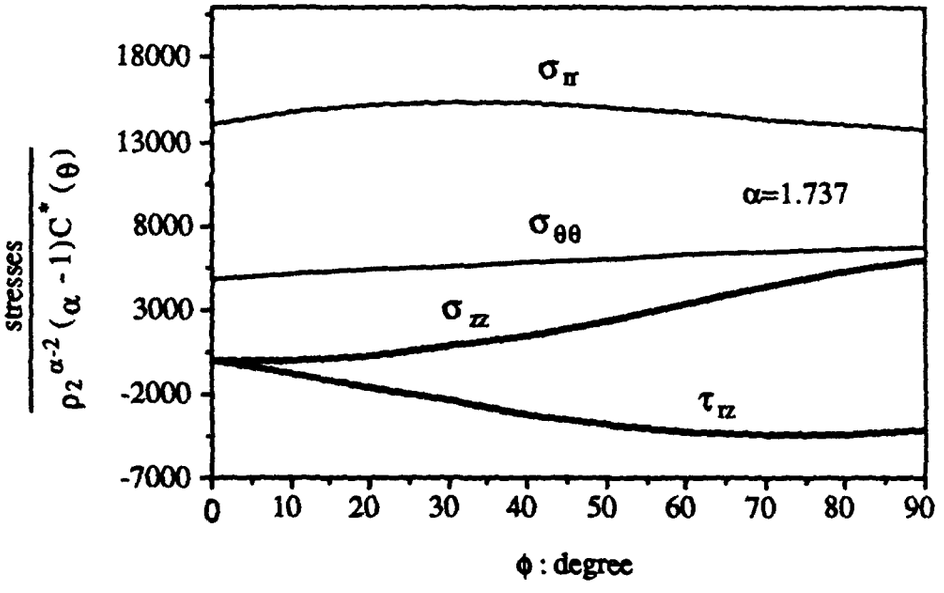

Fig. 5 Stresses versus ϕ for isotropic case

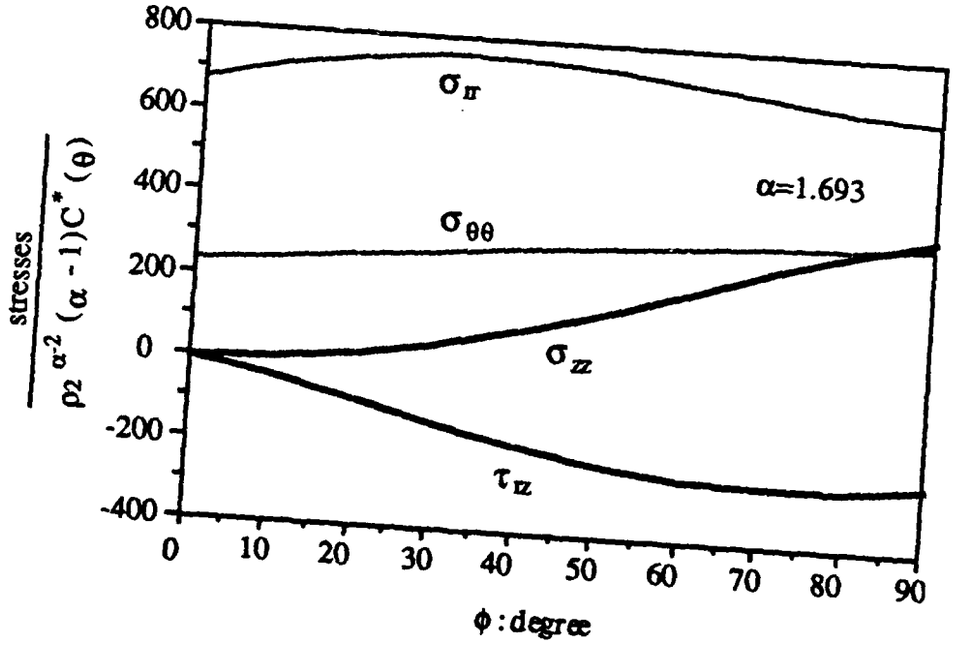

Fig. 6 Stresses versus ϕ for transversely isotropic case

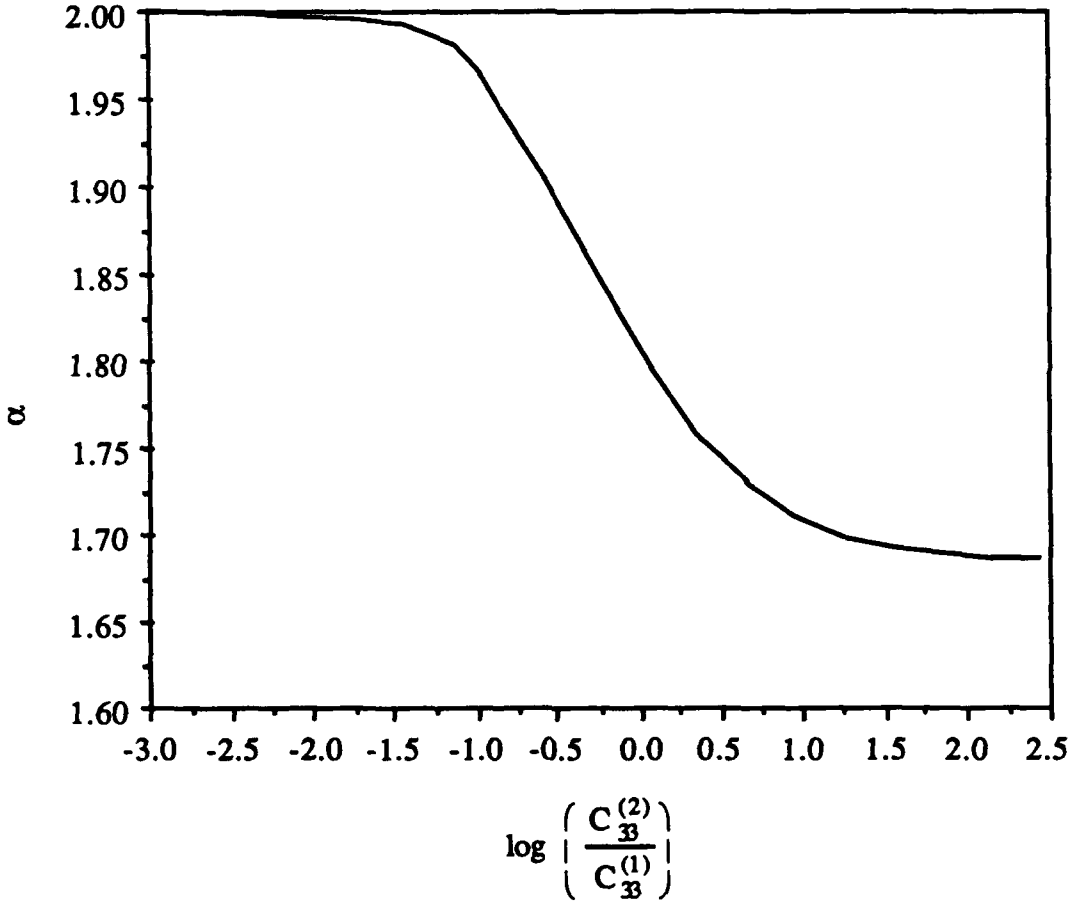

Fig. 7. The value of the characteristic constant α vs $\log(C_{33}^{(2)}/C_{33}^{(1)})$

the function

$$C(\theta) \rightarrow C^{*}(\theta) \tag{41}$$

It is noteworthy to note that, although the displacement and stress profiles corresponding to the two different fibers are very similar, their respective magnitudes are different. Similar trends are also expected to prevail at locations further away from the free surface. Finally, it remains for us to relate the unknown constant $A_2^{(2)}$ to the applied load far away from the vicinity of the fiber. This matter is presently under investigation, and the results will be reported in a future paper where we will also take into account other effects such as stresses due to a temperature mismatch, mechanical loads along and perpendicular to the fiber axis, and a correction factor to account for the presence of a periodic array of fibers embedded into a matrix. Finally, the variation of the exponent α as a function of the material ratio $C_{33}^{(2)}/C_{33}^{(1)}$ is given by Fig. 7.

References

Adams, D. F. and D. R. Doner (1967), "Transverse normal loading of a unidirectional composite", *J. Composite Materials* 1, 152.

Adams, D. F. and D. A. Crane (1984), "Combined loading micro-mechanical analysis of a unidirectional composite", *Composites* 15, 181.

Bogy, D. B. (1968), "Edge-bonded dissimilar orthogonal elastic wedges under normal and shear loading", *J. Appl. Mech.* 35, 460.

Bogy, D. B. (1971), "Two edge-bonded elastic wedges of different materials and wedge angles under surface tractions", *J. Appl. Mech.* 38, 377.

Comninou, M. (1976), "Stress singularity at a sharp edge in contact problems with friction", *J. Appl. Math. Phys. (ZAMP)* 27, 493.

Dundurs, J. and M. S. Lee (1972), "Stress concentration at a sharp edge in contact problems", *J. Elasticity* 2, 109.

Dundurs, J. (1989), "Cavities vis-a-vis rigid inclusions and some related general results in plane elasticity", *J. Appl. Mech.* 56, 786.

Folias, E. S. (1989), "On the stress singularities at the intersection of a cylindrical inclusion with the free surface of a plate", *Int. J. Fracture* 39, 25.

Gdoutos, E. E. and P. S. Theocaris (1975), "Stress concentrations at the apex of a plane indenter acting on an elastic half plane", *J. Appl. Mech.* 42, 688.

Goodier, J. N. (1933), "Concentration of stress around spherical and cylindrical inclusions and flaws",*The American Society of Mechanical Engineers* 55, 39.

Goree, J. G. (1967), "In plane loading in an elastic matrix containing two cylindrical inclusions", *J. Composite Materials* 1, 404.

Haener, J. and N. Ashbaugh (1967), "Three-dimensional stress distribution in a unidirectional composite", *J. Composite Materials* 1, 54.

Hardiman, N. J. (1952), "Elliptic elastic inclusion in an infinite elastic plate", *Q. J. Appl. Math. Mech.* 7, 226.

Haritos, G. K. and L. M. Keer (1979), "Stress analysis for an elastic half space containing an embedded rigid block", *Int. J. Solids Structures* 16, 19.

Hein, V. L. and F. Erdogan (1971), "Stress singularities in a two-material wedge", *Int. J. Fracture* 7, 317.

Keer, L. M., J. Dundurs and K. Kiattikomol (1973), "Separation of a smooth circular inclusion from a matrix", *Int. J. Engng. Sci.* 11, 1221.

Knein, M. (1927), *Zur Theorie der Druckversuchs*, Abhandlungen der Aerodynamishe Inst. u.d. Technishe Hochschule. Aachen, Germany.

Luk, V. K. and L. M. Keer (1979), "Stress analysis for an elastic half space containing an axially-loaded rigid cylindrical rod", *Int. J. Solids Structures* 15, 805.

Marloff, R. H. and I. M. Daniel (1969), "Three-dimensional photoelastic analysis of a fiber-reinforced composite model", *Experimental Mechanics* 9, 156.

Rice, J. R. and G. C. Sih (1965), "Plane problems of cracks in dissimilar media", *J. Appl. Mech.* series E32, 418.

Rongved, L. (1955), "Force interior to one of two jointed semi-infinite solids", Second Midwestern Conference on Solid Mechanics 1.

Rose, L. R. F. (1987), "Crack reinforcement by distributed springs", *J. Mech. Phys. Solids* 35, 383

Sendeckyj, G. P. (1970), "Elastic inclusion problems in plane elastostatics", *Int. J. Solids Structures* 6, 1535.

Tirosh, J. Katz, E. and G. Lifschuetz (1979), "The role of fibrous reinforcements well bonded or parially debonded on the transverse strength of composite materials", *Eng. Fracture Mechanics* 12, 267.

Westmann, R. A. (1975), "Geometrical effects in adhesive joints", *Int. J. Engng. Sci.* 13, 369.

Williams, M. L. (1952), "Stress singularities resulting from various boundary conditions in angular corners of plates in extension", *J. Appl. Mech.* 19, 526.

Williams, M. L. (1959), *Bull. Seismo. Soc. America* 199.

Yu, I. W. and G. P. Sendeckyj (1974), "Multiple circular inclusion problems in plane elastostatics", *J. Appl. Mech.* 41, 215.

PART III

ON THE PREDICTION OF FAILURE AT A FIBER/MATRIX INTERFACE IN A COMPOSITE SUBJECTED TO A TRANSVERSE TENSILE LOAD

by

E.S. Folias

University of Utah
Department of Mechanical Engineering
Salt Lake City, Utah 84112

ABSTRACT

This paper deals with the 3D stress field of a cylindrical fiber which is embedded into a resin matrix. The composite is then subjected to a uniform tensile load σ_0. The strain energy release rate is computed and the criterion is used to predict debonding initiation at the fiber/matrix interface. The analysis shows that this failure is most likely to occur at the free surface, ie the region where the fiber intersects a free surface for example a hole, an edge, or a crack. Moreover, it will occur at approximately (1/10) the load value required for the same failure to commense at the center of the fiber length.

The results are also extended to include a doubly periodic array of fibers which are embedded into a matrix. Based on 3D considerations, the stiffness matrix is shown to increase as the volume fraction of the fibers increases. Similarly, the stress σ_{rr} in the matrix is shown to decrease as the volume fraction of the fibers increases.

INTRODUCTION

It is well recognized that fiber composite materials are very attractive for use in aerospace, automotive and other applications. These composites consist of relatively stiff fibers which are embedded into a lower stiffness matrix. Although in most designs the fibers are aligned so that they are parallel to the direction of the external loads, it is almost impossible to avoid induced transverse stresses which may lead to premature failure of the laminate. An excellent example of this is the case of a filament wound pressure vessel in which the presence of a curvature induces bending as well as transverse stresses (Folias, 1965). However, in order to be able to predict their failing characteristics, particularly in the neighborhood of free surfaces such as holes, edges etc., it is necessary to know the local stress behavior from a 3D point of view.

An overall summary of some of the results, which are based on 2D elasticity considerations can be found in the books by Hull (1981) and by Chamis (1975). In their pioneering work, Adams and Doner (1967) used finite differences to solve the problem of a doubly periodic array of elastic fibers contained in an elastic matrix and subjected to a transverse load. Their results reveal the dependence of the maximum principal stress versus the constituent stiffness ratio (E_f/E_m) for various fiber volume ratios. A few years later, Yu and Sendeckyj (1974) used a complex variable approach to solve the problem of multiple inclusions embedded into an infinite matrix. Their results were subsequently specialized to cases of two and three inclusions thus providing us with futher insight into the strength of the composite. On the other hand, the separation of a smooth circular inclusion from a matrix was investigated by Keer, Dundurs and Kiattikomol (1973). By using finite integral transforms, they were able to reduce the problem to that of a Fredholm integral equation with a weakly singular kernel. Thus, extracting the singular part of the solution, they were able to reduce the remaining problem to a simpler one which lends itself to an effective numerical solution. Their results are very general and are applicable to various combinations of material properties and loads.

In this paper, use of the local, 3D, stress field will be made in order to examine the dependence of the stress σ_{rr}, in the matrix, on the ratio (Gf/Gm). The strain energy release rate will then be computed in order to predict crack initiation at the fiber/matrix interface. Particular emphasis will be placed in the region where fibers meet a free surface as well as at the center of a fiber's length.

FORMULATION OF THE PROBLEM

Let us consider a cylindrical fiber of homogeneous and isotropic material, e.g. a glass fiber, which is embedded into a matrix of also homogeneous and isotropic material.

Futhermore, we assume the matrix to be a rectangular plate with finite dimensions 2w, 2ℓ, and 2h as defined by fig. 1. For simplicity, we assume $\frac{w}{a} > 8$ and $\frac{\ell}{a} > 8$. Such an assumption will guarantee that the boundary planes $x = \pm w$, and $y = \pm \ell$, will not effect the local stress field adjacent to the fiber.* Thus, mathematically, one may consider the boundaries in the x and y directions to extend to infinity. As to loading, the plate is subjected to a uniform tensile load σ_o in the direction of the y-axis and parallel to the bounding planes (see Fig. 1).

In the absence of body forces, the coupled differential equations governing the displacement functions $u_i^{(j)}$ are

$$\frac{1}{1-2\nu_j} \frac{\partial e^{(j)}}{\partial x_i} + \nabla^2 u_i^{(j)} = 0, \; i = 1,2,3, \; j = 1,2, \tag{1}$$

where ∇^2 is the Laplacian operator, ν_j is Poisson's ratio, $u_i^{(1)}$ and $u_i^{(2)}$ represent the displacement functions in media 1 (matrix) and 2 (fiber) respectively, and

$$e^{(j)} = \frac{\partial u_i^{(j)}}{\partial x_i} \; ; \; i = 1,2,3 \; ; \; j = 1,2. \tag{2}$$

The stress-displacement relations are given by Hooke's law as

* This can be seen from the results which were recently reported by (Penado and Folias (1989).

$$\sigma_{i'}^{(j)} = \lambda_j \; e_{kk}^{(j)} \; \delta_{i'} + 2G^{(j)}, \; e_{i'}^{(j)}, \qquad (3)$$

where λ_j and G_j are the Lame' constants describing media 1 and 2.

THE SOLUTION FOR ONE FIBER

A. Region where fiber intersects the free edge

This problem was recently investigated by the author (Folias 1989) who was able to recover, explicitly, the three dimensional stress field adjacent to the surface of the fiber* . Without going into the mathematical details, the displacement and stress fields for the matrix are given in terms of the local coordinate system (see fig. 2) by:

(i) <u>displacement field:</u>

$$u^{(1)} = A_n \rho^{\alpha-1} \sin\theta \{B [2 (1-\nu_1) \cos (\alpha-1)\phi - (\alpha-1) \sin\phi \sin(\alpha-2)\phi] \quad (4)$$
$$- (\alpha+1) [(1-2\nu_1) \sin (\alpha-1)\phi + (\alpha-1) \sin\phi \cos (\alpha-2) \phi]\} \cos(2n\theta)$$

$$v^{(1)} = A_n \rho^{\alpha-1} \cos\theta \{B [2 (1-\nu_1) \cos (\alpha-1)\phi - (\alpha-1) \sin\phi \sin(\alpha-2)\phi] \quad (5)$$
$$- (\alpha+1) [(1-2\nu_1) \sin (\alpha-1) \phi + (\alpha-1) \sin\phi \cos (\alpha-2)\phi] \} \cos(2n\theta)$$

$$w^{(1)} = A_n \rho^{\alpha-1} \{B [- (1-2\nu_1) \sin (\alpha-1)\phi + (\alpha-1) \sin\phi \cos (\alpha-2) \phi] \quad (6)$$
$$- (\alpha+1) [2 (1-\nu_1) \cos (\alpha-1)\phi + (\alpha-1) \sin\phi \sin(\alpha+2) \phi]\} \cos(2n\theta)$$

(ii) <u>stress field:</u>

$$\sigma_{rr}^{(1)} = 2G^{(1)} (\alpha-1) A_n \rho^{\alpha-2} \{B [2 \cos (\alpha-2)\phi - (\alpha-2) \sin\phi \sin(\alpha-3)\phi] \quad (7)$$
$$- (\alpha+1) [\sin (\alpha-2)\phi + (\alpha-2) \sin\phi \cos (\alpha-3)\phi] \} \cos(2n\theta)$$

$$\sigma_{\theta\theta}^{(1)} = 4\nu_1 G^{(1)} (\alpha-1) A_n \rho^{\alpha-2} \{B \cos (\alpha-2)\phi - (\alpha+1) \sin(\alpha-2)\phi\} \cos(2n\theta) \quad (8)$$

---

* A similar analysis for a transversely isotropic fiber meeting a free surface has recently been completed and the results will be reported soon.

$$\sigma_{zz}^{(1)} = 2G^{(1)}\,(\alpha\text{-}1)\,A_n\,\rho^{\alpha-2}\left\{B\,(\alpha\text{-}2)\,\sin\phi\,\sin(\alpha\text{-}3)\phi\right. \tag{9}$$
$$\left. +\,(\alpha+1)\,\left[(\alpha\text{-}2)\,\sin\phi\,\cos\,(\alpha\text{-}3)\phi - \sin(\alpha\text{-}2)\phi\,\right]\right\}\cos(2n\theta)$$

$$\tau_{rz}^{(1)} = 2G^{(1)}\,(\alpha\text{-}1)\,A_n\,\rho^{\alpha-2}\left\{B\left[\sin\,(\alpha\text{-}2)\phi + (\alpha\text{-}2)\,\sin\phi\,\cos\,(\alpha\text{-}3)\phi\right]\right. \tag{10}$$
$$\left. -\,(\alpha+1)\,(\alpha\text{-}2)\,\sin\phi\,\sin(\alpha\text{-}3)\phi\,\right\}\cos(2n\theta)$$

$$\tau_{r\theta}^{(1)} = \tau_{\theta z}^{(1)} = 0\,, \tag{11)-(12}$$

where n = 0,1,2,... and B is a function of the material constants and A_n is a constant to be determined from the boundary conditions far away from the fiber*. In general, the characteristic value of α depends on the material constants of the fiber as well as of the matrix. A typical example is given in fig. 3.

Upon examination of the stress field, the following remarks are worthy of note. First, the stress field in the neighborhood where the fiber meets the free surface is signular. Moreover, in the limiting case of a perfectly rigid inclusion this singularity strength reaches the value of 0.2888. Second, boundary conditions $\sigma_{zz}^{(1)}$, $\tau_{xz}^{(1)}$ and $\tau_{yz}^{(1)}$ are satisfied as a consequence of the odd functional behavior in ϕ, which points to the presence of a boundary layer solution as one approaches the free surface. Third, on the free surface the radial stress is $(1/\nu_1)$ times the circumpherential stress. This suggests, therefore, that if a crack was to initiate, it would propagate along, (or very very close to) the fiber/matrix interface. Clearly, the occurance of either adhesive or cohesive failure will depend on the relative strengths of the interface, of the fiber, and of the matrix. All things being equal, the analysis shows the stresses to be highest at the interface, thus pointing to an adhesive type of failure.

* for one fiber n=0,1., while for a periodic extension n=0,1,2,..

B. Interior region

The, 3D, stress field for this region has also been recovered by Penado and Folias (1989) and the results for various (a/h) and (G_2/G_1) ratios may be found in the literature. The results have subsequently been extended (Folias and Liu, 1990) to also include a layer of modified matrix around the fiber. Thus for $\nu_1 = 0.34$, $\nu_2 = 0.22$ and $(G_2/G_1) = 16.67$ the stresses $\sigma_{rr}^{(1)}$ and $\sigma_{\theta\theta}^{(1)}$ at $r =$ a and for all $|z| \leq h$ are given in figs 4 and 5 respectively. Finally, fig. 6 (for λ=0) shows the variation of the stress $\sigma_{rr}^{(1)}$ as a function of the ratio (G_2/G_1).

INTERFACE FAILURE CLOSE TO THE FREE SURFACE

A closer inspection of the local stress field shows that a crack is most likely to initiate at the location $\theta = 0$ and subsequently propagate along the fiber/matrix interface until it reaches a nominal value of the arc length beyond which it will advance into the matrix. Moreover, once the crack begins to propagate, it will simultaneously propagate along the interface and parallel to the axis of the fiber (mode III). Thus, crack propagation will be governed initially by a mode I failure and subsequently by a combination of mode I and mode III failure. It is now possible for us to examine the first stage of the failing process and to obtain an estimate of the debonded arc length as well as an estimate of the critical transverse stress for crack initiation.

As a practical matter, we will consider the special case of a glass fiber embedded into an epoxy matrix with the following properties

$$\begin{aligned} G_1 &= 2.10\,\text{GPa} & \nu_1 &= 0.34 \\ G_2 &= 35.00\,\text{GPa} & \nu_2 &= 0.22\,. \end{aligned} \qquad (13)$$

Without going into the numerical details, the constants α, A and B for this example are found to be* :

* The constant A has been determined by comparing the displacement $w^{(1)}$, as well as the stress $\sigma_{rr}^{(1)}$ at $\theta = 0$, at $z = h$ and for $(a/h) = 0.5$ with the work of Penado and Folias (1989). $A \equiv \sum_n A_n$.

$$\alpha = 1.7511,\ G^{(1)} \approx a^{\alpha-2} \approx 0.6349\,\sigma_o,\ B \approx 2.1302, \tag{14}$$

where σ_o now has the units of GPa. Thus, from equations (7)-(12) one has

(i) at $\phi = 0$ and $\theta = 0$:

$$\sigma_{rr}^{(1)} \approx 4.0633\,\sigma_o \left(\frac{r-a}{a}\right)^{-0.2489} \tag{15}$$

$$\sigma_{\theta\theta}^{(1)} = \nu_1\ \sigma_{rr}^{(1)}, \tag{16}$$

(ii) at $\phi = \pi/2$ and $\theta = 0$:

$$\sigma_{rr}^{(1)} \approx 1.9163\,\sigma_o \left(\frac{h-z}{h}\right)^{-0.2489} \tag{17}$$

$$\sigma_{\theta\theta}^{(1)} \approx 0.4844\ \sigma_{rr}^{(1)} \tag{18}$$

$$\tau_{rz}^{(1)} \approx -0.2930\,\sigma_{rr}^{(1)}. \tag{19}$$

It is clear now from equations (15) and (16) that crack failure is most likely to initiate and subsequently propagate along the fiber/matrix interface rather than perpendicular to it. Similarly, equations (17) and (19) suggest that failure in the direction parallel to the axis of the fiber is dominated first by a mode I and second by a mode III type of failure. It may also be noted that $\sigma_{rr}^{(1)}$ attains a maximum at $\theta = 0$ and descreases as one travels along the surface of the fiber.

Finally, based on 3D considerations, the stress field away from the edges, $z = \pm h$, and in the interior of the plate was shown to be non-singular (Penado and Folias 1989, Folias and Liu 1990) with*

$$\sigma_{\theta\theta}^{(1)} = 0.4090\ \sigma_{rr}^{(1)} = 0.4090\,(1.4281\,\sigma_o) = 0.5841\,\sigma_o, \text{ at } \theta = 0 \tag{20a}$$

---

* These results are valid for a ratio of $(a/h) \approx 0.05$ and subject to the assumption that $(\frac{w}{a}) > 8$ and $(l/a) > 8$ in which case the end boundaries in x and y have insignificant effects on the local to the fiber stress field.

at r = a and z = 0. Comparing this value with that of the corresponding plane strain solution

$$\sigma_{\theta\theta}^{(1)} = \frac{\nu_1}{1-\nu_1}\ \sigma_{rr}^{(1)} = 0.5152\,\sigma_o\,, \quad \text{at } \theta = 0 \tag{20b}$$

one notices that it is approximately 13% higher in value due to the presence of the stresses in the third dimension.

It is now possible for us to obtain an approximate criterion for debonding along the fiber/matrix interface based on Griffith's theory of fracture. Thus, following the work of Toya (1974), if one assumes the presence of an interface crack of length $2a\beta$ and if futhermore takes into account the local 3D stress field, then Toya's result may be written as

$$(1/16)\,(1.1337\sigma_o)^2\, k\, a\, \tilde{A}_1\, (1+4\,\varepsilon^2)\,\pi\, N_o\, \bar{N}_o \sin\beta \exp\left[2\,\varepsilon\,(\pi-\beta)\right] = 2\gamma_{12} \tag{21}$$

where

$$k = \frac{1+k_2}{1+k_2 + (1+k_1)\ (G_2/G_1)} \tag{22}$$

$$k_i = \begin{cases} 3-4\nu_i & \text{for plane strain} \\ \dfrac{3-\nu_i}{1+\nu_i} & \text{for plane stress} \end{cases} \tag{23}$$

$$\tilde{A}_1 = \frac{k}{4\,G_1}\left\{\,1 + k_1 + (1+k_2)\,(G_1/G_2)\,\right\} \tag{24}$$

$$\varepsilon = -\frac{1}{2\pi}\,\ell n\left[\frac{1+k_2\,(G_1/G_2)}{k_1 + (G_1/G_2)}\right] \tag{25}$$

$$N_o \approx G_o - \frac{1}{k} - \frac{2\,(1-k)}{k}\ \frac{1+k_2\,(G_1/G_2)}{k_1 + (G_1/G_2)}\ \exp\left[\beta\,(2\varepsilon - i)\right] \tag{26}$$

$$G_o \approx \frac{1-(\cos\beta + 2\varepsilon\sin\beta)\exp\left[2\varepsilon\,(\pi-\beta)\right] + (1-k)\,(1+4\varepsilon^2)\sin^2\beta}{2-k-k\,(\cos\beta + 2\varepsilon\sin\beta)\exp\left[2\varepsilon\,(\pi-\beta)\right]}, \tag{27}$$

where $\bar{N}_o$ is the complex conjugate of N_o, γ_{12} is the specific surface energy of the interface and β the angle of debonded interface (see Fig. 7). While it is true that this type of approach does not provide results for the exact initiation of an interface crack problem, ie from a condition of perfectly bonded interface to that of a partially debonded interface, it does, however, provide a very good first approximation to this complex phenomenon. The author is well aware of that and is presently continuing his work along such lines and with some promise.

Upon rearranging, equation (21) can be written in the form*

$$\frac{2\gamma_{12}}{\sigma_o^2 a} = (1.2853)\, F\,(v_i, G_i; \beta), \tag{28}$$

where F is a function of the material constants and the angle β of the debonded interface. A plot of this equation for conditions of plane stress, as well as of plane strain, is given in Fig. 8. In both cases the maximum occurs at $\beta = 60°$. Beyond this angle, the crack will gradually curve away from the interface and into the matrix.

In order for us to obtain an estimate for the critical stress for crack initiation we let $\beta \to 0^+$, ie very small but not zero. Thus, for our example

$$(\sigma_o)_{cr}\ \sqrt{2a\beta} \approx 1.8186\sqrt{\gamma_{12} G_1};\quad \text{at } z = 0. \tag{29a}$$

On the other hand, in the neighborhood of the free surface, the applied stress is much higher because of the singularity presence. In order to overcome this difficulty, one may average the local stress over a distance equal to 10% of that of the radius, ie.

* It should be noted that at the crack ends the stress field oscillates and that some overlap of the crack faces takes place. This matter is well recognized and has been documented by Williams (1952), Rice et al. (1965) and England (1965). The region where this occurs, however, is so small (less than a x 10^{-3}) that eq. (28) provides a good approximation.

$$(\sigma_o)_{eff} = \frac{1}{(0.1a)} \int_0^{0.1a} (4.0633\,\sigma_o) \left(\frac{\xi}{a}\right)^{-0.2489} d\xi \qquad (30)$$

$$\approx 9.5958\,\sigma_o\,.$$

Thus*

$$(9.5958\,\sigma_o)_{cr} \sqrt{2\,a\,\beta} \approx 1.8146 \sqrt{\gamma_{12}\,G_1}\,; \quad \text{at } z \approx \pm h. \qquad (29b)$$

Combining next eqs. (29a) and (29b) one finds

$$\frac{(\sigma_o)_{cr}\,|_{at\ z=h}}{(\sigma_o)_{cr}\,|_{at\ z=0}} \approx 0.10, \qquad (31)$$

ie. the critical loading stress which may cause failure close to a free surface is approximately (1/10) of the critical stress required to cause the same failure at the center of the fiber's length. Thus, all things being equal, a crack will initiate at the free surface and will propagate along the periphery of the fiber/matrix interface as well as parallel to the axis of the fiber.

Focusing next our attention on the advancement of the crack along the periphery of the fiber we conclude that the crack will advance itself to a cricital angle of $\beta \approx 60°$. Once the crack has reached* $\theta = 60°$, the local geometry is similar to that of a hole. This problem has also been investigated for the, 3D, stress field close to a free surface (Folias, 1987), as well as in the interior of the plate (Folias and Wang 1986). Without going into the details, at z=h, it was found that

$$\frac{\sigma^{(1)}_{\theta\theta}}{\sigma^{(1)}_{rr}} = -(1+\nu_1) = -1.34, \qquad (32)$$

suggesting, therefore, that the failure now is governed by the stress $\sigma^{(1)}_{\theta\theta}$ which attains its maximum value at $\theta = \pi/2$. Thus, the crack will begin to curve into

* The reader may notice that the right hand side of equation (29b) differs from (29a) because it is based on plane stress.

the matrix until its direction becomes perpendicular to that of the applied load.

PERIODIC ARRAY OF FIBERS

The previous results were based on the presence of one fiber only. It is now desirable to extend these results to also include a doubly periodic array of fibers which are embedded into a matrix. For this reason, we assume, a periodic arrangement of the type shown in fig. 9. Following the same method of solution as that of Penado and Folias (1989), one finds* at z=0 the stresses $\sigma_{rr}^{(1)}$ and $\sigma_{\theta\theta}^{(1)}$, for $\nu_1 = 0.34$, $\nu_2 = 0.22$ and various (G_2/G_1) ratios, shown in figs. 6 and 10. Two observations are worthy of note. First, beyond a certain ratio of (G_2/G_1) the stress $\sigma_{rr}^{(1)}$ reaches an asymptotic value. Such trend was also found by Adams (1967) based on 2D considerations. Second, as the volume of fibers increases the stress $\sigma_{rr}^{(1)}$ decreases by as much as 40% (see fig. 11).

Returning next to the strain energy release rate, equation (21) is still a good approximation provided that σ_o is replaced by the following effective load stress

$$(\sigma_o)_{\text{effective periodic}} = \left\{ \frac{\sigma_{rr}^{(1)}|_{\lambda}}{\sigma_{rr}^{(1)}|_{\lambda=0}} \right\} \sigma_o = F(V_f)\,\sigma_o \quad ; \text{ for } z = 0. \qquad (33)$$

Thus equation (29a) now becomes

$$(\sigma_0)_{cr} \approx 1.8186 F(V_f) \sqrt{\frac{\pi_2 G_m}{2a_f \beta}} \qquad (34)$$

which is valid for small values of β.

---

* The results are valid for all fibers which are at least four diameters away from the bounding planes $x = \pm w$ and $y = \pm \ell$. The solution and the details are similar to those discussed by Penado and Folias (1989) except that one now has $\cos(2n\theta)$, $n = 0,1,2,\ldots$, where the remaining unknown coefficients are determined from the boundary conditions of the geometrical cell configuration. The present results, are based on $n = 0,\ldots, N = 20$ terms which provide accurate results in the region $|z/h| < 1/2$. However, many more terms are needed in order to obtain accurate results particularly in the neighborhood of $z = \pm h$. We are presently working on this and the results for this problem, as well as for the problem of stresses due to temperature missmatch, will be reported in the near future.

Unfortunately, in order to obtain a similar expression for z=h, one needs to establish whether the order of the singularity strength increases as adjacent fibers approach the fiber in question. In view of some previous work the author conjectures that this may very well be the case. Thus, the following fundamental questions come to mind. How close must adjacent fibers be before the order of the singularity strength is affected? Does a certain separation distance or a certain periodic array of fibers exists which leads to an optimal state of stress? Based on 3D considerations, Penado and Folias (1989) have shown that when fibers are placed four fiber diameters apart, center to center, practically all fiber interactions have subsided, including those at the free surface z=h. The author suspects, however, that when fibers are placed two diameters apart, center to center, the singularity strength will be affected. Naturally, this is a conjecture that needs to be investigated.

As a practical matter, if one uses the approximation given by eq. (30), the critical stress to failure at the fiber edge in a glass fiber/epoxy matrix composite with the properties

$$\begin{array}{llll} G_m = 2.10GPa & \nu_m = 0.34 & a_f \approx 10^{-3}cm & \beta = 60^\circ \\ G_f = 35.00GPa & \nu_f = 0.22 & 2\gamma_{12} \approx 70J/m^2 & V_f = 0.70 \end{array} \qquad (35)$$

becomes

$$(\sigma_o)_{cr} = 20.582\ F(V_f)\ \text{Mpa.}$$
$$= 2.985\ F(V_f)\ \text{ksi} \quad ;\ \text{at the fiber edge} \qquad (36)$$

a plot of which is given in Fig. 12. Edge delamination may now be modeled as the progressive failure of a row of fibers.

CONCLUSIONS

Based on a 3D analytical solution, we have shown that fiber/matrix debonding is most likely to occur close to a free surface. Thus, regions where fibers intersect free surfaces, eg. holes, cut outs, edges, cracks etc. are potential trouble spots. Moreover, the strain energy release rate (eq. 28) may be used to predict crack initiation in the center of the fiber length (eq. 29a), as well as at the free surface (eq. 29b). Moreover, fiber/matrix debonding at a free surface will occur at approximately (1/10) the load value required for the same type of failure to occur at the center of the fiber length. Such information on crack initiation is particularly important for the proper understanding of damage evolution.

Alternatively, the strain energy release rate for a periodic array of fibers of the type shown in fig. 9 may, at z=0, be approximated by eq. (28) in conjunction with eq. (33). A similar expression applicable to the neighborhood of the free surface requires that one must first establish whether the strength of the singularity is indeed affected as the fiber volume increases. For $\bar{V}_f \leq 0.05$, however, it has been shown* that no such interaction effects are present.

As a final remark, we note that if the bond at the interface does not fail the analysis shows that there exists a stress magnification factor in the resin which attains a maximum between the fibers. This maximum stress magnification occurs along the line $\theta = 0°$ and at a distance $r = 1.2a$ from the center of the fiber**.

---

* See Panado and Folias (1989).

** This condition is valid for all $0 \leq z < h$.

REFERENCES

Adams, D.F. and Doner, D.R., 1967, "Transverse Normal Loading of a Unidirectional Composite", J. of Composite Materials, Vol. 1, pp. 152-164.

Chamis, C.C., 1975, Edited, "Composite Materials", Academic Press, Vol. 1-8.

England, A.H., 1965, "A Crack Between Dissimilar Media", Journal of Applied Mechanics pp. 400-402.

Folias, E.S., 1989, "The 3D Stress Singularities at the Intersection of a Cylindrical Inclusion and a Free Surface", International Journal of Fracture, Vol. 39, pp. 25-34.

Folias, E.S., 1987, "The 3D Stress Field at the Intersection of a Hole and a Free Surface", International Journal of Fracture, Vol. 35, No. 3, pp. 187-194.

Folias, E.S., 1965, "An Axial Crack in a Pressurized Cylindrical Shell", International Journal of Fracture, Vol. 1, pp. 20-46.

Folias, E.S. and Liu, J., 1990, "The 3D Stress Field of a Cylindrical Fiber Embedded into a Matrix with a Layer of Modified Matrix Around the Fiber" in preparation.

Folias, E.S. and Wang, J.J., 1986, "On the Three-Dimensional Stress Field Around a Circular Hole in a Plate of an Arbitrary Thickness", University of Utah Technical Report.

Hull, D., 1981, "An Introduction to Composite Materials", Cambridge University Press.

Keer, L.M., Dundurs, J., Kiattikomol, k., 1973, "Separation of a Smooth Cricular Inclusion from a Matrix", Int. Journal of Engineering Science, Vol. 11, pp. 1221-1233.

Penado, F.E., Folias, E.S., 1989, "The Three-Dimensional Stress Field Around a Cylindrical Inclusion in a Plate of Arbitrary Thickness", International Journal of Fracture, Vol. 39, pp. 129-146.

Rice, J.R. and Sih, G.C., 1965, Journal of Applied Mechanics, Transaction ASME, Series E 32, p. 418.

Toya, M., 1974, "A Crack Along the Interface of a Circular Inclusion Embedded in an Infinite Solid", Journal of Mechanics and Physics of Solids, Vol. 22, pp. 325-348.

Williams, M.L., 1952, Journal of Applied Mechanics, Transactions ASME, 19, p. 526.

Yu, I.W. and Sendeckyj, G.P., 1974, "Multiple Circular Inclusion Problems in Plane Elastostatics," pp. 215-220.

FIGURE CAPTIONS

Fig. 1. Geometrical and loading configuration.

Fig. 2. Definition of local coordinates.

Fig. 3. Singularity strength for isotropic fiber and isotropic matrix versus G_2/G_1.

Fig. 4. Stress $\sigma_{rr}^{(1)}$ at r=a, θ=0 and for $\nu_1 = 0.34$, $\nu_2 = 0.22$ and $(G_2/G_1) = 16.67$, accross the thickness.

Fig. 5 Stress $\sigma_{\theta\theta}^{(1)}$ at r=a, θ=0 and for $\nu_1 = 0.34$, $\nu_2 = 0.22$ and $(G_2/G_1) = 16.67$, across the thickness.

Fig. 6 Stress $\sigma_{rr}^{(1)}$ at r=a, θ=0 and for $\nu_1 = 0.34$, $\nu_2 = 0.22$, versus the ratio (G_2/G_1).

Fig. 7 Fiber/matrix interface crack under transverse loading.

Fig. 8 Strain energy release rate for plane stress and plane strain conditions for $\nu_1 = 0.34$, $\nu_2 = 0.22$ and $(G_2/G_1) = 16.67$.

Fig. 9 Periodic array of fibers of length 2h, embedded into a matrix.

Fig. 10 Stress $\sigma_{rr}^{(1)}$ at r=a, θ=0 and for $\nu_1 = 0.34$, $\nu_2 = 0.22$, versus the ratio (G_2/G_1).

Fig. 11 Stress $\sigma_{\theta\theta}^{(1)}$ at r=a, versus V_f, for $(G_2/G_1) = 16.67$ $\nu_1 = 0.34$, $\nu_2 = 0.22$.

Fig. 12. Critical stress versus V_f for $(G_2/G_1) = 16.67$, $\nu_1 = 0.34$ and $\nu_2 = 0.22$.

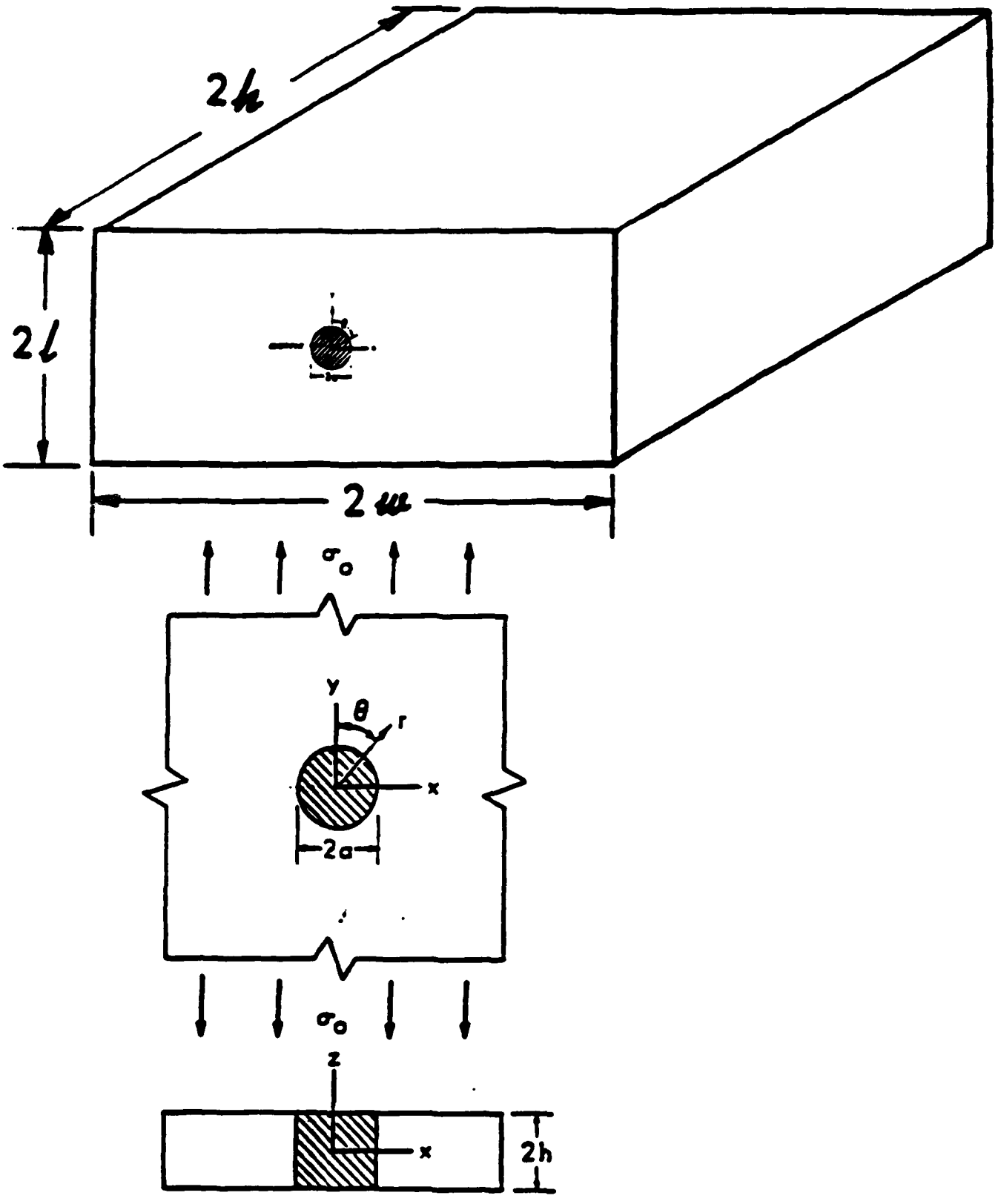

Fig. 1. Geometrical and loading configuration.

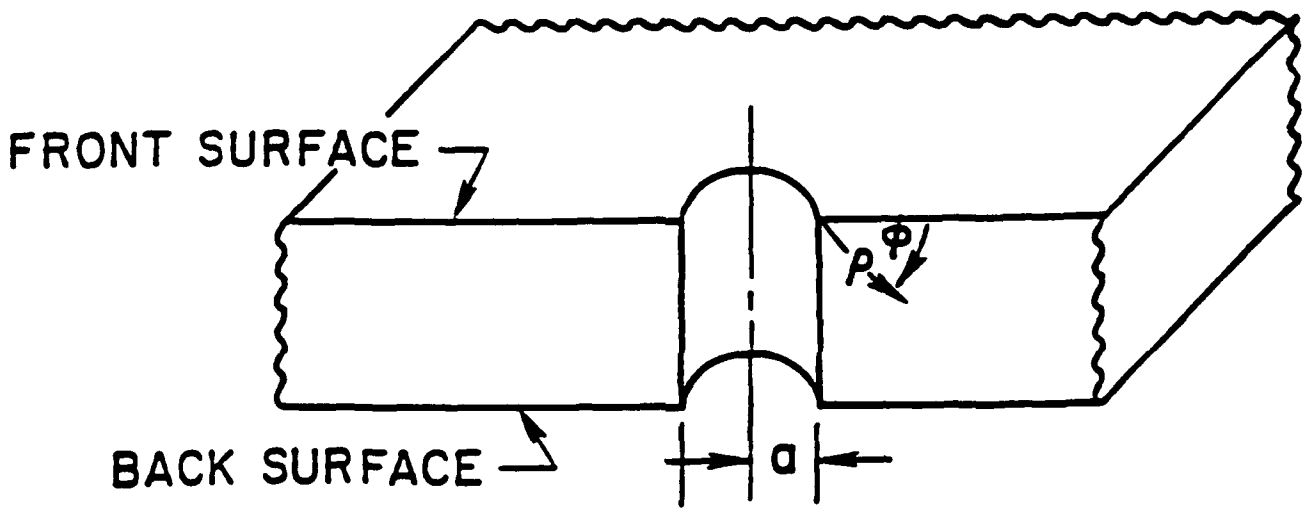

Fig. 2. Definition of local coordinates.

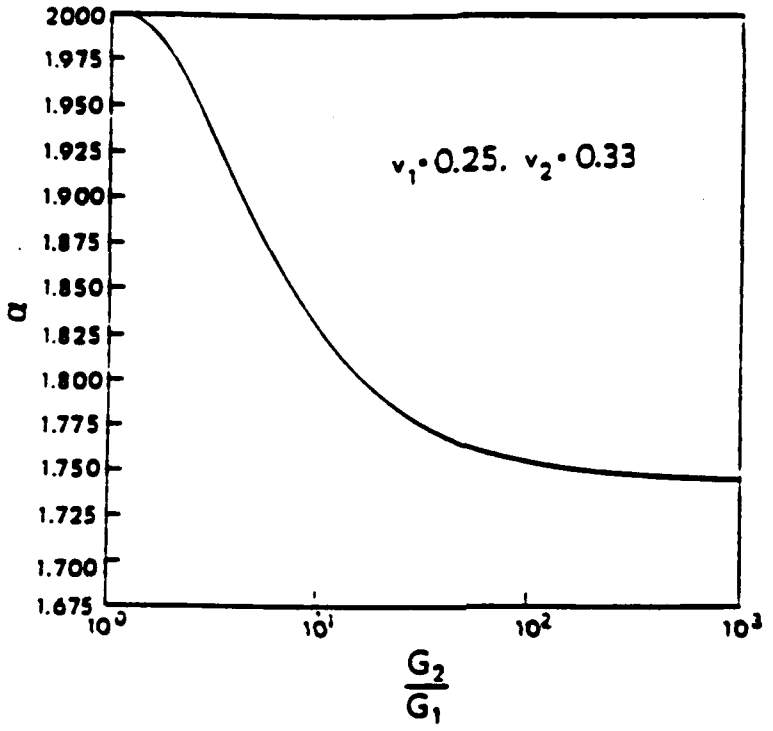

Fig. 3. **Singularity strength for isotropic fiber and isotropic matrix versus G_2/G_1.**

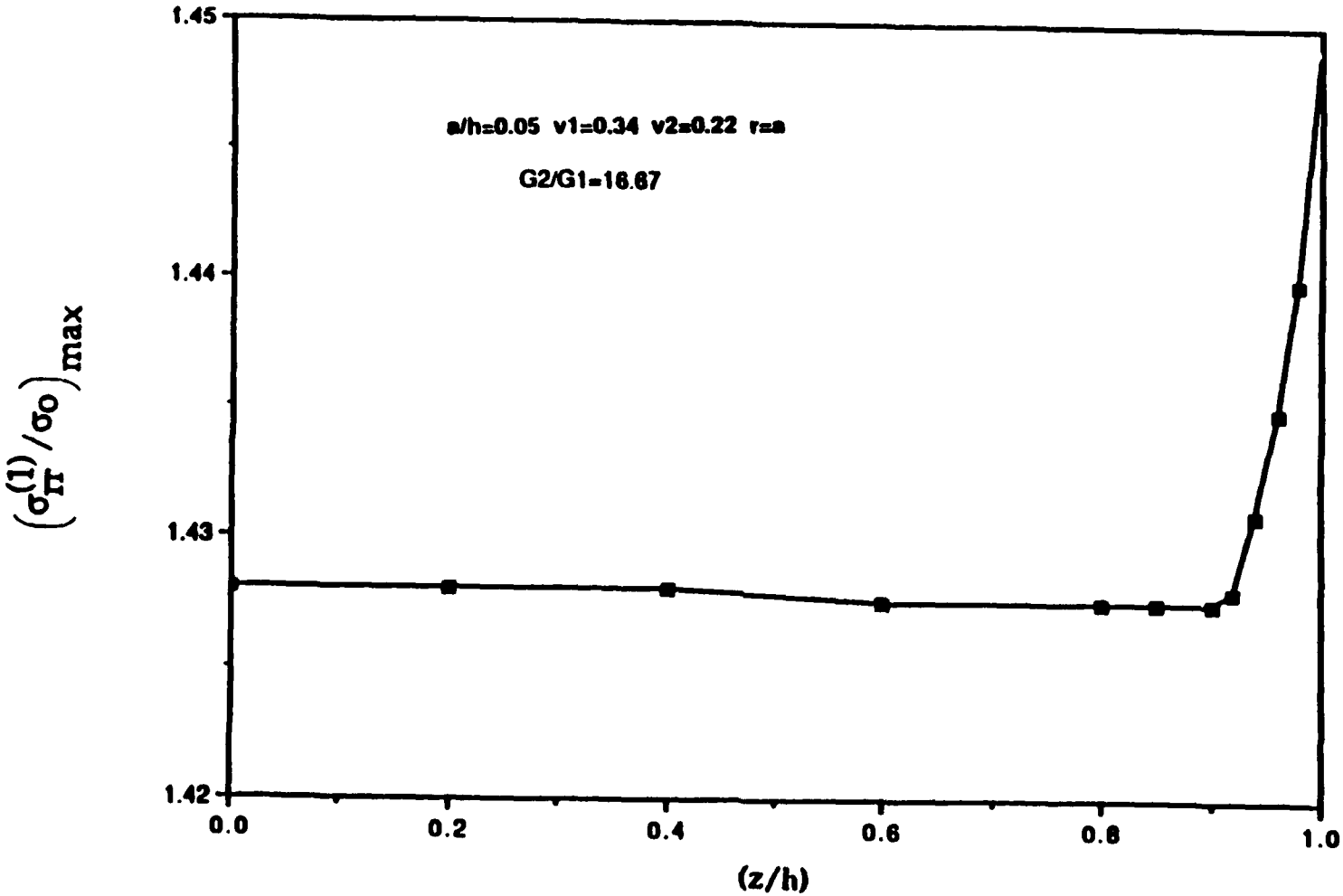

Fig. 4. Stress $\sigma_{rr}^{(1)}$ at r=a, θ=0 and for $\nu_1 = 0.34$, $\nu_2 = 0.22$ and $(G_2/G_1) = 16.67$, accross the thickness.

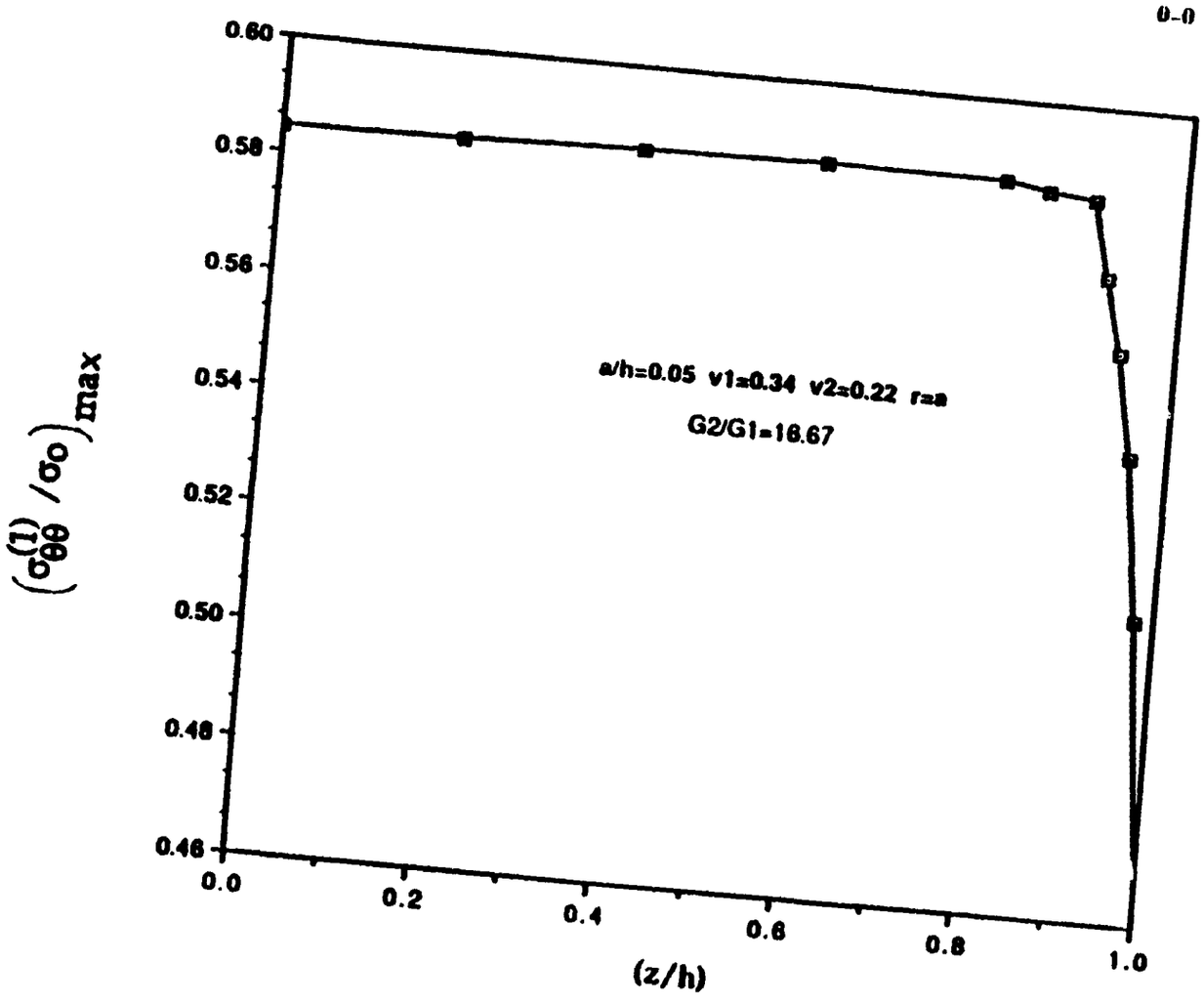

Fig. 5 Stress $\sigma_{\theta\theta}^{(1)}$ at r=a, θ=0 and for $\nu_1 = 0.34$, $\nu_2 = 0.22$ and $(G_2/G_1) = 16.67$, across the thickness.

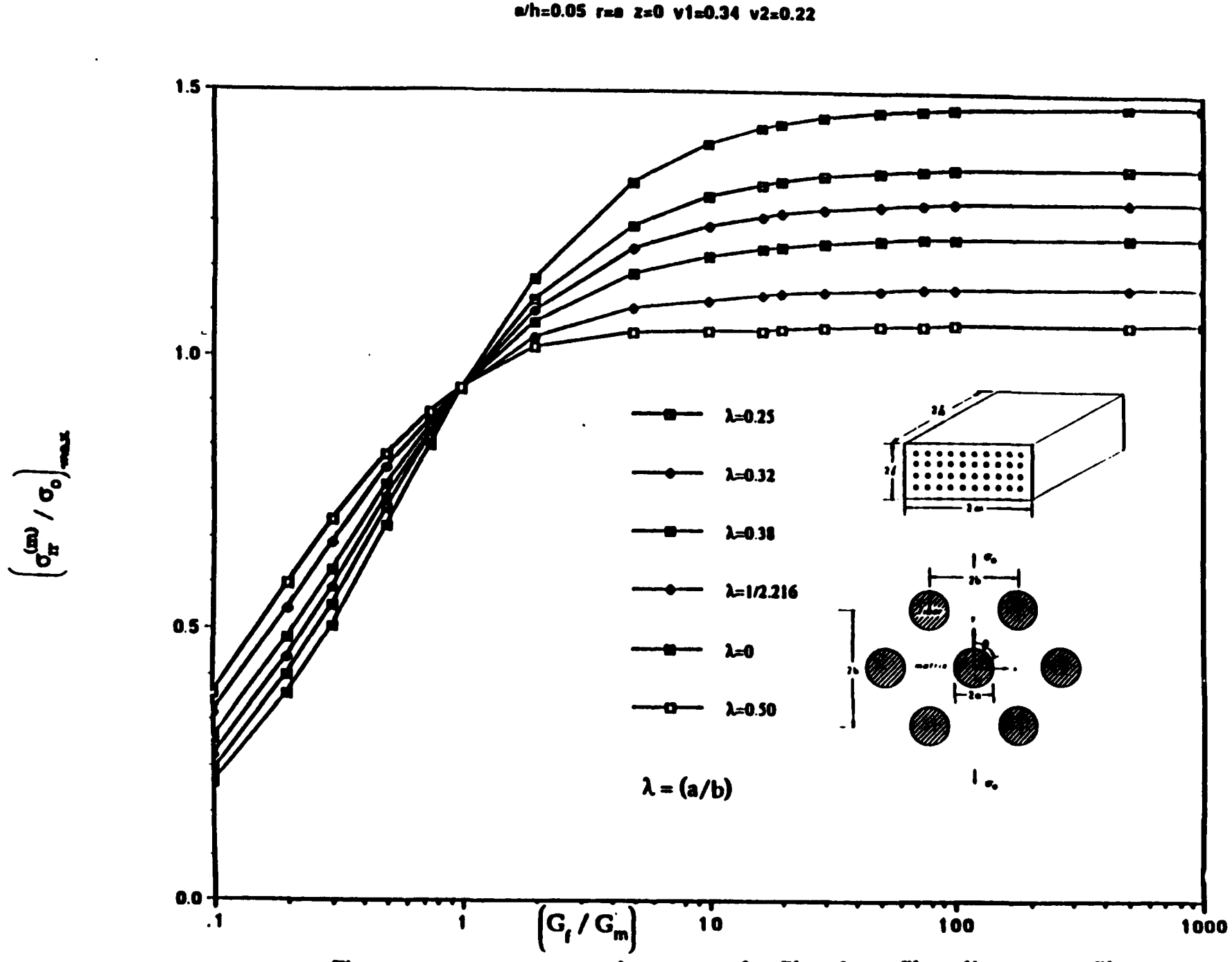

Fig. 6. max stress σ_{rr} at the center of a fiber for a fiber diameter to fiber

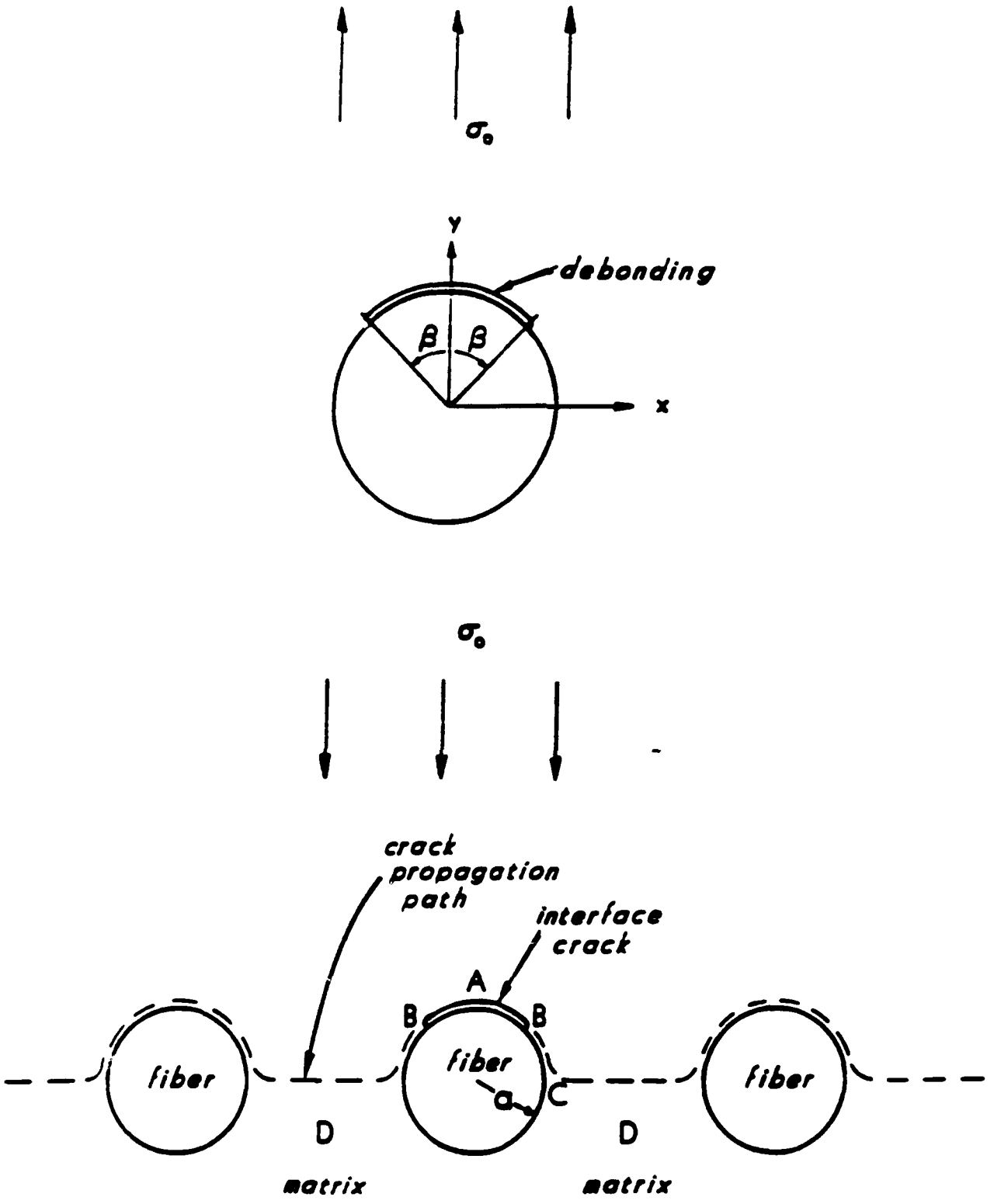

Fig. 7 Fiber/matrix interface crack under transverse loading.

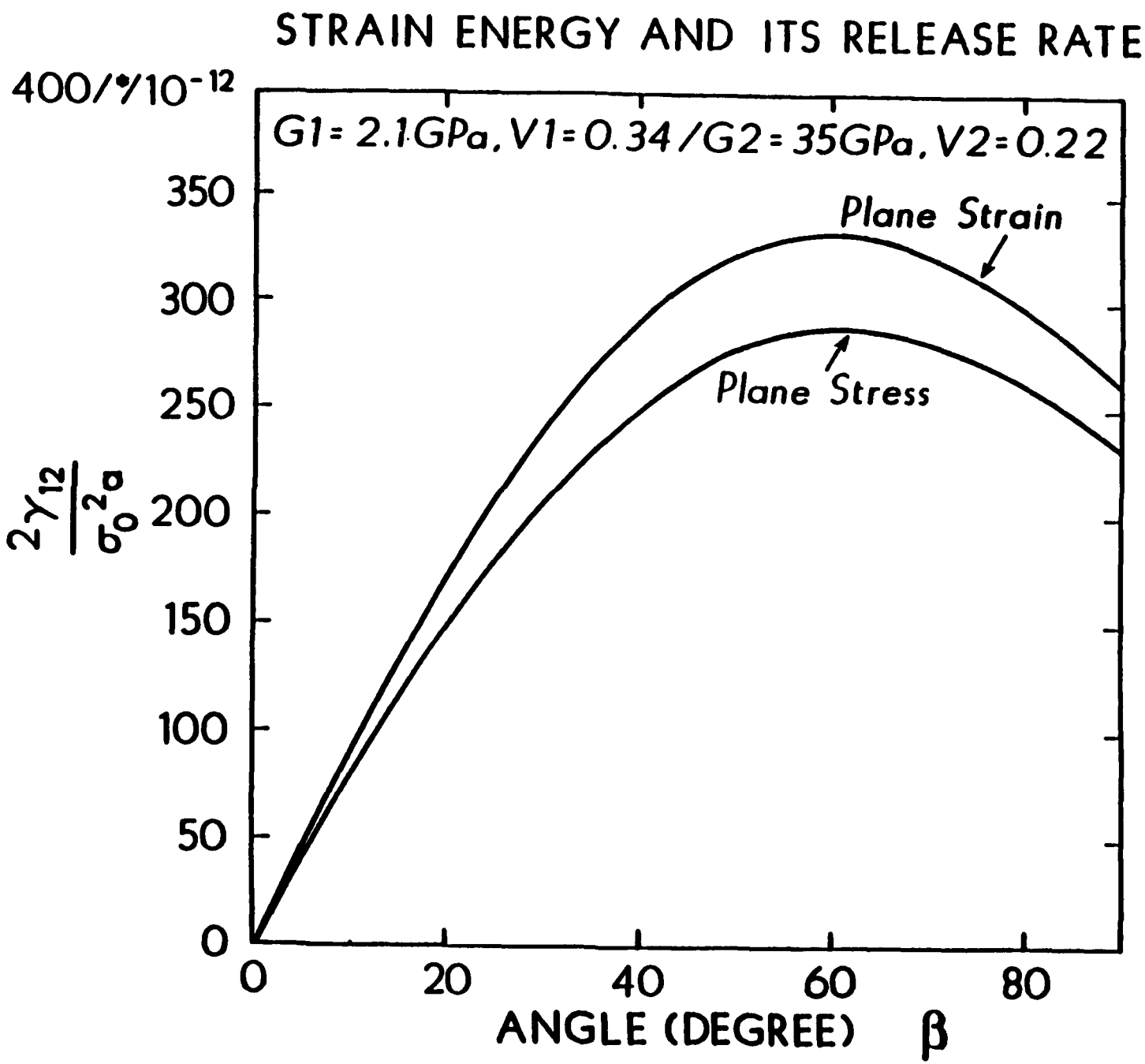

Fig. 8 Strain energy release rate for plane stress and plane strain

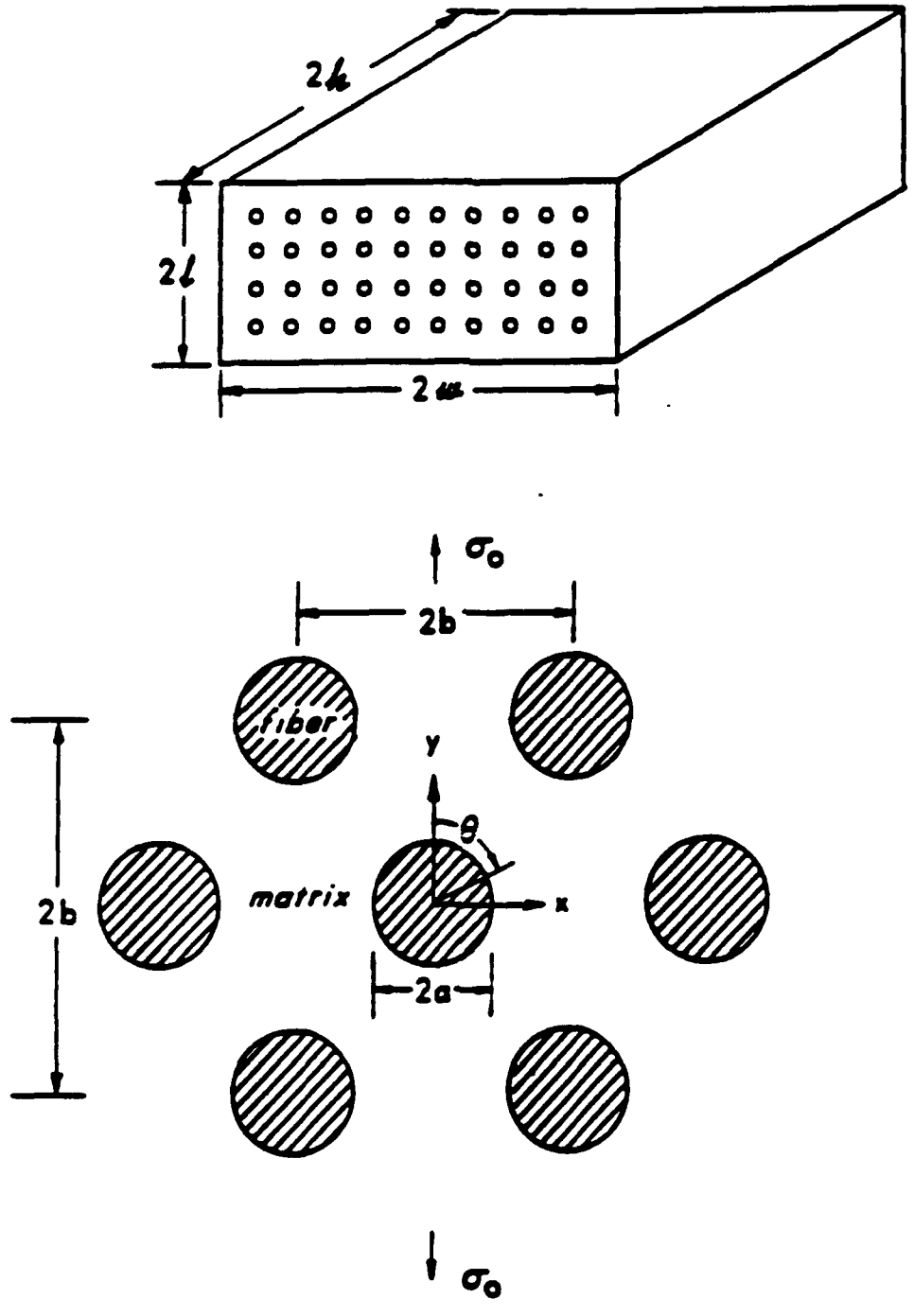

Fig. 9 Periodic array of fibers of length 2h, embedded into a matrix.

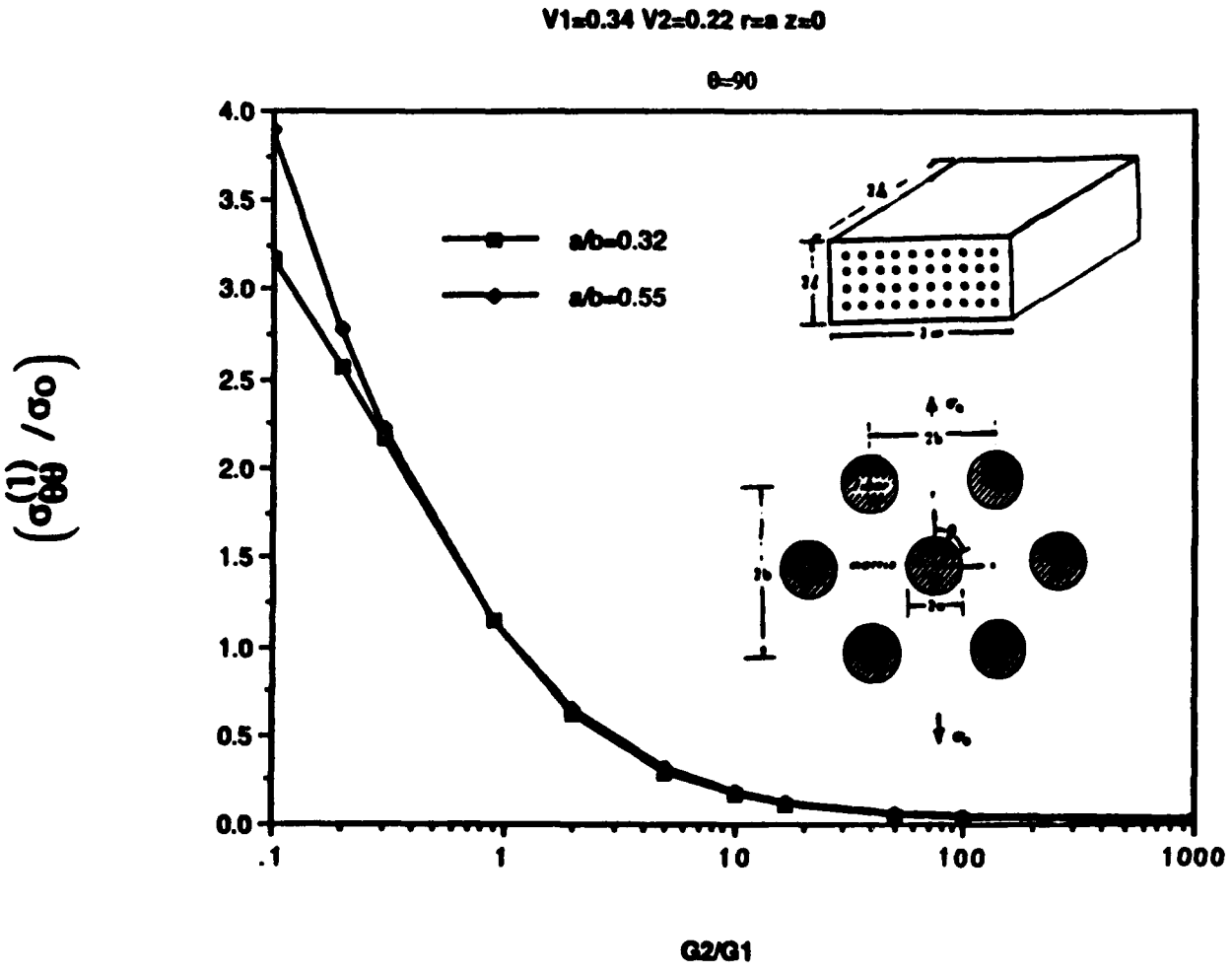

Fig. 10 Stress $\sigma^{(1)}_{\theta\theta}$ at r=a, θ=90 and for $\nu_1 = 0.34$, $\nu_2 = 0.22$, versus the ratio (G_2/G_1).

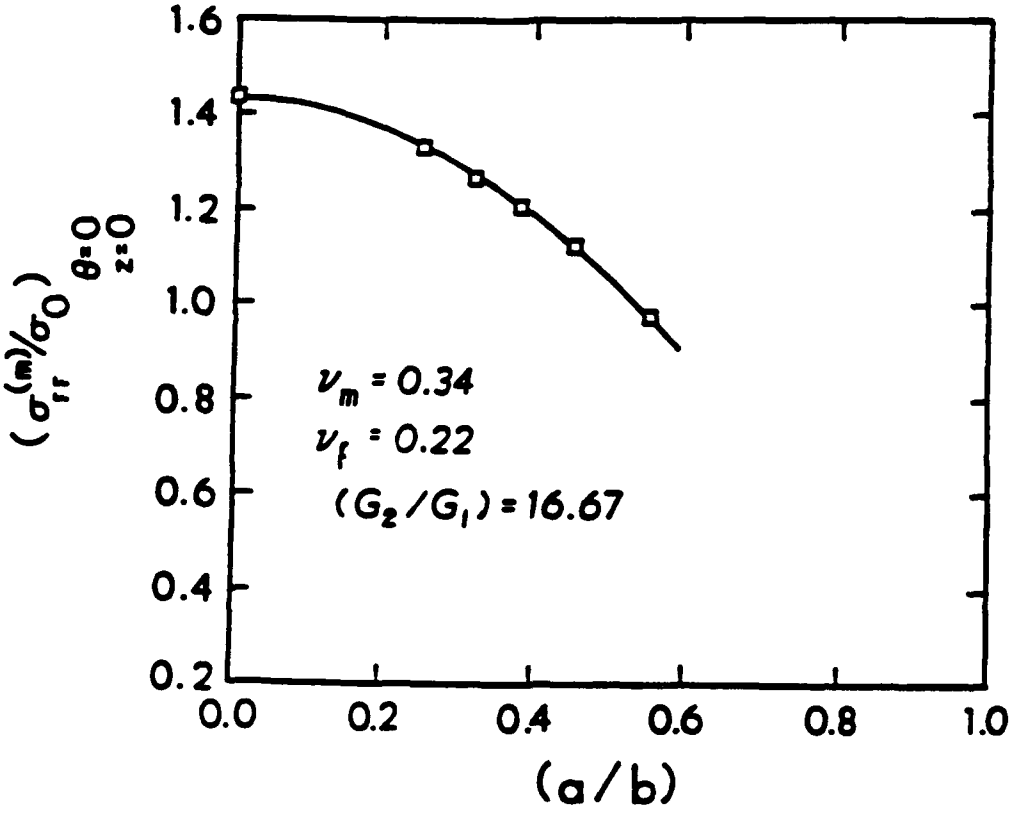

Fig. 11 Stress $\sigma_{rr}^{(1)}$ at r=a, versus a/b for $(G_2/G_1) = 16.67$ $\nu_1 = 0.34$, $\nu_2 = 0.22$.

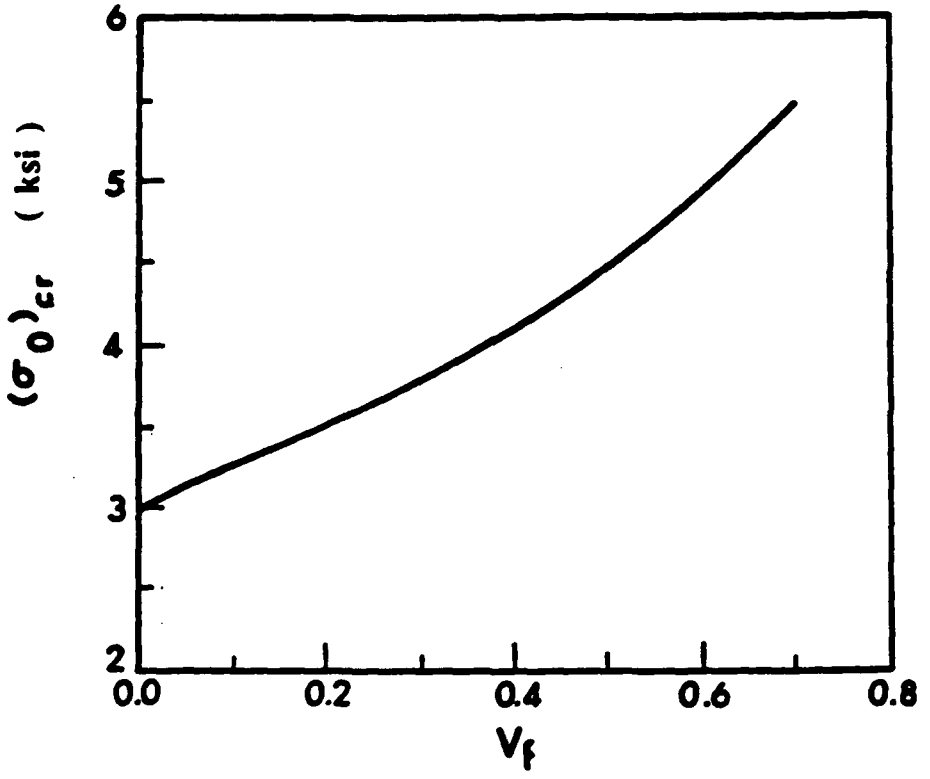

Fig. 12. Critical stress to failure versus V_f for $(G_2/G_1) = 16.67$, $\nu_1 = 0.34$ and $\nu_2 = 0.22$.

PART IV

ON THE 3D MODELING OF A FIBER / MATRIX INTERFACE

by

E. S. FOLIAS and J. H. LIU

Submitted to the
International Journal of Fracture

Department of Mechanical Engineering
University of Utah
Salt Lake City, Utah 84112

Abstract

In this paper, the 3D stress field is derived for a cylindrical fiber consisting of a radius a and surrounded by a modified cylindrical shell matrix of outside radius b. The system is embedded into a plate matrix of arbitrary thickness 2h. All materials are assumed to be isotropic and perfect bonding is assumed to prevail at their respective interfaces. As to loading, a uniform tension is applied in the plane of the matrix plate and at points remote from the interfaces.

The analysis shows that all stresses are sensitive to the radius to half thickness ratio (a/b) as well as the material properties. In general, the effect that a modified shell matrix has on the magnitude of the radial stress σ_{rr} is minimal (approximately 3%). However, the location of its max. depends strongly on the respective shear moduli ratios (G_2/G_1) and (G_3/G_1). The analysis also characterizes the type of fracture process to be primarily cohesive. Moreover, the stresses are shown to be singular in the neighborhood of the intersection of the interface curve with that of the edge plane.

All things being equal, a crack is most likely to originate at the free edge and will propagate , along the interface and towards the interior of the composite ,up to approximately one fiber radius. Whereby it will ,subsequently, curve into the matrix and follow the locus of the max. σ_{rr}. Approximate failure criteria are also suggested.

INTRODUCTION

The properties of fiber reinforced composites are very much dependent upon the stability of the interfacial region between the matrix and the fiber . This is because the primary function of this interface region is to transmit a portion of the load from the matrix to the reinforcing fibers and vise versa. This ability to transmit stress across the phase boundary must , ultimately , depend upon the mechanical properties of the matrix, the load bearing capacity of the fibers as well as the strength of the fiber matrix interface. It is natural ,therefore, to seek the relationship between the overall composite strength and the above variables.

In a recent paper which was based on 3D considerations, Panado and Folias (1989) studied the problem of a cylindrical (isotropic) fiber which is embedded into an epoxy matrix. The interface between the fiber and the matrix was represented as a cylindrical boundary. In reality, however, it should be an interface region rather than an interface boundary the composition of which depends on the specific fiber/matrix combination (Drzal, 1983). There are three reasons for this. First, there exist morphological variations on the surface of the fiber. Second, there is a chemical reaction which takes place in such regions. Third, in order to protect the fibers from mechanical damage and to promote high matrix adhesion, mixtures of sizing and coupling agents are applied to the fiber surfaces during the fiber manufacturing process. The question , therefore, arises as to what effect if any does such an imperfect interface , or modified matrix layer , have on the strength characteristics of the overall system. In order to provide a partial answer to this, Agarwal and Bansal (1979) investigated the effects of such an 'imperfect interface' by considering a thin layer of different material properties to represent the interface region. The analysis was restricted to a load in the longitudinal direction of the fiber and was based on 2D considerations. Subsequently, Tandon and Pagano (1988) developed an approximate model that one may use to predict the overall moduli and coefficients of thermal expansion

of composites in the presence of imperfect bonding and subject to displacement and traction boundary conditions.

The present paper investigates the effect that such a 'modified layer' has on the strength characteristics of an isotopic fiber embedded into a matrix and subjected to a uniform transverse load. Moreover, in order to extract the relevant edge effects the analysis will be based on 3D considerations . It is hoped that this study will compliment the previous investigations and perhaps offer some further insight on the possibilities of cracking due to the external load.

FORMULATION OF THE PROBLEM

Consider the equilibrium of a body which occupies the space $|x| < \infty$, $|y| < \infty$, $|z| \leq h$ and contains three regions with different elastic properties. Their common boundaries consist of through-the-thickness cylindrical surfaces of radii $r = a$ and $r = b$, whose generators are parallel to the z- axis (see Figs 1 and 2). The situation described is that of a fiber, denoted by superscript (3), which is embedded into a matrix, denoted by superscript (1). Moreover, the fiber surface is coated with a thin layer of different material properties, denoted by superscript (2). All three materials are assumed to be homogeneous, isotropic and linear elastic. At the interfaces $r = a$ and $r = b$ perfect bonding is assumed to prevail. As to loading, a uniform tensile stress σ_o is applied at the matrix at points remote from the fiber. In all three regions, the surfaces $|z| = h$ are assumed to be free of stress and contstrain .

In the absence of body forces, the coupled differential equations governing the displacement functions $u_k^{(i)}$ are:

$$\frac{m_i}{m_i - 2} \frac{\partial e^{(i)}}{\partial x_k} + \nabla^2 u_k^{(i)} = 0 \; ; \; i, k = 1, 2, 3 \qquad (1)$$

where ∇^2 is the 3D Laplacian operator, $m_i \equiv \frac{1}{\nu_i}$, ν_i is Poisson's ratio and

$$e^{(i)} \equiv \frac{\partial u_k^{(i)}}{\partial x_k^{(i)}} \; ; \; i, k = 1, 2, 3 \tag{2}$$

- The stress displacement relations are given by Hooke's law as:

$$\sigma_{kl}^{(i)} = 2 G_i \left\{ \frac{1}{m_i - 2} \, e_{jj}^{(i)} \, \delta_{lk} + e_{lk}^{(i)} \right\} \; ; \; i,k,l = 1, 2, 3 \tag{3}$$

where G_i are the respective shear moduli.

As to boundary conditions, we require that:

$$\text{as } |x| \to \infty : \quad \sigma_{xx}^{(1)} = \tau_{xy}^{(1)} = \tau_{xz}^{(1)} = 0 \tag{4}$$

$$\text{as } |y| \to \infty : \quad \tau_{xy}^{(1)} = \tau_{yz}^{(1)} = 0, \; \sigma_{yy}^{(1)} = \sigma_o \tag{5}$$

$$\text{at } |z| = h : \quad \tau_{xz}^{(i)} = \tau_{yz}^{(i)} = \sigma_{zz}^{(i)} = 0 \; ; \; i = 1, 2, 3 \tag{6}$$

$$\text{at } r = b : \quad \sigma_{rr}^{(1)} - \sigma_{rr}^{(2)} = \tau_{r\theta}^{(1)} - \tau_{r\theta}^{(2)} = \tau_{rz}^{(1)} - \tau_{rz}^{(2)} = 0, \tag{7}$$

$$\text{at } r = b : \quad u_r^{(1)} - u_r^{(2)} = v_\theta^{(1)} - v_\theta^{(2)} = w^{(1)} - w^{(2)} = 0 \, , \tag{8}$$

$$\text{at } r = a : \quad \sigma_{rr}^{(2)} - \sigma_{rr}^{(3)} = \tau_{r\theta}^{(2)} - \tau_{r\theta}^{(3)} = \tau_{rz}^{(2)} - \tau_{rz}^{(3)} = 0, \tag{9}$$

$$\text{at } r = a : \quad u_r^{(2)} - u_r^{(3)} = v_\theta^{(2)} - v_\theta^{(3)} = w^{(2)} - w^{(3)} = 0 \, , \tag{10}$$

Finally, at $r = 0$ we must require that all stresses and displacement be bounded.

METHOD OF SOLUTION

A general solution to a certain class of three dimensional boundary value problems which arise in elastostatics, was developed by Folias (1976) and was subsequently put in a much more convenient form (Folias 1990). The general solution was recently used to solve for the 3D stress field of one cylindrical fiber embedded into an infinite matrix

(Penado and Folias 1989). The latter study may now be extended to also account for the effects of a modified shell matrix surrounding the fiber.

The mathematical details, however, are long and tedious but similar to those of the above reference, except that one now has to deal with two interfaces instead of one. Thus for the sake of brevity, the details in the present analysis are omitted . In summary, the displacement fields are expressed in terms of two infinite series, one with complex eigenfunctions and the other with real eigenfunctions. By construction, the general solution automatically satisfies the free of stress boundary conditions at $|z| = h$. The unknown series coefficients are subsequently determined, numerically, from the remaining boundary conditions at the two interfaces $r = a$ and $r = b$. For more details, the reader is referred to the work by Penado and Folias (1989).

NUMERICAL RESULTS

Once the series coefficients have been determined, the 3D displacement and stress fields may then be recovered. Throughout the numerical work, we have used double precision because the system is very sensitive to small changes. Furthermore, the rate of convergence has been addressed in the work by Penado and Folias (1989). The present numerical work also exhibits similar convergence characteristics. Thus, without going into the numerical details, the displacement w , on the surface $z = h$, as a function of $\left(\frac{r-a}{a}\right)$ is shown in Figs. 3 and 4 for various G ratios. This particular displacement is of special interest to the experimentalists for future comparisons.

The behavior of the radial stress σ_{rr}, as a function of the modified layer thickness $\Delta = (b-a)/a$, is shown in Figs 5 and 6 , at the position $\theta = 0$ and $r = b$. It is noted that for the fixed ratios of $(G_3/G_1) = 16.67$ and $(G_2/G_1) = 12$, the relative max. of the radial stress occurs at $\Delta \approx 0.2$, for $z = 0$ and $z = h$. In fact, the same trend prevails throughout the thickness z. In general, the location of the max. is a function of the respective material

properties. Moreover, the behavior of the radial stress σ_{rr} versus (z/h) is similar to that found by Penado and Folias (1989). A typical plot is shown in Fig. 7. On the other hand, the variation of the stress $\sigma_{\theta\theta}$ as a function of Δ, at $\theta = 0$ and $r = b$, is given in Figs. 8 and 9 for $z = 0$ and $z = h$, respectively. Thus as Δ increases, $\sigma_{\theta\theta}$ decreases slightly (by approximately 3%).

Fig. 10, depicts the variation of the radial stress σ_{rr} as a function of the ratio (G_3/G_2) for $\theta = 0$, $z = 0$, $\Delta = 0.2$, $r = b$ and $(G_3/G_1) = 16.67$. Similarly, Figs. 11 and 12 show the variation of σ_{rr}, for $(G_2/G_1) \leq 1$ and for $(G_2/G_1) > 1$ ratios, respectively. Here again the max. change is noted to be approximately 3%.

It is well recognized from experimental observations that debonding along a fiber/matrix interface is a common occurrence in laminated composite plates due to transverse loads. What is not clear, however, is whether the crack originates at the fiber/matrix interface or in the matrix itself but close to the interface. Naturally, all things being equal, a crack is most likely to originate at a location where the radial stress attains its maximum. To provide us with some further insight on this matter, we plot in Fig. 13 the radial stress σ_{rr} versus the distance (r-a), for various (G_2/G_1) ratios. The reader may notice that, although the stress σ_{rr} is continuous at $r = b$, its derivative there is discontinuous. This result meets our expectations for the material properties to the left and to the right are distinct. Furthermore, it may be noted that for $(G_2/G_1) < 2.5$ ratios the max. radial stress occurs within the modified shell matrix, while for $2.5 < (G_2/G_1)$ occurs within the matrix, i.e. past the interface $r = b$. Thus the question as to whether one has adhesive or cohesive fracture really depends on the respective material properties.* It should be emphasized that this comment is applicable not only to the case of one fiber, but also to the case of an infinite periodic array of fibers which are spaced by four (or more) fiber diameters center to center. In the latter case, there exist no significant interactions present between the adjacent fibers (see Figs. 3 and 4). This matter has also been

*From Fig. 13, it is noted that away from the edge, adhesive fracture only takes place at one value which is between $1.7 < (G_2/G_1) < 2.8$.

discussed in a recent paper by Folias (1991) which is based on 3D considerations. In the event that the fibers are closer together, Adams et .al . (1967) have shown, on the bases of 2D considerations, that the max. radial stress σ_{rr} occurs at r = 1.2a, i.e. between the fibers. The same result has subsequently been confirmed by other researchers in the field. On the bases of 3D considerations and the given data , the authors also confirm this result (Liu and Folias 1991) which is valid throughout the interior. In general, given a set of material properties, the location of the maximum is a function of the ratio (a/b). Returning next to the free edges, the stress field in the neighborhood of the intersection of the interface boundary with that of the free surface was shown to be singular (Folias 1989, Li and Folias 1991). The same result is expected to apply here too. In fact, the authors believe that the strength of the stress singularity will increase slightly as the distance between the adjacent fibers decreases and the interaction effects become stronger. Similar trends are also expected to prevail in the case of the modified layer matrix.

CONCLUSIONS

The following conclusions may be drawn from the previous results:

(i) away from the free edge:

- the effect of a modified shell matrix on the magnitude of the radial stress σ_{rr} is negligible, ie. approximately 3%
- the max. value of the radial stress σ_{rr} is approximately the same for all (G_2/G_1) ratios examined
- the location of this max. occurs within the modified layer if $1 < (G_2/G_1) < 2$, and within the matrix if $2 < (G_2/G_1) < 16.67$
- characterization of the fracture process as adhesive or cohesive depends on the material properties (see Fig. 13)
- the modified layer thickness Δ which will make the radial stress σ_{rr} a relative maximum is .20

(ii) within the vicinity of the free edge:

- the max. radial stress σ_{rr} occurs at one of the two interfaces

In conclusion, all things being equal, a crack is most likely to originate in the vicinity of the free edge and along one of the interface boundaries (that of the highest stress singularity). Subsequently, the crack will propagate away from the edge and along the interface up to a distance of one fiber radius at which point it will slowly curve into the matrix and follow the locus of the max. radial stress σ_{rr} (see Fig. 13). Thus, it is now possible to derive two separate failure criteria which will be applicable to the regions (i) close to the free edge and (ii) away from the free edge. The first author has already derived such a criterion for the prediction of failure at a free edge (see Folias, 1991). It remains, therefore, for us to derive a criterion applicable to the latter region.

REFERENCES

1. Drzal, L.T. (1983), "Composite Interface Characterization," SAMPE J., 19, 5, pp. 7-13.

2. Tandon, G.P. and Pagano, N.J. (1988), "A Study of Fiber-Matrix Interfacial Modeling" Proceedings of the fourth Japan - U.S. Conference on Composite Materials, pp. 191-200.

3. Penado, F.E. and Folias, E.S. (1989), "The Three Dimensional Stress Field Around a Cylindrical Inclusion in a Plate of an Arbitrary Thickness," International Journal of Fracture, Vol. 39, pp. 129-146.

4. Folias, E.S. (1989), "On the Stress Singularities at the Intersection of a Cylindrical Inclusion with the Free Surface of a Plate," International Journal of Fracture, Vol. 39, pp. 25-34.

5. Li, P.C. and Folias, E.S. (1970), "The 3D Stress Field of a Carbon Fiber Intersecting a Free Surface and Under the Action of a Uniform Transverse Load," under review.

6. Adams, D.F. and Donner, D.R. (1967), "Transverse Normal Loading of a Unidirectional Composite," Journal of Composite Materials, Vol. 1, pp. 152-164.

7. Folias, E.S. (1991), "On the Prediction of Failure at a Fiber/Matrix Interface in a Composite Subjected to a Transverse Tensile Load," To appear Journal of Composite Materials, 1991.

8. Folias, E.S. and Liu, J.H. (1991), "The 3D Stress Field of a Periodic Array of Fibers Embedded into an Epoxy Matrix," in preparation.

9. Hull, D., (1981), " An Introduction to Composite Materials " , Cambridge University Press.

10. Folias, E. S., (1974),Thin-Shell Structures , Edited by Fung and Sechler, Chapt. 21, pp. 483-518

11. Folias, E. S., and Reuter, W. G.,(1990) , " On the Equilibrium of a Linear Elastic Layer " , Computational Mechanics , Vol. 5 , pp. 459-468.

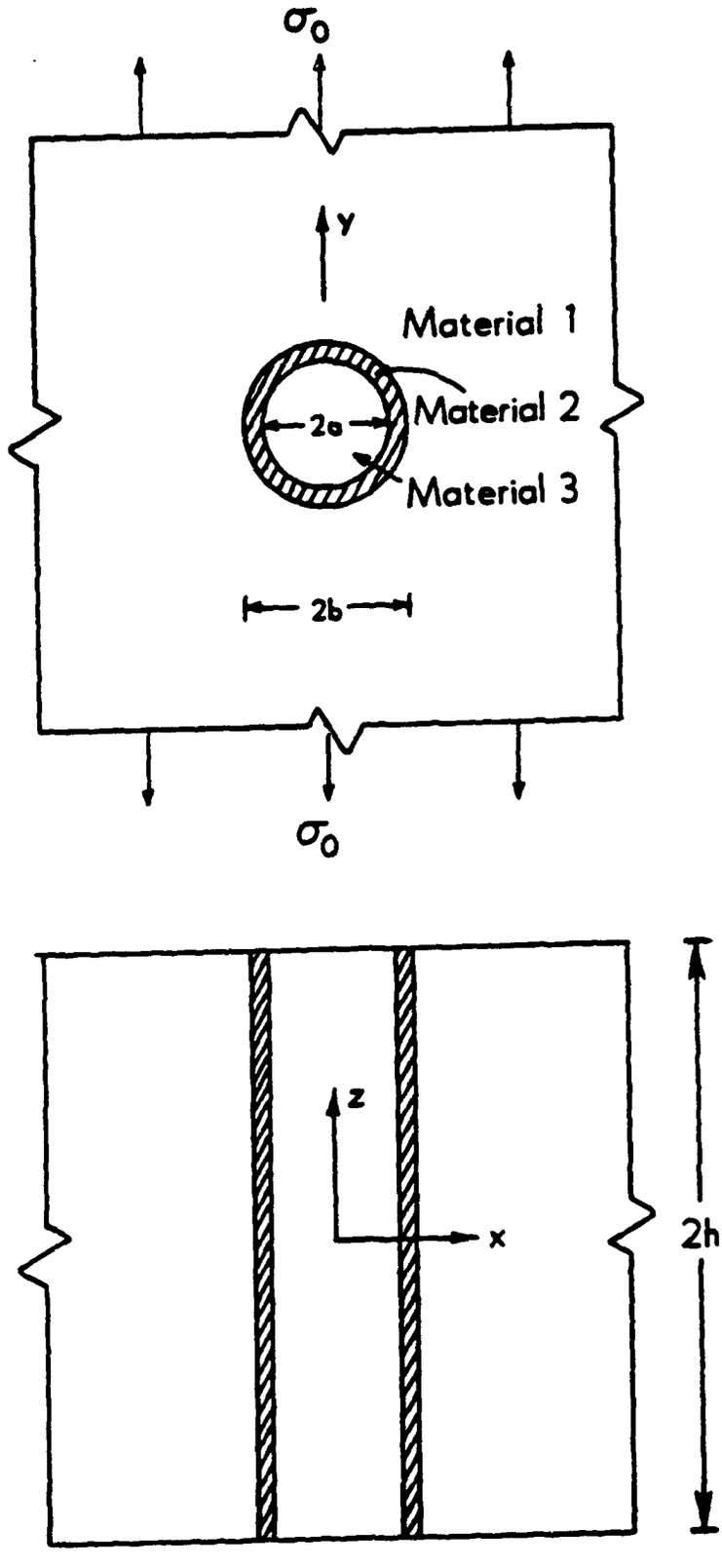

Fig. 1 Geometrical configuration.

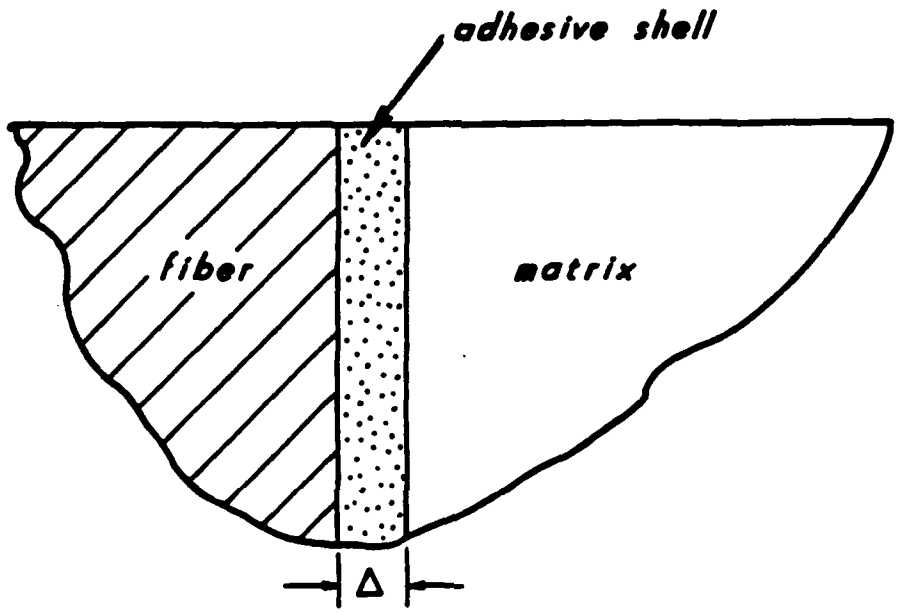

Fig. 2 Geometrical configuration at the free edge.

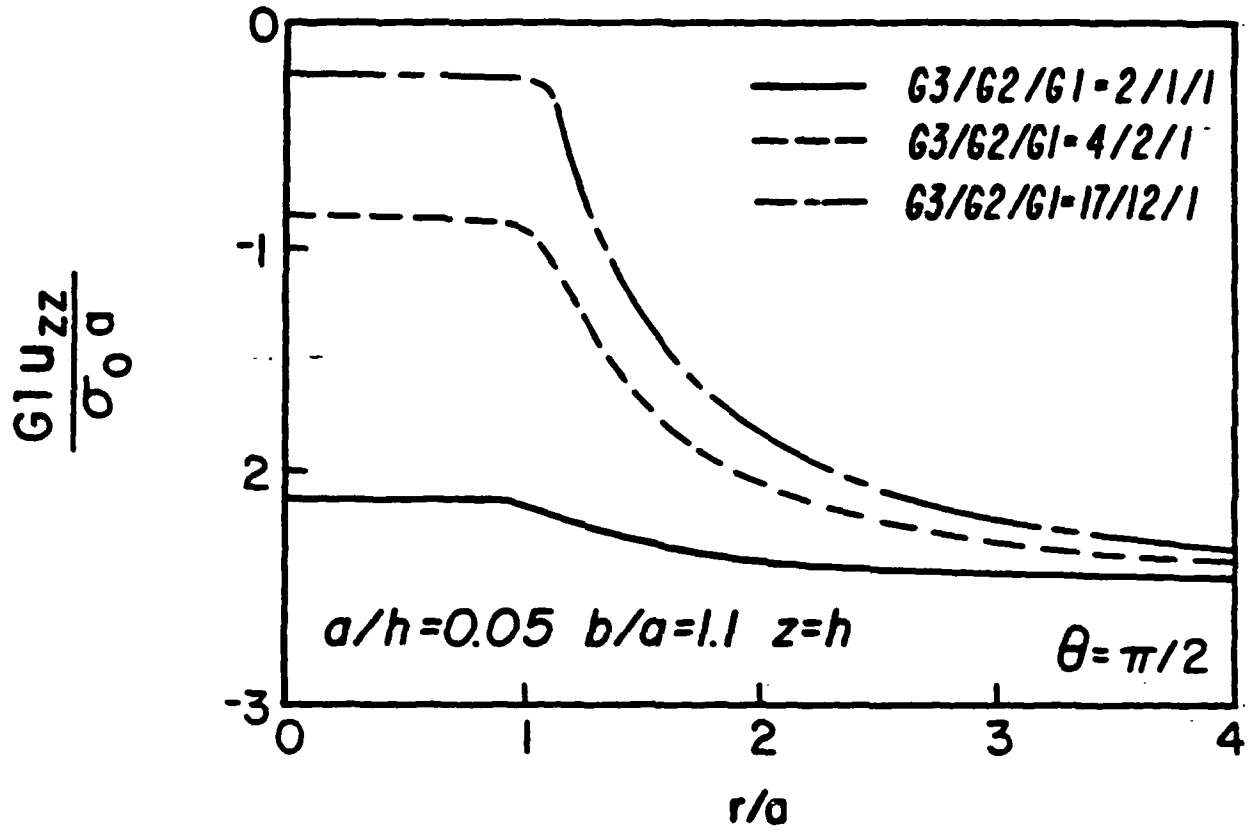

Fig. 3 The displacement w at the free surface z = h vs. (r/a) for (a/h) = 0.05.

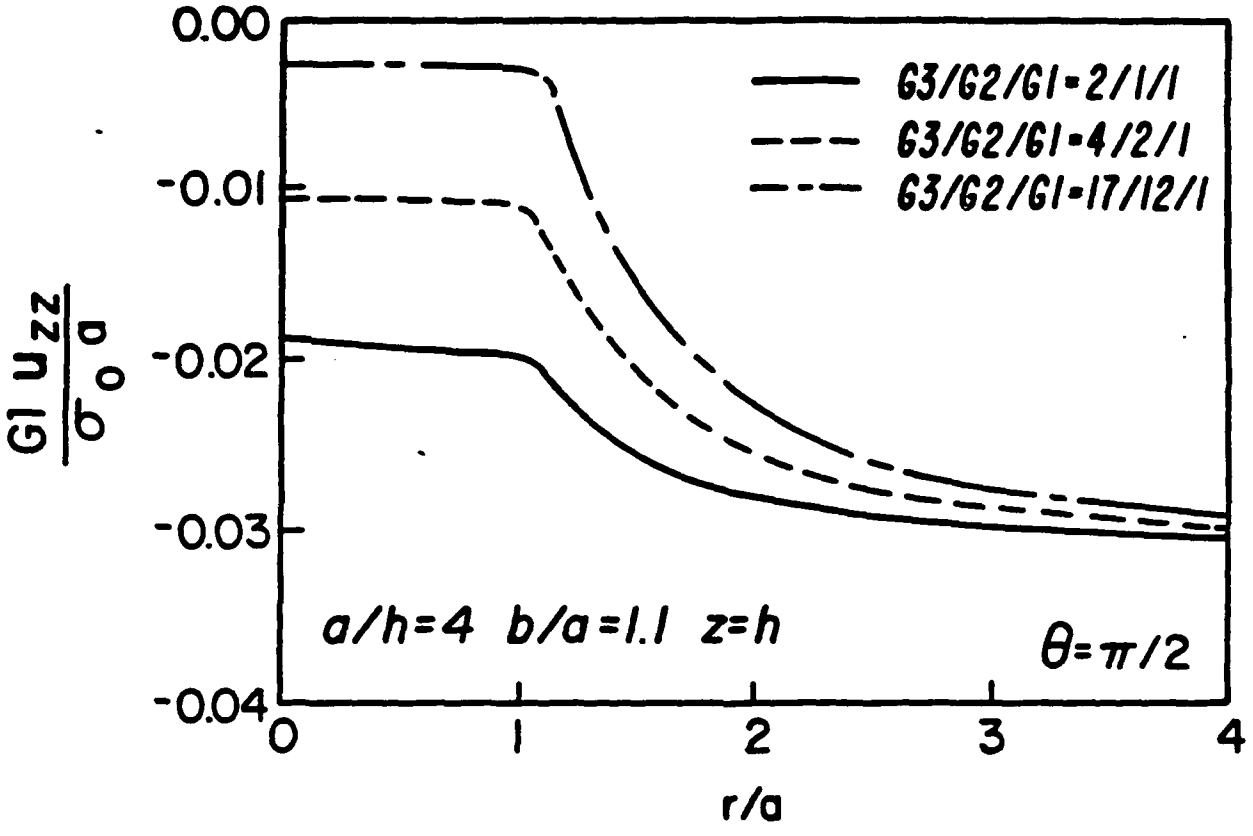

Fig. 4 The displacement w at the free surface z = h vs. (r/a) for (a/h) = 4.

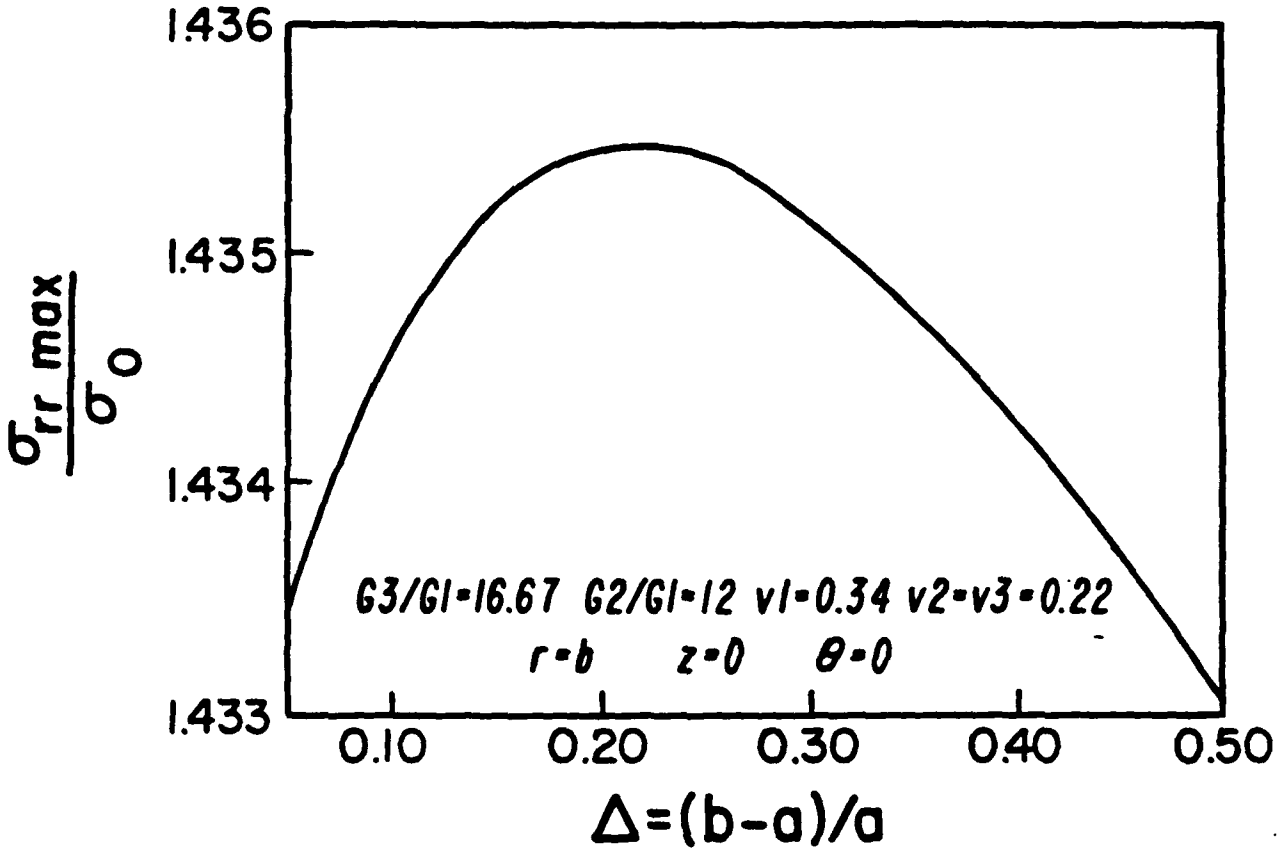

Fig. 5 The radial stress vs. Δ at r=b and z= 0.

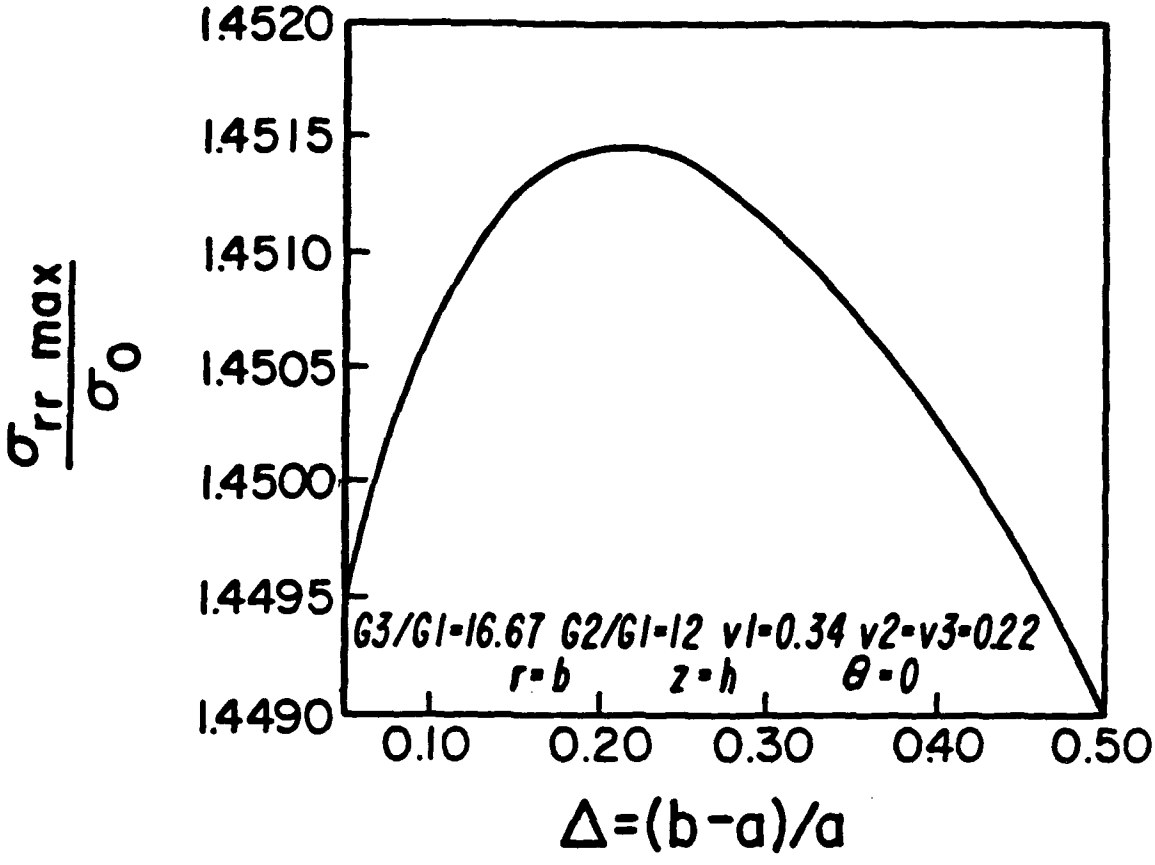

Fig. 6 The radial stress vs. Δ at r=b and z= h.

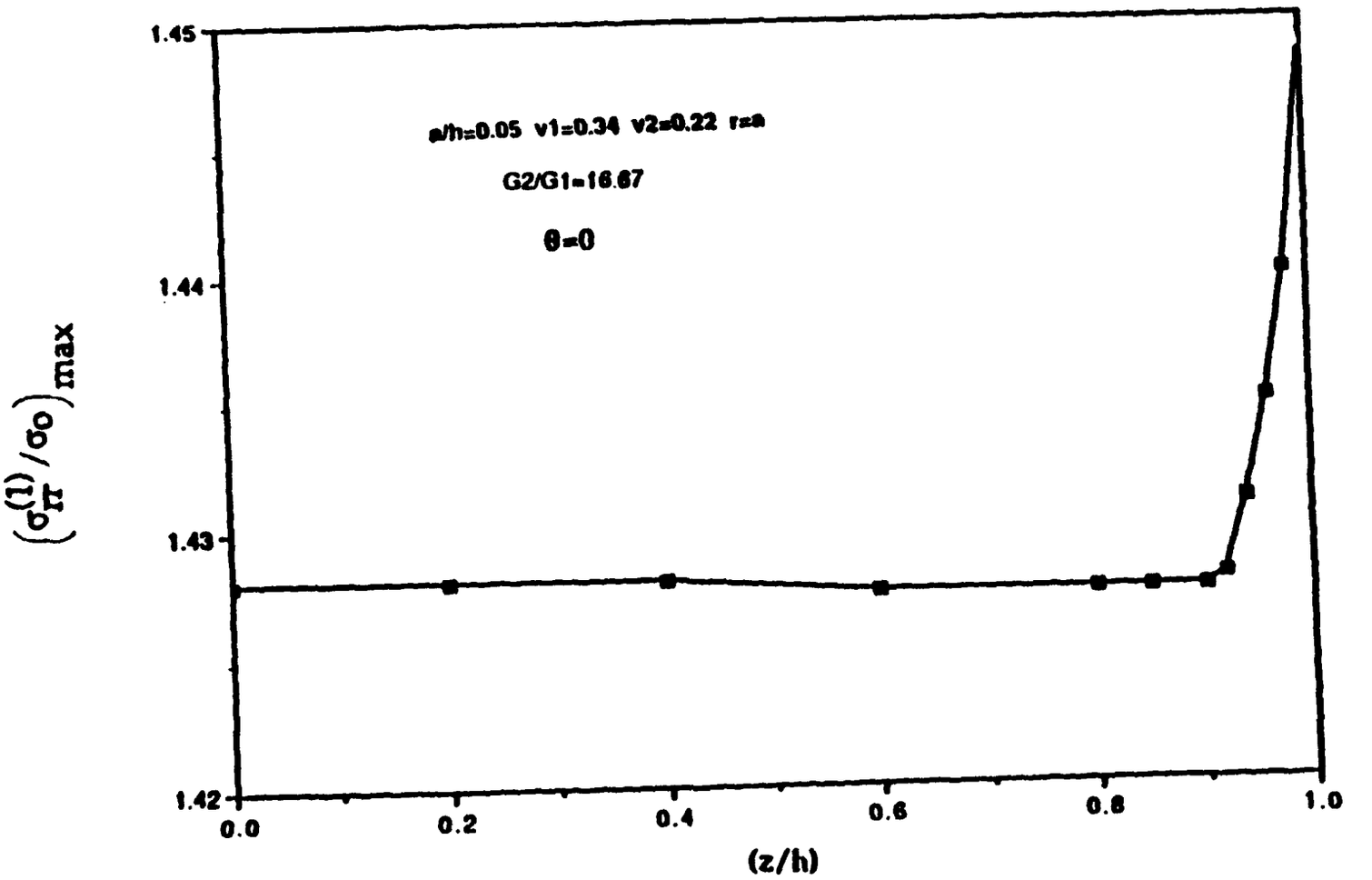

Fig. 7 The max. radial stress vs. (z/h) at r=a and for a/h= 0.05.

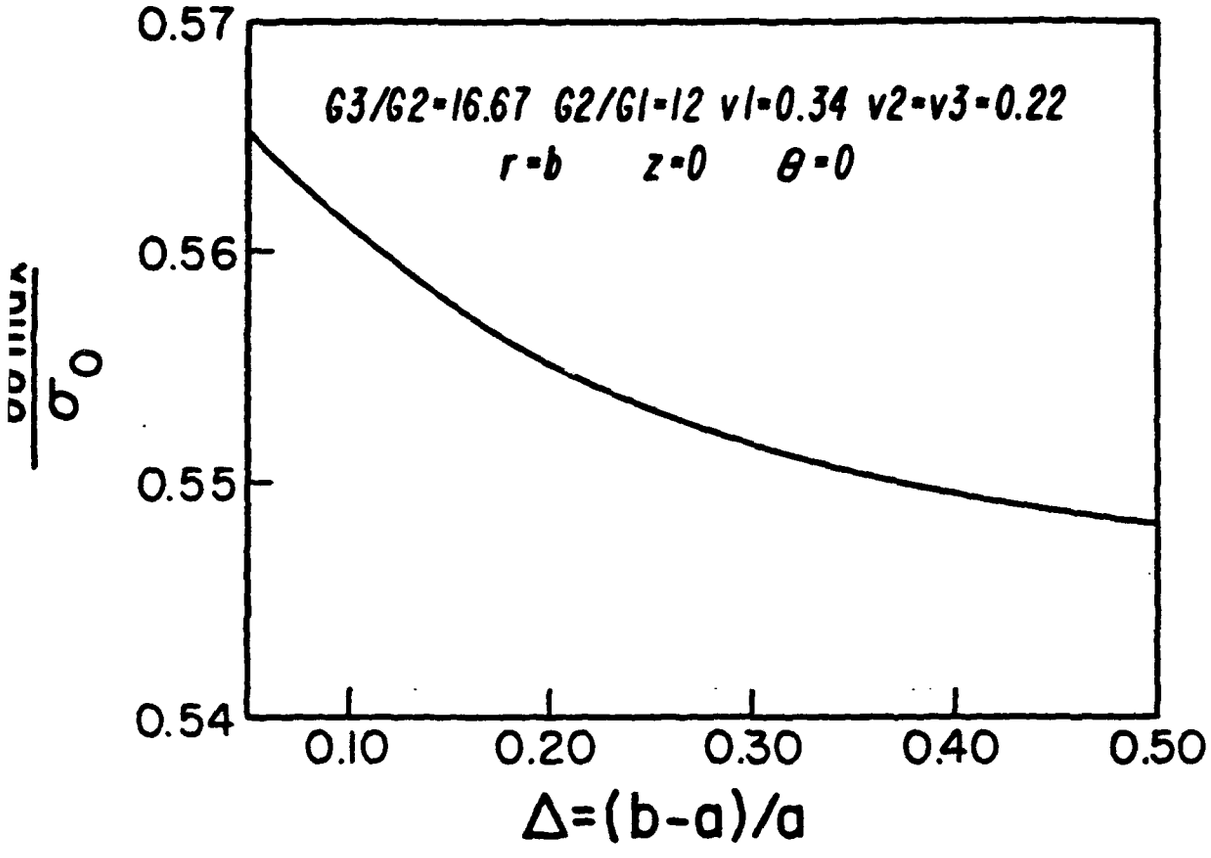

Fig. 8 The max. circumferential stress vs. Δ at $z=0$.

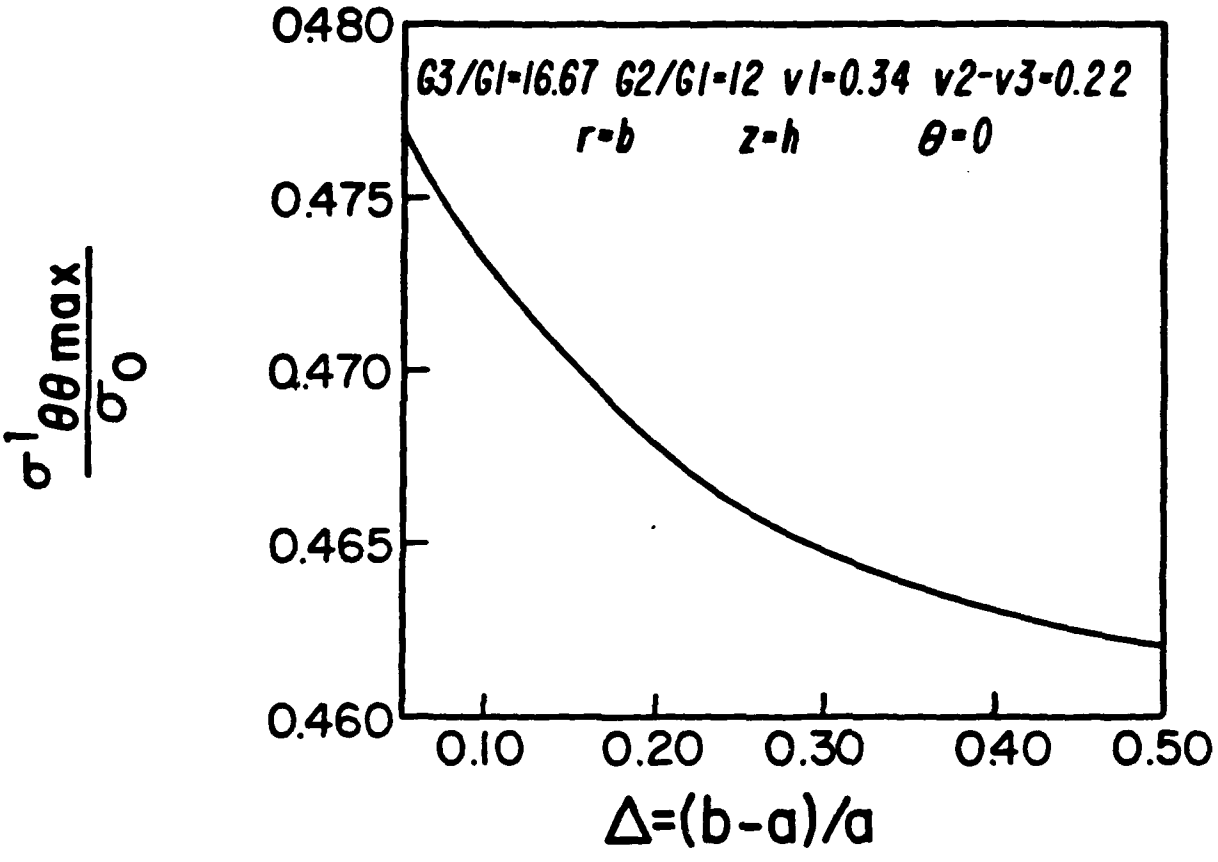

Fig. 9 The max. circumferential stress vs. Δ at z= h.

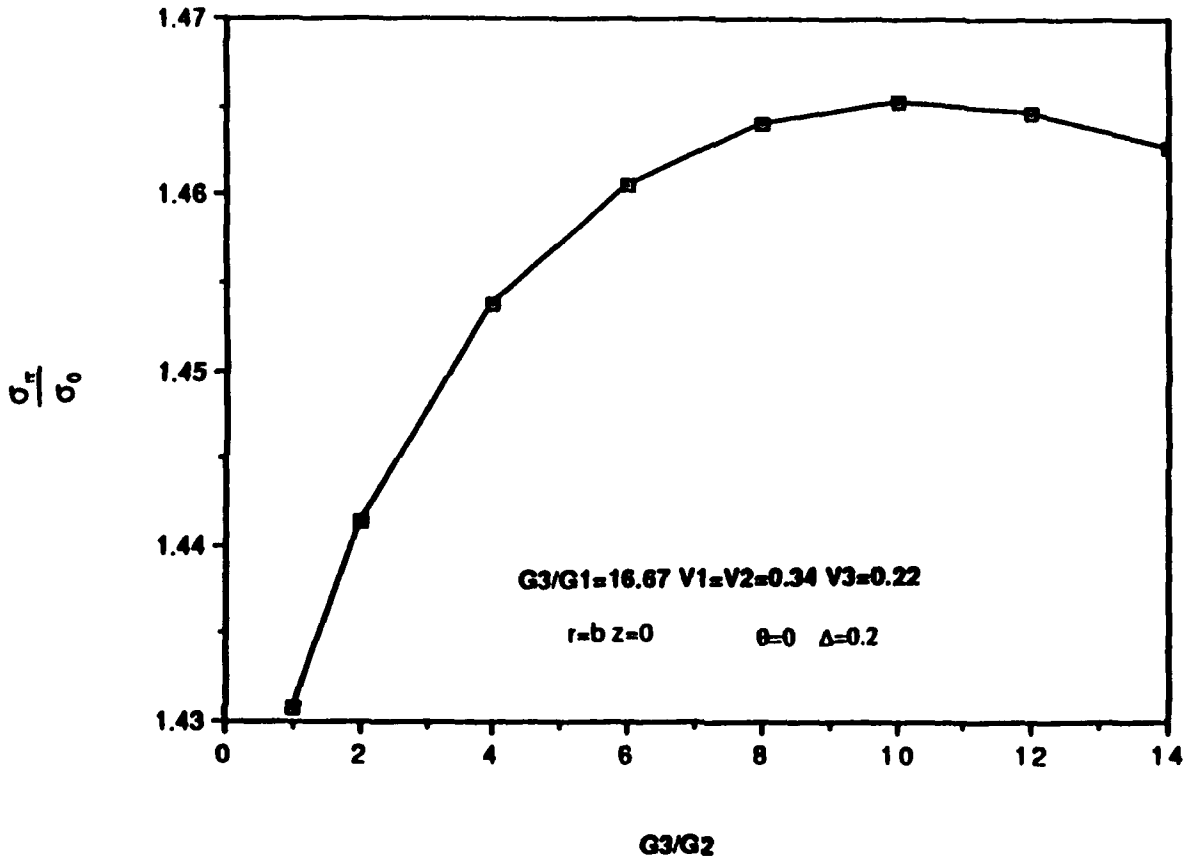

Fig. 10 The max. radial stress vs. the ratio G3/G2 at r=b and z=0.

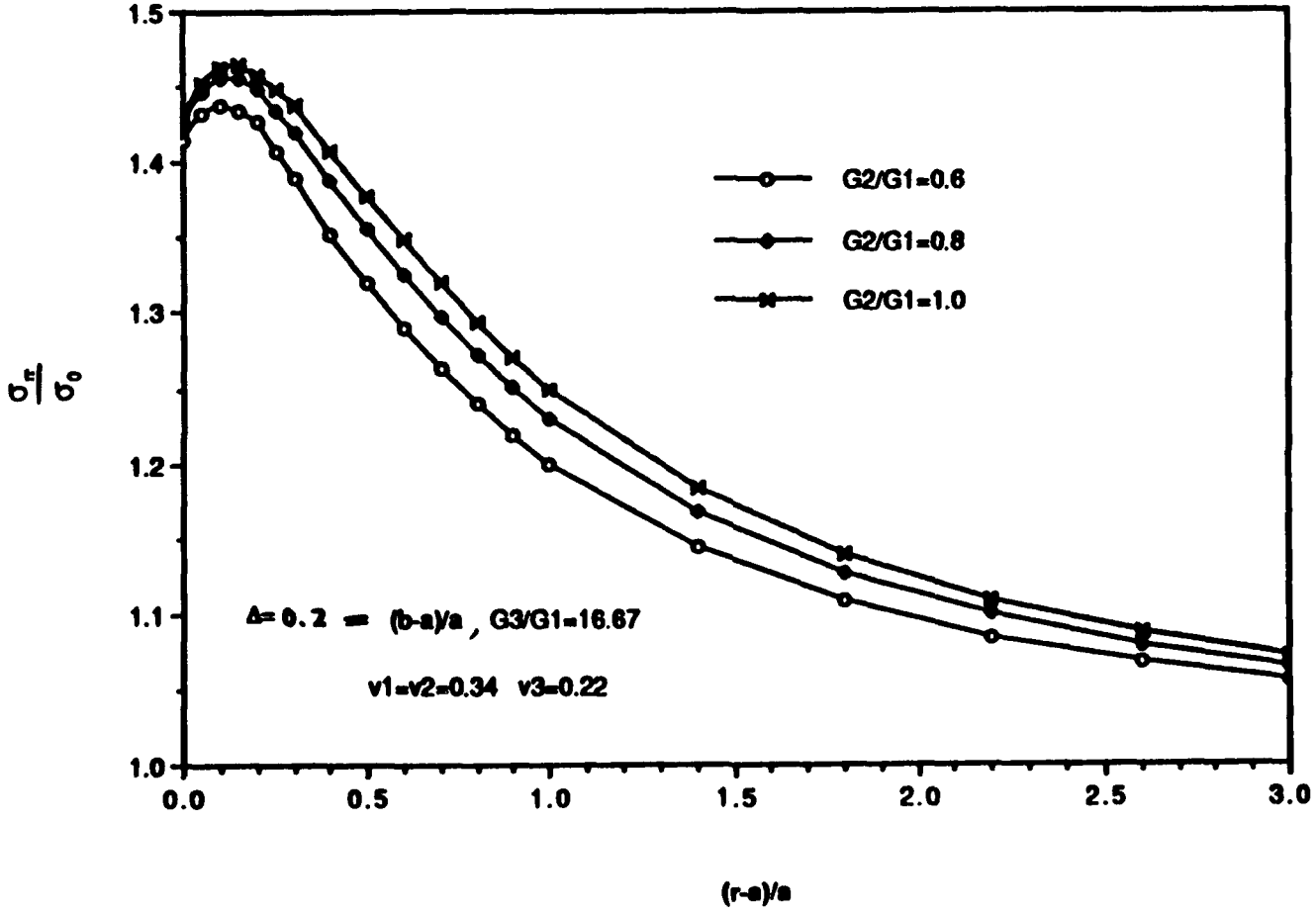

Fig. 11 The max. radial stress vs the ratio (r-a)/a for various G2/G1 ratios at z=0.

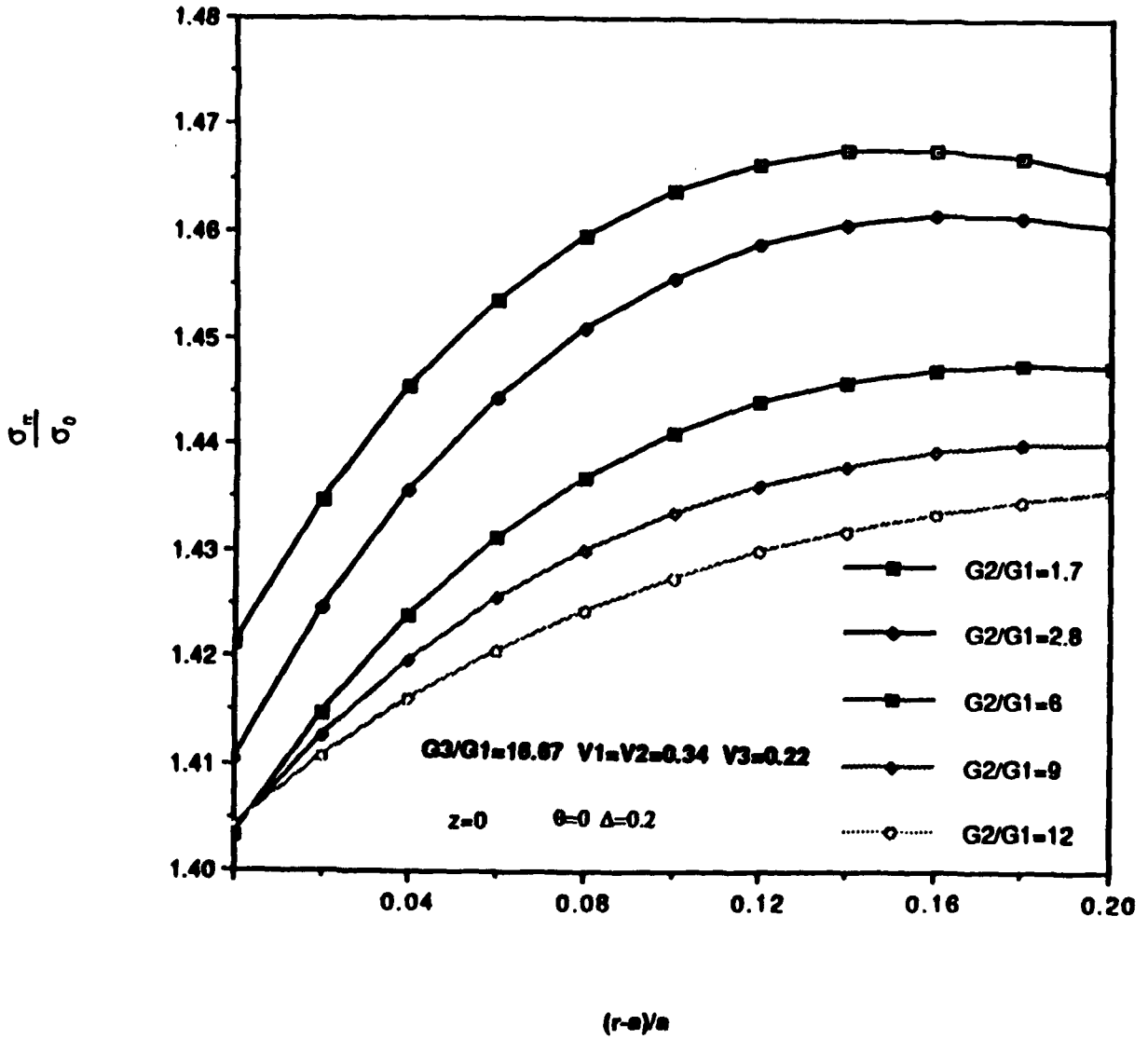

Fig. 12 The max. radial stress vs the ratio (r-a)/a for various G2/G1 ratios at z=0.

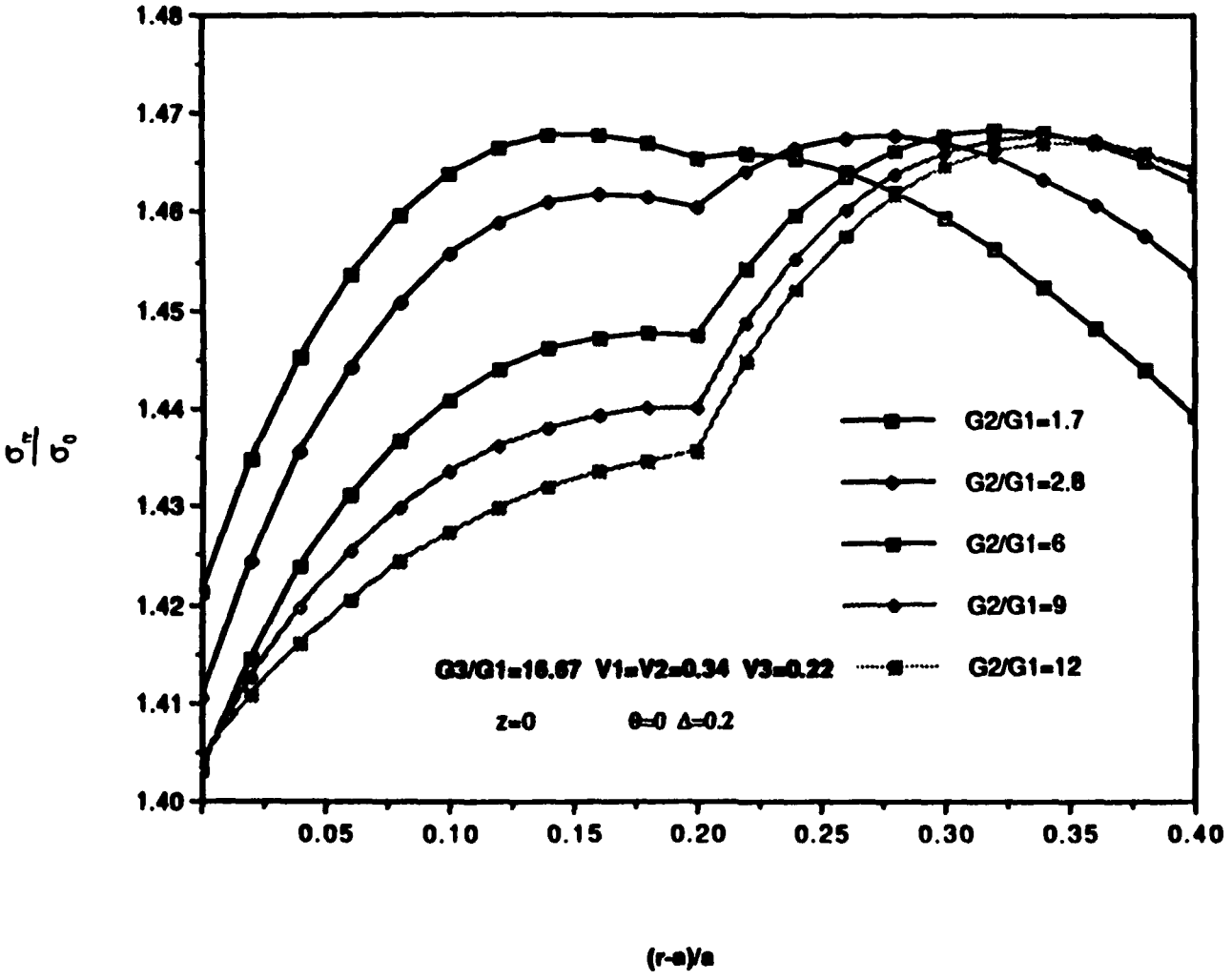

Fig. 13 The max. radial stress vs the ratio (r-a)/a for various G2/G1 ratios at z=0.

A THREE-DIMENSIONAL MODEL FOR THE PREDICTION OF RESIDUAL STRESSES IN A UNIDIRECTIONAL COMPOSITE PLATE

by

J. H. Liu and E.S. Folias

Department of Mechanical Engineering

The University of Utah

ABSTRACT

A three-dimensional (3-D) micromechanical model has been developed to represent a unidirectional composite plate that is subjected to a residual stress load induced due to a temperature mismatch. The model assumes the fibers to be cylindrical inclusions that are periodically embedded into an epoxy matrix plate. At the fiber/matrix interface, perfect bonding conditions are assumed to prevail. The method used in the thesis is based on a 3-D analytic considerations.

The analytical solution shows the maximum stresses to occur at $\theta=0$ for the case of a graphite/epoxy composite plate. The location of the maximum of the stresses, however, may change for other material systems, particularly, for small shear moduli ratios μ_2/μ_1. The solution also shows that the shear moduli ratio μ_2/μ_1 (fiber to matrix), the geometric ratios a/h (fiber radius to thickness of the plate) and a/b (fiber radius to separation distance between adjacent fibers) effect greately the displacement and stress distributions. On the other hand, the ratio of thermal expansion coefficients $\alpha^{(2)}/\alpha^{(1)}$ (fiber to matrix) presents a linear action to the displacement and stress fields. The stress profiles along a fiber length are shown to be constant except in the neighborhood of the fiber edge where a boundary layer is shown to prevail. In this region, a stress singularity is shown to prevail which is a departure from the results obtained by macromechanical theories.

In the limit, as $a/b\rightarrow 0$, the result of one fiber model is recovered; as $a/h\rightarrow\infty$, the plane stress solution is recovered. Similarly, as $\mu_2/\mu_1\rightarrow 0$ the result of a plate with a periodic array of holes is recovered.

CHAPTER 1

INTRODUCTION

It is well recognized that fiber-reinforced composite materials are very attractive for their high strength and stiffness to weight ratios and for their excellent fatigue resistance characteristics. With the advancement of composites and their extensive use in aerospace, automotive and other industries, problems for the determination of the displacement and stress fields have drawn considerable attention. However, the anisotropic behavior of composite materials makes the stress field more complex than that of traditional engineering materials. Many designers encounter difficulties in determining the stress field around the interface of fiber and matrix and a free surface. Thus reliable prediction of the stress field within a composite is an important research topic which needs further investigation.

Basically, there are two categories of factors that may induce materials failure, the first one is due to the external loads and the second is due to localized stress fields, for example residual stresses caused by the environment such as a temperature change. Upon the application of external loads, regions of low toughness values may fail before the bulk of the material does due to the presence of impurities, inclusions, grain boundaries, etc. On the other hand, the residual stresses are present as a result of the manufacturing process of the material. During the change of temperature, residual stresses are induced because of a thermal expansion mismatch, thermal expansion anisotropy, or phase transformation. Depending on the values of the thermal expansion coefficients, the residual stresses may be tensile or compressive in nature and both types of stresses may induce microcracking.

In order to be able to predict the failing characteristics of composite materials, particularly in the neighborhood of a free surface and particularly at the fiber/matrix

interface, it is necessary to know the local stress field from a 3-D point of view. Numerous researchers have focused on the effects which one inclusion has in a composite. In 1942, Reissner [1] introduced a semi-direct variational method consisting of 3-D corrections to the theory of plane stress. In 1948, Green [2] proposed a 3-D solution in terms of infinite series of a very complicated nature. His solution satisfied the governing differential equations, but the boundary conditions were satisfied by an approximate iterative procedure. One year later, Green [3] developed a general method based on infinite series for the solution of 3-D boundary value problems. However, the form of his solution is rather complicated for practical use. Alblas [4], in 1957, used the general procedure proposed by Green to construct an infinite series representation of the solution in a simple form. He expressed the solution to Navier's equations in terms of a set of complex eigenfunctions. In 1961, Reiss [5] sought the correction factor to the plane stress solution on the basis of an asymptotic expansion of the stress field in powers of the thickness parameter. Two years later, he applied his theory to find a 3-D correction to Kirch's solution. The results, however, are valid only for relatively thin plates. Youngdahl et. al.[6], in 1966, presented an integral form of the solution by means of a specially adapted integral transform technique. Their solution, however, is only applicable to the case of a half space. Later, in 1975, Folias [7] developed a method for solving 3D mixed-boundary-value problems that arise in elastostatics. The method is applied to a plate of finite thickness, which contains a finite, through the thickness, line crack. Based on Folias previous work, Folias and Wang (1990) specialized the general solution to the equilibrium of a linear elastic layer for the case of a plate of an arbitrary thickness that has been weakened by a cylindrical hole [8]. The solution satisfied both Navier's equations as well as the plate boundary conditions. Moreover, in 1989 Folias [9] investigated analytically the stress field in the neighborhood of the intersection of a hole and a free surface. The analysis shows the complementary solution to be proportional to ρ^{α}, where ρ is the distance from the point of intersection of the hole and the free surface of the plate. The analysis showed

that no stress singularity was present in this vicinity. In 1989, Penado and Folias [10] extended the previous work to the case of a cylindrical inclusion. Both the plate and the inclusion are assumed to be of homogeneous and isotropic materials with different material properties. In the limit, as the ratio of shear moduli $\mu_2/\mu_1 = 0.00001$, the results for a cylindrical hole are recovered. At the same time, Folias [11] studied analytically the stress field in the neighborhood of the intersection of the cylindrical inclusion and the free surface. The displacement and stress fields were derived explicitly and the presence of a stress singularity was shown to exist. Moreover, this stress singularity is shown to be a function of the ratios of the shear moduli and Poisson's ratios. In 1990, Folias and Liu [12] extended Penado and Folias ' work to a more general case which includes a coating layer between the fiber and the matrix. In 1991, Zhong and Folias [13] investigated the loading transfer characteristics between a fiber and a matrix plate subjected to an axial loading. Both perfect bonding and imperfect bonding conditions were examined.

As for periodical systems, Goree [14] in 1967 presented a solution for the displacements and stresses in an infinite elastic matrix containing two perfectly bounded rigid circular cylindrical inclusions of different radii, and of infinite length normal to the x-y plane. In the same year, Hedgepeth [15] obtained a solution for two stress distribution problems that resulted from breaking of the filaments in a composite material composed of high modulus elements embedded in a low modulus matrix. Subsequently, Adams (1967) presented two papers where the longitudinal shear loading [16] and transverse normal loading [17] were discussed respectively. Using an analysis based on the theory of elasticity , the problem of a doubly periodic rectangular array of elastic filaments in an elastic matrix material was formulated in his papers where the effect of a uniform temperature was also imposed. Later, Haener [18] used the displacement potential method to express the 3-D stress distributions in a unidirectional multi-fiber composite under external and residual loads. He assumed the geometric arrangement of the fibers was hexagonal and the hexagon boundary remained regular under the load. In 1969, Marloff

and Daniel [19] used a experimental method to determine the 3-D stress distribution in a unidirectional composite plate subjected to matrix shrinkage and normal transverse load. In 1973, Keer et al. [20] used finite integral transforms to study the phenomena of the separation of a smooth circular inclusion from a matrix that is subjected to a uniform load. A 2-D solution for plates with perfectly bonded circular inclusions can be found in the papers [21] of Sendeckyj (1970). Based on Sendeckyj's previous work, Yu and Sendeckyj (1974) extended their study to the case of an infinite elastic matrix containing multiple inclusions by using the Schwarz alternating method [22]. Their results were subsequently specialized to cases of two and three inclusions. In 1984, Adams [23] used a finite element method to analyze a microscopic region of a unidirectional composite plate in plane strain case. In 1985, Evans et al. [24] analyzed matrix fracture in brittle-matrix fiber composites. The numerical solution shows that matrix cracks initiate prior to fiber failure and the influence of the fibers that bridge the matrix crack is represented at the crack surfaces. In 1990, based on 2-D consideration, Isida [25] used a complex series approach to solve the problem of an array of periodic inclusions embedded into an infinite matrix subjected to a uniform transverse load. Thus, his contribution provides us with further insight into the strength of the composite plate. In 1991, Folias and Liu extended the previous works from one fiber to an array of periodic fibers. Two investigations have been completed for the model of a matrix plate embedded with a periodic array of fibers subject to different loadings. One is subjected to a uniform transverse loading [26], the other is subjected to a axial loadings [27]. The results show that the effect of the fiber volume fraction v_f is an important parameter that affects greatly the displacement and stress fields. In the limit, as the ratio $a/b \to 0$ (a/b is the ratio of the fiber radius to separation distance between adjacent fibers), the results of Penado and the results of Zhong are recovered, respectively.

In the area of residual stress problems, however, most of the research is limited to a macro-approach which accounts only for the macromechanical behavior of the laminates and neglects the individual behavior of the fibers and of the matrix. Griffin [28] in 1983

used a fully 3-D finite element analysis to predict thermal stress distributions in thick graphite/epoxy laminates. The result shows that high interlaminar thermal tensile stresses are present near the free edges. Later, in another paper [29], provided experimental evidence with which he confirmed his numerical solution. Another practical model for matrix microcracking present in graphite/epoxy composites was examined by Bowles (1984) [30], where finite element analysis was used to predict the effect of different thermal expansion coefficients. In 1987, Evans et al.[31] investigated the high-temperature mechanical properties for a ceramic matrix composite. The change in mechanical behavior has been attributed to a large variation in the shear resistance of the fiber/matrix interface. In 1988, Garg [32] studied the fracture behavior of graphite/epoxy composite effected by the change of temperature with the experimental method. It proves that a temperature change may induce failure in the material. Fang [33] in 1989 presented an experimental and analytical investigation of thermally-induced cracking in graphite/epoxy composites, where the thermal stresses will affect the extent and form of damage. However, his analysis is based only on an approximate, 2-D micro-cracking model, which can not be used to predict the stress distribution along the thickness. In 1985, Mikata et al. [34] calculated a stress field in a coated continuous fiber composite subjected to thermomechanical loadings. The investigation shows that the maximum stress occurs in the coating and it reduces as the volume fraction of fibers and coating thickness increases. A prediction of thermal expansion for unidirectional composites was investigated by Bowles et al. [35] in 1988, where several analyses were compared with each other. Also a sensitivity analysis was conducted to determine the relative influence of constituent properties. In 1988, an investigation was carried out by Delale [36] where the microcracking of ceramic-matrix composite due to residual stresses was studied. Starting with a model of single fiber embedded in an infinite matrix, the critical fiber size was determined and the relationship between critical fiber size and the parameters such as thermal expansion coefficients of fiber and matrix, change of temperature was established. It is shown that a small difference of

the thermal expansion coefficient leads to a large critical fiber size. In 1989, Evans [37] investigated the debonding properties of brittle-matrix composite subjected to residual stresses. The debonding behavior is shown to depend sensitively on the thermal expansion mismatch. Later, in 1990, Evans [38] focused his research on the effect of the interface in fiber-reinforced ceramics. It is shown that the residual stress arisen from thermal contraction mismatch upon cooling has significant effects on both the interface sliding stress and the matrix cracking stress, as well as the ultimate strength.

The purpose of this investigation is to provide a 3-D solution for the case of a matrix plate which is embedded with a periodic array of fibers and is under the action of a temperature change. In this study, a 3-D analytical solution developed by Folias will be specialized to the problem at hand and will be extended to account for the presence of a periodic extension of fibers by satisfying additional boundary conditions within the cell configuration. The solution is subsequently reduced to a matrix system with a large dimension. Our previous experience has shown that this type of system is very sensitive to even small changes of the coefficients. The rate of convergence, however, will be constantly monitored by how well the boundary conditions are satisfied. Sophisticated numerical algorithms have been developed to handle the numerical analysis which will be carried out in double precision. Thus, the 3-D effects including those at the boundary layer close to the free edges will be recovered.

The analysis is expected to provide us with important information for the temperature mismatch. The residual stress field along the three different directions respectively (r, θ and z) will be examined and the location of maximum stress will be established for the subsequent failure analysis. Moreover, the relationship of the stresses versus different ratios of the shear moduli (μ_2/μ_1), the fiber radius to separation distance between adjacent fibers (a/b), the fiber radius to plate thickness (a/h), and the thermal expansion coefficients ($\alpha^{(2)}/\alpha^{(1)}$) will be determined. Such information will not only help us understand the

failure mechanism better but it will also reveal how the critical stress to failure is dependant upon the respective material properties.

CHAPTER 2

FORMULATION OF THE PROBLEMS

2.1 One Fiber Model

Consider the equilibrium of a body that occupies the space $|x|<\infty$, $|y|<\infty$, $|z|\leq h$ and contains two different elastic materials (fibers and matrix) whose common boundary is given by a through-the thickness cylindrical surface of radius r=a whose generators are parallel to the z-axis (see Figure 2.1). Both the matrix and the fibers are considered to be made of homogeneous, isotropic and linearly elastic materials. At the interface perfect bonding is assumed to prevail. The surfaces $|z|=h$ for both regions are free of stresses and constraints.

Considering the case of a temperature change, which is the same at any point of the body, and considering the absence of body forces, the coupled differential equations (Navier's equations) governing the displacement functions $u^{(i)}$, $v^{(i)}$, $w^{(i)}$ (i= 1, 2, where i= 1 applies to the region r>a and i= 2 to the region r<a) are:

$$\frac{m_i}{m_i - 2}\frac{\partial}{\partial x}e^{(i)} + \nabla^2 u^{(i)} = 0 \tag{2.1}$$

$$\frac{m_i}{m_i - 2}\frac{\partial}{\partial y}e^{(i)} + \nabla^2 v^{(i)} = 0 \tag{2.2}$$

$$\frac{m_i}{m_i - 2}\frac{\partial}{\partial z}e^{(i)} + \nabla^2 w^{(i)} = 0 \tag{2.3}$$

where

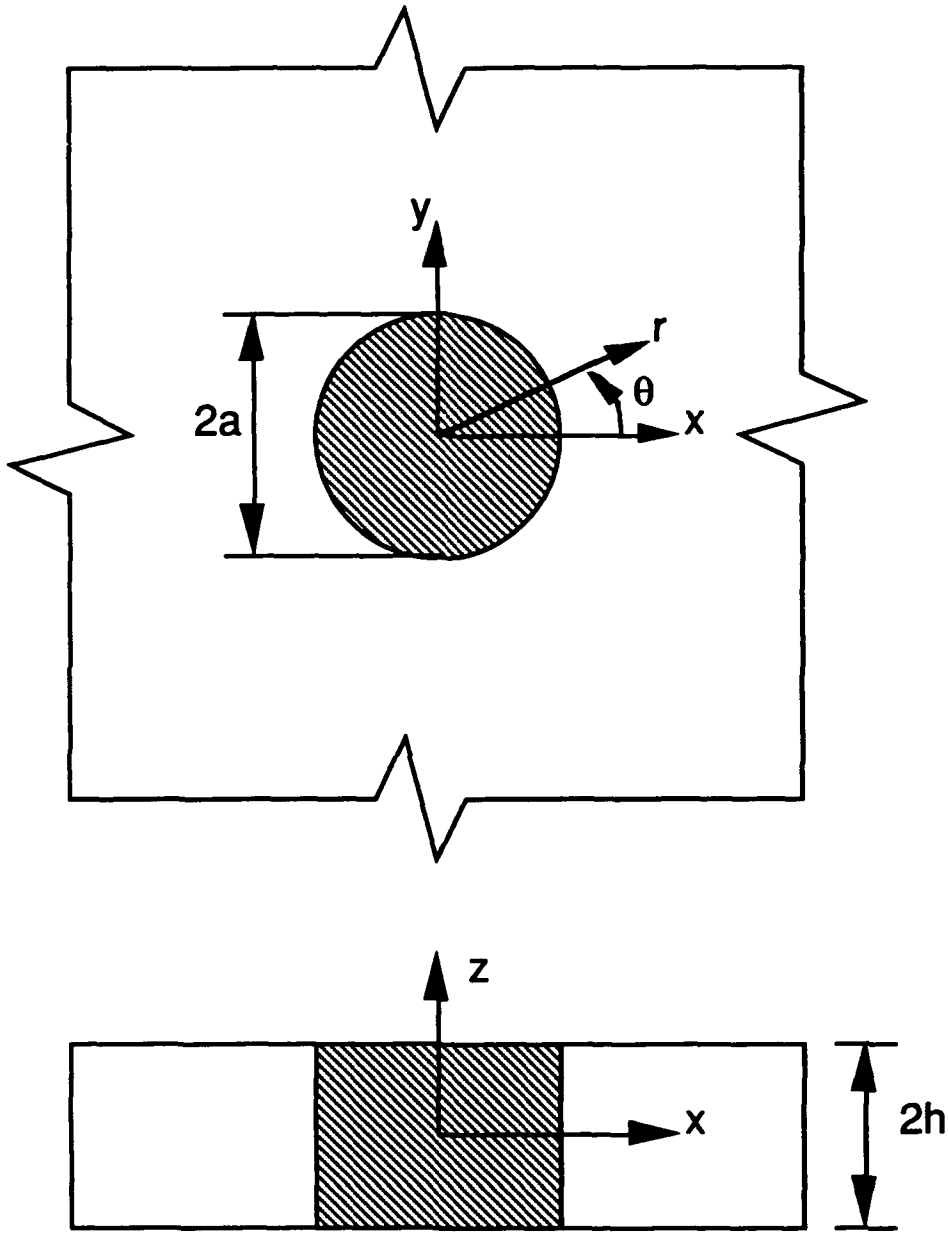

Figure 2.1 One Fiber Model: Infinite Plate

of Arbitrary Thickness with One Cylindrical Inclusion

$$\nabla^2 \equiv \frac{\partial^2}{\partial x^2} + \frac{\partial^2}{\partial y^2} + \frac{\partial^2}{\partial z^2} \quad \text{(Laplacian operator)} \tag{2.4}$$

$$m_i \equiv \frac{1}{v_i} \quad (i=1,2) \tag{2.5}$$

v_i (i=1,2) = Poisson's ratio of matrix, fiber (2.6)

$$e^{(i)} \equiv \frac{\partial u^{(i)}}{\partial x} + \frac{\partial v^{(i)}}{\partial y} + \frac{\partial w^{(i)}}{\partial z} \ , \quad (i=1,2) \tag{2.7}$$

The stress-displacement relations including the thermal stresses are given by Hooke's law as:

$$\sigma_{xx}^{(i)} = 2\mu_i \left(\frac{\partial u^{(i)}}{\partial x} + \frac{e^{(i)}}{m_i - 2} \right) - \frac{1+v_i}{1-2v_i} 2\mu_i \alpha^{(i)} \Delta T \tag{2.8}$$

$$\sigma_{yy}^{(i)} = 2\mu_i \left(\frac{\partial v^{(i)}}{\partial y} + \frac{e^{(i)}}{m_i - 2} \right) - \frac{1+v_i}{1-2v_i} 2\mu_i \alpha^{(i)} \Delta T \tag{2.9}$$

$$\sigma_{zz}^{(i)} = 2\mu_i \left(\frac{\partial w^{(i)}}{\partial z} + \frac{e^{(i)}}{m_i - 2} \right) - \frac{1+v_i}{1-2v_i} 2\mu_i \alpha^{(i)} \Delta T \tag{2.10}$$

$$\tau_{xy}^{(i)} = \mu_i \left(\frac{\partial u^{(i)}}{\partial y} + \frac{\partial v^{(i)}}{\partial x} \right) \tag{2.11}$$

$$\tau_{yz}^{(i)} = \mu_i \left(\frac{\partial v^{(i)}}{\partial z} + \frac{\partial w^{(i)}}{\partial y} \right) \tag{2.12}$$

$$\tau_{xz}^{(i)} = \mu_i \left(\frac{\partial w^{(i)}}{\partial x} + \frac{\partial u^{(i)}}{\partial z} \right) \tag{2.13}$$

where μ_i , $\alpha^{(i)}$ (i=1,2) are , respectively, the shear moduli and the thermal expansion coefficients of the matrix and the fiber.

As to the boundary conditions, one must require that

as $|x| \to \infty$:

$$\sigma_{xx}^{(1)} = \tau_{xy}^{(1)} = \tau_{xz}^{(1)} = 0 \tag{2.14}$$

as $|y| \to \infty$:

$$\sigma_{yy}^{(1)} = \tau_{xy}^{(1)} = \tau_{yz}^{(1)} = 0 \tag{2.15}$$

at $|z| = h$:

$$\sigma_{zz}^{(i)} = \tau_{xz}^{(i)} = \tau_{yz}^{(i)} = 0 \tag{2.16}$$

at r=a :

$$\sigma_{rr}^{(1)} = \sigma_{rr}^{(2)} \tag{2.17}$$

$$\tau_{r\theta}^{(1)} = \tau_{r\theta}^{(2)} \tag{2.18}$$

$$\tau_{rz}^{(1)} = \tau_{rz}^{(2)} \tag{2.19}$$

$$u_r^{(1)} = u_r^{(2)} \tag{2.20}$$

$$u_\theta^{(1)} = u_\theta^{(2)} \tag{2.21}$$

$$w^{(1)} = w^{(2)} \tag{2.22}$$

also the following continuity condition must hold:

at r=0 : all stresses and displacements for the inclusion must be bounded (2.23)

It will be convenient to seek the solution in the form

$$u^{(i)} = u^{(p)(i)} + u^{(c)(i)} \tag{2.24}$$

$$v^{(i)} = v^{(p)(i)} + v^{(c)(i)} \tag{2.25}$$

$$w^{(i)} = w^{(p)(i)} + w^{(c)(i)} \tag{2.26}$$

where the component with the superscript (p) represents the particular solution whereas the component with the superscript (c) represents the complementary solution, which is a function of the x, y, and z coordinates.

The particular solution is relatively easy to construct. In cylindrical coordinates, the particular solution of the matrix (i=1) is of the form

$$\sigma_{rr}^{(p)(1)} = \frac{A_o}{r^2} \tag{2.27}$$

$$\sigma_{\theta\theta}^{(p)(1)} = -\frac{A_o}{r^2} \tag{2.28}$$

$$\tau_{r\theta}^{(p)(1)} = \tau_{rz}^{(p)(1)} = \tau_{\theta z}^{(p)(1)} = \sigma_{zz}^{(p)(1)} = 0 \tag{2.29}$$

Integration of equations (2.27)-(2.29) gives:

$$u_r^{(p)(1)} = -\frac{1}{\mu_1}\frac{A_0}{2r} + \alpha^{(1)}\,\Delta T\, r \tag{2.30}$$

$$u_\theta^{(p)(1)} = 0 \tag{2.31}$$

$$w^{(p)(1)} = \alpha^{(1)}\,\Delta T\, z \tag{2.32}$$

For the fiber (i=2), the particular solution has the same form as the matrix. Thus:

$$\sigma_{rr}^{(p)(2)} = 2b_o \tag{2.33}$$

$$\sigma_{\theta\theta}^{(p)(2)} = 2b_o \tag{2.34}$$

$$\tau_{r\theta}^{(p)(2)} = \tau_{rz}^{(p)(2)} = \tau_{\theta z}^{(p)(2)} = \sigma_{zz}^{(p)(2)} = 0 \tag{2.35}$$

$$u_r^{(p)(2)} = \frac{1}{\mu_2}\frac{1-\nu_2}{1+\nu_2} b_0\, r + \alpha^{(2)}\Delta T\, r \tag{2.36}$$

$$u_\theta^{(p)(2)} = 0 \tag{2.37}$$

$$w^{(p)(2)} = -\frac{1}{\mu_2}\frac{2\nu_2}{1+\nu_2} b_0 z + \alpha^{(2)} \Delta T z \tag{2.38}$$

where A_o and b_o are constants to be determined later from the boundary conditions. Note that the above particular solution for the fiber (i=2) satisfies the continuity conditions at r=0 , i.e., equation (2.23).

In view of the particular solution, one needs to find six functions; $u^{(c)(i)}$, $v^{(c)(i)}$, $w^{(c)(i)}$,(i=1,2) such that they satisfy simultaneously the partial differential equations (2.1)-(2.3) and the following boundary conditions:

at $|z| = h$:

$$\tau_{xz}^{(c)(i)} = \tau_{yz}^{(c)(i)} = \sigma_{zz}^{(c)(i)} = 0 \tag{2.39}$$

at r=a :

$$\sigma_{rr}^{(c)(1)} - \sigma_{rr}^{(c)(2)} = \sigma_{rr}^{(p)(2)} - \sigma_{rr}^{(p)(1)} \tag{2.40}$$

$$\tau_{r\theta}^{(c)(1)} - \tau_{r\theta}^{(c)(2)} = \tau_{r\theta}^{(p)(2)} - \tau_{r\theta}^{(p)(1)} \tag{2.41}$$

$$\tau_{rz}^{(c)(1)} - \tau_{rz}^{(c)(2)} = \tau_{rz}^{(p)(2)} - \tau_{rz}^{(p)(1)} \tag{2.42}$$

$$u_r^{(c)(1)} - u_r^{(c)(2)} = u_r^{(p)(2)} - u_r^{(p)(1)} \tag{2.43}$$

$$u_\theta^{(c)(1)} - u_\theta^{(c)(2)} = u_\theta^{(p)(2)} - u_\theta^{(p)(1)} \tag{2.44}$$

$$w^{(c)(1)} - w^{(c)(2)} = w^{(p)(2)} - w^{(p)(1)} \tag{2.45}$$

as $r \to \infty$:

all complementary displacements and stresses for the matrix must vanish. (2.46)

at r=0 :

all complementary displacements and stresses for the fiber must be bounded. (2.47)

2.2 Periodic Fibers Model

The above discussions are based on the assumption that the matrix plate is embedded with one fiber only and that the entire system is subjected to a temperature change. Such a model is often used to illustrate how the residual stresses between a fiber and a matrix develop as a result of thermal expansion mismatch. In practice, however, numerous fibers are embedded into a matrix plate. One may conjecture, therefore, that the residual stress in a composite plate will depend strongly on the properties of the fiber/matrix interface as well as on the fiber packing sequence. Consequently, this model must account for the presence of a periodic array of fibers that are embedded into the matrix plate. This model is shown in Figure 2.2.

Most of the formulas developed for the one fiber model are still applicable to the case of periodic inclusions with the exception that additional boundary conditions need to be satisfied within the cell configuration. Symmetric conditions may be used to simplify the problem reflecting the periodic fibers model. From Figure 2.2 , it is clear that lines O-B, O-C, and B-C are symmetric boundaries. Thus, one may consider the triangle OBC and concentrate on how to deal with the continuity conditions on the fiber/matrix interface and on the symmetric boundary line B-C.

For convenience, all displacements and stresses will be expressed in a form that automatically satisfy the symmetric boundary conditions along the lines O-B and O-C. It remains, therefore, for us to satisfy the symmetric boundary conditions along the line B-C. In particular,

$$\tau_{rt}^{(1)} = 0 \tag{2.48}$$

$$\tau_{rz}^{(1)} = 0 \tag{2.49}$$

$$F_n^{(1)} = \int_B^C \sigma_n^{(1)} \, ds = 0 \tag{2.50}$$

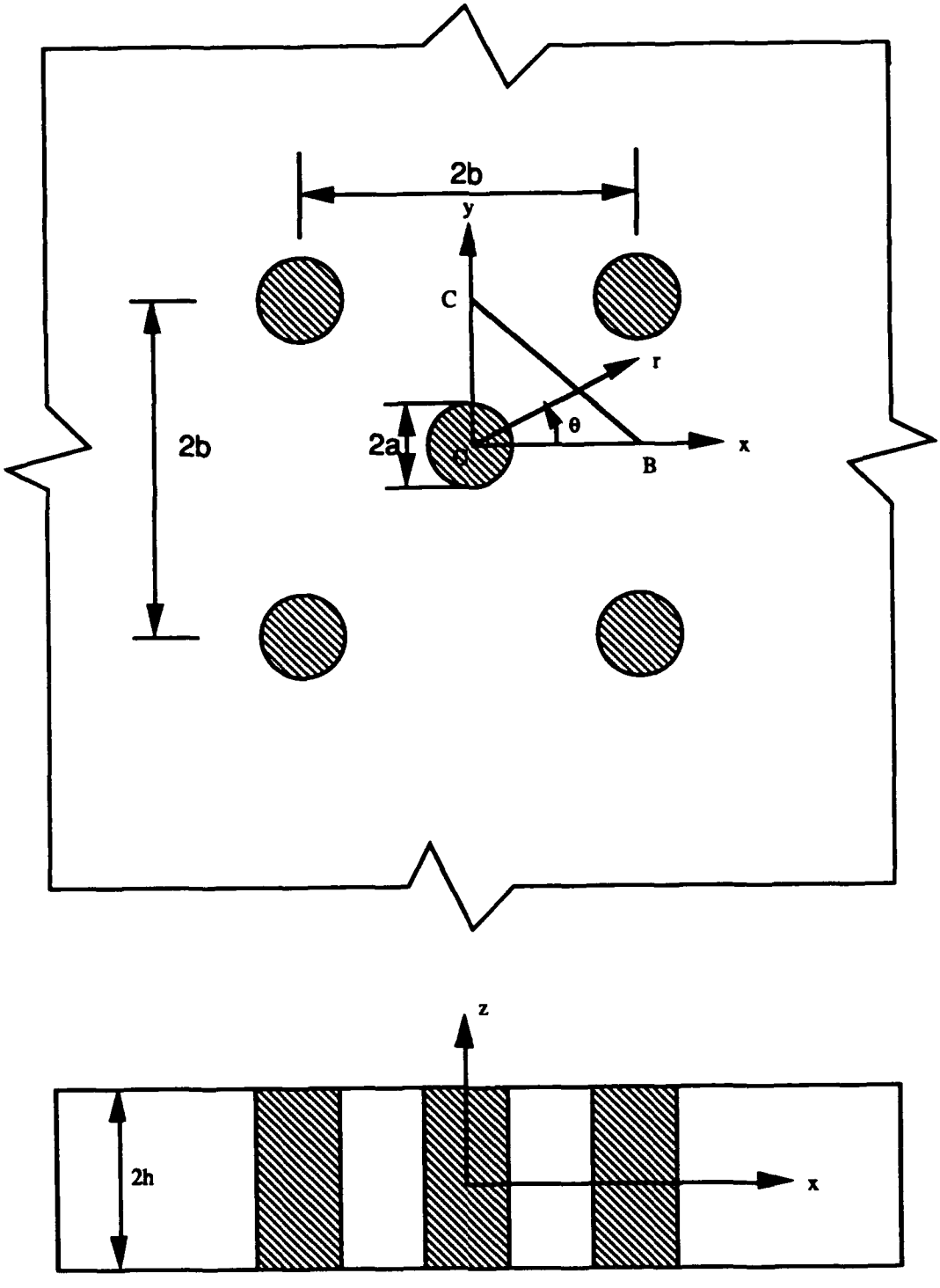

Figure 2.2 Periodic Fibers Model: Infinite Plate

of Arbitrary Thickness with Periodic Cylindrical Inclusions

$$u_n^{(1)} = \text{constant} \tag{2.51}$$

where n and t are the normal and parallel directions of the line B-C, respectively.

After separating the solution into a complementary and a particular part, one may write:

$$\tau_{nt}^{(c)(1)} = - \tau_{nt}^{(p)(1)} \tag{2.52}$$

$$\tau_{nz}^{(c)(1)} = - \tau_{nz}^{(p)(1)} \tag{2.53}$$

$$F_n^{(c)(1)} = \int_B^C \sigma_n^{(c)(1)} \, ds = - \int_B^C \sigma_n^{(p)(1)} \, ds = - F_n^{(p)(1)} \tag{2.54}$$

$$u_n^{(c)(1)} - u_r^{(c)(1)}(\frac{\pi}{4}) = u_r^{(p)(1)}(\frac{\pi}{4}) - u_n^{(p)(1)} \tag{2.55}$$

CHAPTER 3

METHOD OF SOLUTION

3.1 Complementary Solution

A general method for constructing solutions to some 3-D mixed boundary-value problems that arise in elastostatics was developed by Folias. Based upon these results, one may assume the general form of the solution to system (2.1)-(2.3) which automatically satisfies the boundary conditions at the plate faces, equation (2.39), to be of the form:

$$u^{(c)(i)} = \frac{1}{m_i-2}\sum_{v=1}^{\infty}\frac{\partial H_v^{(i)}}{\partial x}\left[\,2(m_i-1)\,f_1(\beta_v z) + m_i\,f_2(\beta_v z)\,\right] + \sum_{n=1}^{\infty}(-1)^n\frac{\partial H_n^{(i)}}{\partial y}\cos(\alpha_n z) + \lambda_1^{(i)} - y\frac{\partial \lambda_3^{(i)}}{\partial x} + \frac{1}{m_i+1}z^2\frac{\partial^2 \lambda_3^{(i)}}{\partial x \partial y} \tag{3.1}$$

$$v^{(c)(i)} = \frac{1}{m_i-2}\sum_{v=1}^{\infty}\frac{\partial H_v^{(i)}}{\partial y}\left[\,2(m_i-1)\,f_1(\beta_v z) + m_i\,f_2(\beta_v z)\,\right] - \sum_{n=1}^{\infty}(-1)^n\frac{\partial H_n^{(i)}}{\partial x}\cos(\alpha_n z) + \frac{3m_i-1}{m_i+1}\lambda_3^{(i)} + \lambda_2^{(i)} - y\frac{\partial \lambda_3^{(i)}}{\partial y} - \frac{1}{m_i+1}z^2\frac{\partial^2 \lambda_3^{(i)}}{\partial x^2} \tag{3.2}$$

$$w^{(c)(i)} = \frac{1}{m_i-2}\sum_{v=1}^{\infty}H_v^{(i)}\beta_v\left[\,(m_i-2)\,f_3(\beta_v z) - m_i\,f_4(\beta_v z)\,\right]$$

$$-\frac{1}{m_i+1} z \frac{\partial \lambda_3^{(i)}}{\partial y} \tag{3.3}$$

Furthermore, the stresses are given by equations (2.8)-(2.13). These expressions, however, do not include the thermal stress component:

$$\frac{1}{2\mu_i}\sigma_{xx}^{(c)(i)} = \frac{1}{m_i-2}\sum_{v=1}^{\infty}\{\,2\beta_v^2 H_v^{(i)} f_1(\beta_v z) + \frac{\partial^2 H_v^{(i)}}{\partial x^2}[2(m_i-1) f_1(\beta_v z) + m_i f_2(\beta_v z)]\,\}$$
$$+\sum_{n=1}^{\infty}(-1)^n \frac{\partial^2 H_n^{(i)}}{\partial x \partial y}\cos(\alpha_n z) + \frac{\partial \lambda_1^{(i)}}{\partial x} - y\frac{\partial^2 \lambda_3^{(i)}}{\partial x^2}$$
$$+\frac{2}{m_i+1}\frac{\partial \lambda_3^{(i)}}{\partial y} + \frac{1}{m_i+1} z^2 \frac{\partial^3 \lambda_3^{(i)}}{\partial x^2 \partial y} \tag{3.4}$$

$$\frac{1}{2\mu_i}\sigma_{yy}^{(c)(i)} = \frac{1}{m_i-2}\sum_{v=1}^{\infty}\{\,2\beta_v^2 H_v^{(i)} f_1(\beta_v z) + \frac{\partial^2 H_v^{(i)}}{\partial y^2}[2(m_i-1) f_1(\beta_v z) + m_i f_2(\beta_v z)]\,\}$$
$$-\sum_{n=1}^{\infty}(-1)^n \frac{\partial^2 H_n^{(i)}}{\partial y^2}\cos(\alpha_n z) + \frac{2m_i}{m_i+1}\frac{\partial \lambda_3^{(i)}}{\partial y} - \frac{\partial \lambda_1^{(i)}}{\partial x}$$
$$+y\frac{\partial^2 \lambda_3^{(i)}}{\partial x^2} - \frac{1}{m_i+1} z^2 \frac{\partial^3 \lambda_3^{(i)}}{\partial x^2 \partial y} \tag{3.5}$$

$$\frac{1}{2\mu_i}\sigma_{zz}^{(c)(i)} = \frac{m_i}{m_i-2}\sum_{v=1}^{\infty} H_v^{(i)} \beta_v^2 \{-f_2(\beta_v z)\} \tag{3.6}$$

$$\frac{1}{2\mu_i}\tau_{xy}^{(c)(i)} = \frac{1}{m_i-2}\sum_{v=1}^{\infty}\frac{\partial^2 H_v^{(i)}}{\partial x \partial y}\{2(m_i-1)f_1(\beta_v z) + m_i f_2(\beta_v z)\}$$
$$-\sum_{v=1}^{\infty}(-1)^n\{\frac{\partial^2 H_n^{(i)}}{\partial x^2} - \frac{1}{2}\alpha_n^2 H_n^{(i)}\}\cos(\alpha_n z) + \frac{m_i-1}{m_i+1}\frac{\partial \lambda_3^{(i)}}{\partial x}$$

$$+\frac{\partial \lambda_2^{(i)}}{\partial x} - y\frac{\partial^2 \lambda_3^{(i)}}{\partial x \partial y} - \frac{1}{m_i+1} z^2 \frac{\partial^3 \lambda_3^{(i)}}{\partial x^3} \tag{3.7}$$

$$\frac{1}{2\mu_i}\tau_{yz}^{(c)(i)} = -\frac{m_i}{m_i-2}\sum_{v=1}^{\infty}\frac{\partial H_v^{(i)}}{\partial y}\beta_v \{ f_3(\beta_v z) + f_4(\beta_v z) \}$$

$$+\frac{1}{2}\sum_{n=1}^{\infty}(-1)^n \frac{\partial H_n^{(i)}}{\partial x}\sin(\alpha_n z) \tag{3.8}$$

$$\frac{1}{2\mu_i}\tau_{xz}^{(c)(i)} = -\frac{m_i}{m_i-1}\sum_{v=1}^{\infty}\frac{\partial H_v^{(i)}}{\partial x}\beta_v \{ f_3(\beta_v z) + f_4(\beta_v z) \}$$

$$-\frac{1}{2}\sum_{n=1}^{\infty}(-1)^n \frac{\partial H_n^{(i)}}{\partial y}\alpha_n \sin(\beta_v z) \tag{3.9}$$

where

$$\alpha_n = \frac{n\pi}{h}\ , \qquad n=1,2,3.....\ , \tag{3.10}$$

and β_v are the roots of the equation

$$\sin(2\beta_v h) = -(2\beta_v h) \tag{3.11}$$

$H_v^{(i)}$ and $H_n^{(i)}$ are functions of x and y (or r and θ depending upon the system of coordinates used) that satisfy the reduced wave equation:

$$\left(\frac{\partial^2}{\partial x^2} + \frac{\partial^2}{\partial y^2} - \beta_v^2\right) H_v^{(i)} = 0 \tag{3.12}$$

$$\left(\frac{\partial^2}{\partial x^2} + \frac{\partial^2}{\partial y^2} - \alpha_n^2\right) H_n^{(i)} = 0 \tag{3.13}$$

$\lambda_1^{(i)}$, $\lambda_2^{(i)}$, and $\lambda_3^{(i)}$ are functions of x and y (or r and θ depending upon the system of coordinates used) that satisfy Laplace's equation:

$$\left(\frac{\partial^2}{\partial x^2}+\frac{\partial^2}{\partial y^2}\right)\lambda_k^{(i)}=0, \qquad k=1,2,3. \tag{3.14}$$

In addition, $\lambda_1^{(i)}$ and $\lambda_2^{(i)}$ satisfy the relation:

$$\frac{\partial \lambda_1^{(i)}}{\partial x}=-\frac{\partial \lambda_2^{(i)}}{\partial y}\ . \tag{3.15}$$

Finally,

$$f_1(\beta_v z) \equiv \cos(\beta_v h)\cos(\beta_v z) \tag{3.16}$$

$$f_2(\beta_v z) \equiv \beta_v h \sin(\beta_v h)\cos(\beta_v z) - \beta_v z \cos(\beta_v h)\sin(\beta_v z) \tag{3.17}$$

$$f_3(\beta_v z) \equiv \cos(\beta_v h)\sin(\beta_v z) \tag{3.18}$$

$$f_4(\beta_v z) \equiv \beta_v h \sin(\beta_v h)\sin(\beta_v z) + \beta_v z \cos(\beta_v h)\cos(\beta_v z) \tag{3.19}$$

Because the above complementary solution satisfies the boundary conditions (2.39), all that remains now is to satisfy the continuity conditions at the fiber/matrix interface, equations (2.40)-(2.45), and for the periodic fibers model only, the additional symmetric boundary conditions along the line B-C, equations (2.52)-(2.55), as well as continuity conditions (2.46)-(2.47).

3.2 One Fiber Model

In the case of one fiber model, there is only one kind of boundary condition that needs to be satisfied, that is the continuity condition at r=a . By using the coordinate transformations of displacements and stresses, the complementary solution can be

transformed from the rectangular to cylindrical coordinates in order to take advantage of the symmetry. Thus, equations (2.40)-(2.45) may be written in the following form :

$$\sin^2\theta\,(\sigma_{xx}^{(c)(1)} - \sigma_{xx}^{(c)(2)}) + \cos^2\theta\,(\sigma_{yy}^{(c)(1)} - \sigma_{yy}^{(c)(2)}) + \sin(2\theta)(\tau_{xy}^{(c)(1)} - \tau_{xy}^{(c)(2)})$$

$$= 2b_o - \frac{A_o}{r^2} \tag{3.20}$$

$$\frac{1}{2}\sin(2\theta)\,(\sigma_{xx}^{(c)(1)} - \sigma_{xx}^{(c)(2)}) - \frac{1}{2}\sin(2\theta)\,(\sigma_{yy}^{(c)(1)} - \sigma_{yy}^{(c)(2)}) + \cos(2\theta)\,(\tau_{xy}^{(c)(1)} - \tau_{xy}^{(c)(2)})$$

$$= 0 \tag{3.21}$$

$$\sin\theta\,(\tau_{xy}^{(c)(1)} - \tau_{xy}^{(c)(2)}) + \cos\theta\,(\tau_{yz}^{(c)(1)} - \tau_{yz}^{(c)(2)}) = 0 \tag{3.22}$$

$$\sin\theta\,(u^{(c)(1)} - u^{(c)(2)}) + \cos\theta\,(v^{(c)(1)} - v^{(c)(2)})$$

$$= \frac{1}{\mu_2}\frac{1-\nu_2}{1+\nu_2} b_0\, r + \frac{1}{\mu_1}\frac{A_0}{2r} + (\alpha^{(2)} - \alpha^{(1)})\,\Delta T\, r \tag{3.23}$$

$$\cos\theta\,(u^{(c)(1)} - u^{(c)(2)}) - \sin\theta\,(v^{(c)(1)} - v^{(c)(2)}) = 0 \tag{3.24}$$

$$w^{(c)(1)} - w^{(c)(2)} = -\frac{1}{\mu_2}\frac{2\nu_2}{1+\nu_2} b_0\, z + (\alpha^{(2)} - \alpha^{(1)})\,\Delta T\, z \tag{3.25}$$

Taking into account the symmetry of the problem (θ independence), one finds:

$$H_v^{(1)} = a_{0v} K_0(\beta_v r) \tag{3.26}$$

$$H_v^{(2)} = b_{0v} I_0(\beta_v r) \tag{3.27}$$

$$H_n^{(1)} = c_{0n} K_0(\alpha_n r) \tag{3.28}$$

$$H_n^{(2)} = d_{0n} I_0(\alpha_n r) \tag{3.29}$$

and all λ=0, where I_0 and K_0 are, respectively, the modified Bessel functions of the first and second kind of order zero; a_{0v} and b_{0v} are complex constants; and c_{0n} , d_{0n} are real constants.

It is found convenient to nondimensionalize the expressions by introducing the following definitions:

$$A_{0v}^{(1)} = \frac{1}{\alpha^{(1)} \Delta T} a_{0v} \beta_v^2 K_0(\beta_v a) \tag{3.30}$$

$$A_{0v}^{(2)} = \frac{1}{\alpha^{(1)} \Delta T} b_{0v} \beta_v^2 I_0(\beta_v a) \tag{3.31}$$

$$B_{on}^{(1)} = \frac{1}{\alpha^{(1)} \Delta T} c_{0n} \alpha_n^2 K_0(\alpha_n a) \tag{3.32}$$

$$B_{0n}^{(2)} = \frac{1}{\alpha^{(1)} \Delta T} d_{0n} \alpha_n^2 I_0(\alpha_n a) \tag{3.33}$$

$$A_0^* = \frac{1}{\alpha^{(1)} \Delta T \mu_1 a^2} A_0 \tag{3.34}$$

$$b_0^* = \frac{1}{\alpha^{(1)} \Delta T \mu_2} b_0 \tag{3.35}$$

Substituting equations (3.26)-(3.35) into (3.20)-(3.25), one has

$$\frac{1}{m_1\text{-}2} \sum_{v=1}^{\infty} A_{0v}^{(1)} \{ 2f_1(\beta_v z) + [2(m_1 - 1)f_1(\beta_v z) + m_1 f_2(\beta_v z)] \frac{K_0''(\beta_v a)}{\beta_v^2 K_0(\beta_v a)} \}$$

$$- \frac{1}{m_2\text{-}2} \sum_{v=1}^{\infty} A_{0v}^{(2)} \{ 2f_1(\beta_v z) + [2(m_2 - 1)f_1(\beta_v z) + m_2 f_2(\beta_v z)] \frac{I_0''(\beta_v a)}{\beta_v^2 I_0(\beta_v a)} \} \frac{\mu_2}{\mu_1}$$

$$+\frac{A_0^*}{2} - \frac{\mu_2}{\mu_1} b_0^* = 0 \tag{3.36}$$

$$\sum_{n=1}^{\infty} B_{0n}^{(1)} \left\{ \frac{1}{2} - \frac{1}{\alpha_n^2 a} \frac{K_0'(\alpha_n a)}{K_0(\alpha_n a)} \right\} (-1)^n \cos(\alpha_n z)$$

$$- \sum_{n=1}^{\infty} B_{0n}^{(2)} \left\{ \frac{1}{2} - \frac{1}{\alpha_n^2 a} \frac{I_0'(\alpha_n a)}{I_0(\alpha_n a)} \right\} \frac{\mu_2}{\mu_1} = 0 \tag{3.37}$$

$$- \frac{m_1}{m_1 - 2} \sum_{v=1}^{\infty} A_{0v}^{(1)} \frac{K_0'(\beta_v a)}{\beta_v K_0(\beta_v a)} [f_3(\beta_v z) + f_4(\beta_v z)]$$

$$+ \frac{m_2}{m_2 - 2} \sum_{v=1}^{\infty} A_{0v}^{(2)} \frac{I_0'(\beta_v a)}{\beta_v I_0(\beta_v a)} [f_3(\beta_v z) + f_4(\beta_v z)] \frac{\mu_2}{\mu_1} = 0 \tag{3.38}$$

$$\frac{1}{m_1 - 2} \sum_{v=1}^{\infty} A_{0v}^{(1)} [2(m_1 - 1) f_1(\beta_v z) + m_1 f_2(\beta_v z)] \frac{1}{\beta_v^2 a} \frac{K_0'(\beta_v a)}{K_0(\beta_v a)}$$

$$- \frac{1}{m_2 - 2} \sum_{v=1}^{\infty} A_{0v}^{(2)} [2(m_2 - 1) f_1(\beta_v z) + m_2 f_2(\beta_v z)] \frac{1}{\beta_v^2 a} \frac{I_0'(\beta_v a)}{I_0(\beta_v a)}$$

$$- \frac{A_0^*}{2} - \frac{1 - \nu_2}{1 + \nu_2} b_0^* + 1 - \frac{\alpha^{(2)}}{\alpha^{(1)}} = 0 \tag{3.39}$$

$$\sum_{n=1}^{\infty} B_{0n}^{(1)} \frac{1}{\alpha_n^2 a} \frac{K_0'(\alpha_n a)}{K_0(\alpha_n a)} (-1)^n \cos(\alpha_n z)$$

$$- \sum_{n=1}^{\infty} B_{0n}^{(2)} \frac{1}{\alpha_n^2 a} \frac{I_0'(\alpha_n a)}{I_0(\alpha_n a)} (-1)^n \cos(\alpha_n a) = 0 \tag{3.40}$$

$$\frac{1}{m_1 - 2} \sum_{v=1}^{\infty} A_{0v}^{(1)} \frac{1}{\beta_v a} [(m_1 - 2) f_3(\beta_v z) - m_1 f_4(\beta_v z)]$$

$$-\frac{1}{m_2-2}\sum_{v=1}^{\infty} A_{0v}^{(2)}\frac{1}{\beta_v a}[(m_2-2)f_3(\beta_v z)-m_2 f_4(\beta_v z)]$$

$$+\frac{2v_2}{1+v_2}b_0^*\frac{z}{a}+\left(1-\frac{\alpha^{(2)}}{\alpha^{(1)}}\right)\frac{z}{a}=0 \qquad (3.41)$$

3.3 Periodic Fibers Model

For the periodic fibers model, one needs to consider the additional boundary condition along the line B-C. From Figure 2.2, it is noted that the displacement and stress distributions are now θ-dependent. In order to satisfy the symmetric conditions at $\theta=0$ and $\theta=\pi/2$ respectively (see Fig.2.2), one needs to chose the solution in the form of a summation of $\cos(2k\theta)$ or $\sin(2k\theta)$. Thus, the symmetric conditions along lines O-B and O-C will be satisfied automatically. Moreover, the summation provides a sufficient number of coefficients so that the symmetric condition along the line B-C may be satisfied. Thus, the complementary solution may be chosen in the form:

$$H_v^{(1)}=\sum_{k=0}^{M} a_{kv}K_{2k}(\beta_v r)\cos(2k\theta) \qquad (3.42)$$

$$H_v^{(2)}=\sum_{k=0}^{M} b_{kv}I_{2k}(\beta_v r)\cos(2k\theta) \qquad (3.43)$$

$$H_n^{(1)}=\sum_{k=0}^{M} c_{kn}K_{2k}(\alpha_n r)\sin(2k\theta) \qquad (3.44)$$

$$H_n^{(2)}=\sum_{k=0}^{M} d_{kn}I_{2k}(\alpha_n r)\sin(2k\theta) \qquad (3.45)$$

$$\lambda_1^{(1)}=\sum_{k=1}^{M}\frac{e_k}{r^{2k+1}}\sin[(2k+1)\theta]+\sum_{k=1}^{M} f_k r^{2k-1}\sin[(2k-1)\theta] \qquad (3.46)$$

$$\lambda_2^{(1)} = \sum_{k=1}^{M} \frac{e_k}{r^{2k+1}} \cos[(2k+1)\theta] - \sum_{k=1}^{M} f_k r^{2k-1} \cos[(2k-1)\theta] \tag{3.47}$$

$$\lambda_3^{(1)} = \sum_{k=0}^{M-1} \frac{g_k}{r^{2k+1}} \cos[(2k+1)\theta] \tag{3.48}$$

$$\lambda_1^{(2)} = \sum_{k=1}^{M} h_k r^{2k-1} \sin[(2k-1)\theta] \tag{3.49}$$

$$\lambda_2^{(2)} = - \sum_{k=1}^{M} h_k r^{2k-1} \cos[(2k-1)\theta] \tag{3.50}$$

$$\lambda_3^{(2)} = \sum_{k=0}^{M-1} i_k r^{2k+1} \cos[(2k+1)\theta] \tag{3.51}$$

where I_{2k} and K_{2k} are , respectively, the modified Bessel functions of the first and second kind of order 2k, and a_{kv}, b_{kv}, c_{kn}, d_{kn} (k=0,1,2...M; v,n=1,2,3....), e_k , f_k , g_k , h_k , i_k are arbitrary constants that are to be determined later.

For numerical calculations, it is found convenient at this stage to nondimensionalize the expressions by introducing the following definitions:

$$A_{kv}^{(1)} = \frac{1}{\alpha^{(1)} \Delta T} a_{kv} \beta_v^2 K_{2k}(\beta_v a) \tag{3.52}$$

$$A_{kv}^{(2)} = \frac{1}{\alpha^{(1)} \Delta T} b_{kv} \beta_v^2 I_{2k}(\beta_v a) \tag{3.53}$$

$$B_{kn}^{(1)} = \frac{1}{\alpha^{(1)} \Delta T} c_{kn} \alpha_n^2 K_{2k}(\alpha_n a) \tag{3.54}$$

$$B_{kn}^{(2)} = \frac{1}{\alpha^{(1)} \Delta T} d_{kn} \alpha_n^2 I_{2k}(\alpha_n a) \tag{3.55}$$

$$e_k^* = \frac{1}{\alpha^{(1)} \Delta T \, a^{2k+2}} e_k \tag{3.56}$$

$$f_k^* = \frac{a^{2k-2}}{\alpha^{(1)}\Delta T} f_k \tag{3.57}$$

$$g_k^* = \frac{1}{\alpha^{(1)}\Delta T\, a^{2k+2}} g_k \tag{3.58}$$

$$h_k^* = \frac{a^{2k-2}}{\alpha^{(1)}\Delta T} h_k \tag{3.59}$$

$$i_k^* = \frac{a^{2k}}{\alpha^{(1)}\Delta T} i_k \tag{3.60}$$

Now the solutions of both particular and complementary parts have been found. The only problem remaining is to determine the unknown coefficients. Thus one needs to concentrate on how to deal with both the continuity conditions at the fiber/matrix interface (r=a) and the symmetric boundary conditions along the line B-C (see Fig.2.2) For the first boundary, one can use a Fourier expansion in order to eliminate the z-dependency and thus recover a set of simultaneous linear equations of the unknown coefficients. For the second boundary (line B-C), one can use an appropriate numerical scheme, which may match the symmetric condition.

CHAPTER 4

NUMERICAL CALCULATIONS

4.1 Fourier Expansions for One Fiber Model

In order to simplify the numerical calculations, one must first eliminate the z-dependence at the boundary r=a and thus recover a set of simultaneous linear equations with the coefficients as the unknowns. It is quite interesting to note that $B_{0n}^{(1)}$ and $B_{0n}^{(2)}$ are not coupled in the system (3.36)-(3.41). That means equations (3.37) and (3.40) may be treated separately from the remaining four boundary conditions and the following solution is obvious:

$$B_{0n}^{(1)} = B_{0n}^{(2)} = 0 \tag{4.1}$$

In view of equation (4.1), two of the boundary conditions are now automatically satisfied and only four are remaining. The relative balance between unknowns and number of equations does not change because two group of constants are satisfied by (4.1) and these two relative group of equations are automatically satisfied.

The technique for solving such a system is given by Folias. More specifically, one expands the functions $f_1(\beta_v z)$, $f_2(\beta_v z)$, and $(z/a)^2$ in terms of $\cos(\alpha_n z)$ and the function $f_3(\beta_v z)$, $f_4(\beta_v z)$ and (z/a) in terms of $\sin(\alpha_n z)$. Equating next the coefficients of similar functions of z , one arrives at the following equations, which may then be used directly for the numerical calculations. The reader may note that for convenience, the following notation is introduced :

$$\Gamma_{nv} \equiv \frac{\beta_v^2}{\beta_v^2 - \alpha_n^2} \tag{4.2}$$

$$\frac{2}{m_1 - 2} \sum_{v=1}^{\infty} A_{0v}^{(1)} \left[-1 + \frac{K_0''(\beta_v a)}{\beta_v^2 K_0(\beta_v a)} \right] - \frac{2}{m_2 - 2} \sum_{v=1}^{\infty} A_{0v}^{(2)} \left[-1 + \frac{I_0''(\beta_v a)}{\beta_v^2 I_0(\beta_v a)} \right] \frac{\mu_2}{\mu_1}$$

$$= -\frac{A_0^*}{2} + b_0^* \frac{\mu_2}{\mu_1} \tag{4.3}$$

$$\frac{2}{m_1 - 2} \sum_{v=1}^{\infty} A_{0v}^{(1)} \frac{1}{\beta_v^2 a} \frac{K_0'(\beta_v a)}{K_0(\beta_v a)} - \frac{2}{m_2 - 2} \sum_{v=1}^{\infty} A_{0v}^{(2)} \frac{1}{\beta_v^2 a} \frac{I_0'(\beta_v a)}{I_0(\beta_v a)}$$

$$= \frac{A_0^*}{2} + \frac{1 - \nu_2}{1 + \nu_2} b_0^* + \frac{\alpha^{(2)}}{\alpha^{(1)}} - 1 \tag{4.4}$$

$$\frac{1}{m_1 - 2} \sum_{v=1}^{\infty} A_{0v}^{(1)} \frac{\Gamma_{nv}}{\beta_v a} (-m_1 + 1 + m_1 \Gamma_{nv}) \frac{K_0'(\beta_v a)}{K_0(\beta_v a) \beta_v}$$

$$- \frac{1}{m_2 - 2} \sum_{v=1}^{\infty} A_{0v}^{(2)} \frac{\Gamma_{nv}}{\beta_v^2 a} (-m_2 + 1 + m_2 \Gamma_{nv}) \frac{I_0'(\beta_v a)}{I_0(\beta_v a)} = 0 \tag{4.5}$$

$$- \frac{2}{m_1 - 2} \sum_{v=1}^{\infty} A_{0v}^{(1)} \frac{\alpha_n}{\beta_v^2 a} (m_1 - 1 + m_1 \Gamma_{nv}) \Gamma_{nv}$$

$$+ \frac{2}{m_2 - 2} \sum_{v=1}^{\infty} A_{0v}^{(2)} \frac{\alpha_n}{\beta_v^2 a} (m_2 - 1 + m_2 \Gamma_{nv}) \Gamma_{nv}$$

$$= \frac{1}{\alpha_n a} \left(1 - \frac{\alpha^{(2)}}{\alpha^{(1)}} \right) \tag{4.6}$$

$$\frac{1}{m_1 - 2} \sum_{v=1}^{\infty} A_{0v}^{(1)} \Gamma_{nv} \left\{ -1 + \left(-m_1 + 1 + m_1 \Gamma_{nv} \right) \frac{K_0''(\beta_v a)}{\beta_v^2 K_0(\beta_v a)} \right\}$$

$$-\frac{1}{m_2-2}\sum_{v=1}^{\infty} A_{0v}^{(2)}\frac{\Gamma_{nv}}{\beta_v^2}\{-1+(-m_2+1+m_2\Gamma_{nv})\frac{I_0'(\beta_v a)}{I_0(\beta_v a)}\}\frac{\mu_2}{\mu_1}=0 \qquad (4.7)$$

$$\frac{m_1}{m_1-2}\sum_{v=1}^{\infty} A_{0v}^{(1)}\frac{\alpha_n}{\beta_v^2}\Gamma_{nv}^2\frac{K_0'(\beta_v a)}{K_0(\beta_v a)}$$

$$-\frac{1}{m_2-2}\sum_{v=1}^{\infty} A_{0v}^{(2)}\frac{\alpha_n}{\beta_v^2}\Gamma_{nv}^2\frac{I_0'(\beta_v a)}{I_0(\beta_v a)}\frac{\mu_2}{\mu_1}=0 \qquad (4.8)$$

This linear system can be solved by a modified Gaussian elimination method with pivoting. Double precision is used throughout the computational analysis because of the high sensitivity of the system.

The reader can show that the solution, by virtue of its construction, satisfies (i) Navier's equations (2.1)-(2.3), (ii) all the boundary conditions and (iii) all the continuity conditions. Moreover, the following three special cases will serve as a limit check of the numerical results. The three special limit cases are a continuous plate; a thin plate; and a plate with a cylindrical hole.

(1) Continuous plate. If $\nu_1 = \nu_2$, $\mu_1 = \mu_2$ and $\alpha^{(1)} = \alpha^{(2)}$. Then:

$$A_{0v}^{(1)} = A_{0v}^{(2)} = B_{0n}^{(1)} = B_{0n}^{(2)} = A_0^* = b_0^* = 0 \qquad (4.9)$$

So the solutions reduce to the particular solutions and all of the residual stresses go to zero and the displacements reduce to the linear forms along the different directions.

(2) Thin plate. If $h/a \approx 0$, then the right hand side of equation (4.6) will be:

$$\frac{1}{\alpha_n a}=\frac{1}{\alpha_n h}\frac{h}{a}=\frac{1}{n\pi}\frac{h}{a}\to 0\ , \qquad \text{as } (\frac{h}{a})\to 0 \qquad (4.10)$$

from equations (4.3)-(4.8), one has :

$$A_{0v}^{(1)} = A_{0v}^{(2)} = B_{0n}^{(1)} = B_{0n}^{(2)} = 0 \tag{4.11}$$

It is seen that one recovers precisely the particular solution, that is the plane stress solution given by Delale.

(3) Cylindrical hole. In the case of $\mu_2/\mu_1=0$, which is numerically represented by a very very soft inclusion, i.e., $\mu_2/\mu_1=0.00001$. One can see from equations (4.7)-(4.8) and from equation (4.3) that:

$$A_{0v}^{(1)} \cong 0 \tag{4.12}$$

$$A_0^* \cong 0 \tag{4.13}$$

which suggests, therefore, that in the case of a matrix plate with a cylindrical hole there is no residual stress present as a result of a change in temperature.

4.2 Fourier Expansions for Periodic Fibers Model

As for periodic fibers model, there are two different kinds of boundary conditions that need to be satisfied. Similarly, for the continuity conditions at r=a, Fourier expansions are used to recover sets of linear equations with unknown coefficients. Without going into mathematical details, the following equations can be used as the boundary conditions at r=a:

$$\frac{2}{m_1-2}\sum_{v=1}^{\infty} A_{0v}^{(1)} \frac{1}{\beta_v^2 a} \frac{K_0'(\beta_v a)}{K_0(\beta_v a)} - \frac{2}{m_2-2}\sum_{v=1}^{\infty} A_{0v}^{(2)} \frac{1}{\beta_v^2 a} \frac{I_0'(\beta_v a)}{I_0(\beta_v a)}$$

$$= -\frac{1}{2}\left(\frac{3m_1-1}{m_1+1} + 1\right) g_0^* + \frac{1}{2}\left(\frac{3m_2-1}{m_2+1} - 1\right) i_0^*$$

$$+ \frac{A_0^*}{2} + \frac{1-\nu_2}{1+\nu_2} b_0^* + \frac{\alpha^{(2)}}{\alpha^{(1)}} - 1 \tag{4.14}$$

$$\frac{2}{m_1-2}\sum_{v=1}^{\infty} A_{0v}^{(1)}\left[-1+\frac{K_0''(\beta_v a)}{\beta_v^2 K_0(\beta_v a)}\right]-\frac{2}{m_2-2}\sum_{v=1}^{\infty} A_{0v}^{(2)}\left[-1+\frac{I_0''(\beta_v a)}{\beta_v^2 I_0(\beta_v a)}\right]\frac{\mu_2}{\mu_1}$$

$$=\left(\frac{m_1-1}{m_1+1}+1\right) g_0^* + i_0^*\frac{\mu_2}{\mu_1} - \frac{A_0^*}{2} + b_0^*\frac{\mu_2}{\mu_1} \qquad (4.15)$$

$$\frac{1}{m_1-2}\sum_{v=1}^{\infty} A_{0v}^{(1)}\frac{\Gamma_{nv}}{\beta_v a}\left(-m_1+1+m_1\Gamma_{nv}\right)\frac{K_0'(\beta_v a)}{K_0(\beta_v a)\beta_v}$$

$$-\frac{1}{m_2-2}\sum_{v=1}^{\infty} A_{0v}^{(2)}\frac{\Gamma_{nv}}{\beta_v^2 a}\left(-m_2+1+m_2\Gamma_{nv}\right)\frac{I_0'(\beta_v a)}{I_0(\beta_v a)}=0 \qquad (4.16)$$

$$-\frac{2}{m_1-2}\sum_{v=1}^{\infty} A_{0v}^{(1)}\frac{\alpha_n}{\beta_v^2 a}\left(m_1-1+m_1\Gamma_{nv}\right)\Gamma_{nv}$$

$$+\frac{2}{m_2-2}\sum_{v=1}^{\infty} A_{0v}^{(2)}\frac{\alpha_n}{\beta_v^2 a}\left(m_2-1+m_2\Gamma_{nv}\right)\Gamma_{nv}$$

$$=\frac{2}{\alpha_n a}\frac{1}{m_2+1} i_0^* + \frac{1}{\alpha_n a}\left(1-\frac{\alpha^{(2)}}{\alpha^{(1)}}\right) \qquad (4.17)$$

$$\frac{1}{m_1-2}\sum_{v=1}^{\infty} A_{0v}^{(1)}\Gamma_{nv}\left\{-1+\left(-m_1+1+m_1\Gamma_{nv}\right)\frac{K_0''(\beta_v a)}{\beta_v^2 K_0(\beta_v a)}\right\}$$

$$-\frac{1}{m_2-2}\sum_{v=1}^{\infty} A_{0v}^{(2)}\frac{\Gamma_{nv}}{\beta_v^2}\left\{-1+\left(-m_2+1+m_2\Gamma_{nv}\right)\frac{I_0''(\beta_v a)}{I_0(\beta_v a)}\right\}\frac{\mu_2}{\mu_1}=0 \qquad (4.18)$$

$$\frac{m_1}{m_1-2}\sum_{v=1}^{\infty} A_{0v}^{(1)}\frac{\alpha_n}{\beta_v^2}\Gamma_{nv}^2\frac{K_0'(\beta_v a)}{K_0(\beta_v a)}$$

$$-\frac{1}{m_2-2}\sum_{v=1}^{\infty} A_{0v}^{(2)}\frac{\alpha_n}{\beta_v^2}\Gamma_{nv}^2\frac{I_0'(\beta_v a)}{I_0(\beta_v a)}\frac{\mu_2}{\mu_1}=0 \tag{4.19}$$

$$\frac{2}{m_1-2}\sum_{v=1}^{\infty} A_{kv}^{(1)}\frac{1}{\beta_v^2 a}\frac{K_{2k}'(\beta_v a)}{K_{2k}(\beta_v a)}-\frac{2}{m_2-2}\sum_{v=1}^{\infty} A_{kv}^{(2)}\frac{1}{\beta_v^2 a}\frac{I_{2k}'(\beta_v a)}{I_{2k}(\beta_v a)}$$

$$=-\frac{1}{2}\left(\frac{3m_1-1}{m_1+1}+2k+1\right)g_k^*-\frac{1}{2}\left(\frac{3m_1-1}{m_1+1}+2k-1\right)g_{k-1}^*-\frac{1}{3}\left(\frac{h}{a}\right)^2\frac{1}{m_1+1}(2k-1)(2k)\,g_{k-1}^*$$

$$+\frac{1}{2}\left(\frac{3m_2-1}{m_2+1}-2k-1\right)i_k^*+\frac{1}{2}\left(\frac{3m_2+1}{m_2+1}-2k+1\right)i_{k-1}^*+\frac{1}{3}\left(\frac{h}{a}\right)^2\frac{1}{m_2+1}(2k+1)(2k)\,i_k^*$$

$$+f_k^*-e_k^*-h_k^* \tag{4.20}$$

$$-\frac{4}{m_1-2}\sum_{v=1}^{\infty} A_{kv}^{(1)}\frac{k}{(\beta_v a)^2}+\frac{4}{m_2-2}\sum_{v=1}^{\infty} A_{kv}^{(2)}\frac{k}{(\beta_v a)^2}$$

$$=-\frac{1}{2}\left(\frac{3m_1-1}{m_1+1}+2k+1\right)g_k^*-\frac{1}{2}\left(-\frac{3m_1-1}{m_1+1}+2k-1\right)g_{k-1}^*-\frac{1}{3}\left(\frac{h}{a}\right)^2\frac{1}{m_1+1}(2k-1)(2k)\,g_{k-1}^*$$

$$+\frac{1}{2}\left(\frac{3m_2-1}{m_2+1}+2k+1\right)i_k^*+\frac{1}{2}\left(-\frac{3m_2-1}{m_2+1}-2k-1\right)i_{k-1}^*-\frac{1}{3}\left(\frac{h}{a}\right)^2\frac{1}{m_2+1}(2k+1)(2k)\,i_k^*$$

$$-f_k^*-e_k^*+h_k^* \tag{4.21}$$

$$\frac{1}{m_1-2}\sum_{v=1}^{\infty} A_{kv}^{(1)}\left\{-2+\frac{2}{\beta_v^2}\frac{K_{2k}''(\beta_v a)}{K_{2k}(\beta_v a)}\right\}-\frac{1}{m_2-2}\sum_{v=1}^{\infty} A_{kv}^{(2)}\left\{-2-\frac{2}{\beta_v^2}\frac{I_{2k}''(\beta_v a)}{I_{2k}(\beta_v a)}\right\}\frac{\mu_2}{\mu_1}$$

$$=(2k+1)\left(\frac{m_1-1}{m_1+1}+k+1\right)g_k^*+(2k-1)(k+1)\,g_{k-1}^*+\frac{1}{3}\left(\frac{h}{a}\right)^2\frac{1}{m_1+1}(2k-1)(2k)(2k+1)\,g_{k-1}^*$$

$$+(2k+1)(1-k)\,i_k^*\frac{\mu_2}{\mu_1}+(2k-1)\left(\frac{m_2-1}{m_2+1}-k+1\right)i_{k-1}^*\frac{\mu_2}{\mu_1}$$

$$+\frac{1}{3}\left(\frac{h}{a}\right)^2\frac{1}{m_2+1}(2k+1)(2k-1)(2k)\,i_k^*\frac{\mu_2}{\mu_1}-(1-2k)\,f_k^*$$

$$+(1+2k)\,e_k^*+(1-2k)\,h_k^*\frac{\mu_2}{\mu_1} \qquad (4.22)$$

$$\frac{4}{m_1-2}\sum_{v=1}^{\infty}A_{kv}^{(1)}\left\{\frac{-k}{\beta_v^2 a}\frac{K_{2k}'(\beta_v a)}{K_{2k}(\beta_v a)}+\frac{k}{(\beta_v a)^2}\right\}$$

$$-\frac{4}{m_2-2}\sum_{v=1}^{\infty}A_{kv}^{(2)}\left\{\frac{-k}{\beta_v^2 a}\frac{I_{2k}'(\beta_v a)}{I_{2k}(\beta_v a)}+\frac{k}{(\beta_v a)^2}\right\}\frac{\mu_2}{\mu_1}$$

$$=(2k+1)\left(\frac{m_1-1}{m_1+1}+k+1\right)g_k^*+(2k-1)k\,g_{k-1}^*+\frac{1}{3}\left(\frac{h}{a}\right)^2\frac{1}{m_1+1}(2k-1)(2k)(2k+1)\,g_{k-1}^*$$

$$+(2k+1)k\,i_k^*\frac{\mu_2}{\mu_1}-(2k-1)\left(\frac{m_2-1}{m_2+1}-k+1\right)i_{k-1}^*\frac{\mu_2}{\mu_1}$$

$$-\frac{1}{3}\left(\frac{h}{a}\right)^2\frac{1}{m_2+1}(2k+1)(2k-1)(2k)\,i_k^*\frac{\mu_2}{\mu_1}-(2k-1)\,f_f^*$$

$$+(2k+1)\,e_k^*+(2k-1)\,h_k^*\frac{\mu_2}{\mu_1} \qquad (4.23)$$

$$\frac{2}{m_1-2}\sum_{v=1}^{\infty}A_{kv}^{(1)}\frac{\Gamma_{nv}}{\beta_v^2 a}\left\{-m_1+1+m_1\Gamma_{nv}\right\}\frac{K_{2k}'(\beta_v a)}{K_{2k}(\beta_v a)}$$

$$-\frac{2}{m_2-2}\sum_{v=1}^{\infty}A_{kv}^{(2)}\frac{\Gamma_{nv}}{\beta_v^2 a}\left\{-m_2+1+m_2\Gamma_{nv}\right\}\frac{I_{2k}'(\beta_v a)}{I_{2k}(\beta_v a)}$$

$$-B_{kn}^{(1)}\frac{k}{(\alpha_n a)^2}+B_{kn}^{(2)}\frac{k}{(\alpha_n a)^2}+\frac{2}{(\alpha_n a)^2}\frac{1}{m_1+1}(2k-1)(2k)\,g_{k-1}^*$$

$$-\frac{2}{(\alpha_n a)^2}\frac{1}{m_2+1}(2k+1)(2k)\,i_k^*=0 \qquad (4.24)$$

$$\frac{-8}{m_1-2}\sum_{v=1}^{\infty} A_{kv}^{(1)}\frac{k}{(\beta_v a)^2}\{-m_1+1+m_1\Gamma_{nv}\}\Gamma_{nv}$$

$$+\frac{8}{m_2-2}\sum_{v=1}^{\infty} A_{kv}^{(2)}\frac{k}{(\beta_v a)^2}\{-m_2+1+m_2\Gamma_{nv}\}\Gamma_{nv}$$

$$+B_{kn}^{(1)}\frac{1}{\alpha_n^2 a}\frac{K'_{2k}(\alpha_n a)}{K_{2k}(\alpha_n a)}-B_{kn}^{(2)}\frac{1}{\alpha_n^2 a}\frac{I'_{2k}(\alpha_n a)}{I_{2k}(\alpha_n a)}$$

$$+\frac{4}{(\alpha_n a)^2}\frac{1}{m_1+1}(2k-1)(2k)\,g_{k-1}^{*}+\frac{4}{(\alpha_n a)^2}\frac{1}{m_2+1}(2k-1)(2k)\,i_k^{*}=0 \qquad (4.25)$$

$$-\frac{1}{m_1-2}\sum_{v=1}^{\infty} A_{kv}^{(1)}\frac{\alpha_n}{\beta_v^2 a}\{m_1-1+m_1\Gamma_{nv}\}\Gamma_{nv}$$

$$+\frac{1}{m_2-2}\sum_{v=1}^{\infty} A_{kv}^{(2)}\frac{\alpha_n}{\beta_v^2 a}\{m_2-1+m_2\Gamma_{nv}\}\Gamma_{nv}$$

$$-\frac{1}{\alpha_n a}\frac{1}{m_1+1}(2k-1)\,g_{k-1}^{*}-\frac{1}{\alpha_n a}\frac{1}{m_2+1}(2k+1)\,i_k^{*}=0 \qquad (4.26)$$

$$\frac{2}{m_1-2}\sum_{v=1}^{\infty} A_{kv}^{(1)}\Gamma_{nv}\{-1+[-m_1+1+m_1\Gamma_{nv}]\frac{K''_{2k}(\beta_v a)}{\beta_v^2 K_{2k}(\beta_v a)}\}$$

$$\frac{2}{m_2-2}\sum_{v=1}^{\infty} A_{kv}^{(2)}\frac{\Gamma_{nv}}{\beta_v^2}\{-1+[-m_2+1+m_2\Gamma_{nv}]\frac{I''_{2k}(\beta_v a)}{I_{2k}(\beta_v a)}\}\frac{\mu_2}{\mu_1}$$

$$-B_{kn}^{(1)}\{\frac{k}{\alpha_n^2 a}\frac{K'_{2k}(\alpha_n a)}{K_{2k}(\alpha_n a)}-\frac{k}{(\alpha_n a)^2}\}+B_{kn}^{(2)}\frac{k}{\alpha_n^2 a}\{\frac{I'_{2k}(\alpha_n a)}{I_{2k}(\alpha_n a)}-\frac{1}{a}\}\frac{\mu_2}{\mu_1}$$

$$-\frac{2}{(\alpha_n a)^2}\frac{1}{m_1+1}(2k-1)(2k)(2k+1)\,g_{k-1}^{*}$$

$$-\frac{2}{(\alpha_n a)^2}\frac{1}{m_2+1}(2k+1)(2k-1)(2k)\,i_k^{*}\frac{\mu_2}{\mu_1}=0 \qquad (4.27)$$

$$\frac{4}{m_1-2}\sum_{v=1}^{\infty} A_{kv}^{(1)}\Gamma_{nv}\,[-m_1+1+m_1\Gamma_{nv}]\,\{\frac{-2k}{\beta_v^2 a}\frac{K'_{2k}(\beta_v a)}{K_{2k}(\beta_v a)}+\frac{2k}{(\beta_v a)^2}\}$$

$$-\frac{4}{m_2-2}\sum_{v=1}^{\infty} A_{kv}^{(2)}\Gamma_{nv}\,[-m_2+1+m_2\Gamma_{nv}]\,\{\frac{-2k}{\beta_v^2 a}\frac{I'_{2k}(\beta_v a)}{I_{2k}(\beta_v a)}+\frac{2k}{(\beta_v a)^2}\}\frac{\mu_2}{\mu_1}$$

$$-B_{kn}^{(1)}\{\frac{1}{\alpha_n^2 a}\frac{K'_{2k}(\alpha_n a)}{K_{2k}(\alpha_n a)}-\frac{4k^2}{(\alpha_n a)^2}-\frac{1}{2}\}$$

$$+B_{kn}^{(2)}\{\frac{1}{\alpha_n^2 a}\frac{I'_{2k}(\alpha_n a)}{I_{2k}(\alpha_n a)}-\frac{4k^2}{(\alpha_n a)^2}-\frac{1}{2}\}\frac{\mu_2}{\mu_1}$$

$$-\frac{4}{(\alpha_n a)^2}\frac{1}{m_1+1}(2k-1)(2k)(2k+1)\,g_{k-1}^{*}$$

$$+\frac{4}{(\alpha_n a)^2}\frac{1}{m_2+1}(2k+1)(2k-1)(2k)\,i_k^{*}\frac{\mu_2}{\mu_1}=0 \qquad (4.28)$$

$$-\frac{4m_1}{m_1-2}\sum_{v=1}^{\infty} A_{kv}^{(1)}\frac{\alpha_n}{\beta_v^2}\Gamma_{nv}^2\frac{K'_{2k}(\beta_v a)}{K_{2k}(\beta_v a)}+\frac{4m_2}{m_2-2}\sum_{v=1}^{\infty} A_{kv}^{(2)}\frac{\alpha_n}{\beta_v^2}\Gamma_{nv}^2\frac{I'_{2k}(\beta_v a)}{I_{2k}(\beta_v a)}\frac{\mu_2}{\mu_1}$$

$$+B_{kn}^{(1)}\frac{k}{\alpha_n a}-B_{kn}^{(2)}\frac{k}{\alpha_n a}\frac{\mu_2}{\mu_1}=0 \qquad (4.29)$$

As for another group of boundary conditions at line B-C, Fourier expansions are also used to eliminate the z-dependency. Then the collocation method is used to force the conditions (2.52)-(2.55) to be satisfied. Without going into mathematical details, the following equations can be used directly in the numerical calculations where the following definitions have been used:

$$\xi_i=\frac{b}{\sin(\theta_i)+\cos(\theta_i)} \qquad (4.30)$$

$$\xi^* = \frac{b}{\sqrt{2}} \tag{4.31}$$

$$\delta\theta = \frac{\pi}{2P}, \text{ (P is the number of points along B-C line)} \tag{4.32}$$

$$\delta S_i = \frac{\sqrt{2}\,b}{a} \frac{\sin(\delta\theta)}{\sin(2\theta_i+\delta\theta)+\cos(\delta\theta)} \tag{4.33}$$

at B-C line:

$$\frac{1}{m_1-2} \sum_{k=0}^{M} \sum_{v=1}^{\infty} A_{kv}^{(1)} \Gamma_{nv}(-m_1+1+m_1\Gamma_{nv}) \{ - \frac{K_{2k}''(\beta_v\xi_i)}{K_{2k}(\beta_v a)\beta_v^2} + \frac{1+4k}{\beta_v^2 \xi_i} \frac{K_{2k}'(\beta_v \xi_i)}{K_{2k}(\beta_v a)}$$

$$- \frac{4k(k+1)}{(\beta_v \xi_i)^2} \frac{K_{2k}(\beta_v \xi_i)}{K_{2k}(\beta_v a)} \} \cos[(2k+2)\theta_i]$$

$$+ \frac{1}{m_1-2} \sum_{k=0}^{M} \sum_{v=1}^{\infty} A_{kv}^{(1)} \Gamma_{nv}(-m_1+1+m_1\Gamma_{nv}) \{ - \frac{K_{2k}''(\beta_v\xi_i)}{K_{2k}(\beta_v a)\,\beta_v^2} + \frac{1-4k}{\beta_v^2\xi_i} \frac{K_{2k}'(\beta_v\xi_i)}{K_{2k}(\beta_v a)}$$

$$- \frac{4k(k-1)}{(\beta_v \xi_1)^2} \frac{K_{2k}(\beta_v \xi_i)}{K_{2k}(\beta_v a)} \} \cos[(2k-2)\theta_i]$$

$$+ \sum_{k=0}^{M} B_{kn}^{(1)} \{ \frac{k+0.5}{\alpha_n^2 \xi_i} \frac{K_{2k}'(\alpha_n \xi_i)}{K_{2k}(\alpha_n a)} - [\frac{k(1+2k)}{(\alpha_n \xi_i)^2} + \frac{1}{4}] \frac{K_{2k}(\alpha_n \xi_i)}{K_{2k}(\alpha_n a)} \} \cos[(2k+2)\theta_i]$$

$$+ \sum_{k=0}^{M} B_{kn}^{(1)} \{ \frac{k-0.5}{\alpha_n^2 \xi_i} \frac{K_{2k}'(\alpha_n \xi_i)}{K_{2k}(\alpha_n a)} - [\frac{k(1-2k)}{(\alpha_n \xi_i)^2} - \frac{1}{4}] \frac{K_{2k}(\alpha_n \xi_i)}{K_{2k}(\alpha_n a)} \} \cos[(2k-2)\theta_i]$$

$$+ \frac{1}{m_1+1} \frac{4}{(\alpha_n a)^2} \sum_{k=1}^{M} (2k-1)(2k)(2k+1) (\frac{a}{\xi_i})^{2k+2} g_{k-1}^* \cos[(2k+2)\theta_i] = 0$$

(4.34)

$$\frac{\sqrt{2}}{m_1-2}\sum_{k=0}^{M}\sum_{v=1}^{\infty}A_{kv}^{(1)}\frac{1}{\beta_v^2 a}(-m_1+1+m_1\Gamma_{nv})\,\Gamma_{nv}\left\{\frac{K'_{2k}(\beta_v\xi_i)}{K_{2k}(\beta_v a)}-\frac{2k}{\xi_i}\frac{K_{2k}(\beta_v\xi_i)}{K_{2k}(\beta_v a)}\right\}$$

$$\{\cos[(2k+1)\theta_i] + \sin[(2k+1)\theta_i]\}$$

$$+\frac{\sqrt{2}}{m_1-2}\sum_{k=0}^{M}\sum_{v=1}^{\infty}A_{kv}^{(1)}\frac{1}{\beta_v^2 a}(-m_1+1+m_1\Gamma_{nv})\,\Gamma_{nv}\left\{\frac{K'_{2k}(\beta_v\xi_i)}{K_{2k}(\beta_v a)}+\frac{2k}{\xi_i}\frac{K_{2k}(\beta_v\xi_i)}{K_{2k}(\beta_v a)}\right\}$$

$$\{\cos[(2k-1)\theta_i] - \sin[(2k-1)\theta_i]\}$$

$$-\frac{4}{m_1-2}\sum_{k=0}^{M}\sum_{v=1}^{\infty}A_{kv}^{(1)}\frac{1}{\beta_v^2 a}(-m_1+1+m_1\Gamma_{nv})\,\Gamma_{nv}\frac{K'_{2k}(\beta_v\xi^*)}{K_{2k}(\beta_v a)}\cos(\frac{k\pi}{2})$$

$$+\frac{\sqrt{2}}{4}\sum_{k=0}^{M}B_{kn}^{(1)}\frac{1}{\alpha_n^2 a}\left\{-\frac{2k}{\xi_i}\frac{K_{2k}(\alpha_n\xi_i)}{K_{2k}(\alpha_n a)}+\frac{K'_{2k}(\alpha_n\xi_i)}{K_{2k}(\alpha_n a)}\right\}$$

$$\{\cos[(2k+1)\theta_i] + \sin[(2k+1)\theta_i]\}$$

$$-\frac{\sqrt{2}}{4}\sum_{k=0}^{M}B_{kn}^{(1)}\frac{1}{\alpha_n^2 a}\left\{\frac{2k}{\xi_i}\frac{K_{2k}(\alpha_n\xi_i)}{K_{2k}(\alpha_n a)}+\frac{K'_{2k}(\alpha_n\xi_i)}{K_{2k}(\alpha_n a)}\right\}$$

$$\{\cos[(2k-1)\theta_i] - \sin[(2k-1)\theta_i]\}$$

$$+\sum_{k=0}^{M}B_{kn}^{(1)}\frac{2k}{\alpha_n^2 a\,\xi^*}\frac{K_{2k}(\alpha_n\xi^*)}{K_{2k}(\alpha_n a)}\cos(\frac{k\pi}{2})$$

$$+\frac{2\sqrt{2}}{m_1+1}\frac{1}{(\alpha_n a)^2}\sum_{k=1}^{M}(2k-1)(2k)(\frac{a}{\xi_i})^{2k+1}g_{k-1}^*$$

$$\{\cos[(2k+1)\theta_i] + \sin[(2k+1)\theta_i]\}$$

$$-\frac{1}{m_1+1}\frac{4}{(\alpha_n a)^2}\sum_{k=1}^{M}(2k-1)(2k)(\frac{a}{\xi^*})^{2k+1}g_{k-1}^*\cos(\frac{k\pi}{2}) = 0 \qquad (4.35)$$

$$\frac{2}{m_1-2}\sum_{k=0}^{M}\sum_{v=1}^{\infty}A_{kv}^{(1)}\Gamma_{nv}\{\sum_{i=1}^{P}\{-\frac{2K_{2k}(\beta_v\xi_i)}{K_{2k}(\beta_v a)}+(-m_1+1+m_1\Gamma_{nv})$$

$$[\frac{K''_{2k}(\beta_v\xi_i)}{\beta_v^2K_{2k}(\beta_v a)}+\frac{1}{\beta_v^2\xi_i}\frac{K'_{2k}(\beta_v\xi_i)}{K_{2k}(\beta_v a)}-\frac{4k^2}{(\beta_v\xi_i)^2}\frac{K_{2k}(\beta_v\xi_i)}{K_{2k}(\beta_v a)}]\}\delta S_i\cos(2k\theta_i)\}$$

$$+\frac{1}{m_1-2}\sum_{k=0}^{M}\sum_{v=1}^{\infty}A_{kv}^{(1)}\Gamma_{nv}(-m_1+1+m_1\Gamma_{nv})\{\sum_{i=1}^{P}[\frac{K''_{2k}(\beta_v\xi_i)}{\beta_v^2K_{2k}(\beta_v a)}-\frac{1+4k}{\beta_v^2\xi_i}$$

$$\frac{K'_{2k}(\beta_v\xi_i)}{K_{2k}(\beta_v a)}+\frac{4k(k+1)}{(\beta_v\xi_i)^2}\frac{K_{2k}(\beta_v\xi_i)}{K_{2k}(\beta_v a)}]\delta S_i\sin[(2k+2)\theta_i]\}$$

$$+\frac{1}{m_1-2}\sum_{k=0}^{M}\sum_{v=1}^{\infty}A_{kv}^{(1)}\Gamma_{nv}(-m_1+1+m_1\Gamma_{nv})\{\sum_{i=1}^{P}[-\frac{K''_{2k}(\beta_v\xi_i)}{\beta_v^2K_{2k}(\beta_v a)}$$

$$+\frac{1-4k}{\beta_v^2\xi_i}\frac{K'_{2k}(\beta_v\xi_i)}{K_{2k}(\beta_v a)}-\frac{4k(k-1)}{(\beta_v\xi_i)^2}\frac{K_{2k}(\beta_v\xi_i)}{K_{2k}(\beta_v a)}]\delta S_i\sin[(2k-2)\theta_i]\}$$

$$+\sum_{k=0}^{M}B_{kn}^{(1)}\{\sum_{i=1}^{P}[-\frac{k+0.5}{\alpha_n^2\xi_i}\frac{K'_{2k}(\alpha_n\xi_i)}{K_{2k}(\alpha_n a)}+\frac{k(1+2k)}{(\alpha_n\xi_i)^2}\frac{K_{2k}(\alpha_n\xi_i)}{K_{2k}(\alpha_n a)}$$

$$+\frac{1}{4}\frac{K_{2k}(\alpha_n\xi_i)}{K_{2k}(\alpha_n a)}]\delta S_i\sin[(2k+2)\theta_i]\}$$

$$+\sum_{k=0}^{M}B_{kn}^{(1)}\{\sum_{i=1}^{P}[\frac{k-0.5}{\alpha_n^2\xi_i}\frac{K'_{2k}(\alpha_n\xi_i)}{K_{2k}(\alpha_n a)}-\frac{k(1-2k)}{(\alpha_n\xi_i)^2}\frac{K_{2k}(\alpha_n\xi_i)}{K_{2k}(\alpha_n a)}$$

$$+\frac{1}{4}\frac{K_{2k}(\alpha_n\xi_i)}{K_{2k}(\alpha_n a)}]\delta S_i\sin[(2k-2)\theta_i]\}$$

$$-\frac{1}{m_1+1}\frac{4}{(\alpha_n a)^2}\sum_{k=1}^{M}(2k-1)(2k)(2k+1)\,g_{k-1}^{*}\{\sum_{i=1}^{P}(\frac{a}{\xi_i})^{2k+2}\delta S_i$$

$$\sin[(2k+2)\theta_i] \} = 0 \qquad (4.36)$$

$$\frac{1}{2}\frac{1}{m_1-2}\sum_{k=0}^{M}\sum_{v=1}^{\infty}A_{kv}^{(1)}\{-\frac{K_{2k}''(\beta_v\xi_i)}{\beta_v^2 K_{2k}(\beta_v a)}+\frac{1+4k}{\beta_v^2\xi_i}\frac{K_{2k}'(\beta_v\xi_i)}{K_{2k}(\beta_v a)}$$

$$-\frac{4k(k+1)}{(\beta_v\xi_i)^2}\frac{K_{2k}(\beta_v\xi_i)}{K_{2k}(\beta_v a)}\}\cos[(2k+2)\theta_i]$$

$$+\frac{1}{2}\frac{1}{m_1-2}\sum_{k=0}^{M}\sum_{v=1}^{\infty}A_{kv}^{(1)}\{-\frac{K_{2k}''(\beta_v\xi_i)}{\beta_v^2 K_{2k}(\beta_v a)}+\frac{1-4k}{\beta_v^2\xi_i}\frac{K_{2k}'(\beta_v\xi_i)}{K_{2k}(\beta_v a)}$$

$$-\frac{4k(k-1)}{(\beta_v\xi_i)^2}\frac{K_{2k}(\beta_v\xi_i)}{K_{2k}(\beta_v a)}\}\cos[(2k-2)\theta_i]\}$$

$$+\sum_{k=0}^{M-1}(2k+1)\left(\frac{m_1-1}{m_1+1}+k+1\right)\left(\frac{a}{\xi_i}\right)^{2k+2}g_k^*\cos[(2k+2)\theta_i]$$

$$+\sum_{k=1}^{M}(2k-1)k\left(\frac{a}{\xi_i}\right)^{2k}g_{k-1}^*\cos[(2k+2)\theta_i]$$

$$+\frac{1}{3}\frac{1}{m_1+1}\left(\frac{h}{a}\right)^2\sum_{k=1}^{M}(2k-1)(2k)(2k+1)\left(\frac{a}{\xi_i}\right)^{2k+2}g_{k-1}^*\cos[(2k+2)\theta_i]$$

$$+\sum_{k=1}^{M}(2k+1)\left(\frac{a}{\xi_i}\right)^{2k+2}e_k^*\cos[(2k+2)\theta_i]$$

$$+\sum_{k=1}^{M}(2k-1)\left(\frac{\xi_i}{a}\right)^{2k-2}f_k^*\cos[(2k-2)\theta_i]$$

$$-\frac{1}{2}A_0^*\left(\frac{a}{\xi_i}\right)^2\cos(2\theta_i)=0 \qquad (4.37)$$

$$\frac{\sqrt{2}}{2}\frac{1}{m_1-2}\sum_{k=0}^{M}\sum_{v=1}^{\infty}A_{kv}^{(1)}\frac{1}{\beta_v^2 a}\left\{\frac{K'_{2k}(\beta_v\xi_i)}{K_{2k}(\beta_v a)}-\frac{2k}{\xi_i}\frac{K_{2k}(\beta_v\xi_i)}{K_{2k}(\beta_v a)}\right\}$$

$$\{\cos[(2k+1)\theta_i]+\sin[(2k+1)\theta_i]\}$$

$$+\frac{\sqrt{2}}{2}\frac{1}{m_1-2}\sum_{k=0}^{M}\sum_{v=1}^{\infty}A_{kv}^{(1)}\frac{1}{\beta_v^2 a}\left\{\frac{K'_{2k}(\beta_v\xi_i)}{K_{2k}(\beta_v a)}+\frac{2k}{\xi_i}\frac{K_{2k}(\beta_v\xi_i)}{K_{2k}(\beta_v a)}\right\}$$

$$\{\cos[(2k-1)\theta_i]-\sin[(2k-1)\theta_i]\}$$

$$-\frac{2}{m_1-2}\sum_{k=0}^{M}\sum_{v=1}^{\infty}A_{kv}^{(1)}\frac{1}{\beta_v^2 a}\frac{K'_{2k}(\beta_v\xi^*)}{K_{2k}(\beta_v a)}\cos(\frac{k\pi}{2})$$

$$+\frac{\sqrt{2}}{4}\sum_{k=0}^{M-1}\left[\frac{3m_1-1}{m_1+1}+2k+1\right](\frac{a}{\xi_i})^{2k+1}g_k^*\{\cos[(2k+1)\theta_i]+\sin[(2k+1)\theta_i]\}$$

$$+\frac{\sqrt{2}}{4}\sum_{k=1}^{M}(2k-1)(\frac{a}{\xi_i})^{2k-1}g_{k-1}^*\{\cos[(2k+1)\theta_i]+\sin[(2k+1)\theta_i]\}$$

$$+\frac{\sqrt{2}}{4}\sum_{k=1}^{M}\frac{3m_1-1}{m_1+1}(\frac{a}{\xi_i})^{2k-1}g_{k-1}^*\{\cos[(2k-1)\theta_i]-\sin[(2k-1)\theta_i]\}$$

$$+\frac{\sqrt{2}}{6}\frac{1}{m_1+1}(\frac{h}{a})^2\sum_{k=1}^{M}(2k-1)(2k)(\frac{a}{\xi_i})^{2k+1}g_{k-1}^*\{\cos[(2k+1)\theta_i]+\sin[(2k+1)\theta_i]\}$$

$$-\frac{1}{2}\sum_{k=0}^{M-1}\left\{\frac{3m_1-1}{m_1+1}+2k+1\right\}(\frac{a}{\xi^*})^{2k+1}g_k^*\cos(\frac{k\pi}{2})$$

$$-\frac{1}{2}\sum_{k=1}^{M}\left\{\frac{3m_1-1}{m_1+1}+2k+1\right\}(\frac{a}{\xi^*})^{2k-1}g_{k-1}^*\cos(\frac{k\pi}{2})$$

$$-\frac{1}{3}\frac{1}{m_1+1}(\frac{h}{a})^2\sum_{k=1}^{M}(2k-1)(2k)(\frac{a}{\xi^*})^{2k+1}g_{k-1}^*\cos(\frac{k\pi}{2})$$

$$+\frac{\sqrt{2}}{2}\sum_{k=1}^{M}\left(\frac{a}{\xi_i}\right)^{2k+1} e_k^* \{\cos[(2k+1)\theta_i] + \sin[(2k+1)\theta_i]\}$$

$$-\frac{\sqrt{2}}{2}\sum_{k=1}^{M}\left(\frac{\xi_i}{a}\right)^{2k-1} f_k^* \{\cos[(2k-1)\theta_i] - \sin[(2k-1)\theta_i]\}$$

$$-\sum_{k=1}^{M}\left(\frac{a}{\xi^*}\right)^{2k+1} e_k^* \cos\left(\frac{k\pi}{2}\right) + \sum_{k=1}^{M}\left(\frac{\xi^*}{a}\right)^{2k-1} f_k^* \cos\left(\frac{k\pi}{2}\right)$$

$$+\left\{-\frac{\sqrt{2}}{4} A_0^* \left(\frac{a}{\xi_i}\right) + \frac{\sqrt{2}}{2}\frac{\xi_i}{a}\right\}(\cos\theta_i + \sin\theta_i)$$

$$+\frac{A_0^*}{2}\left(\frac{a}{\xi^*}\right) - \left(\frac{\xi^*}{a}\right) = 0 \qquad (4.38)$$

$$\frac{1}{m_1-2}\sum_{k=0}^{M}\sum_{v=1}^{\infty} A_{kv}^{(1)} \left\{\sum_{i=1}^{P} \left\{-\left[2+\frac{4k^2}{(\beta_v a)^2}\right]\frac{K_{2k}(\beta_v\xi_i)}{K_{2k}(\beta_v a)} + \frac{K_{2k}''(\beta_v\xi_i)}{\beta_v^2 K_{2k}(\beta_v a)}\right.\right.$$

$$\left.\left.+\frac{1}{\beta_v^2\xi_i}\frac{K_{2k}'(\beta_v\xi_i)}{K_{2k}(\beta_v a)}\right\}\delta S_i \cos(2k\theta_i)\right\}$$

$$-\frac{1}{2}\frac{1}{m_1-2}\sum_{k=0}^{M}\sum_{v=1}^{\infty} A_{kv}^{(1)} \left\{\sum_{i=1}^{P} \left\{-\frac{K_{2k}''(\beta_v\xi_i)}{\beta_v^2 K_{2k}(\beta_v a)} + \frac{1+4k}{\beta_v^2\xi_i}\frac{K_{2k}'(\beta_v\xi_i)}{K_{2k}(\beta_v a)}\right.\right.$$

$$\left.\left.-\frac{4k(k+1)}{(\beta_v\xi_i)^2}\frac{K_{2k}(\beta_v\xi_i)}{K_{2k}(\beta_v a)}\right\}\delta S_i \sin[(2k+2)\theta_i]\right\}$$

$$+\frac{1}{2}\frac{1}{m_1-2}\sum_{k=0}^{M}\sum_{v=1}^{\infty} A_{kv}^{(1)} \left\{\sum_{i=1}^{P} \left\{-\frac{K_{2k}''(\beta_v\xi_i)}{\beta_v^2 K_{2k}(\beta_v a)} + \frac{1-4k}{\beta_v^2\xi_i}\frac{K_{2k}'(\beta_v\xi_i)}{K_{2k}(\beta_v a)}\right.\right.$$

$$\left.\left.-\frac{4k(k-1)}{(\beta_v\xi_i)^2}\frac{K_{2k}(\beta_v\xi_i)}{K_{2k}(\beta_v a)}\right\}\delta S_i \sin[(2k-2)\theta_i]\right\}$$

$$- \sum_{k=1}^{M} (2k-1)\, g_{k-1}^{*} \left\{ \sum_{i=1}^{P} \left(\frac{a}{\xi_i}\right)^{2k} \delta S_i \cos(2k\theta_i) \right\}$$

$$- \sum_{k=0}^{M-1} (2k+1)\left(\frac{m_1-1}{m_1+1}+k+1\right) g_k^{*} \left\{ \sum_{i=1}^{P} \left(\frac{a}{\xi_i}\right)^{2k+2} \delta S_i \sin[(2k+2)\theta_i] \right\}$$

$$- \sum_{k=1}^{M} (2k-1)k\, g_{k-1}^{*} \left\{ \sum_{i=1}^{P} \left(\frac{a}{\xi_i}\right)^{2k} \delta S_i \sin[(2k+2)\theta_i] \right\}$$

$$- \frac{1}{3}\frac{1}{m_1+1}\left(\frac{h}{a}\right)^2 \sum_{k=1}^{M} (2k-1)(2k)(2k+1)\, g_{k-1}^{*} \left\{ \sum_{i=1}^{P} \left(\frac{a}{\xi_i}\right)^{2k+2} \delta S_i \sin[(2k+2)\theta_i] \right\}$$

$$- \sum_{k=1}^{M} (2k+1)\, e_k^{*} \left\{ \sum_{i=1}^{P} \left(\frac{a}{\xi_i}\right)^{2k+2} \delta S_i \sin[(2k+2)\theta_i] \right\}$$

$$+ \sum_{k=1}^{M} (2k-1)\, f_k^{*} \left\{ \sum_{i=1}^{P} \left(\frac{\xi_i}{a}\right)^{2k-2} \delta S_i \sin[(2k-2)\theta_i] \right\}$$

$$+ \frac{A_0^{*}}{2}\left(\frac{a}{\xi_i}\right)^2 \sin(2\theta_i) = 0 \qquad (4.39)$$

These two linear systems (2.14)-(2.39) can be dealt with by a modified Gaussian elimination method with pivoting. Also double precision is used throughout the numerical analysis because of the high sensitivity of the system.

4.3 Convergence of the Fourier Expansions

The convergence of the Fourier expansions obtained above determines whether the solution approach is a success or a failure. In general, including the problem under consideration, the convergence of the solution is constantly monitored by (i) how well the series coefficients converge and (ii) how well the boundary conditions are satisfied within the specified allowable error.

Many calculations for various parameter combinations have been completed in this thesis. Theoretically speaking, the large linear system (4.14)-(4.39) can be solved by the use of a general numerical scheme with pivoting. However, because in some systems the rate of convergence may be slow, the weighted residual method is also used to eliminate possible ill conditions.

A typical example of the convergent coefficients for three different sets of roots is given in Table 4.1. From the table, it is observed that the coefficients converge slowly and that 200 or 300 roots are sufficient to provide us a solution with the desired accuracy. Figures 4.1 and 4.2 show how well the boundary conditions for the displacement u_r and the stress σ_{rr} are satisfied, at the interface r=a, for three different sets of roots. It is noted that as the number of roots increases, the error on the boundary conditions decreases accordingly.

Table 4.1 The convergence of coefficients with different roots

(ν_1=0.34, ν_2=0.22, μ_2/μ_1=16.67 and a/h=0.05)

The real part of the coefficients $A_\nu^{(1)}$

ν	200 roots case	100 roots case	50 roots case
1	-1.670072099D-3	-1.668732365D-3	-1.664213512D-3
3	-6.191873001D-4	-6.188071283D-4	-6.163917258D-4
5	-3.247367113D-4	-3.245851946D-4	-3.225395566D-4
7	-1.963034675D-4	-1.962027912D-4	-1.941973547D-4
9	-1.298964396D-4	-1.297835499D-4	-1.277112265D-4
11	-9.167471579D-5	-9.152634067D-5	-8.934720024D-5
13	-6.790033712D-5	-6.770911603D-5	-6.540784728D-5
15	-5.220702888D-5	-5.197208492D-5	-4.954277114D-5
17	-4.134962215D-5	-4.107248438D-5	-3.851230089D-5

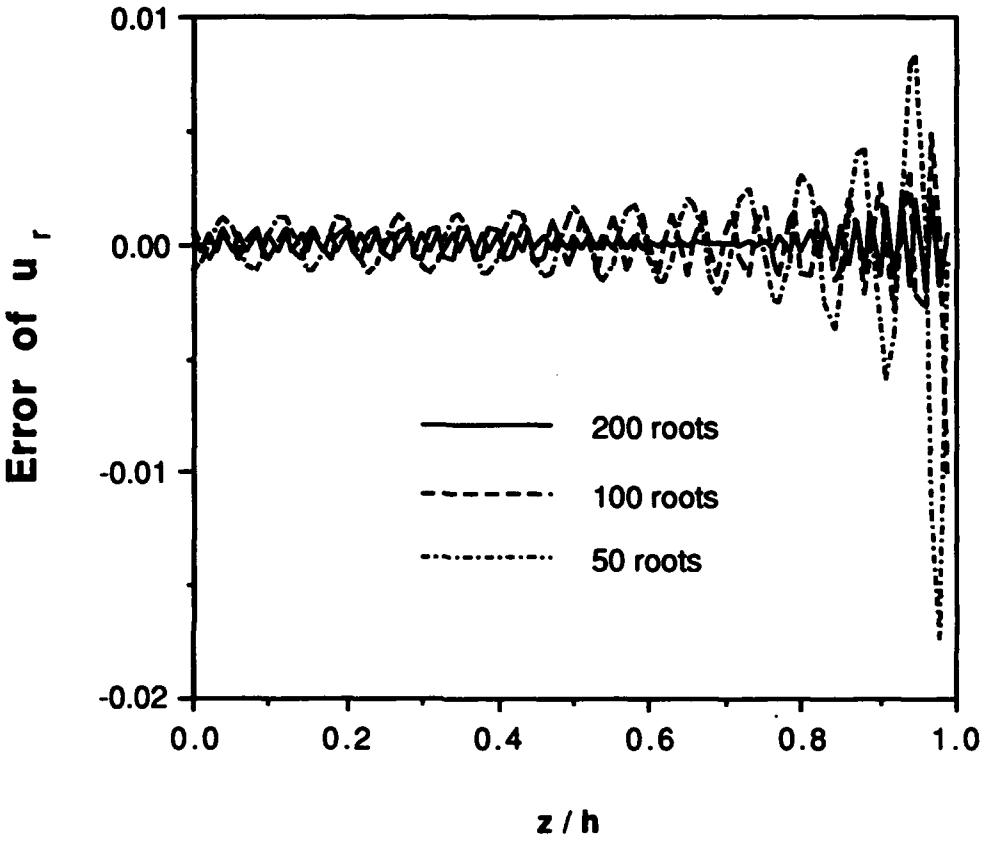

Figure 4.1. Error of boundary condition at r=a for u_r where v_1=0.34, v_2=0.22, μ_2/μ_1=16.67 and a/h=0.05

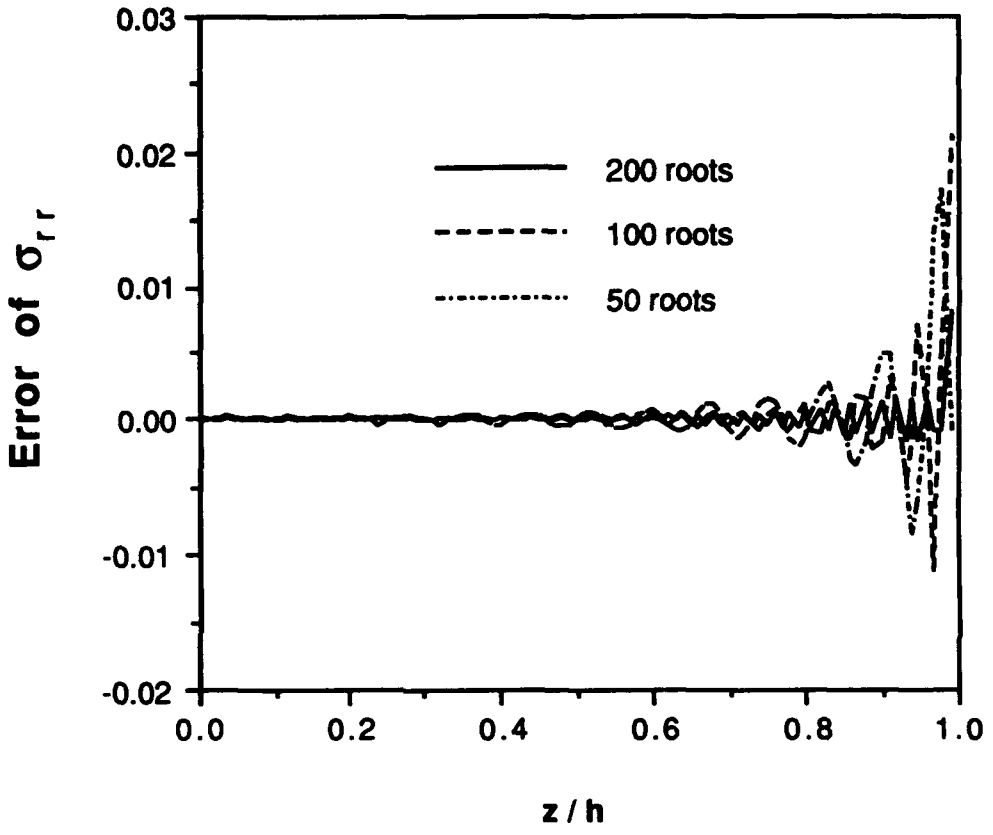

Figure 4.2. Error of boundary condition at r=a for σ_{rr}

where v_1=0.34, v_2=0.22, μ_2/μ_1=16.67 and a/h=0.05

CHAPTER 5

RESULTS AND DISCUSSION

5.1 One Fiber Model

Once the coefficients have numerically been determined from equations (4.3)-(4.8), the displacements and stresses may then be computed at any point in the plate. In the case of one fiber, the displacement and stress fields are independent of θ because of symmetry. Thus, the displacement u_θ and stresses $\tau_{r\theta}$, $\tau_{\theta z}$ will be automatically zero. On the other hand, because the ratio of thermal expansion coefficients $\alpha^{(2)}/\alpha^{(1)}$ presents a linear action to the displacement and stress field, the ratio $\alpha^{(2)}/\alpha^{(1)}=0.075$ is fixed throughout the discussion in this thesis. It is assumed in the thesis that the residual stresses arose from thermal contraction mismatch upon cooling.

Because the residual stresses are induced by the mismatch of the different material properties of the fiber and matrix, such as the differences of the thermal expansion coefficients, the shear moduli and Poisson's ratios, the interface of fiber and matrix is of greatest practical interest. Plots at r=a are given from Fig.5.1 to Fig.5.18 for the displacements and stresses as functions of z. In order to examine how the material properties affect the field of displacement and stress, two different ratios of shear moduli and Poisson's ratios are chosen to represent two practical composite materials. One is the glass fiber/epoxy matrix composite with a shear moduli ratio of $\mu_2/\mu_1=16.67$ and Poisson's ratios of $v_1=0.34$, $v_2=0.22$. The other is boron fiber/aluminum matrix composite with the shear moduli ratio of $\mu_2/\mu_1=6.3$ and Poisson's ratios $v_1=0.2$, $v_2=0.33$. Each plot here consists of three curves corresponding to different geometrical ratios a/h. Superscripts areusedtodistinguish

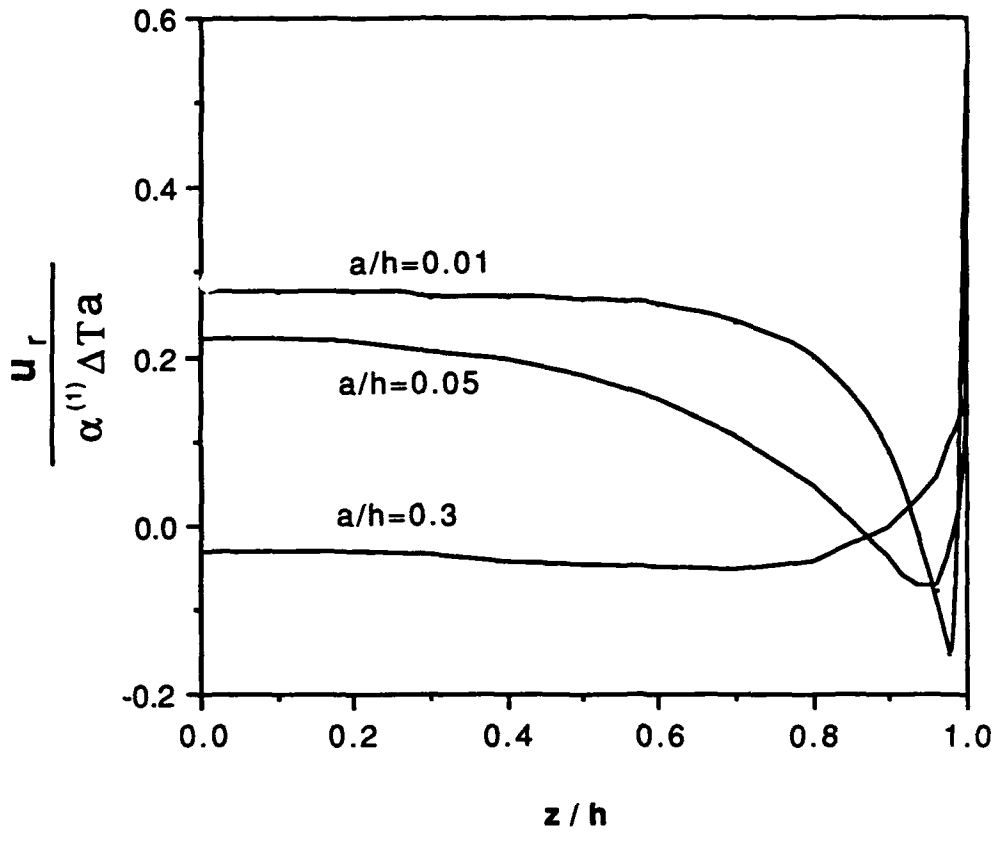

Figure 5.1. Displacement u_r at r=a vs z/h for one fiber model where v_1=0.34,v_2=0.22,μ_2/μ_1=16.67

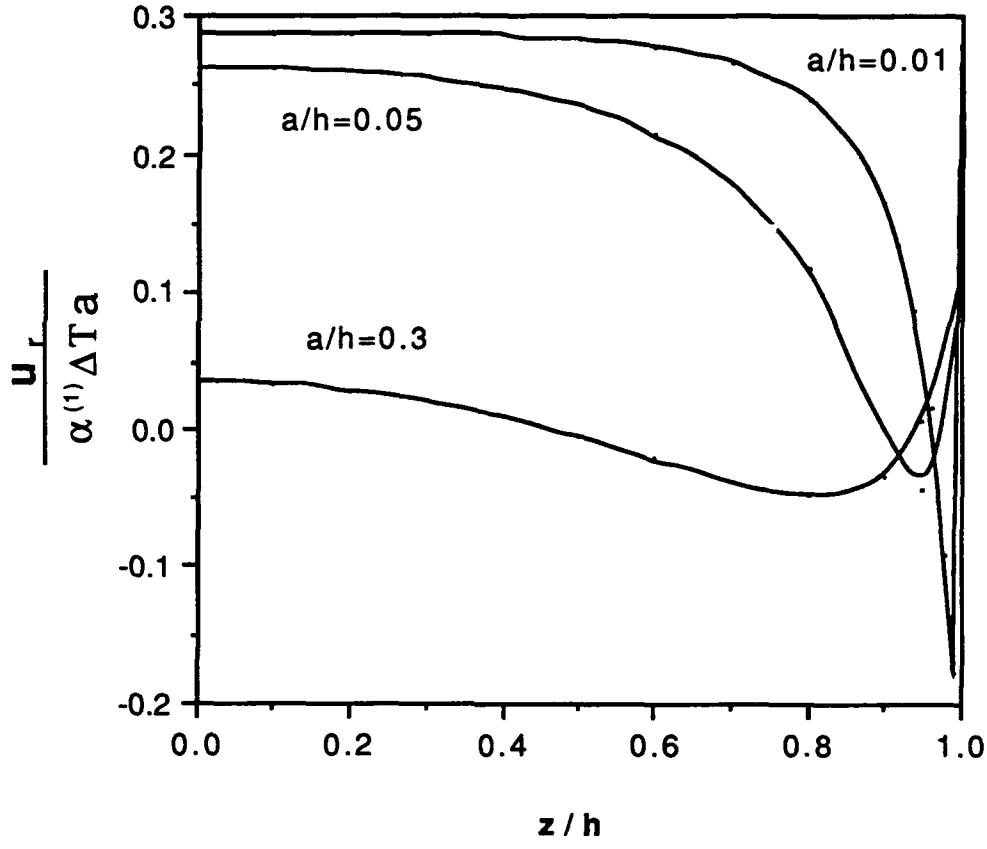

Figure 5.2. Displacement u_r at r=a vs z/h for one fiber model where v_1=0.2,v_2=0.33,μ_2/μ_1=6.3

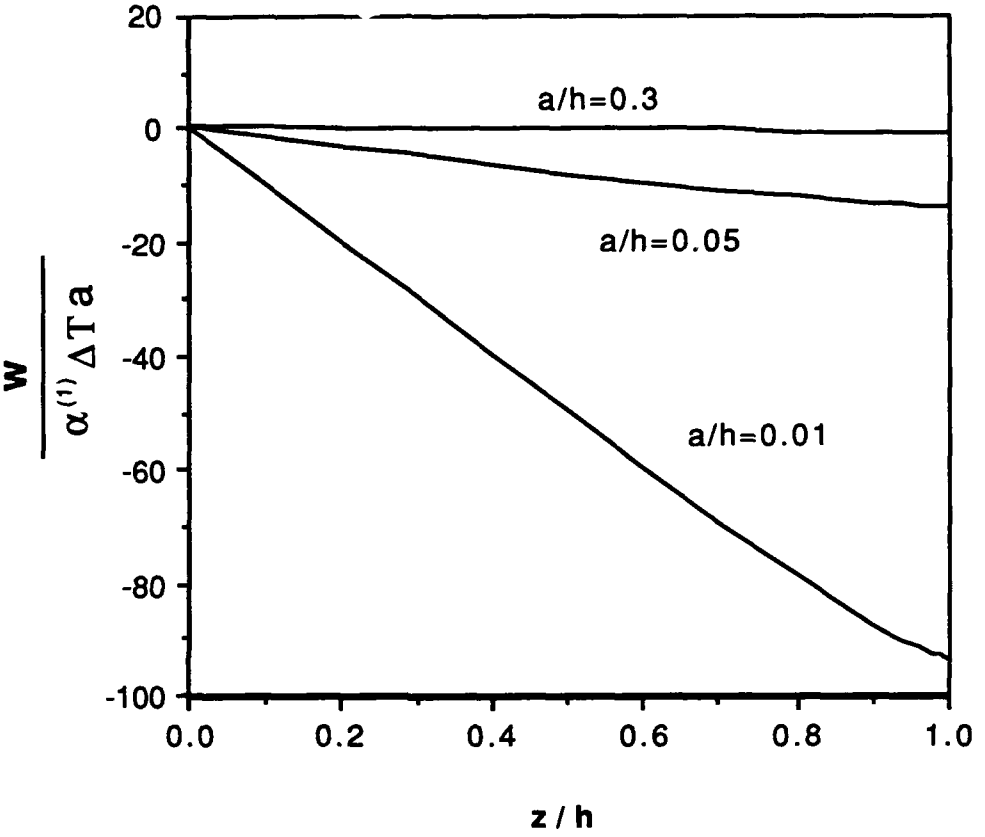

Figure 5.3. Displacement w at r=a vs z/h for one fiber model where v_1=0.34,v_2=0.22,μ_2/μ_1=16.67

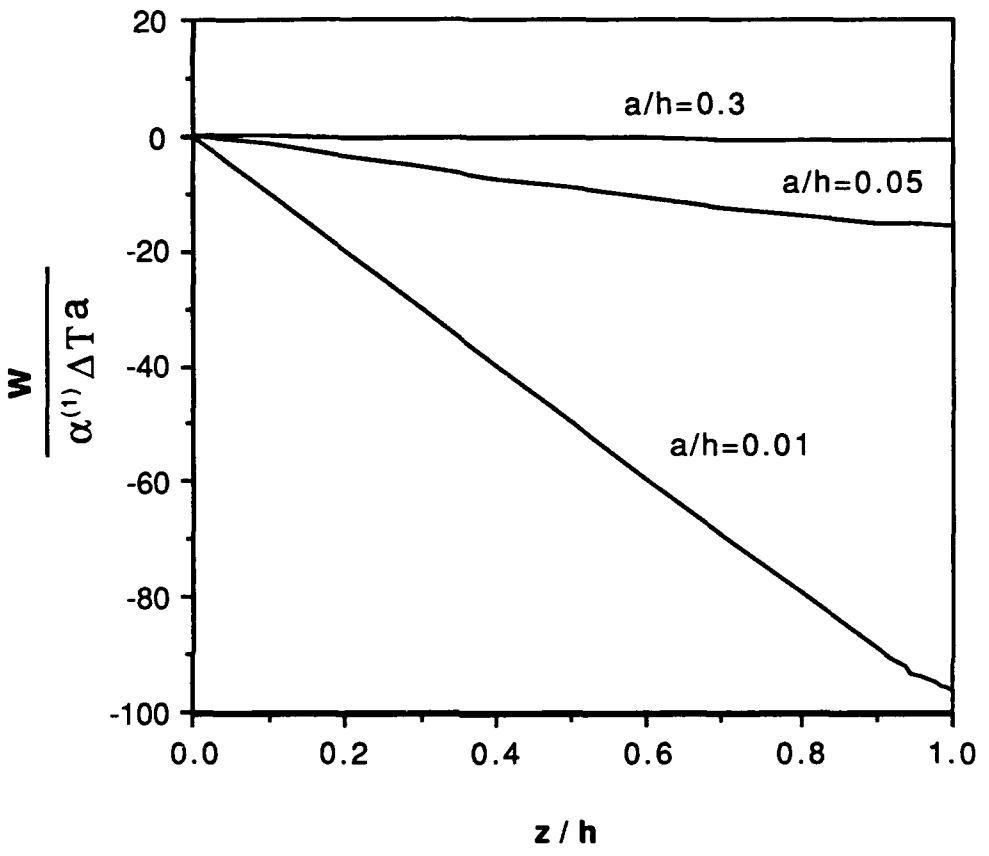

Figure 5.4. Displacement w at r=a vs z/h for one fiber model where v_1=0.2,v_2=0.33,μ_2/μ_1=6.3

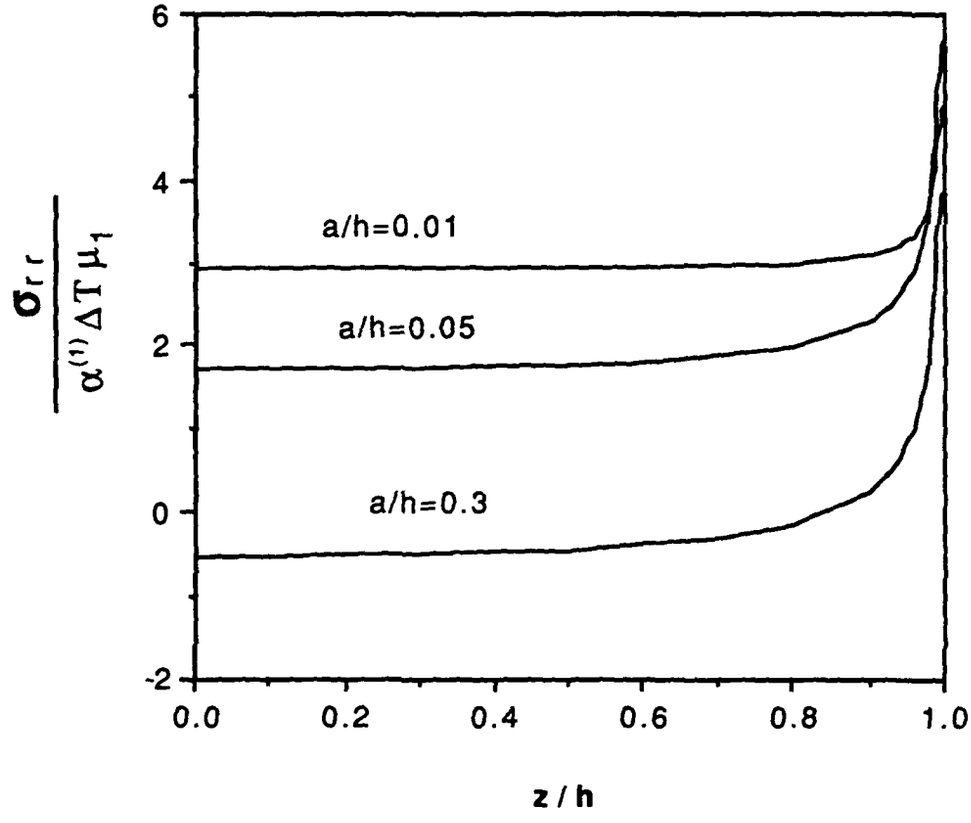

Figure 5.5. Stress σ_{rr} at r=a vs z/h for one fiber model

where v_1=0.34,v_2=0.22,μ_2/μ_1=16.67

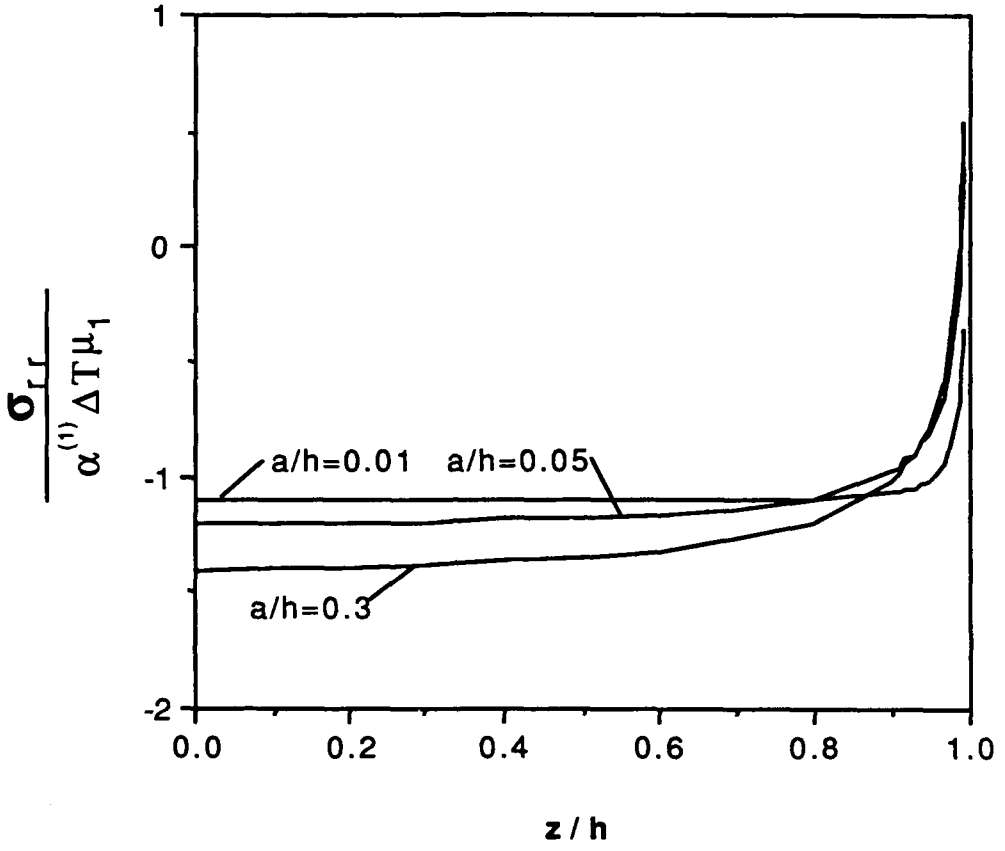

Figure 5.6. Stress σ_{rr} at r=a vs z/h for one fiber model where v_1=0.2,v_2=0.33,μ_2/μ_1=6.3

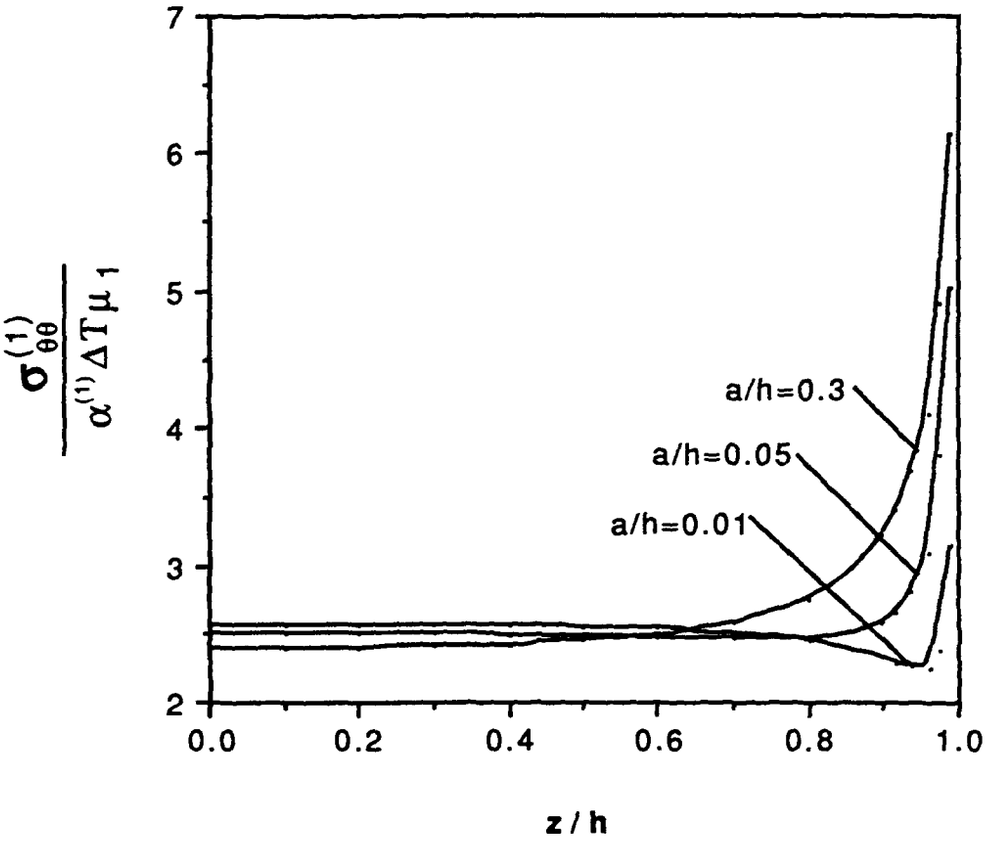

Figure 5.7. Stress $\sigma_{\theta\theta}^{(1)}$ at r=a vs z/h for one fiber model where v_1=0.34,v_2=0.22,μ_2/μ_1=16.67

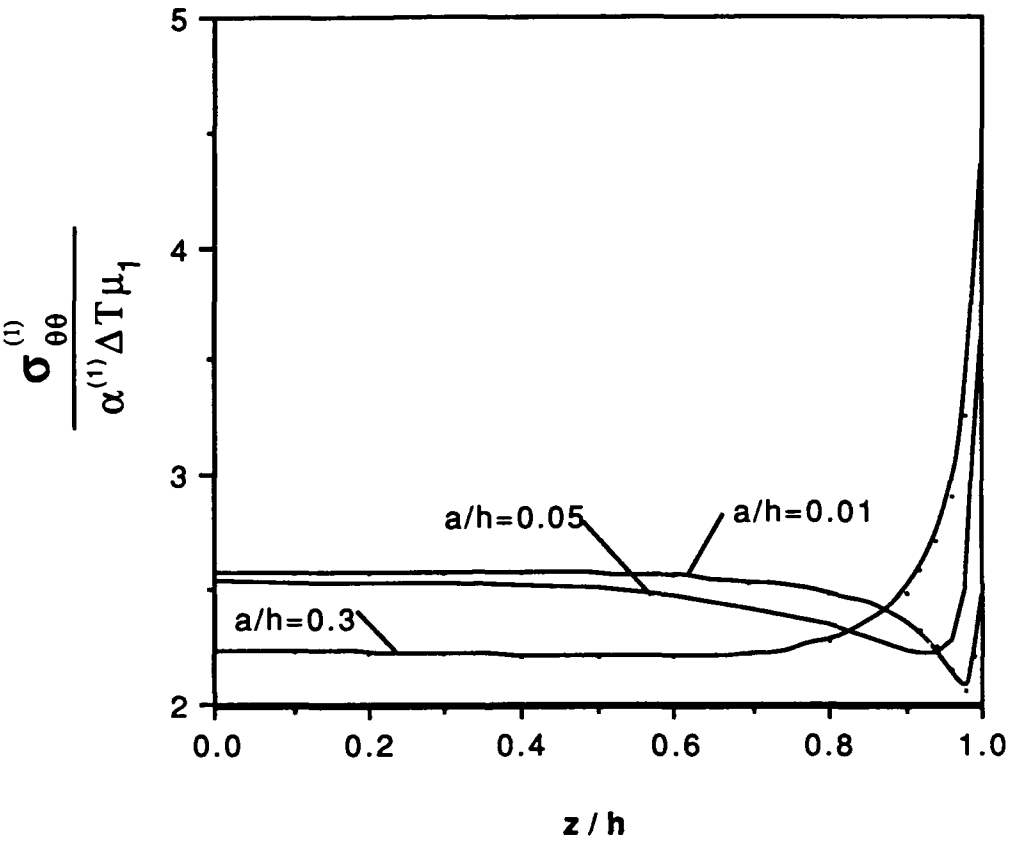

Figure 5.8. Stress $\sigma_{\theta\theta}^{(1)}$ at r=a vs z/h for one fiber model where $v_1=0.2, v_2=0.33, \mu_2/\mu_1=6.3$

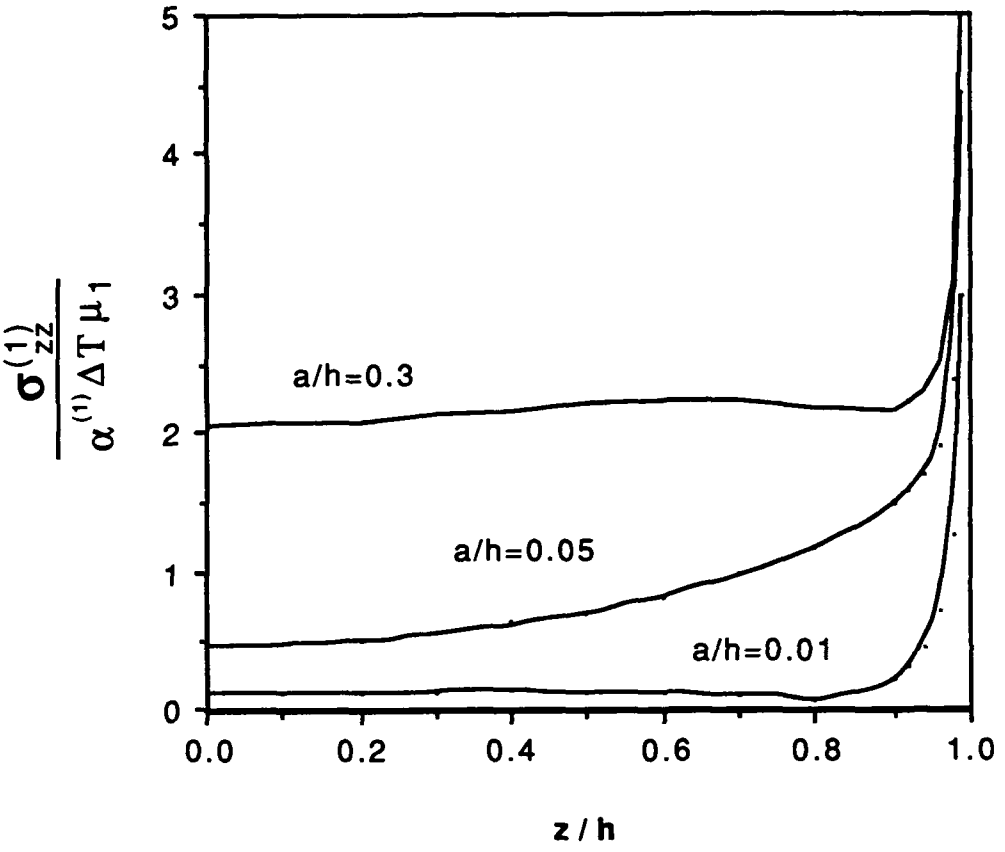

Figure 5.9. Stress $\sigma_{zz}^{(1)}$ at r=a vs z/h for one fiber model where v_1=0.34,v_2=0.22,μ_2/μ_1=16.67

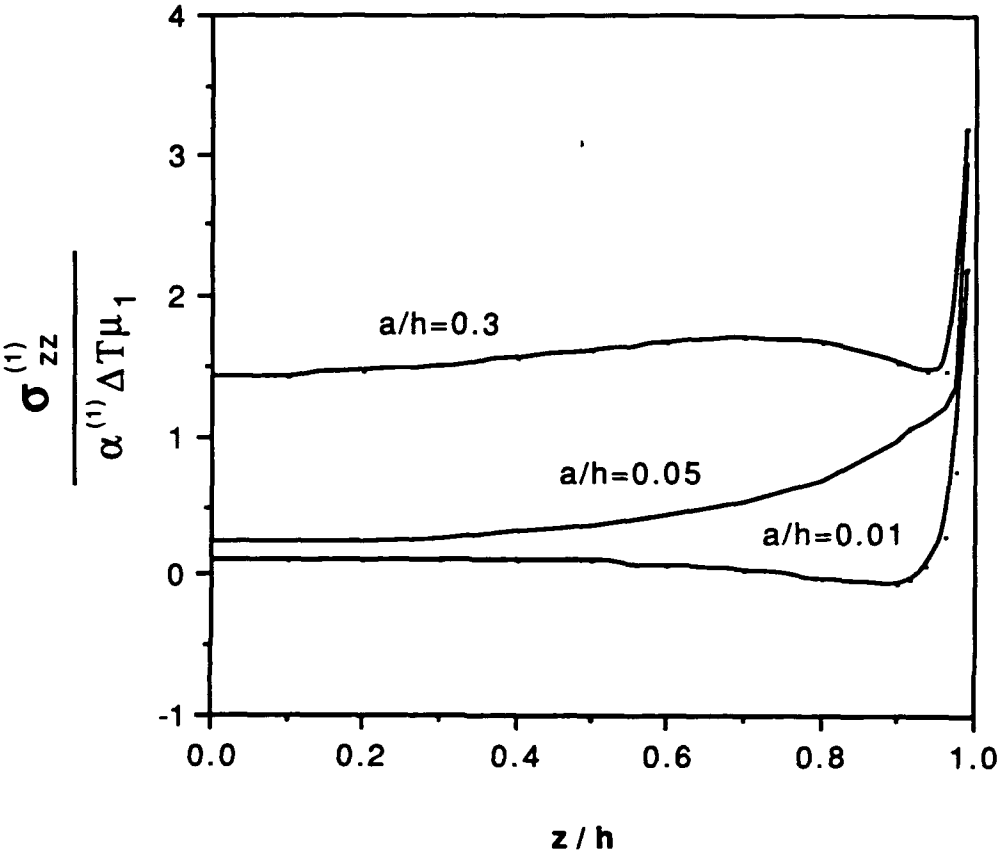

Figure 5.10. Stress $\sigma_{zz}^{(1)}$ at r=a vs z/h for one fiber model where $\nu_1=0.2, \nu_2=0.33, \mu_2/\mu_1=6.3$

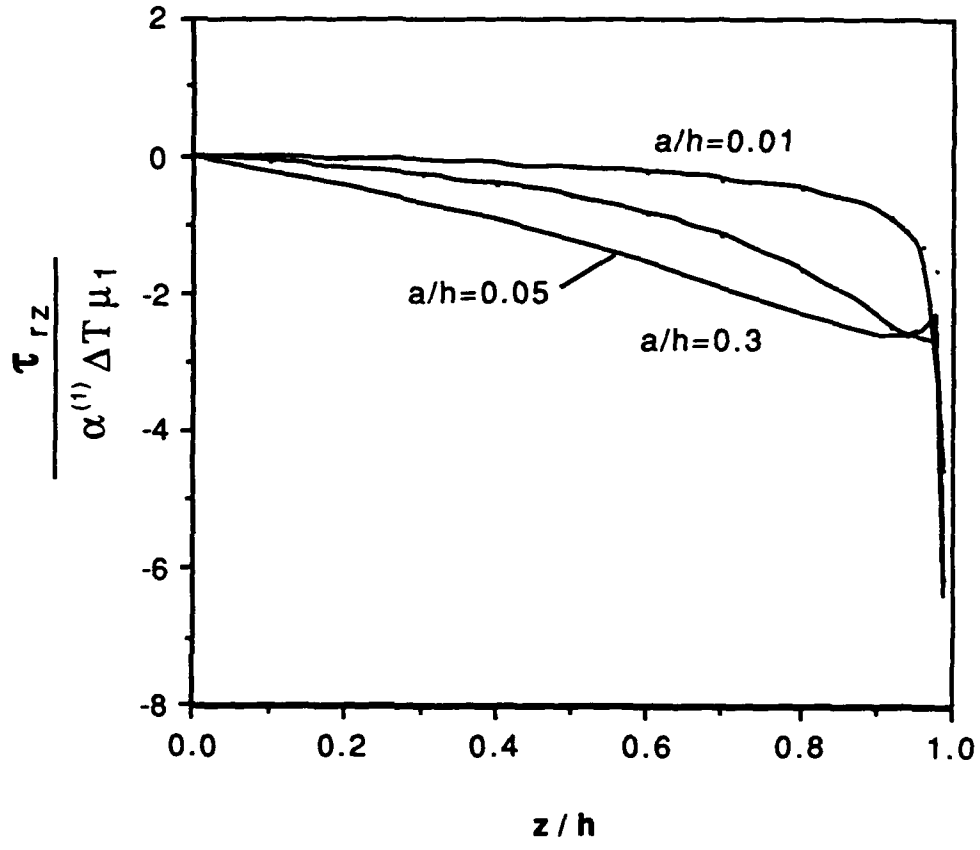

Figure 5.11. Stress τ_{rz} at r=a vs z/h for one fiber model where ν_1=0.34,ν_2=0.22,μ_2/μ_1=16.67

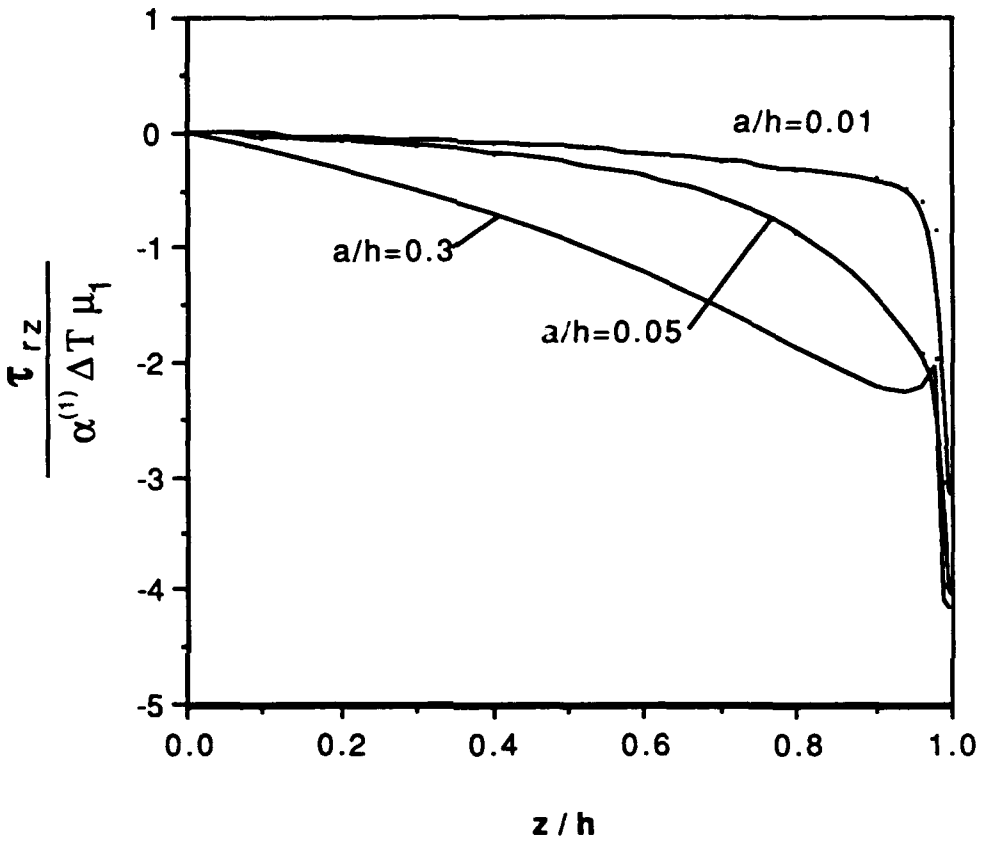

Figure 5.12. Stress τ_{rz} at r=a vs z/h for one fiber model where v_1=0.2,v_2=0.33,μ_2/μ_1=6.3

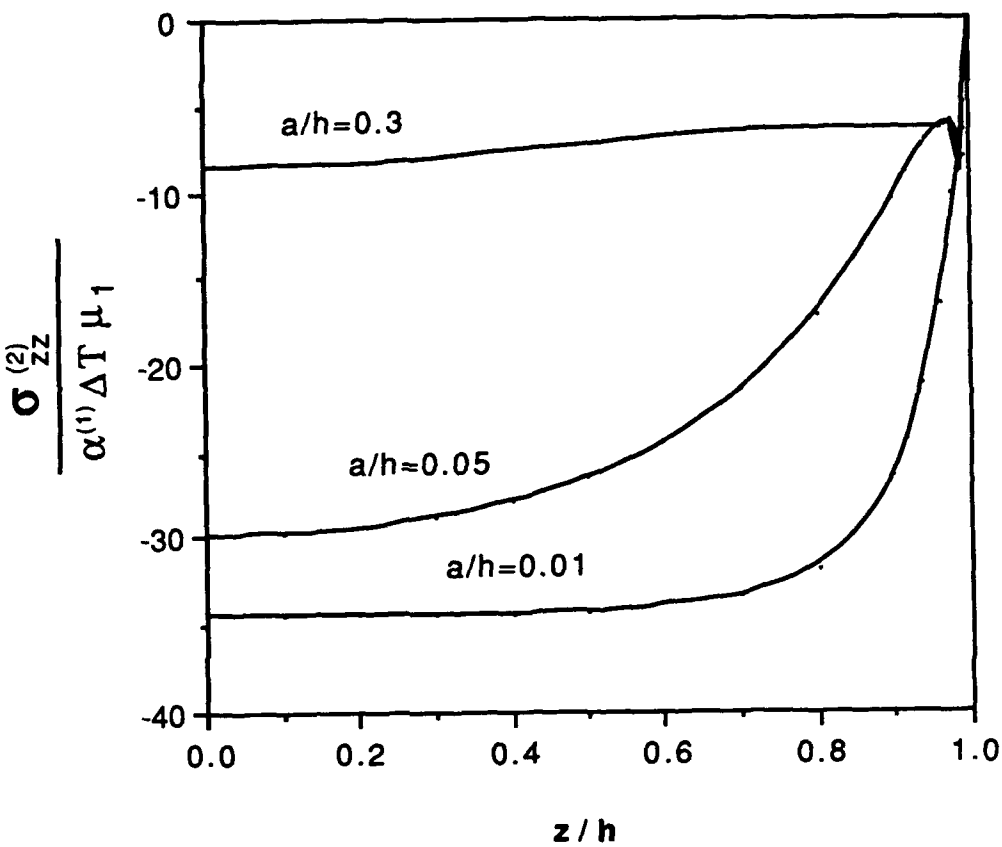

Figure 5.13. Stress $\sigma_{zz}^{(2)}$ at r=a vs z/h for one fiber model where v_1=0.34,v_2=0.22,μ_2/μ_1=16.67

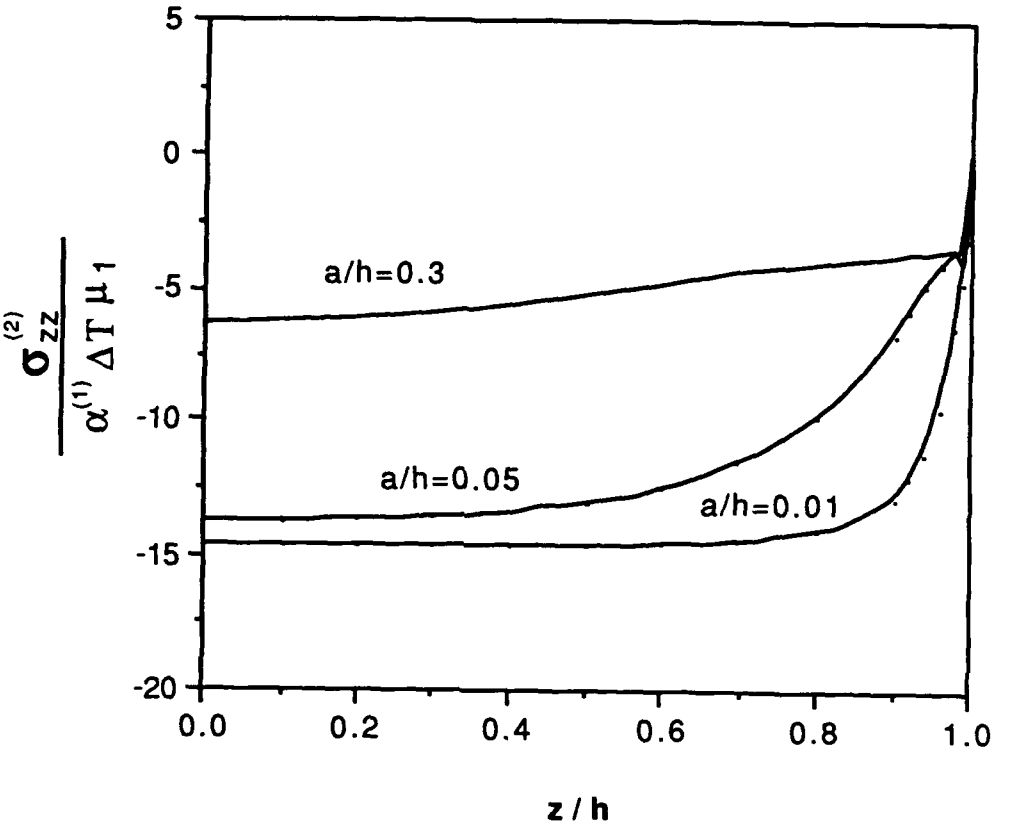

Figure 5.14. Stress $\sigma_{zz}^{(2)}$ at r=a vs z/h for one fiber model where v_1=0.2,v_2=0.33,μ_2/μ_1=6.3

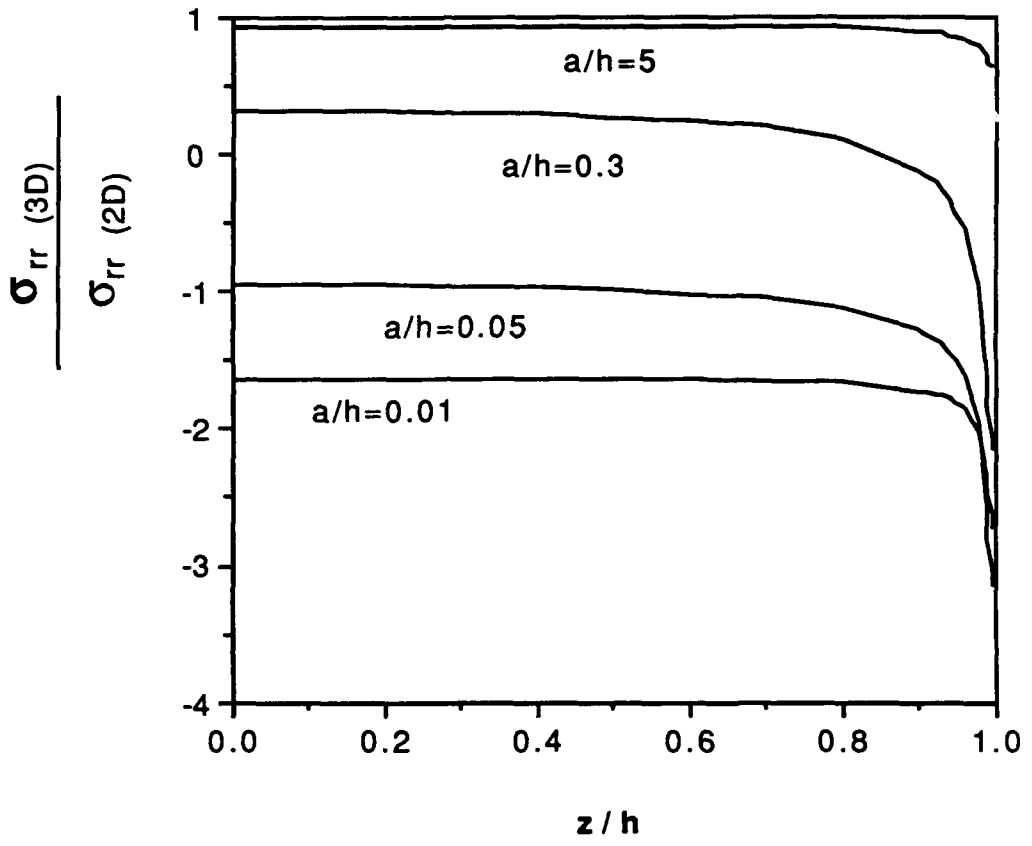

Figure 5.15. The ratio of stress σ_{rr} (3D/2D) at r=a vs z/h for one fiber model where v_1=0.34,v_2=0.22,μ_2/μ_1=16.67

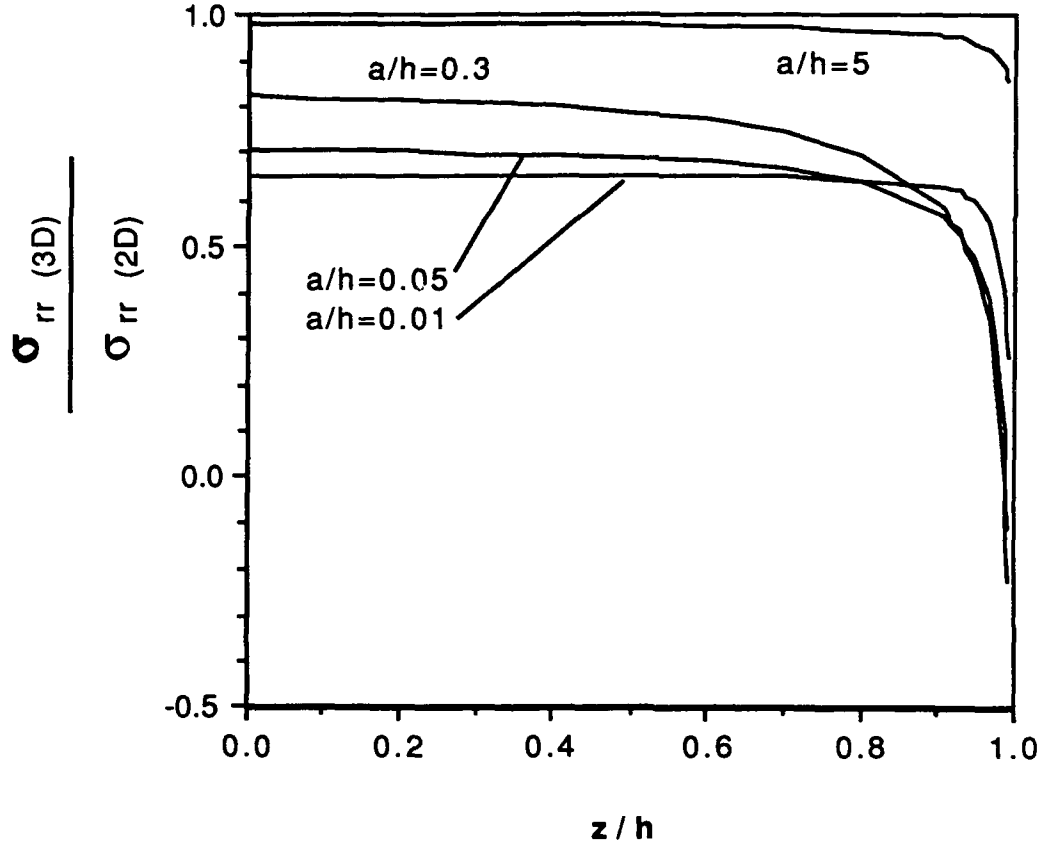

Figure 5.16. The ratio of stress σ_{rr} (3D/2D) at r=a vs z/h for one fiber model where v_1=0.2,v_2=0.33,μ_2/μ_1=6.3

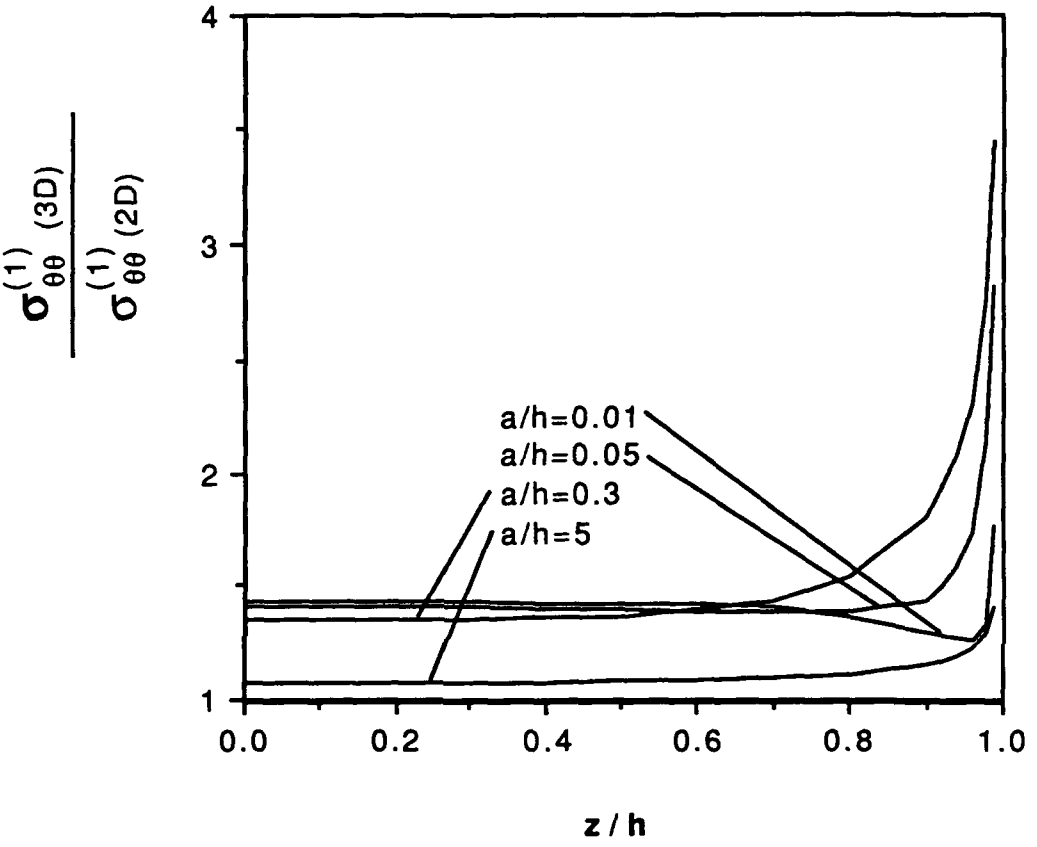

Figure 5.17. The ratio of stress $\sigma_{\theta\theta}^{(1)}$ (3D/2D) at r=a vs z/h for one fiber model where v_1=0.34,v_2=0.22,μ_2/μ_1=16.67

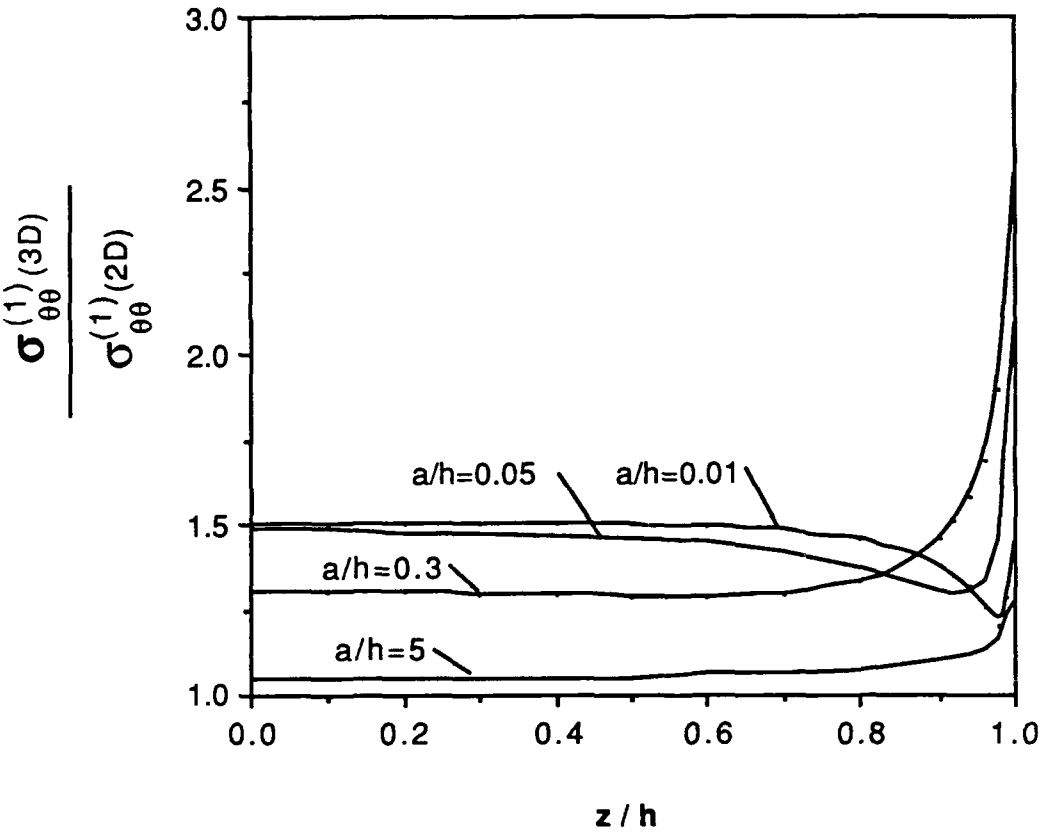

Figure 5.18. The ratio of stress $\sigma_{\theta\theta}^{(1)}$ (3D/2D) at r=a vs z/h for one fiber model where v_1=0.2,v_2=0.33,μ_2/μ_1=6.3

whether the displacement or stress is in the fiber or in the matrix. If the displacement or the stress is the same at the interface r=a, then the superscripts will be omitted.

Figs. 5.1-5.2 show the displacement u_r vs z/h for two different composites. The positive value of u_r in most of the center region indicates that as the plate cools down, both fiber and matrix will shrink in the radial direction, which implies a negative displacement u_r. On the other hand, the thermal expansion mismatch between fiber and matrix will induce a large compressive stress $\sigma_{zz}^{(2)}$ in the fiber, which forces the fiber to expand in the radial direction. For most thick plates, this effect plays a much more important role than the radial shrinkage of the fiber itself. It is interesting to note that in the case of a thin plate (large ratio of a/h), the displacement presents a negative value at the center region of the plate (see Fig. 5.1 for a/h=0.3 case). This result seems reasonable if one more closely examines the limit case. Suppose the plate is very thin (i.e., large a/h case). A lesser compressive stress $\sigma_{zz}^{(2)}$ will be induced in the fiber to expand it in the radial direction and the shrinkage itself in the radial direction due to the decrease of the temperature will be the governing factor, which leads the displacement to be a negative value over a wide span of the center region. In the vicinity of the free surface, the slope of each curve increases rapidly because of the presence of a stress singularity at z=h, which will be discussed later. It is also interesting to note that as the a/h increases (the thin plate case), the curve around the free surface tends to smooth. Because as the plate tends to be thinner, the interaction of the fiber and the matrix in the axial direction tends to be weaker, which implies that the displacement u_r tends to be a constant along the thickness.

Displacement w is shown in Figs. 5.3 and 5.4. These curves start from zero (center layer must be zero because of the symmetry in z) and they are almost the linear functions of z. Only in the vicinity of the free surface, these curves present nonlinear properties. As the ratio of a/h decreases (thick plate case), the value of w becomes much larger in comparison to those obtained for large a/h ratios. In the case of a/h=0.01, for instance, suppose the inclusion is made of the same material as the matrix (continuous plate). No mismatch

occurs under the change of temperature and the value of this displacement w at free surface

z=h will be found easily as -100. From Fig 5.3, however, the curve of a/h=0.01 attains the value of -90. This difference suggests, therefore, that the inclusion tries to resist matrix shrinkage along the axial direction.

The plot of the stress σ_{rr} in Fig. 5.5 shows that each curve looks parallel at a wide span of the center region and there is only a slight change in the magnitude of the stress. Near the surface of the plate, the stress jumps suddenly to a large value. In view of some previous work (Folias, 1989), a stress singularity is present in the neighborhood of the intersection of the fiber and the free surface, i.e., at r=a and z=h. Therefore the numerical results shown in Fig. 5.5 may not be reliable near z=h because the presence of singularities slows down the convergence of the series representation of the stresses near the singularity point. Be that as it may, the curves show the trend of the stress at z=h and confirm Folias's conclusions [11]. It may also be noted that as the shear moduli ratio changes from μ_2/μ_1=16.67 to μ_2/μ_1=6.3 (see Fig. 5.6) the radial stress becomes negative over a wide span of the center region and the curves no longer appear to be parallel, but mix together at about four-fifths the span of the thickness. The reason for this may be explained as the following: the radial stress σ_{rr} induced by thermal contraction mismatch consists of two different parts. First, in the radial direction, it is observed that the inclusion presents a resistance to the shrinkage of the matrix, which leads to a negative part of the radial stress. On the other hand, the inclusion also functions as a resistance to the shrinkage of the matrix in the axial direction, which induces a positive part of the radial stress in the matrix. The final sign of the radial stress σ_{rr} depends on which part of the effects is larger. From Figs. 5.5 and 5.6 one can see that as the case of shear moduli ratio μ_2/μ_1 increased or the ratio of a/h decreased, the second effect will be the controlling factor to the radial stress σ_{rr}.

The profiles of the stress $\sigma_{\theta\theta}^{(1)}$ in the matrix (see Fig. 5.7) are very close at the center region for different ratios of a/h. Then they increase rapidly near the free surface due to the presence of a stress singularity. Fig. 5.8 shows another case representing a different material. Both plots show that the stress $\sigma_{\theta\theta}^{(1)}$ attains positive values for various a/h and μ_2/μ_1 ratios. This result is expected because both kinds of effects explained for the radial stress σ_{rr} above are also valid for the stress $\sigma_{\theta\theta}^{(1)}$. The only difference for the circumferential stress $\sigma_{\theta\theta}^{(1)}$ is that both parts of the effects lead to positive values.

Perhaps it may be appropriate here to note that previous research by Delale (1988) focused on a 2-D consideration [36]. As for the plane stress case, the stress $\sigma_{\theta\theta}^{(1)}$ presents a positive value and the stress σ_{rr} presents the same magnitude but negative value as the stress $\sigma_{\theta\theta}^{(1)}$ in his paper. Both the stresses are constants along the thickness of the plate. So the conclusion is clear, that is, a through the thickness crack will initiate at the fiber/matrix interface in the radial direction as the temperature cools down to a certain degree. Based on his solution, if the plate is thick enough, here a real important fact has been neglected, that is the effect of mismatch of the fiber and matrix in the axial direction. On the basis of 3-D considerations as discussed in this thesis, a crack will most likely initiate at the stress singularity point near the free surface and compare the plots of stress σ_{rr} with the plots of stress $\sigma_{\theta\theta}^{(1)}$ from Figs. 5.5 to 5.7, it is difficult to conclude which stress is the maximum because it depends on the ratios of a/h and μ_2/μ_1. One may focus on the central region of the plate, in the case of a/h=0.01 and μ_2/μ_1=16.67, the stress σ_{rr} is larger than the stress $\sigma_{\theta\theta}^{(1)}$. In the case of a/h=0.05 and the case of a/h=0.3, however, the stress $\sigma_{\theta\theta}^{(1)}$ becomes the maximum stress. This means that the direction of the crack initiation is a function of the ratio a/h and of the shear moduli ratio μ_2/μ_1.

The plots seen in Fig. 5.9 and Fig. 5.10 show a sharp increase of the stress $\sigma_{zz}^{(1)}$ for the plate in the vicinity of z=h. As the ratio of a/h decreases, the central region of the plate may not take vertical load (see curves with a/h=0.01). As the ratio of a/h increases, the stress level also increases. In addition, after comparing the plot of Fig. 5.9 with the plot of

Fig. 5.10, one can note that the curves corresponding to μ_2/μ_1=16.67 show a higher stress level than those corresponding to μ_2/μ_1=6.3. The implication of this is that a higher ratio ofμ_2/μ_1 will induce higher mismatch and as a result it will translate a larger vertical stress to the plate.

The shear stress τ_{rz} (see Fig. 5.11- 5.12) starts from zero at the center of the plate and then increases in absolute value as one travels along the interface. A sudden jump of this stress near the point z=h is also observed and may very well suggest why a crack is most likely to initiate at such regions. The negative sign means that the shear stress will always be opposing the direction of the axial stress $\sigma_{zz}^{(2)}$ of the inclusion in order to satisfy the equilibrium in the axial direction for the fiber.

The vertical stress $\sigma_{zz}^{(2)}$ in the fiber presents a negative value in any circumstance because the shrinkage of the matrix in the axial direction is much larger than the shrinkage of the fiber and it will pull the fiber down in order to satisfy the perfect boundary condition at the interface. The small ratio of a/h will induce a large axial compressive stress in the fiber, which increases further as the ratio of μ_2/μ_1 also increases. The maximum compressive axial stress is located at the center of the fiber length (i.e., z=0). It is interesting to compare the curves of $\sigma_{zz}^{(1)}$ with the curves of $\sigma_{zz}^{(2)}$, which will show us a dramatic situation: as the thickness of the plate increases (i.e., small a/h), the axial stress in the matrix decreases while the axial stress in the fiber increases rapidly, which suggests, therefore, that the gap of the stress discontinuity at the interface will increase. Thus, the ratio of a/h may be used to control the stress distribution between the fiber and the matrix.

The comparisons of current solutions with the solutions of Delade [36] (based on 2D plane stress consideration) are shown in Fig.5.15 to Fig. 5.18. One is able to extract directly from those plots that as the thickness of the plate decreases (i.e., a/h increases), the 2-D solution is recovered for both radial stress and circumferential stress. This conclusion can be proved easily from the equations (4.3)-(4.8). Readers may note that as the thickness

of plate increases, the ratio of radial stress $\sigma_{rr}(3D)/\sigma_{rr}(2D)$ decreases (<1) whereas the ratio of circumferential stress $\sigma_{\theta\theta}(3D)/\sigma_{\theta\theta}(2D)$ increases (>1).

5.2 Periodic Fibers Model

In as much as, in practice, the composite plate is not embedded with only one fiber, it is desirable now to extend the model to a more general case where an array of periodic fibers is introduced to embed into the matrix. As for this periodic fibers model, all the displacements and stresses will be θ-dependent due to the interaction of adjacent fibers. A new ratio a/b (the ratio of fiber radius to separation distance between adjacent fibers) is introduced here to correspond to the fiber volume fraction v_f. The displacement u_θ and the stresses $\tau_{r\theta}$, $\tau_{\theta z}$ are no longer zero here but they are still not the important factors compared with the other ones. Therefore, they will not be discussed in this thesis.

The shear moduli ratio μ_2/μ_1 used here is fixed at 16.67 throughout the discussion. Several different geometrical ratios a/b are chosen: they are a/b=0.55, a/b=0.45, a/b=0.32 or a/b=0.2. Another geometrical ratio a/h is taken as before, that is, 0.01, 0.05 and 0.3. The plots are presented in six stages. In the first stage, the displacement and stress fields are shown as the function of θ and are compared with different ratios of a/b. In the second stage, the effect of different plate thickness is investigated where the displacement and stress fields are functions of z. In the third part, the stresses vs a/b are examined. Again, the stress field is presented as a function of z in the fourth part, but here it is used to compare with different ratios of a/b instead of the different ratios of a/h. In the fifth stage, the displacement and stress fields are examined as a function of the radial coordinate r. Finally, the effect of different shear moduli μ_2/μ_1 is investigated.

Fig. 5.19 shows the displacement u_r vs θ at the interface and along the center of the plate. The maximum deformation occurs at θ=0. It is interesting to note that as the ratio a/b increases, the value of the displacement increases at θ=0 and decreases at θ=45. As the ratio a/b decreases (the distance of adjacent fibers increases), the curve tends to be constant in the θ direction, which seems reasonable if one thinks of a limit case a/b$\rightarrow$0, the result of the one fiber model is recovered (θ-independence).

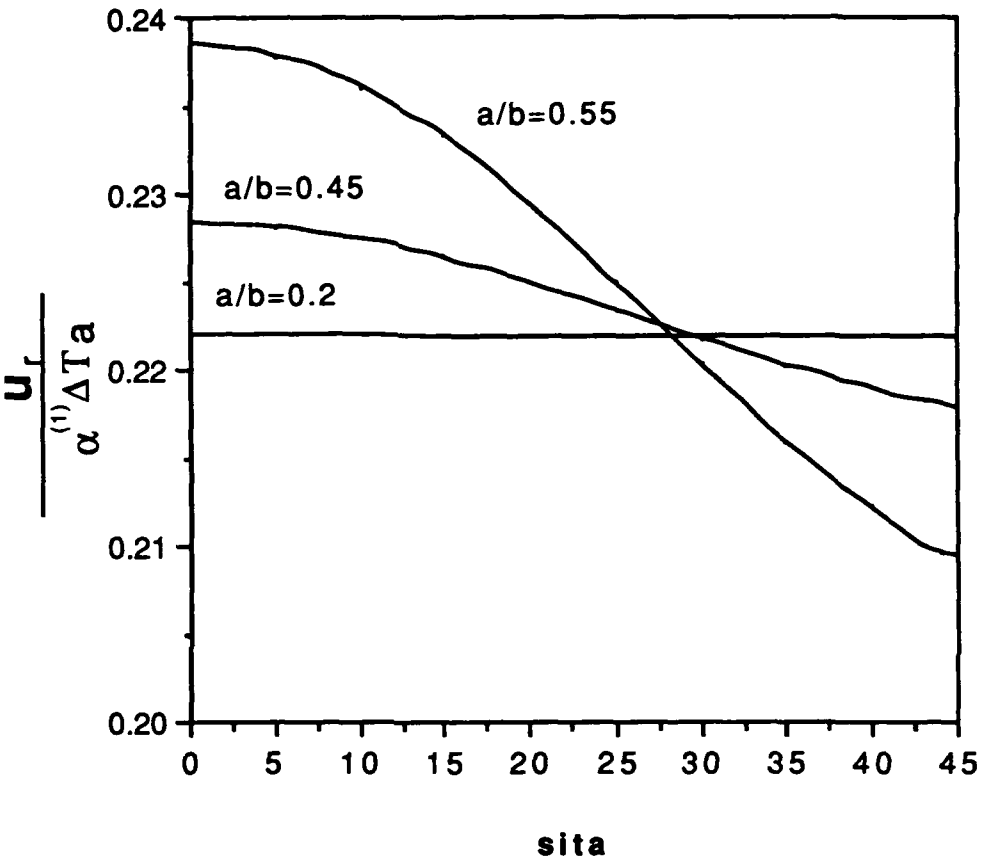

Figure 5.19. Displacement u_r at r=a,z=0 vs θ for periodic fibers model where v_1=0.34,v_2=0.22,μ_2/μ_1=16.67 and a/h=0.05

The displacement w at the free surface is shown in Fig. 5.20. The curves are close at θ=0, then separate in the other side (θ=45). The maximum value in magnitude is also at θ=0 and as the ratio a/b decreases, the displacement also tends to be independent of θ.

The value of radial stress σ_{rr} (Fig. 5.21) increases at one side (θ=0) and decreases at the other side (θ=45) as a/b increases. The circumferential stress $\sigma_{\theta\theta}^{(1)}$ shown in Fig. 5.22 presents a similar condition. The maximum stress for both σ_{rr} and $\sigma_{\theta\theta}^{(1)}$ is located at θ=0 for any different ratios of a/b. Fig.5.23 shows us the profiles of axial stress $\sigma_{zz}^{(1)}$ vs θ. All curves merge together at about θ=45. The maximum axial stress of $\sigma_{zz}^{(1)}$ is also located at θ=0 but the axial stress is small in comparison to the radial stress σ_{rr} and the circumferential stress $\sigma_{\theta\theta}^{(1)}$.

Figs. 5.24 to 5.34 show the displacement and stress fields vs z/h at the interface of fiber and matrix for both θ=0 and θ=45 cases where the ratio a/b is fixed at 0.55. As it has been shown in Figs. 5.19 to 5.23, the maximum stress is located at θ=0. Thus in the subsequent discussion, one need only concentrate on the case θ=0.

The plots of the displacement u_r shown in Figs. 5.24 and 5.25 provide us different profiles for the displacement at θ=0 and θ=45. The variation of the curves seems more regular in the position of θ=0 than the curves of θ=45 because the curves of the former one cross at about the same point (z/h=0.8) where the value of each curve is almost zero. As the ratio a/h decreases, the value of the displacement increases at the central region (0<z/h<0.8), and at the region of 0.8<z/h<1, it increases again but in a negative sense. It may also be noted that for a large ratio of a/h (the case of a/h=0.3), the displacement u_r vanishes in a wide span from the central region and one is able to extract that this displacement tends to be a negative value as the a/h increases again. The displacement w (Figs. 5.26 and 5.27), on the other hand, looks more regular than other components because it presents a linear relationship along the z direction except the values near the free surface.

Figs. 5.28 and 5.29 show the curves of radial stress σ_{rr} at the interface corresponding

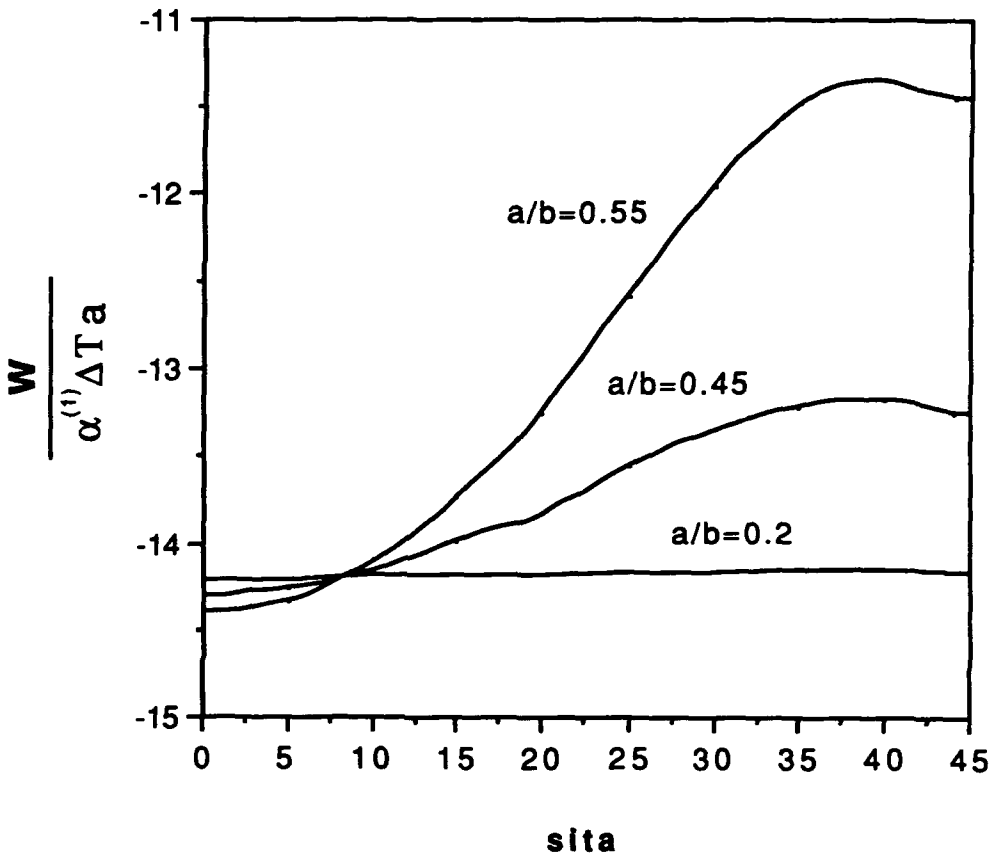

Figure 5.20. Displacement w at r=a, z=h vs θ for periodic fibers model where v_1=0.34,v_2=0.22,μ_2/μ_1=16.67 and a/h=0.05

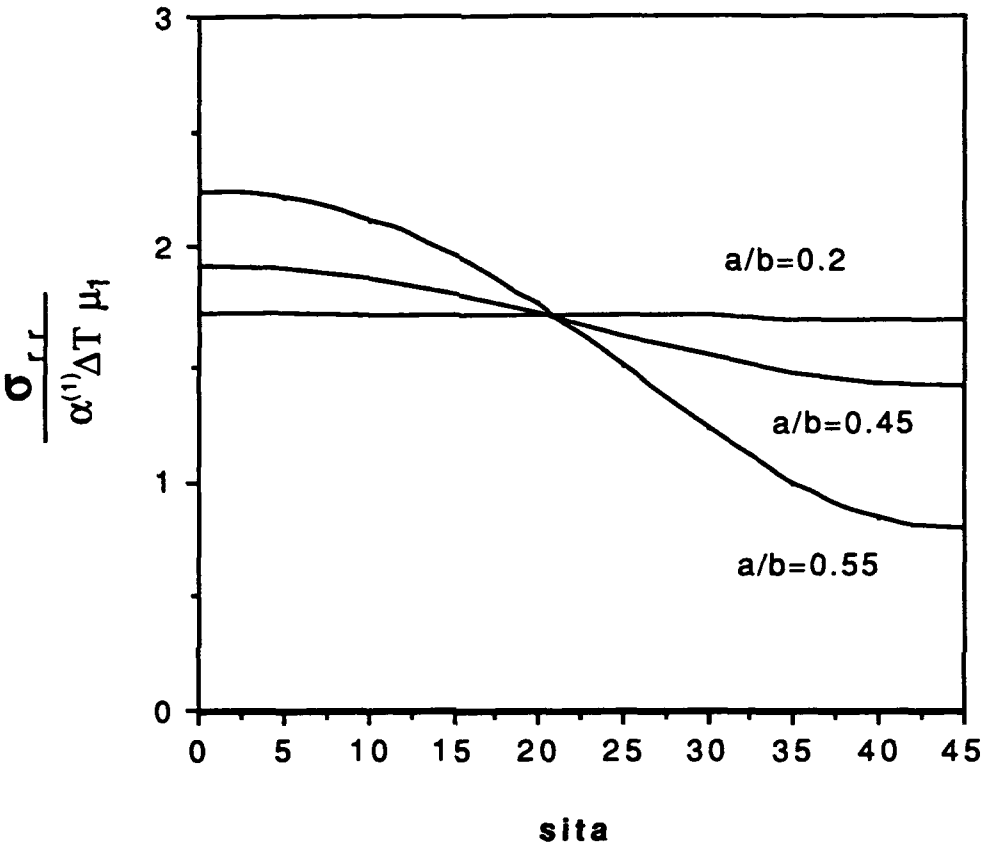

Figure 5.21. Stress σ_{rr} at r=a,z=0 vs θ for periodic fibers model where v_1=0.34,v_2=0.22,μ_2/μ_1=16.67 and a/h=0.05

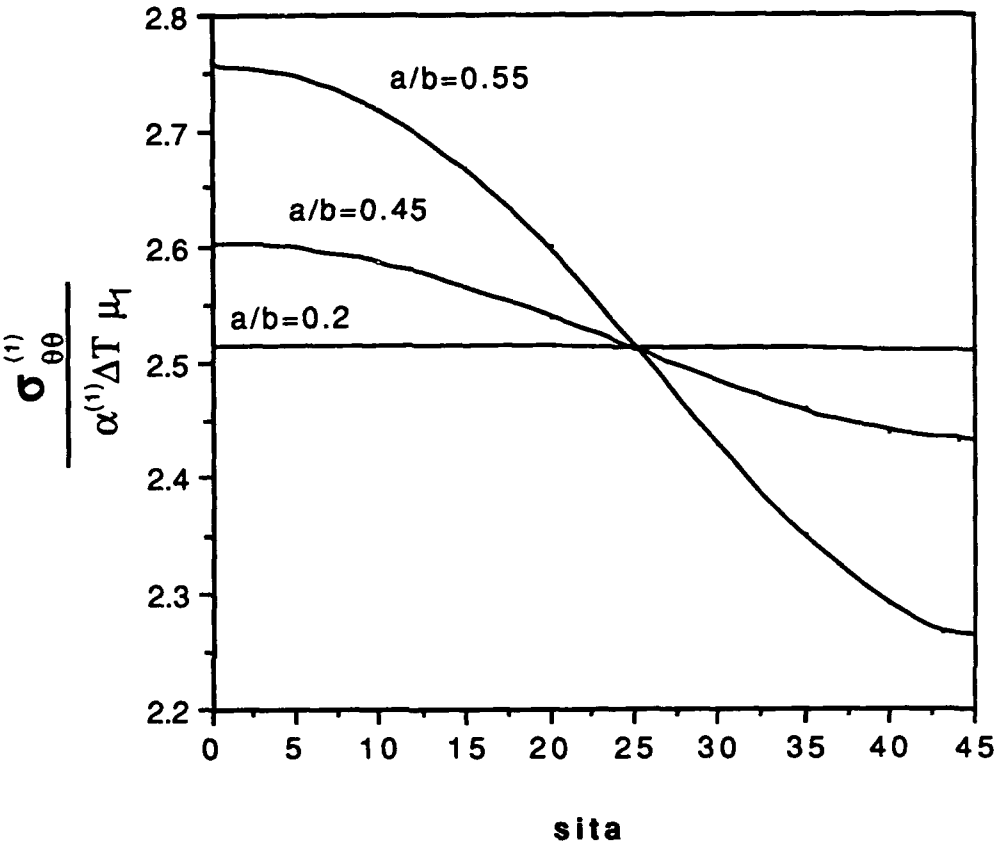

Figure 5.22. Stress $\sigma_{\theta\theta}^{(1)}$ at r=a,z=0 vs θ for periodic fibers model where v_1=0.34,v_2=0.22,μ_2/μ_1=16.67 and a/h=0.05

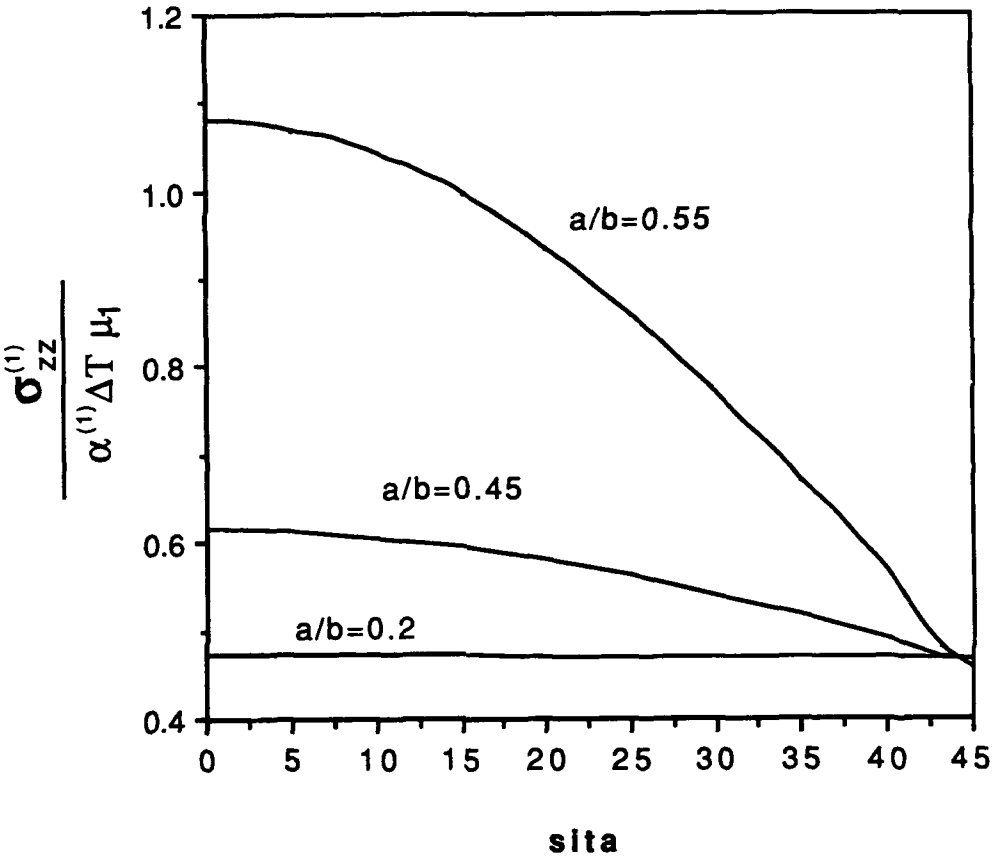

Figure 5.23. Stress $\sigma_{zz}^{(1)}$ at r=a, z=0 vs θ for periodic fibers model where v_1=0.34,v_2=0.22,μ_2/μ_1=16.67 and a/h=0.05

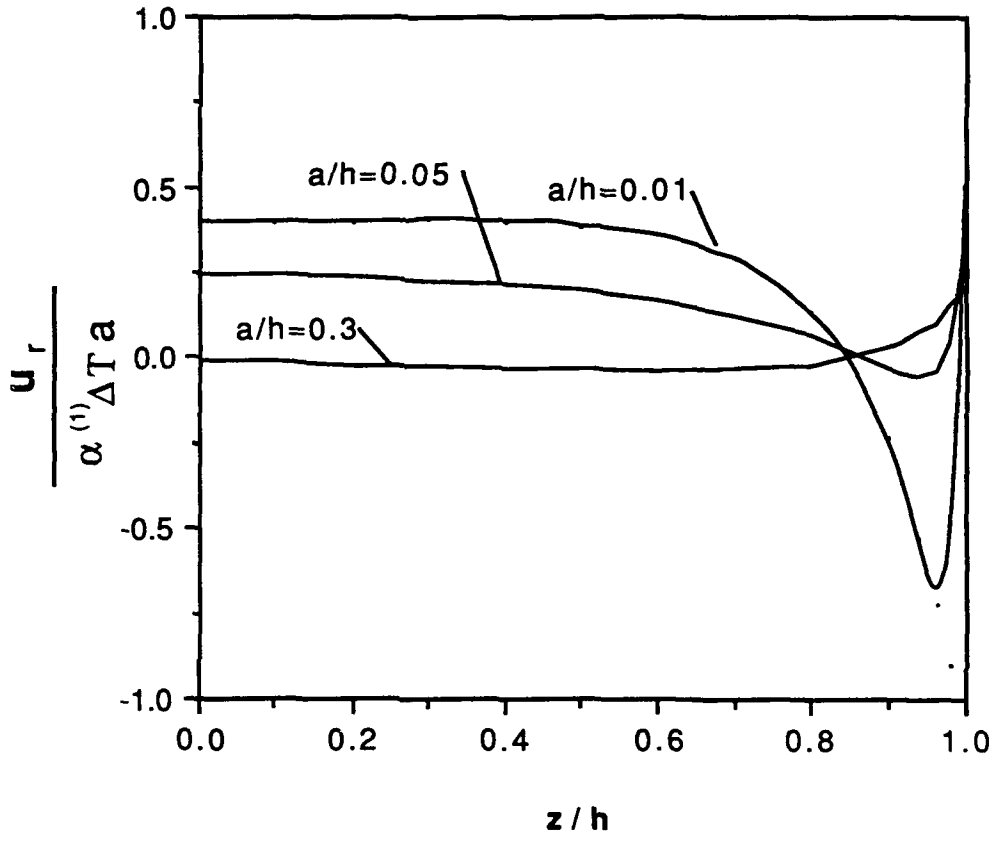

Figure 5.24. Displacement u_r at r=a,θ=0 vs z/h for periodic fibers model where v_1=0.34,v_2=0.22,μ_2/μ_1=16.67 and a/b=0.55

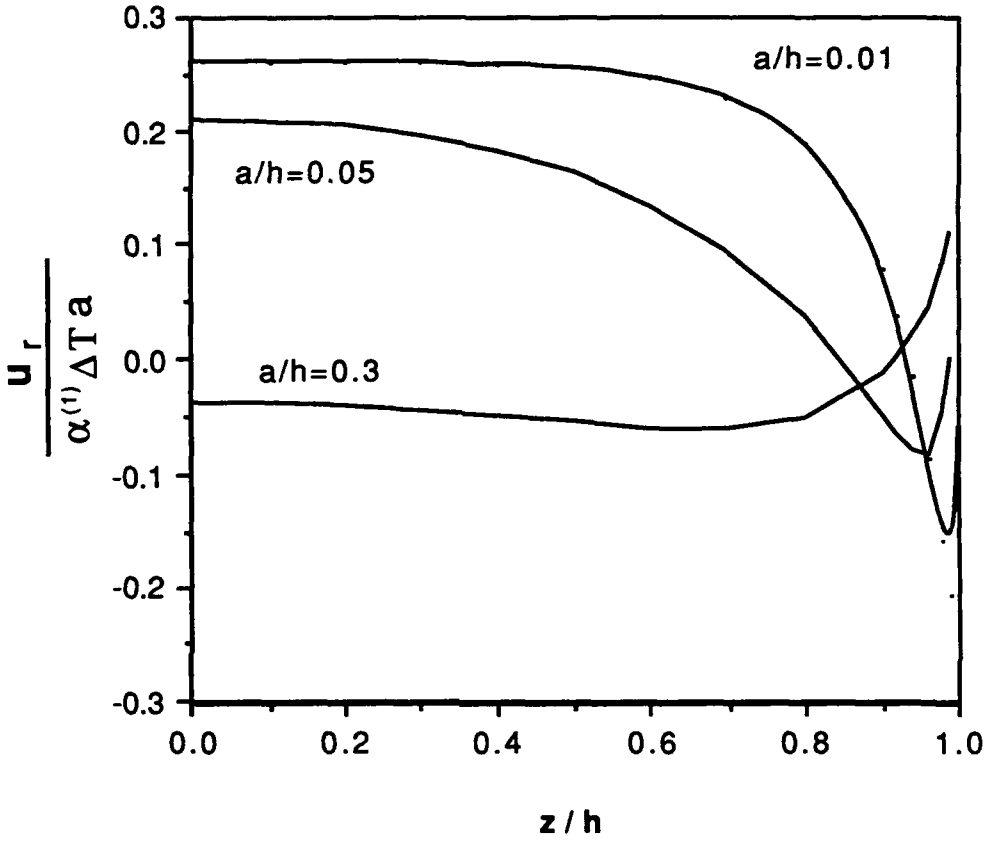

Figure 5.25. Displacement u_r at r=a,$\theta=\pi/4$ vs z/h for periodic fibers model where v_1=0.34,v_2=0.22,μ_2/μ_1=16.67 and a/b=0.55

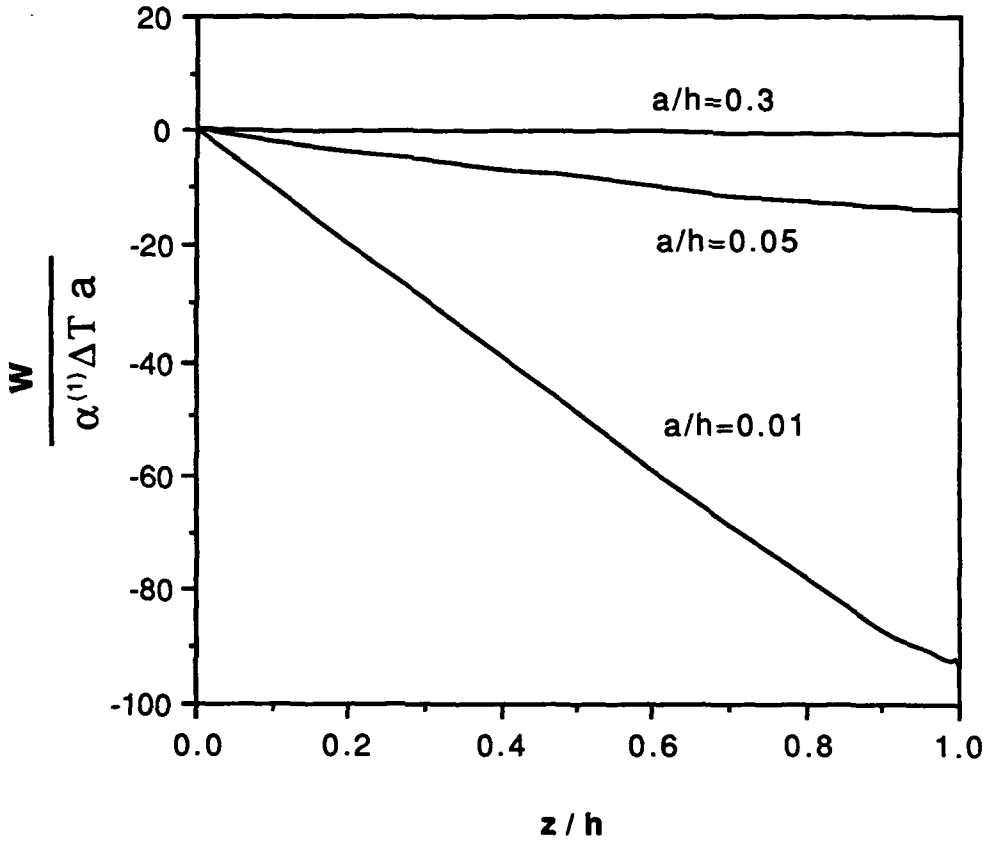

Figure 5.26. Displacement w at r=a,θ=0 vs z/h for periodic fibers model where v_1=0.34,v_2=0.22,μ_2/μ_1=16.67 and a/b=0.55

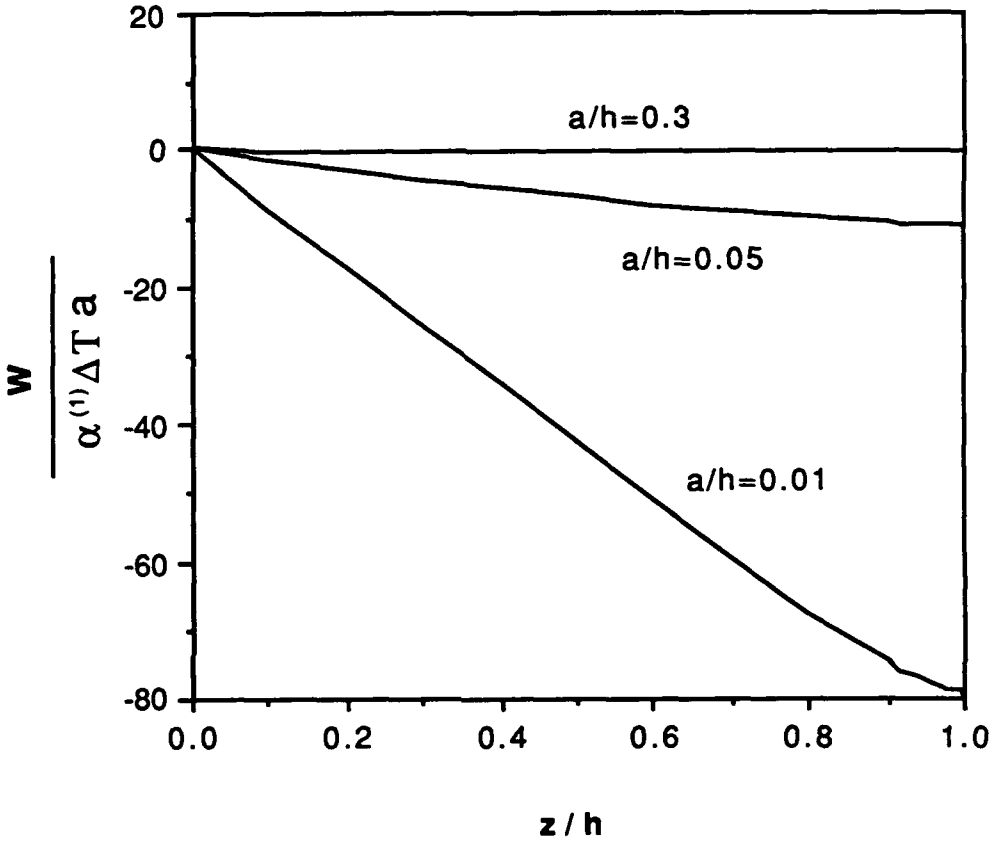

Figure 5.27. Displacement w at r=a,θ=π/4 vs z/h for periodic fibers model where v_1=0.34,v_2=0.22,μ_2/μ_1=16.67 and a/b=0.55

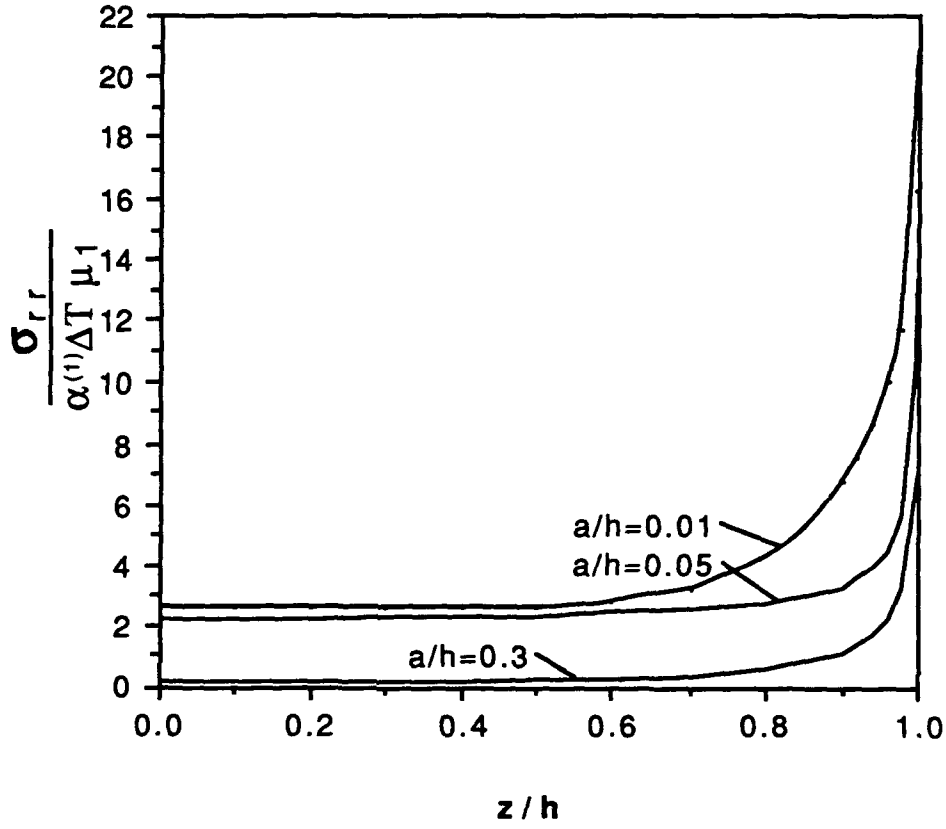

Figure 5.28. Stress σ_{rr} at r=a,θ=0 vs z/h for periodic fibers model where v_1=0.34,v_2=0.22,μ_2/μ_1=16.67 and a/b=0.55

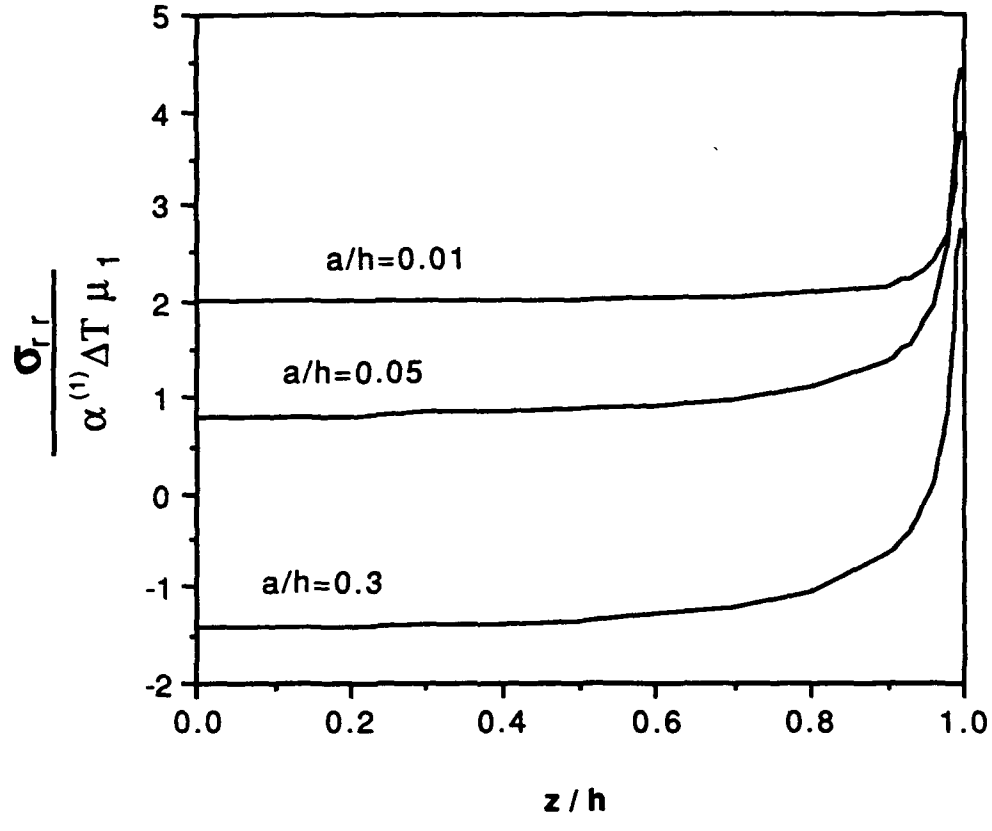

Figure 5.29. Stress σ_{rr} at r=a,$\theta=\pi/4$ vs z/h for periodic fibers model where v_1=0.34,v_2=0.22,μ_2/μ_1=16.67 and a/b=0.55

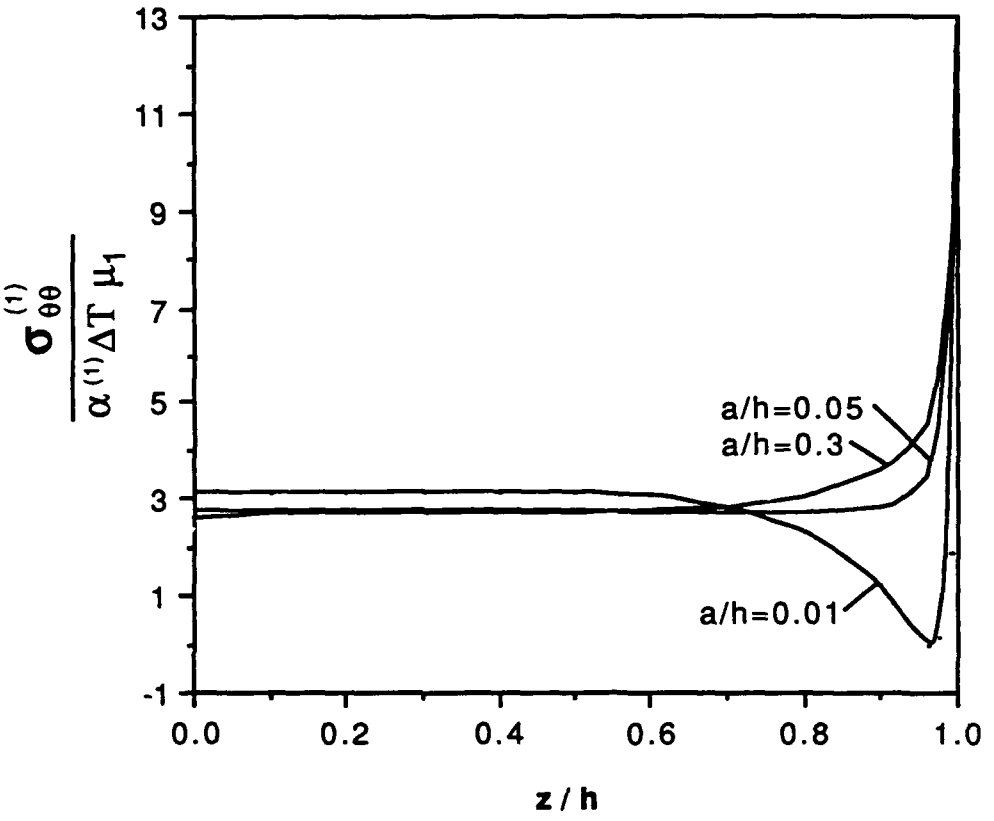

Figure 5.30. Stress $\sigma_{\theta\theta}^{(1)}$ at r=a,θ=0 vs z/h for periodic fibers model where v_1=0.34,v_2=0.22,μ_2/μ_1=16.67 and a/b=0.55

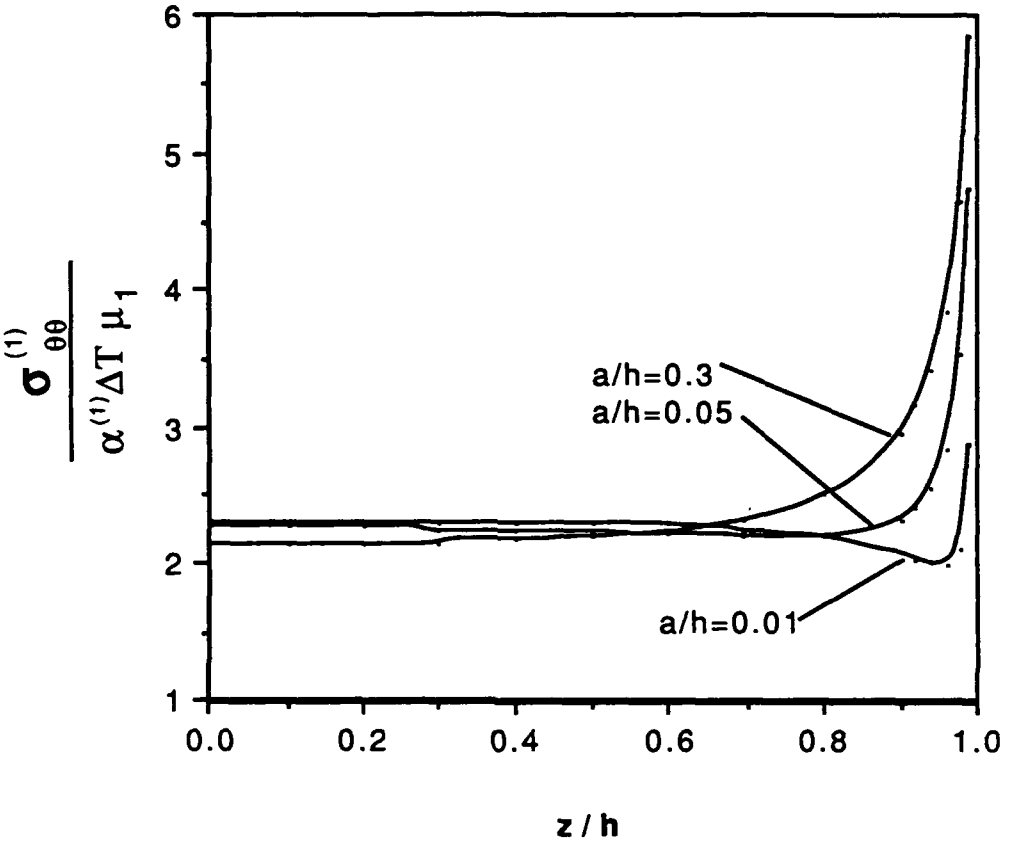

Figure 5.31. Stress $\sigma_{\theta\theta}^{(1)}$ at r=a,$\theta=\pi/4$ vs z/h for periodic fibers model where v_1=0.34,v_2=0.22,μ_2/μ_1=16.67 and a/b=0.55

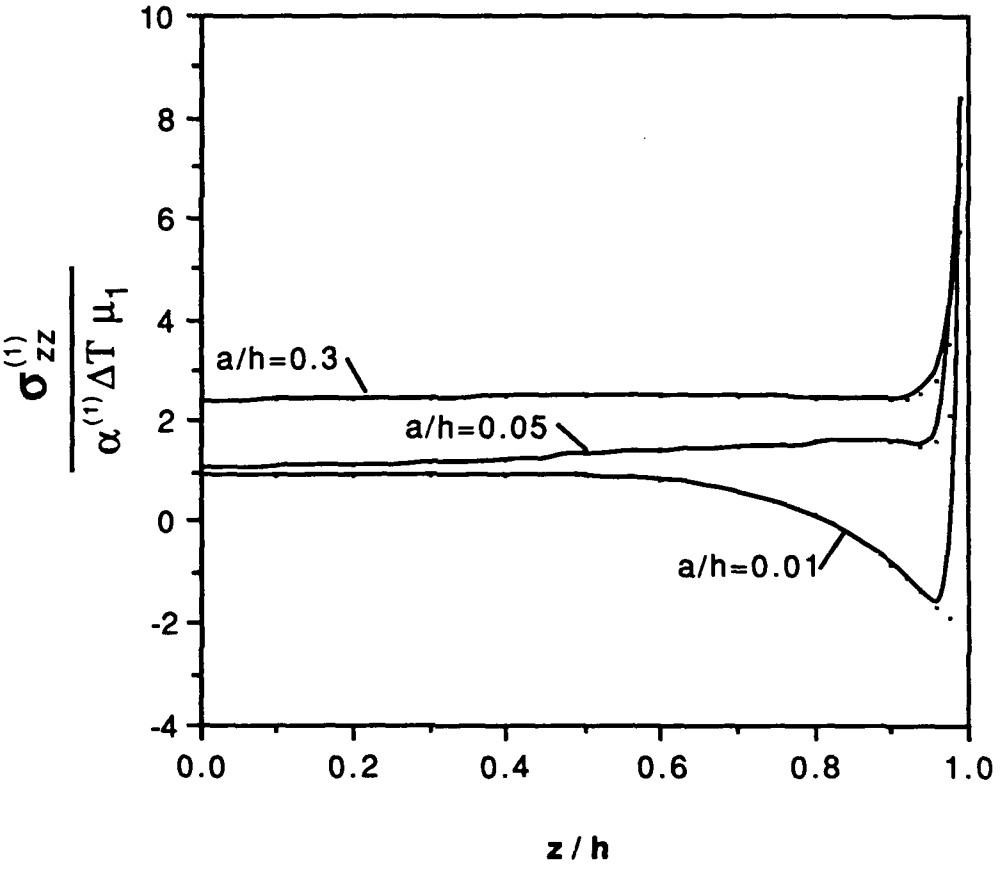

Figure 5.32. Stress $\sigma_{zz}^{(1)}$ at r=a,θ=0 vs z/h for periodic fibers model where v_1=0.34,v_2=0.22,μ_2/μ_1=16.67 and a/b=0.55

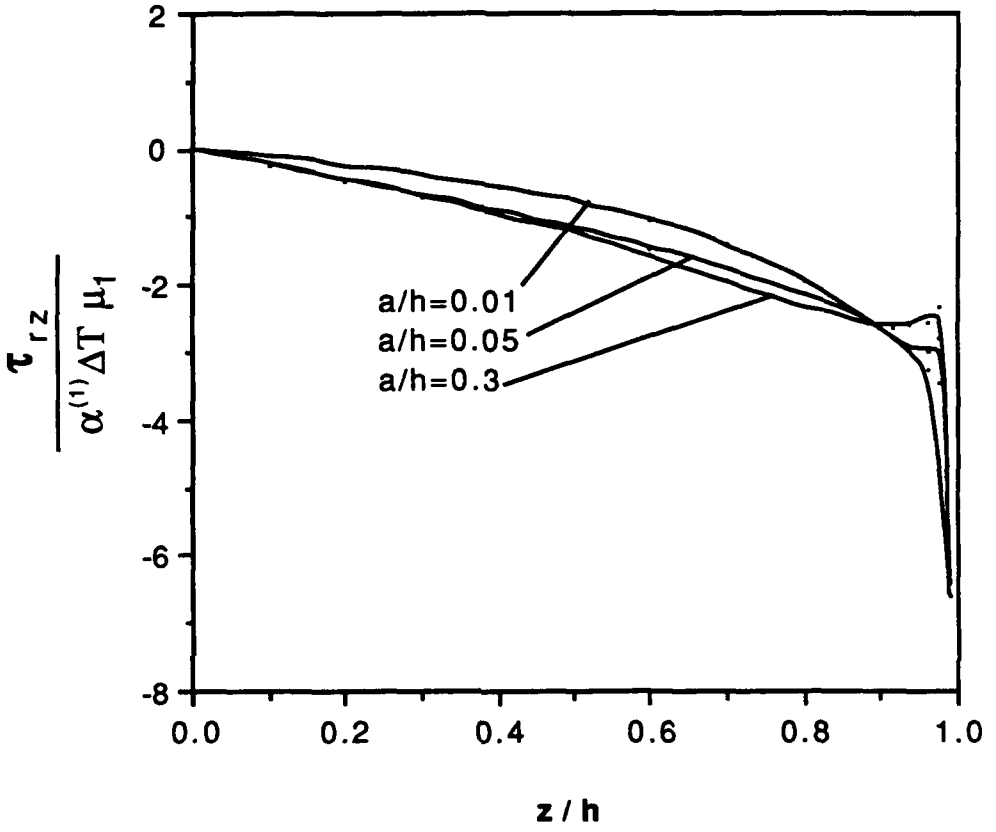

Figure 5.33. Stress τ_{rz} at r=a,θ=0 vs z/h for periodic fibers model where v_1=0.34,v_2=0.22,μ_2/μ_1=16.67 and a/b=0.55

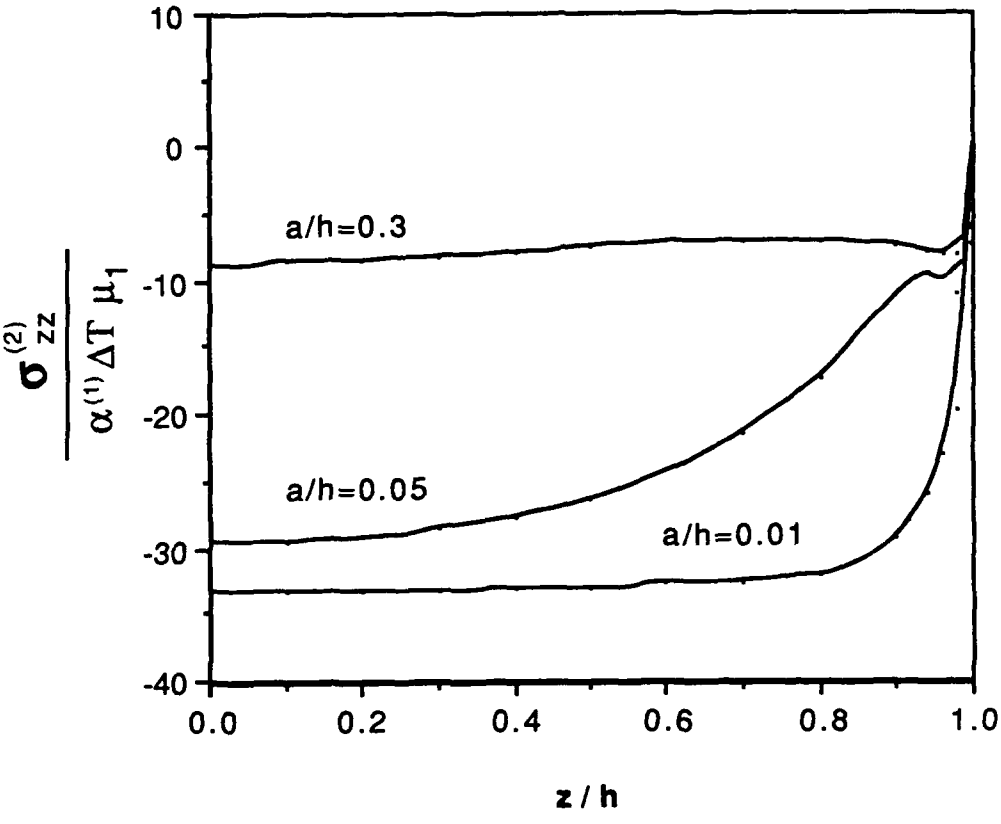

Figure 5.34. Stress $\sigma_{zz}^{(2)}$ at r=a,θ=0 vs z/h for periodic fibers model where v_1=0.34,v_2=0.22,μ_2/μ_1=16.67 and a/b=0.55

to two different locations θ=0 and θ=45. The radial stress increases with the decrease of a/h in both directions. Readers can note from Fig. 5.28 that as a/h reaches a certain value (small a/h), all the curves tend to merge together at the central region of the plate, which reveals that as the thickness of the plate increases to a certain degree, the radial stress will stop increasing and reach a limit value in the central region of the plate.

The circumferential tress $\sigma_{\theta\theta}^{(1)}$ is shown in Figs. 5.30 and 5.31, where there is only a slight change of the magnitude at the central region. However, the circumferential stress jumps suddenly to a large value near the plate surface. A special case is the curve of a/h=0.01 at θ=0. In this case, the circumferential stress decreases suddenly from the point of about z/h=0.7 then returns back rapidly from about z/h=0.95 to a large value. The axial stress $\sigma_{zz}^{(1)}$ (Fig.5.32) for the case of a/h=0.01 has a phenomenon similar to $\sigma_{\theta\theta}^{(1)}$. The shear stress τ_{rz} (see Fig. 5.33) increases in magnitude almost linearly at the central region for every ratio a/h then increases fast near the free surface where the stress singularity is located. Finally, the vertical stress of the inclusion $\sigma_{zz}^{(2)}$ is examined in Fig. 5.34. Comparing the plot with the plot in Fig. 5.13, one can note that both plots look similar , which reveals that the effect of the ratio a/b to the stress $\sigma_{zz}^{(2)}$ is negligible.

Figs. 5.35 to 5.37 show the variation of the stress profiles σ_{rr}, $\sigma_{\theta\theta}^{(1)}$ and $\sigma_{zz}^{(1)}$ vs a/b for the case of a/h=0.01, respectively. Each of these plots contains two curves that represent two different points at θ=0 and θ=45 in the center of the interface. In Fig. 5.35, the radial stress σ_{rr} decreases in both directions as the ratio a/b increases. On the other hand, the curves of the circumferential stress shown in Fig. 5.36 are separated in different directions with the increase of a/b. It is of interst to note that as the distance of the adjacent fibers decreases, parts of the stress $\sigma_{\theta\theta}^{(1)}$ will transfer from θ=45 to θ=0 to add the magnitude of the circumferential stress $\sigma_{\theta\theta}^{(1)}$ at θ=0. The axial stress $\sigma_{zz}^{(1)}$ vs a/b is attained in Fig.5.37. It is observed that this axial stress increases fast at θ=0 with the increase of ratio a/b whereas it changes only slightly at θ=45.

Figs. 5.38 to 5.42 show the profiles of those normal stresses σ_{rr}, $\sigma_{\theta\theta}^{(1)}$ and $\sigma_{zz}^{(1)}$

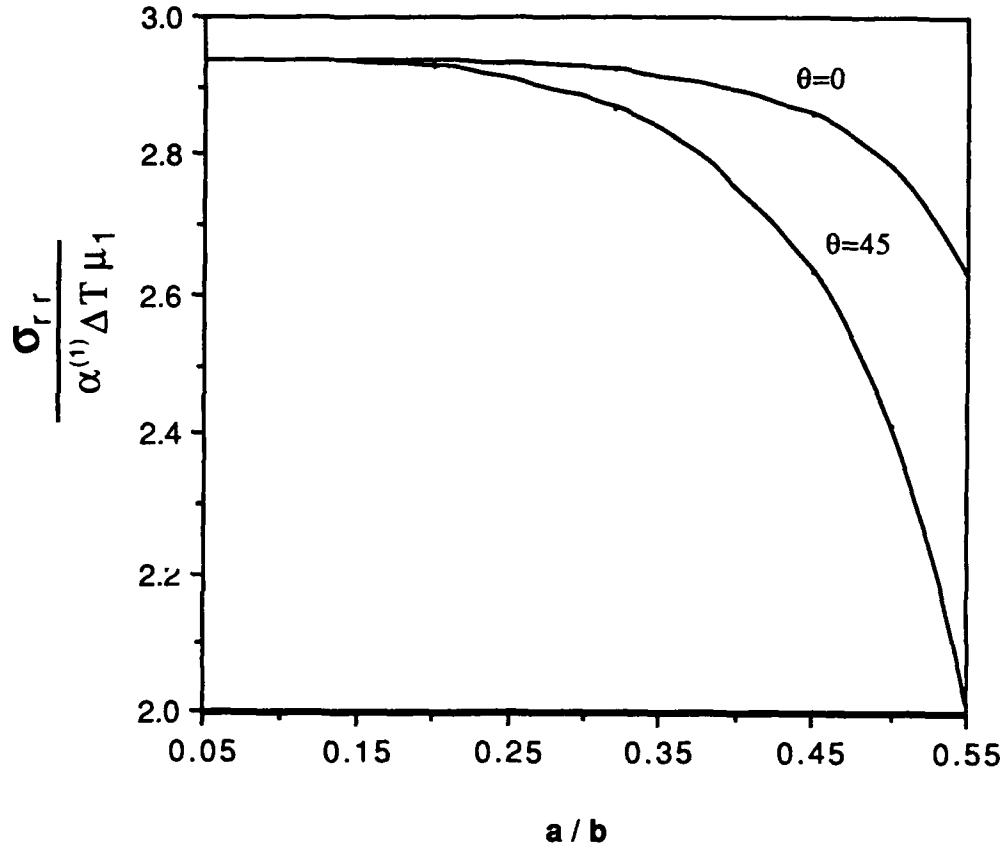

Figure 5.35. Stress σ_{rr} at r=a,z=0 vs a/b for periodic fibers model where v_1=0.34,v_2=0.22,μ_2/μ_1=16.67 and a/h=0.01

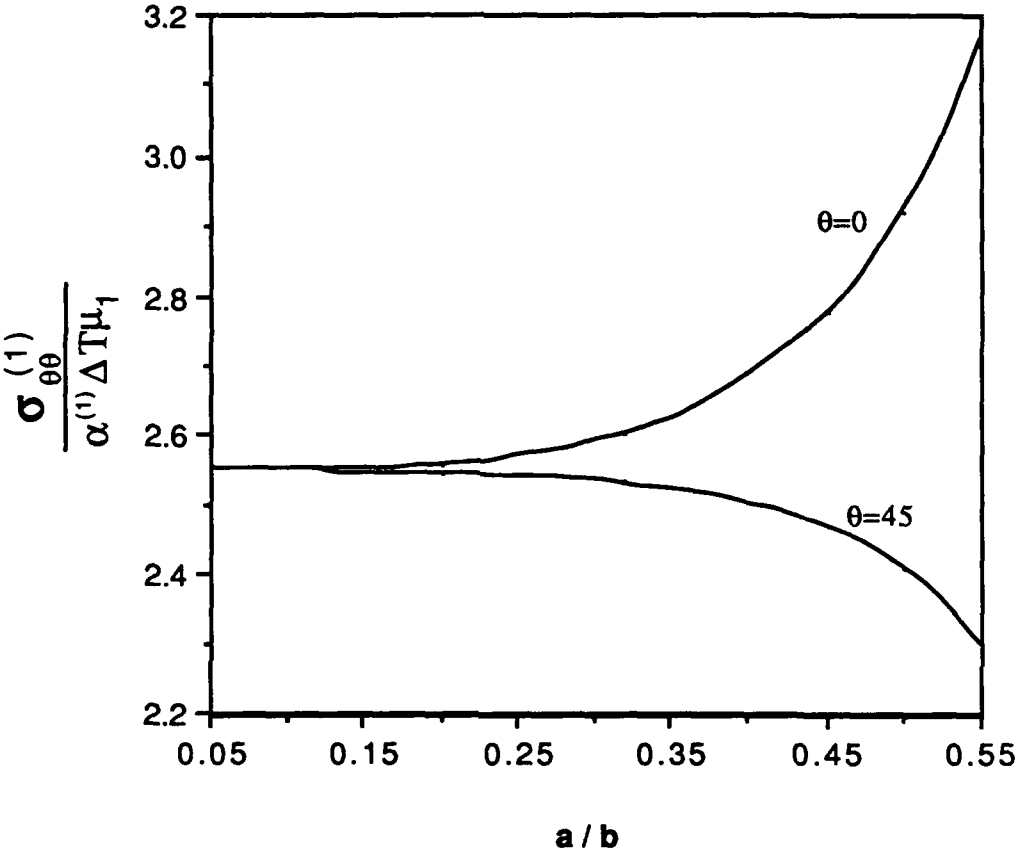

Figure 5.36. Stress $\sigma_{\theta\theta}^{(1)}$ at r=a,z=0 vs a/b for periodic fibers model where v_1=0.34,v_2=0.22,μ_2/μ_1=16.67 and a/h=0.01

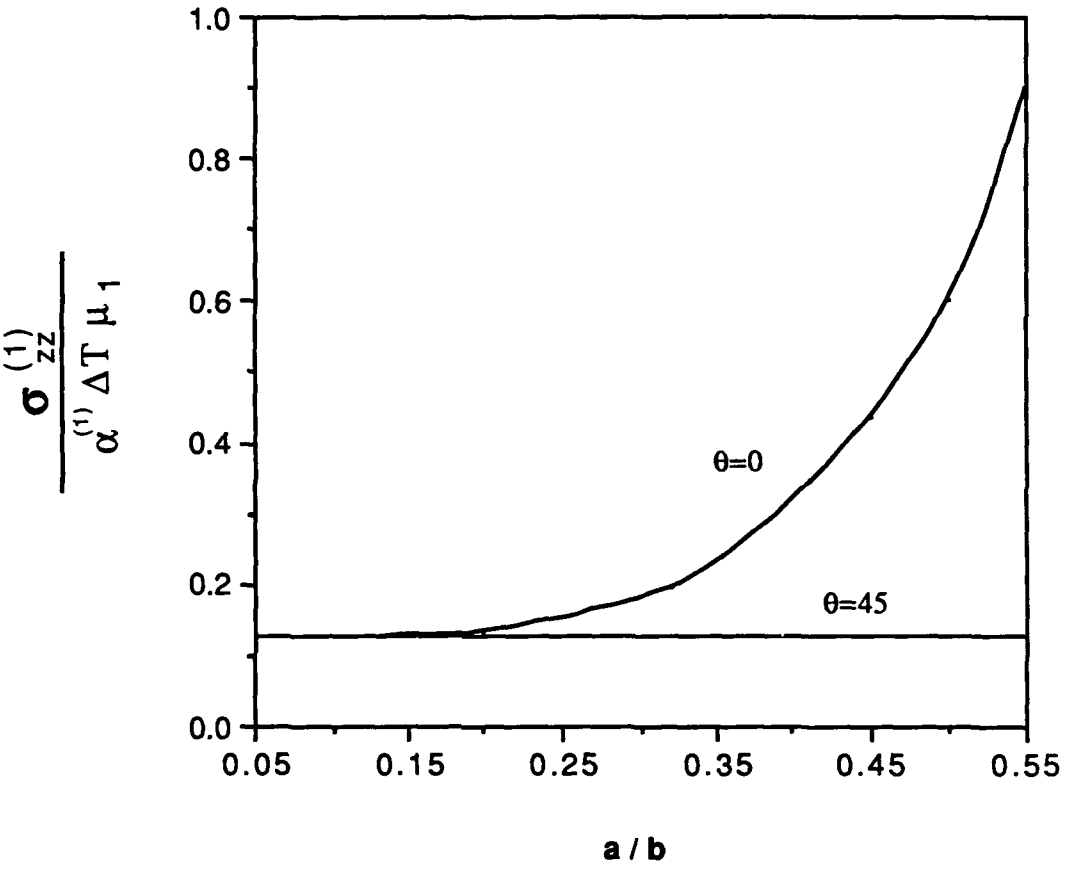

Figure 5.37. Stress $\sigma_{zz}^{(1)}$ at r=a,z=0 vs a/b for periodic fibers model where v_1=0.34,v_2=0.22,μ_2/μ_1=16.67 and a/h=0.01

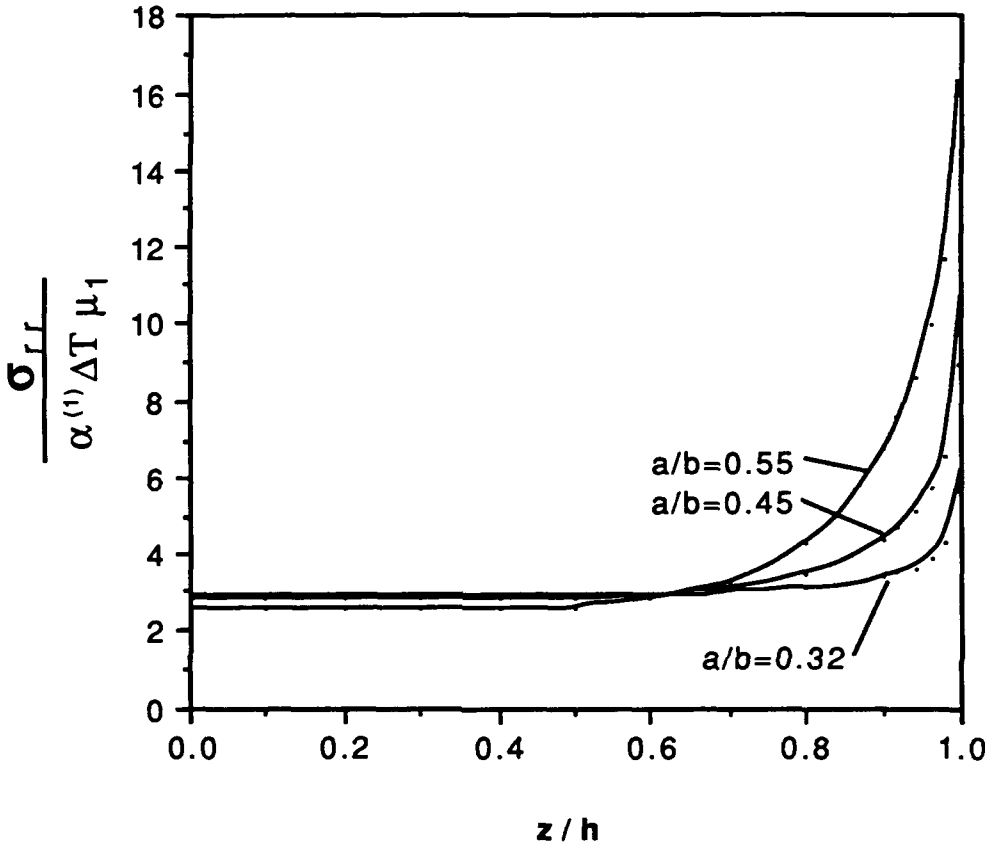

Figure 5.38. Stress σ_{rr} at r=a, θ=0 vs z/h for periodic fibers model where v_1=0.34,v_2=0.22,μ_2/μ_1=16.67 and a/h=0.01

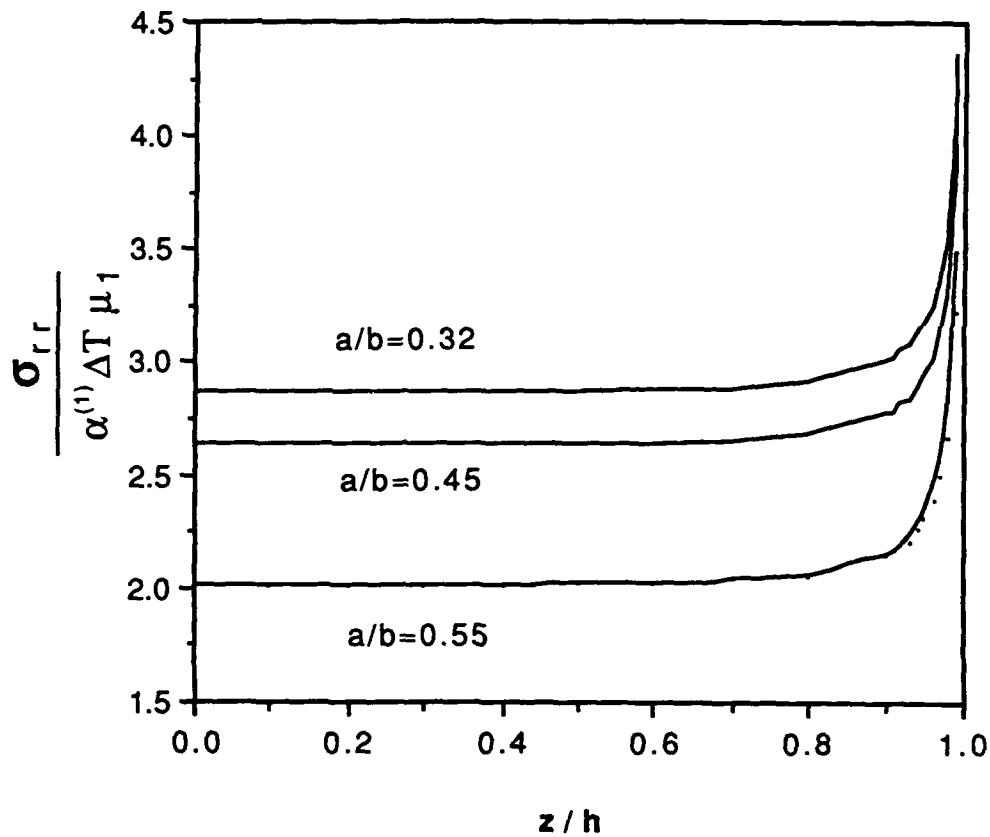

Figure 5.39. Stress σ_{rr} at r=a, $\theta=\pi/4$ vs z/h for periodic fibers model where $v_1=0.34, v_2=0.22, \mu_2/\mu_1=16.67$ and a/h=0.01

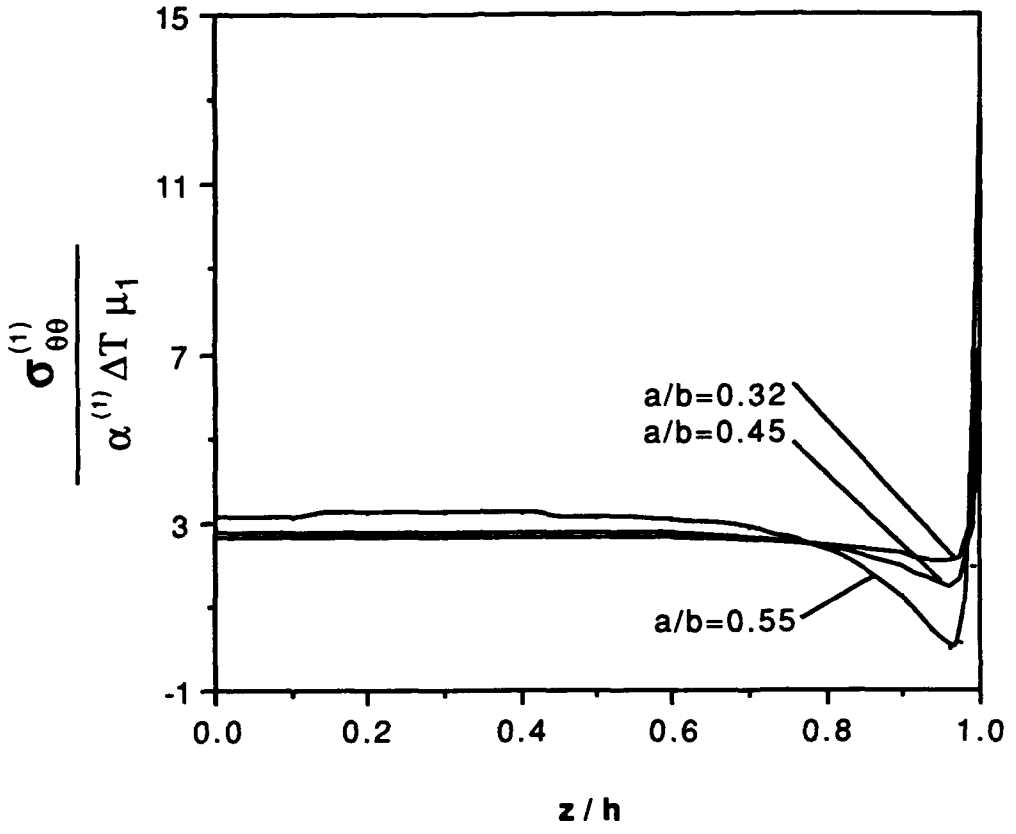

Figure 5.40. Stress $\sigma_{\theta\theta}^{(1)}$ at r=a, θ=0 vs z/h for periodic fibers model where v_1=0.34,v_2=0.22,μ_2/μ_1=16.67 and a/h=0.01

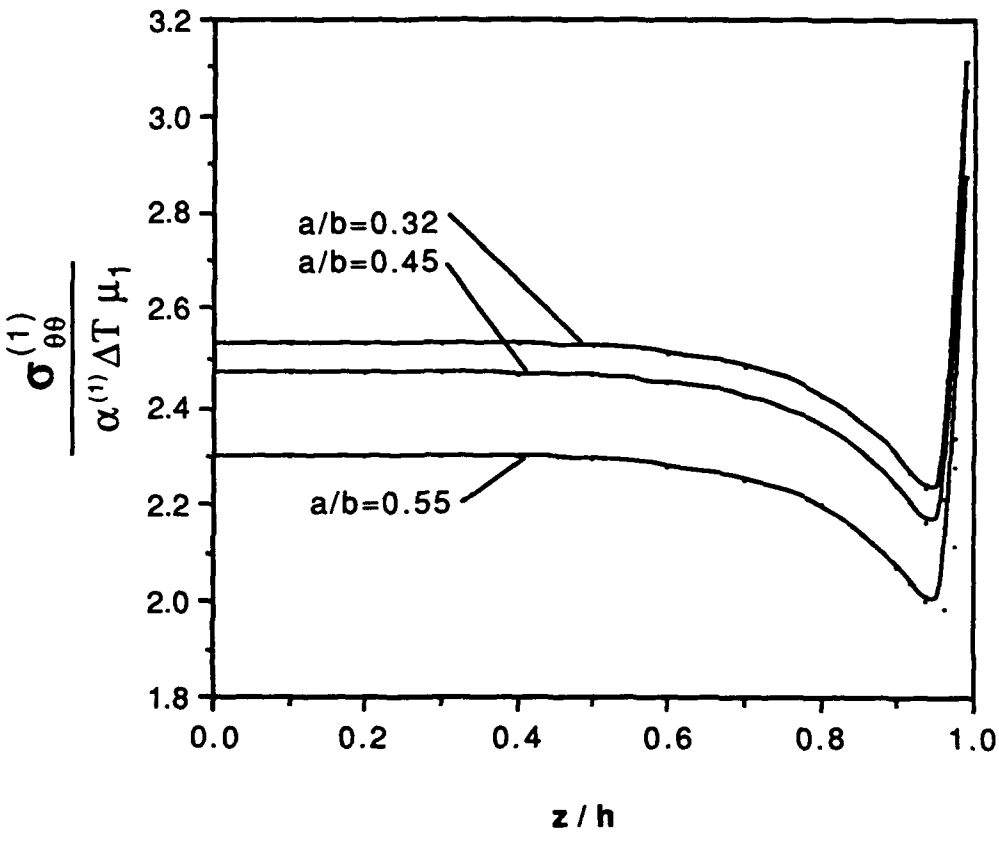

Figure 5.41. Stress $\sigma_{\theta\theta}^{(1)}$ at r=a, $\theta=\pi/4$ vs z/h for periodic fibers model where $v_1=0.34, v_2=0.22, \mu_2/\mu_1=16.67$ and a/h=0.01

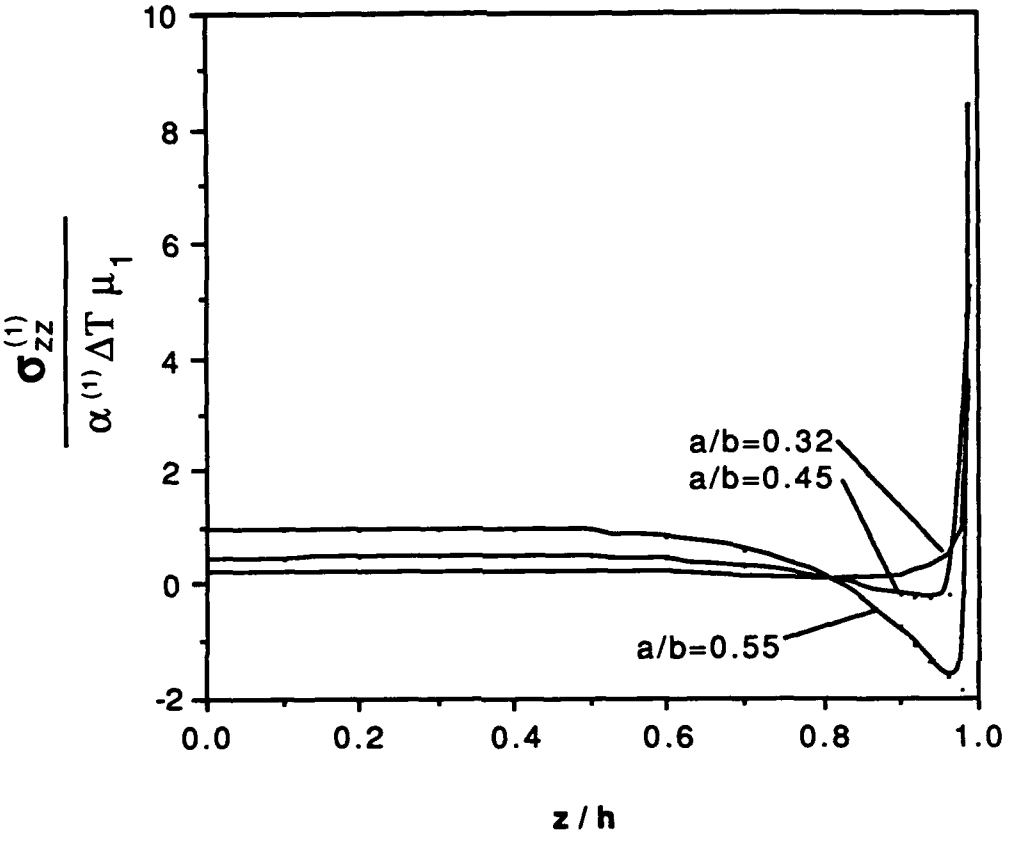

Figure 5.42. Stress $\sigma_{zz}^{(1)}$ at r=a, θ=0 vs z/h for periodic fibers model where v_1=0.34,v_2=0.22,μ_2/μ_1=16.67 and a/h=0.01

again but using different ratios of a/b instead of different ratios of a/h in order to observe more clearly the effect of the ratio a/b on the stresses along the thickness and at the interface. In the position of θ=0, the effect of ratio a/b is small to the radial stress in the central region (see Fig. 5.38). In the position of θ=45, however, the different ratios of a/b separate the radial stress as a group of parallel curves (see Fig. 5.39). The same phenomenon can also be seen in the profile of the circumferential stress (Figs. 5.40 and 5.41). On the other hand, the axial stress $\sigma_{zz}^{(1)}$ with different ratios of a/b at θ=0 is shown in Fig. 5.42. The stress is redistributed by different ratios a/b along the thickness. As a/b increases, the stress in the central region increases but the stress near the free surface decreases to a negative value, then goes back again to a big value.

So far, all of the plots discussed above are focused on the interface of the fiber and the matrix (r=a) where a maximum stress is presented. The displacement and stress distribution along the radial direction is also important for us in order to understand the material properties. For this reason, the plots (Figs.5.43 to 5.51) are made here to examine how displacements and stresses will decay as a function of the radial distance . All of the curves discussed here are within the region begining at the interface r=a and ending at the symmetric line B-C (see Fig. 2.2).

The displacement w at the free surface z=h is shown in Figs. 5.43 and 5.44 as a function of the radial coordinate r. At θ=0, the displacement looks more complicated than the displacement at θ=45 because the curve at θ=0 changes from a concave shape to a convex shape as the ratio a/b increases and the curves at θ=45 look more smooth and regular. The values of the displacement at the interface r=a, which is smaller than 100 in magnitude, reveal that the inclusion resists the shrinkage of the matrix.

The radial stress profiles σ_{rr} at the center of the plate (z=0) are shown in Figs. 5.45 and 5.46 along the two radial directions of θ=0 and θ=45, respectively, for different ratios of a/b. The stress tends to decrease as the distance away from the interface increases. It may also be noted that the stress along the direction θ=0 decays faster than the stress in the other

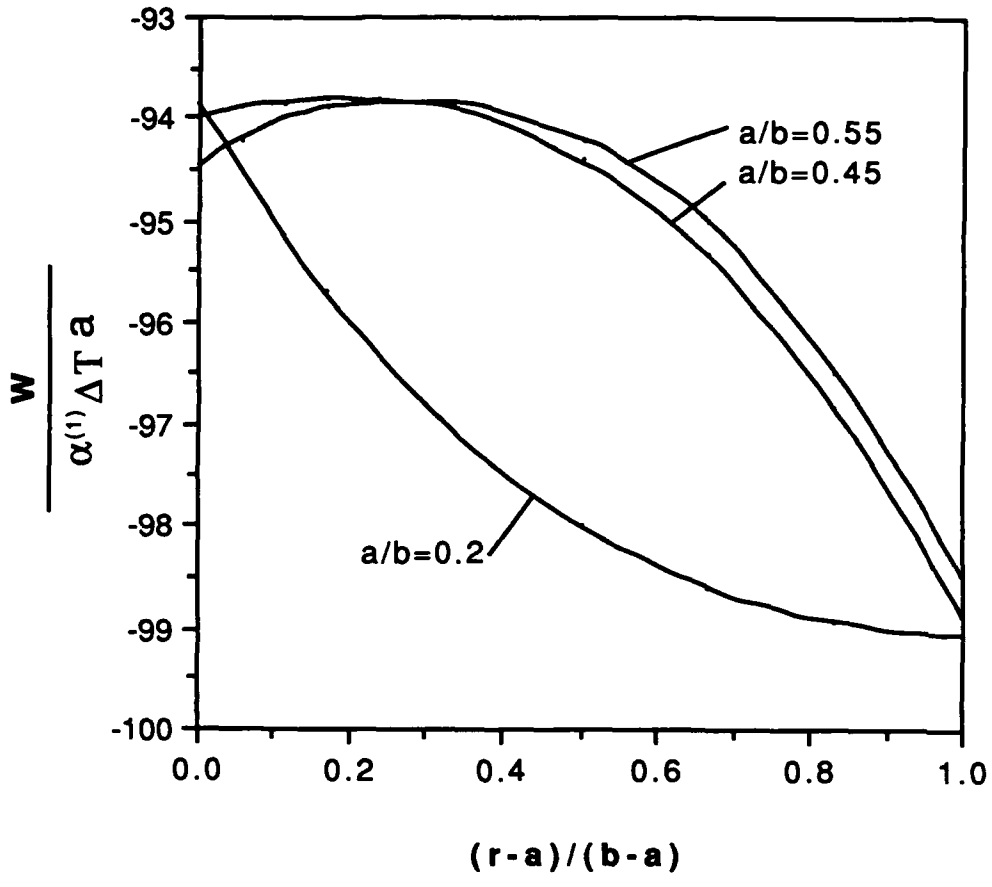

Figure 5.43. Displacement w at z=h, θ=0 vs (r-a)/(b-a) for periodic fibers model where v_1=0.34,v_2=0.22,μ_2/μ_1=16.67 and a/h=0.01

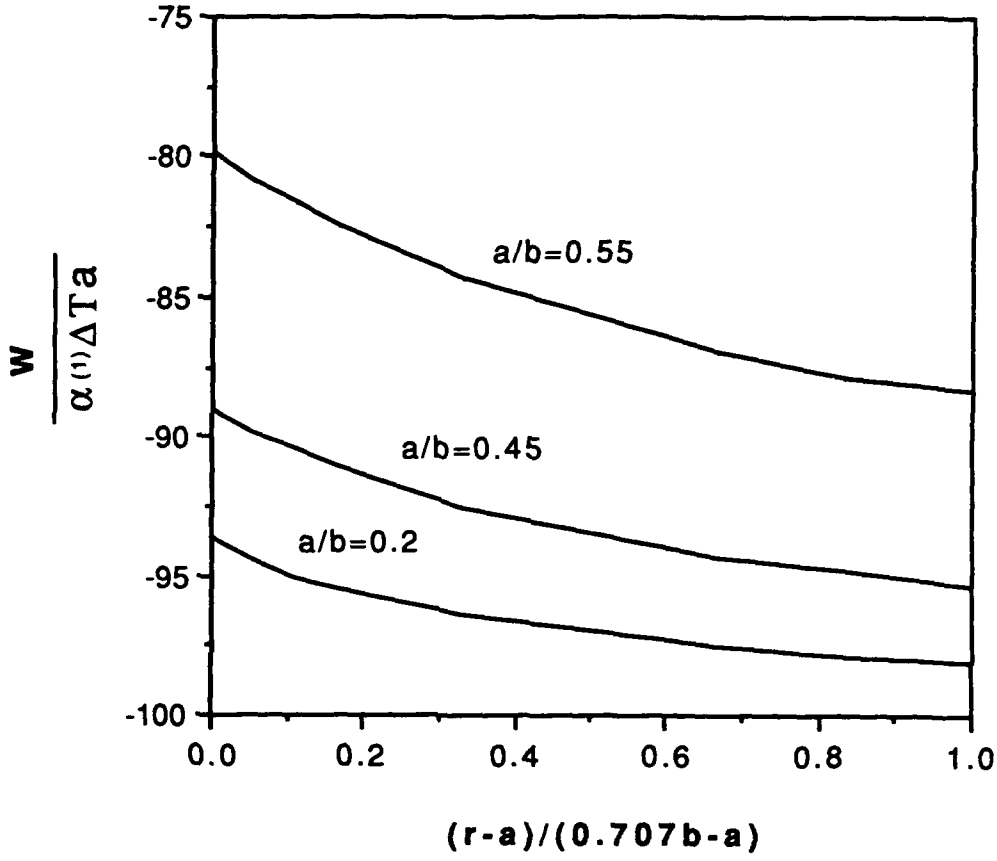

Figure 5.44. Displacement w at z=h, $\theta=\pi/4$ vs (r-a)/(0.707b-a) for periodic fibers model where $v_1=0.34, v_2=0.22, \mu_2/\mu_1=16.67$ and a/h=0.01

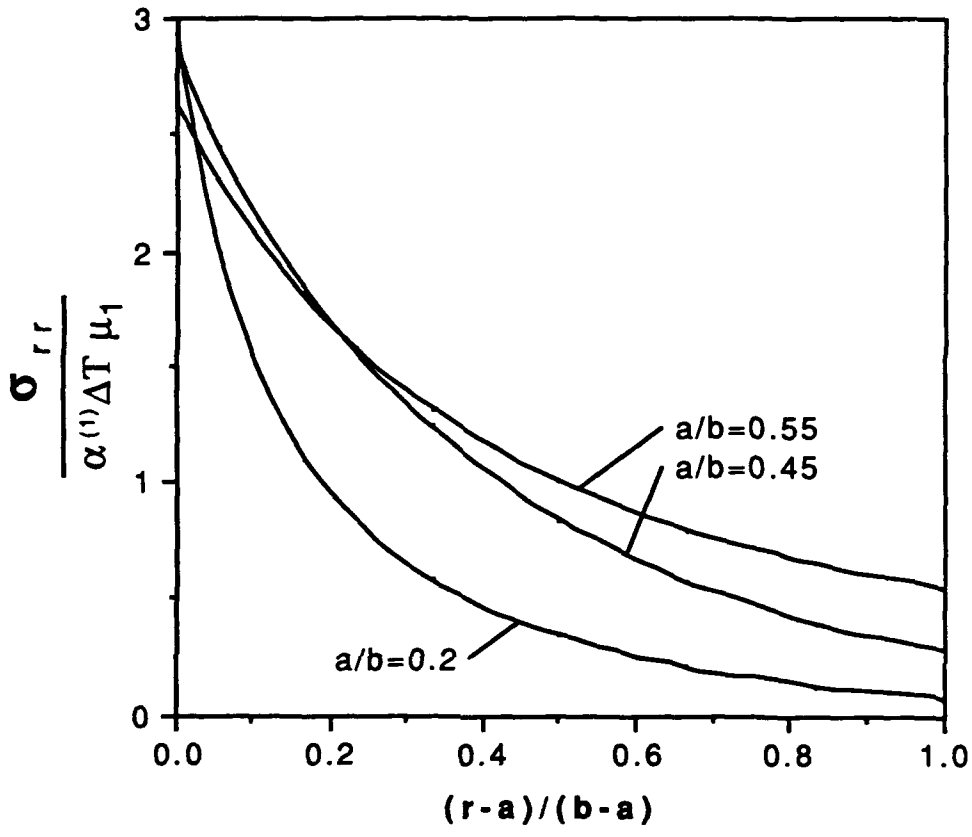

Figure 5.45. Stress σ_{rr} at z=0, θ=0 vs (r-a)/(b-a) for periodic fibers model where v_1=0.34,v_2=0.22,μ_2/μ_1=16.67 and a/h=0.01

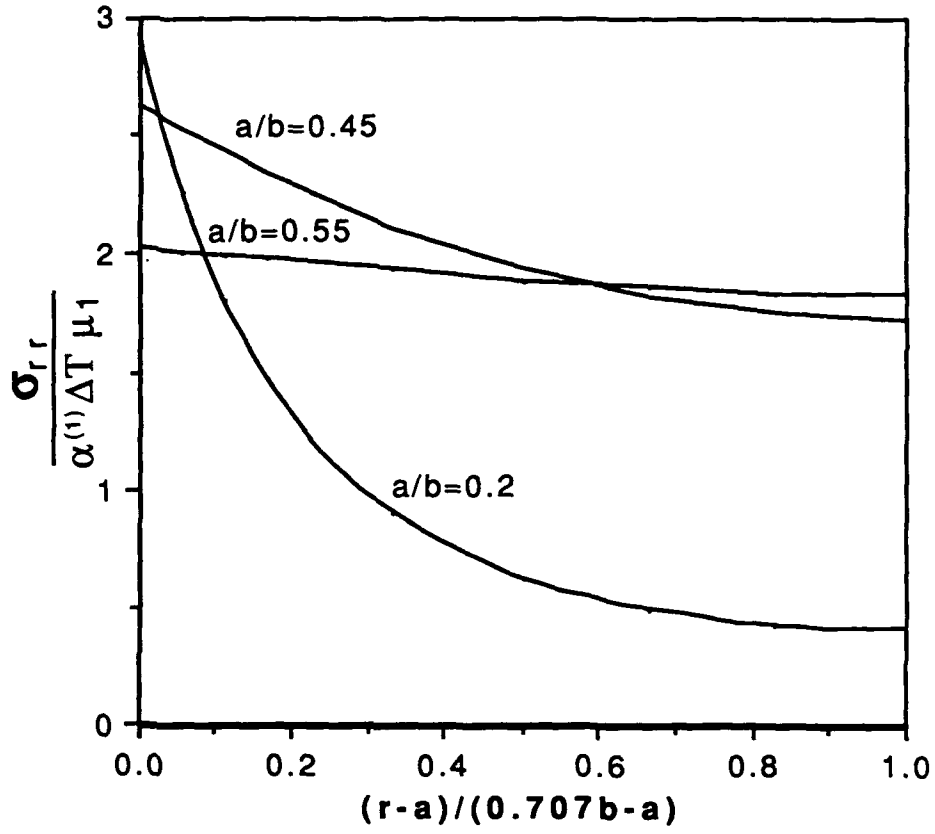

Figure 5.46. Stress σ_{rr} at z=0, $\theta=\pi/4$ vs (r-a)/(0.707b-a) for periodic fibers model where v_1=0.34,v_2=0.22,μ_2/μ_1=16.67 and a/h=0.01

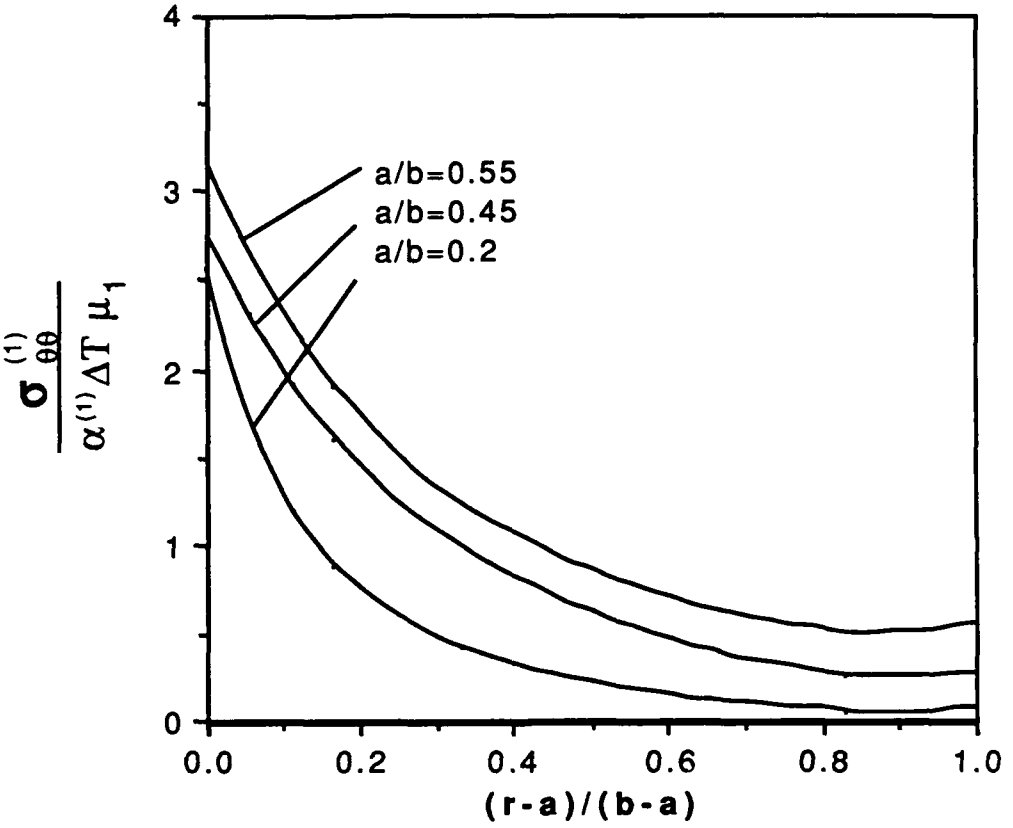

Figure 5.47.Stress $\sigma_{\theta\theta}^{(1)}$ at z=0, θ=0 vs (r-a)/(b-a) for periodic fibers model where v_1=0.34,v_2=0.22,μ_2/μ_1=16.67 and a/h=0.01

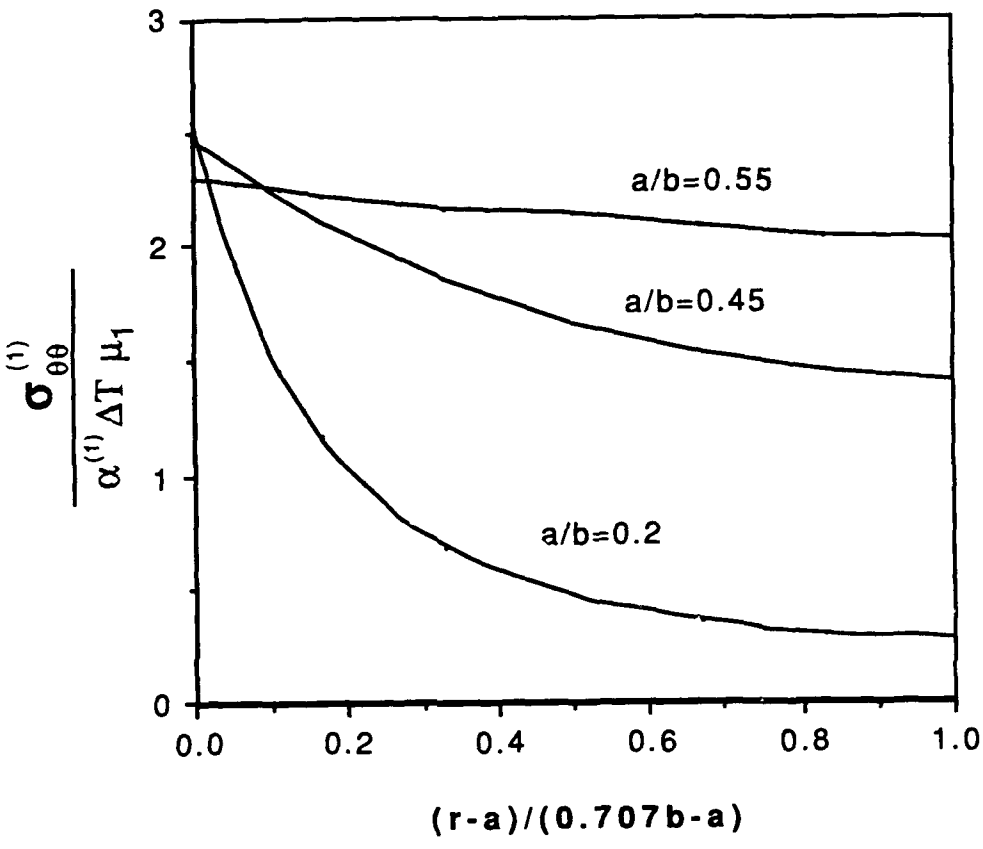

Figure 5.48.Stress $\sigma_{\theta\theta}^{(1)}$ at z=0, $\theta=\pi/4$ vs (r-a)/(0.707b-a) for periodic fibers model where $v_1=0.34, v_2=0.22, \mu_2/\mu_1=16.67$ and a/h=0.01

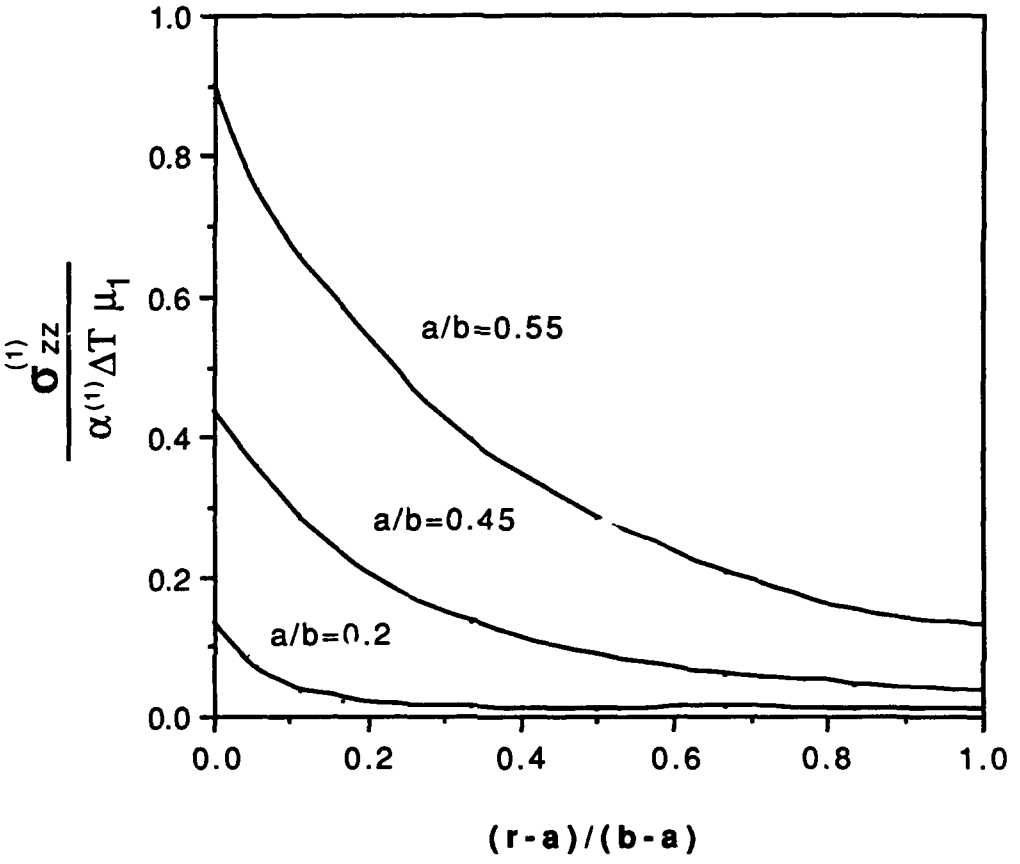

Figure 5.49.Stress $\sigma_{zz}^{(1)}$ at z=0, θ=0 vs (r-a)/(b-a) for periodic fibers model where v_1=0.34,v_2=0.22,μ_2/μ_1=16.67 and a/h=0.01

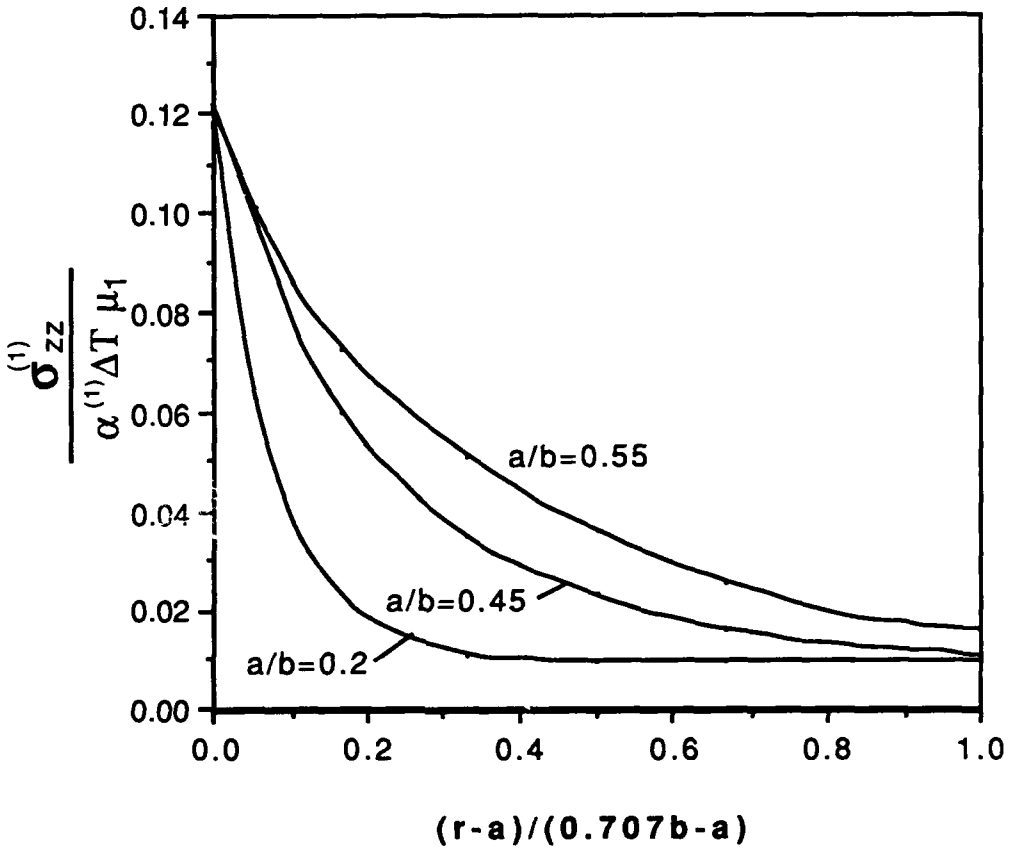

Figure 5.50. Stress $\sigma_{zz}^{(1)}$ at z=0, $\theta=\pi/4$ vs (r-a)/(0.707b-a) for periodic fibers model where $v_1=0.34, v_2=0.22, \mu_2/\mu_1=16.67$ and a/h=0.01

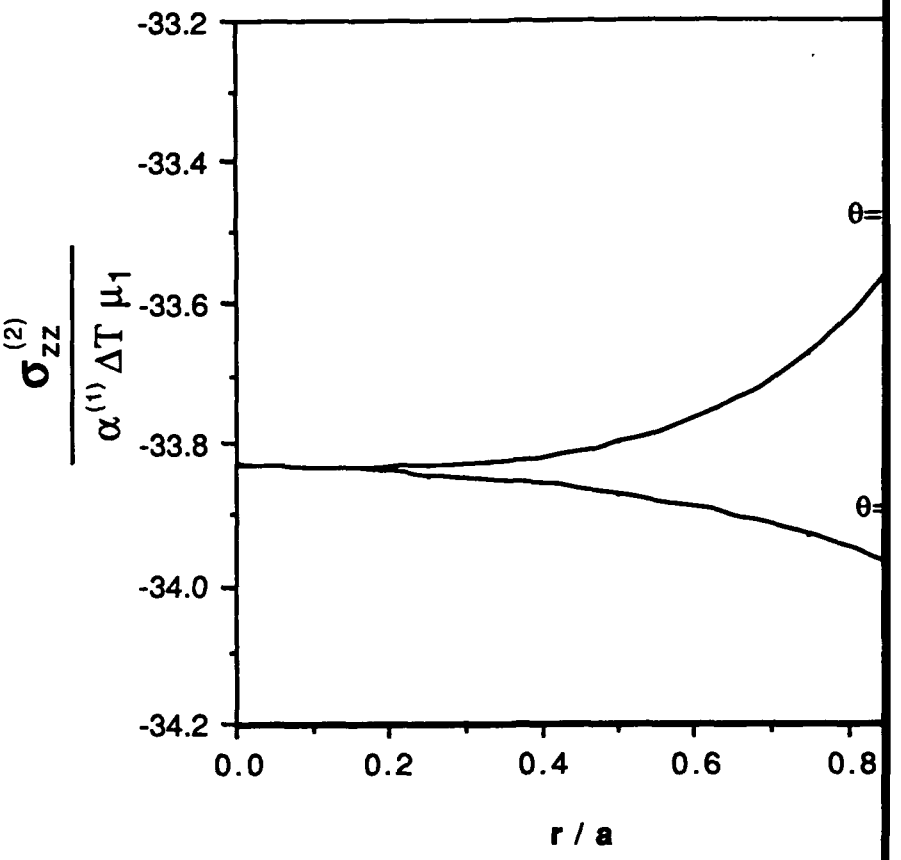

Figure 5.51.Stress $\sigma_{zz}^{(2)}$ at z=0, vs r/a for periodic fibers m

where v_1=0.34,v_2=0.22,μ_2/μ_1=16.67 and a/h=0.01,a/b=0.

direction (θ=45). A similar trend also prevails for the circumferential stress $\sigma_{\theta\theta}^{(1)}$ (see Figs. 5.47 and 5.48). As for the stress $\sigma_{zz}^{(1)}$ (see Figs. 5.49 and 5.50), on the other hand, one can note that both groups of curves along different radial directions (i.e., θ=0 and θ=45) approach to the value of zero .

Fig. 5.51 shows the axial stress $\sigma_{zz}^{(2)}$ in the fibers vs r/a. At the interface r=a, the magnitude of the axial stress increases along θ=45 and decreases along θ=0. It seems reasonable if one compares these curves with the curve of a/b=0.55 in Fig. 5.20. The shrinkage in vertical direction at the interface is resisted much more at θ=45 than at θ=0 (if without the resistance, the value of the shrinkage is -100), which induces a higher compressive stress $\sigma_{zz}^{(2)}$ at the point θ=45 than at the point of θ=0.

Finally, the stresses σ_{rr} and $\sigma_{\theta\theta}^{(1)}$, which are two of the most important stresses under consideration, are shown again as a function of shear moduli ratio μ_2/μ_1 in Figs. 5.52 and 5.53, respectively. Starting from μ_2/μ_1 =0.01, one can travel along the curves and note that both radial stress σ_{rr} and circumferential stress $\sigma_{\theta\theta}^{(1)}$ are close to zero in the region of small shear moduli ratios. This result seems reasonable if one examines the limit case of a plate with periodic holes. From Fig.5.52, the reader may note that the radial stress σ_{rr} appears to be low for a wide span of the ratio μ_2/μ_1. Beyond the ratio of μ_2/μ_1 =10, it increases rapidly . From those four curves with different parameters, one is able to extract directly that the effect of the ratio a/h to the radial stress is much higher than the effect of the ratio a/b. The circumferential stress $\sigma_{\theta\theta}^{(1)}$, on the other hand, has a large slope in the region for small ratios of μ_2/μ_1 , while the rate of increase slows down in the region of high ratios of μ_2/μ_1. A reverse condition appears for this circumferential stress (see Fig. 5.53), that is, the effect of the ratio a/b to this circumferential stress is higher than that of the ratio a/h. Thus, the following conclusion may be drawn that in the case of small ratios of μ_2/μ_1 , a radial crack is most likely to initiate first, while in the case of large ratios of μ_2/μ_1 a fiber-matrix interface crack is most most likely to develop.

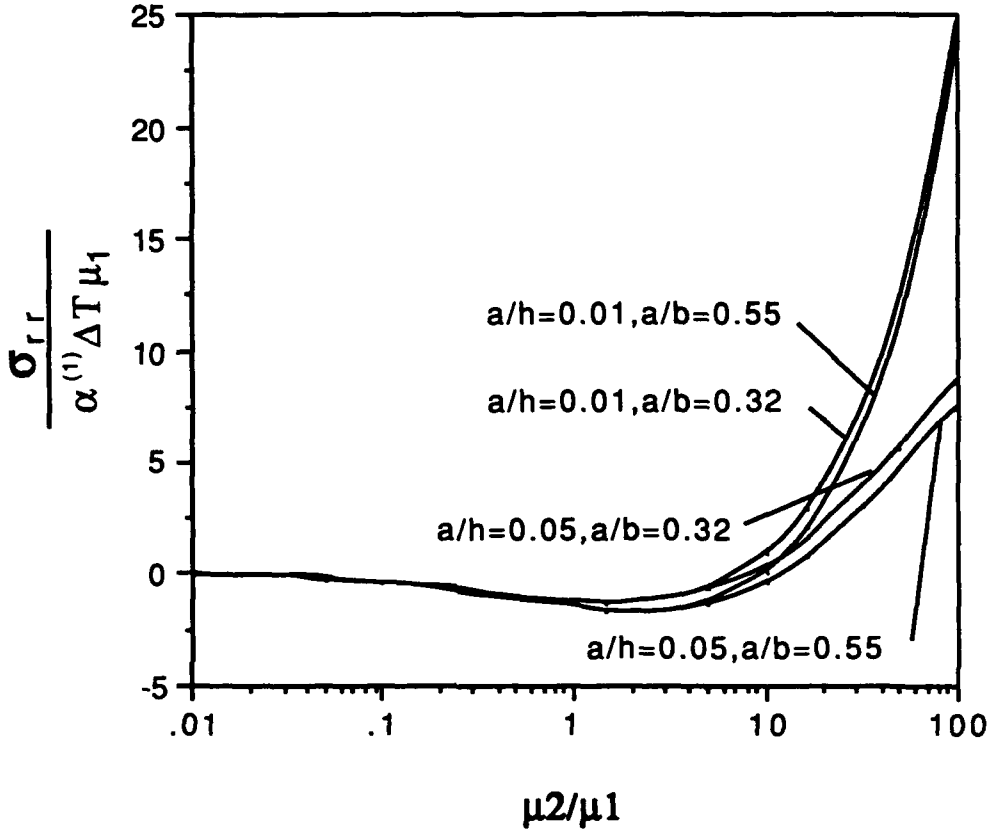

Figure 5.52. Stress σ_{rr} at r=a z=0, $\theta=\pi/4$ vs μ_2/μ_1 for periodic fibers model where $v_1=0.34, v_2=0.22$

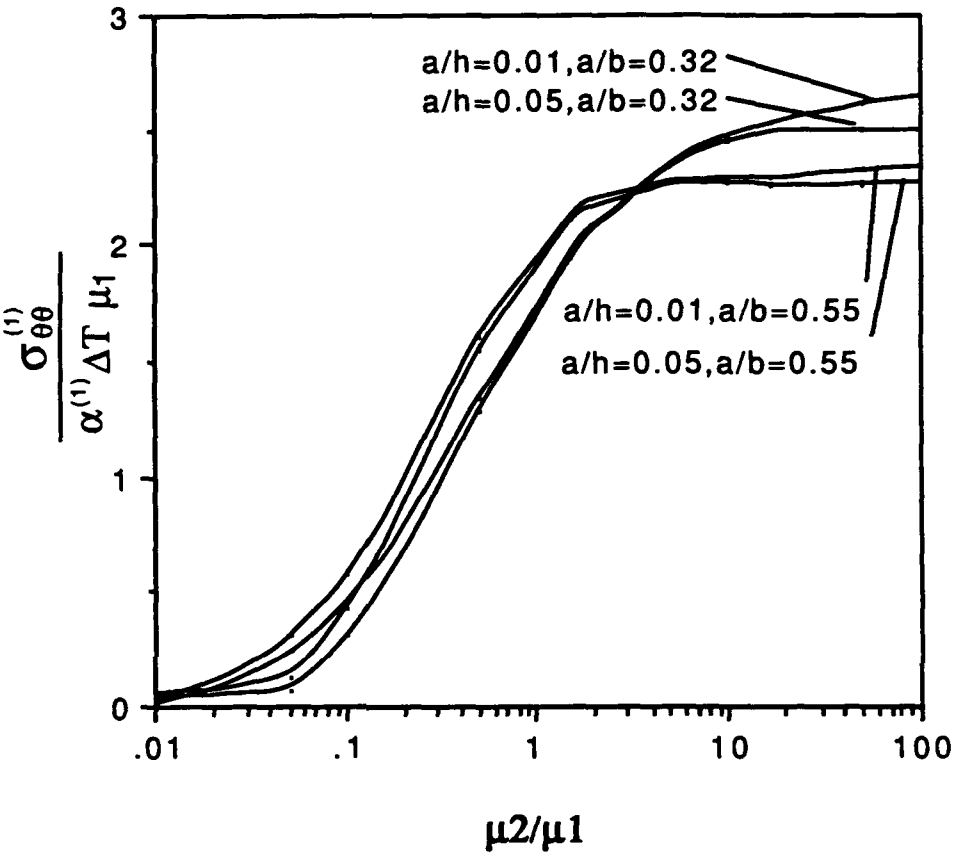

Figure 5.53.Stress $\sigma_{\theta\theta}^{(1)}$ at r=a z=0, $\theta=\pi/4$ vs μ_2/μ_1 for periodic fibers model where $v_1=0.34, v_2=0.22$

CHAPTER 6

CONCLUSIONS AND RECOMMENDATIONS

6.1 Conclusions

In view of the numerical results discussed above, the following conclusions may be made:

1. The thickness and distance of adjacent fibers of a plate , as well as the material properties, play a fundamental role in the failure mechanism of a plate with one or periodic cylindrical inclusions. More specifically, the geometric parameters a/h, a/b and the shear moduli ratio μ_2/μ_1 are three important ratios that not only control the location where a failure initiation may occur, but may also determine the direction where the crack propagates.

2. The value of shear moduli ratio μ_2/μ_1 may also be used to predict the direction of a crack initiation. As for a small ratio of μ_2/μ_1 (<10), a radial crack may initiate first whereas for a large ratio of μ_2/μ_1 (>15), a crack along the fiber-matrix interface may initiate first then.

3. The ratio of thermal expansion coefficient $\alpha^{(2)}/\alpha^{(1)}$ presents a linear action to the displacement and stress fields.

4. Under the cooling process as discussed in this thesis, the failure (debonding, slippage and breakage) will most likely be induced by the effect of the radial stress σ_{rr} or the circumferential stress $\sigma_{\theta\theta}^{(1)}$. One can predict, however, a conclusion based on the information discussed in Chapter 5, if the plate is subjected to a high temperature. In the case of an airplane with a high speed, a crack may initiate at the central region of the fiber

because in this circumstance, the axial stress $\sigma_{zz}^{(2)}$ in the fiber tends to be a large tensile stress that will control the failure of the plate.

5. The comparison of the current result with the result of Delale (1988) indicates that the current solution can predict the interfacial shear stress quite satisfactorily throughout the interface, whereas the 2-D solution obtained by Delale [36] neglects the effect of the mismatch along the axial direction, which has been proved to be a very important factor to the stress field for a thick plate.

6. An edge effect is confirmed to exist in the vicinity of the intersection of the interface (r=a) and the free surface (z=h) where the presence of a stress singularity may result in crack initiation.

7. Finally, to avoid unnecessary damage induced by the residual stress, an optimal design of fiber-reinforced composite material may be recommended to manufacturing engineers:

(a). The shear moduli ratio μ_2/μ_1 (fiber to matrix) is a factor that needs to be optimized. A high value of this ratio may cause a fiber/matrix interface crack (see Fig. 5.52) and therefore should be avoided in most circumstances.

(b). The fiber volume fraction v_f (i.e., the ratio of a/b) as well as the ratio a/h are also factors that need to be optimized. The maximum stress may change between the radial stress and the circumferential stress with the change of the ratios a/b and a/h. Thus, two types of failure immediately come to mind: a fiber/matrix interface crack and a radial matrix crack. One is able to deduce that the minimum critical residual stress occurs at the position where the radial stress σ_{rr} equals the circumferential stress $\sigma_{\theta\theta}^{(1)}$. The ratios of a/b and a/h may then be thought of as the optimal ratios to reduce the residual stress effect.

(c). The thermal expansion coefficients ratio $\alpha^{(2)}/\alpha^{(1)}$ presents a linear action to the residual stresses. It is optimal to use the materials of fiber and matrix with close thermal expansion coefficients to minimize the effect of the residual stresses.

6.2 Recommendations for Further Work

The present analysis does give some important information that can be used in the study of composite materials. However, much work still remains to be done in the future. General speaking, Folias' 3-D solution can be developed to solve more complicated problems if one knows how to modify the program to remedy the ill conditions. Based on the author's experience and knowledge, the following problems need to be addressed in the future:

(1). Perfect bonding and isotropic material of both fiber and matrix were assumed to prevail in this paper. However, a large mismatch has been found in the interface along the thickness. A slip in the axial direction may occur. So a new model that relaxes the assumption of perfect bonding to a partial debonding case must be dealt with. On the other hand, anisotropic properties exist in some materials, such as the carbon fiber. So the solution at hand may be developed to a more general case that is valid for an anisotropic material.

(2). Some pre-existing cracks can be introduced to the investigation. The particular solution in the method needs to be modified to handle the mixed condition at crack region.

(3). All of the previous research is limited to the " micro-approach," which considers the micromechanical behavior of only one ply of laminate. In practice, the interaction of the laminates and edge effect between the plies with different phases is also very important. How to develop a model that can be used to solve the multiply composites is an important consideration for future research.

APPENDIX A

THE SMALL CONTRIBUTIONS OF THE MODIFIED BESSEL FUNCTION I TO THE STRESS FIELD IN THE MATRIX

In this thesis, only the Bessel function K is used to match the stress field in the matrix (r > a region). Because the residual stresses are induced by the mismatch of fiber/matrix interface (r=a), the stresses in the matrix decrease along the radial direction r, which matches the trend of the modified Bessel function K. The other modified Bessel function, I, however, goes to infinity as r increases; therefore it is expected that the coefficient that multiplies this function must decrease rather rapidly.

In order to confirm that the effect of adding the term of the modified Bessel function I to the matrix can be neglected, an efficient procedure is as follows. Consider the linear system of both the governing equations and boundary conditions, which may be expressed as follows:

$$L[U] = \quad \text{(governing equations)} \qquad \text{(A-1)}$$

$$M[U] = 0 \quad \text{(boundary conditions)} \qquad \text{(A-2)}$$

Let:

$$U = u + u^*, \qquad \text{(A-3)}$$

where u represents the part that is used in this thesis and u^* represents the solution with the modified Bessel function I. Then from equations (D-1)-(D-3), one gets:

$$L[u+u^*] = L[u] + L[u^*] = 0 + L[u^*] = L[u^*] = 0 \qquad \text{(A-4)}$$

$$M[u+u^*] = M[u] + M[u^*] = \varepsilon + M[u^*] = 0 \qquad \text{(A-5)}$$

where ε is the error of the boundary conditions obtained before. It may be noted that equation (D-4) is satisfied automatically and that the only problem remaining is to solve equation (D-5), which may be expressed as a new linear system:

$$A^* x = C = -\varepsilon \qquad \text{(A-6)}$$

Solving for the constants x and computing the additional stress field σ^*, one can see clearly that the contribution of the modified Bessel function I to the stress field in the matrix is negligible.

Figs.D.1 to D.4 show us the profiles of the ratio of this additional stress to the stresses obtained before. Both the radial stress σ_{rr} and the circumferential stress $\sigma_{\theta\theta}$ are shown as a function of r/a or z/h, respectively. Two different sets of roots are given in the plots to show the difference of the value. It is noted from these plots that the contribution due to the extra term is less than 0.5% of the stress field, which was obtained previously. This confirms the assumption that the contributions due to the modified Bessel function I may be neglected and still have accuracy up to 1%. By utilizing, however, both solutions, one may calculate the stress field to within an error of less than 0.1%.

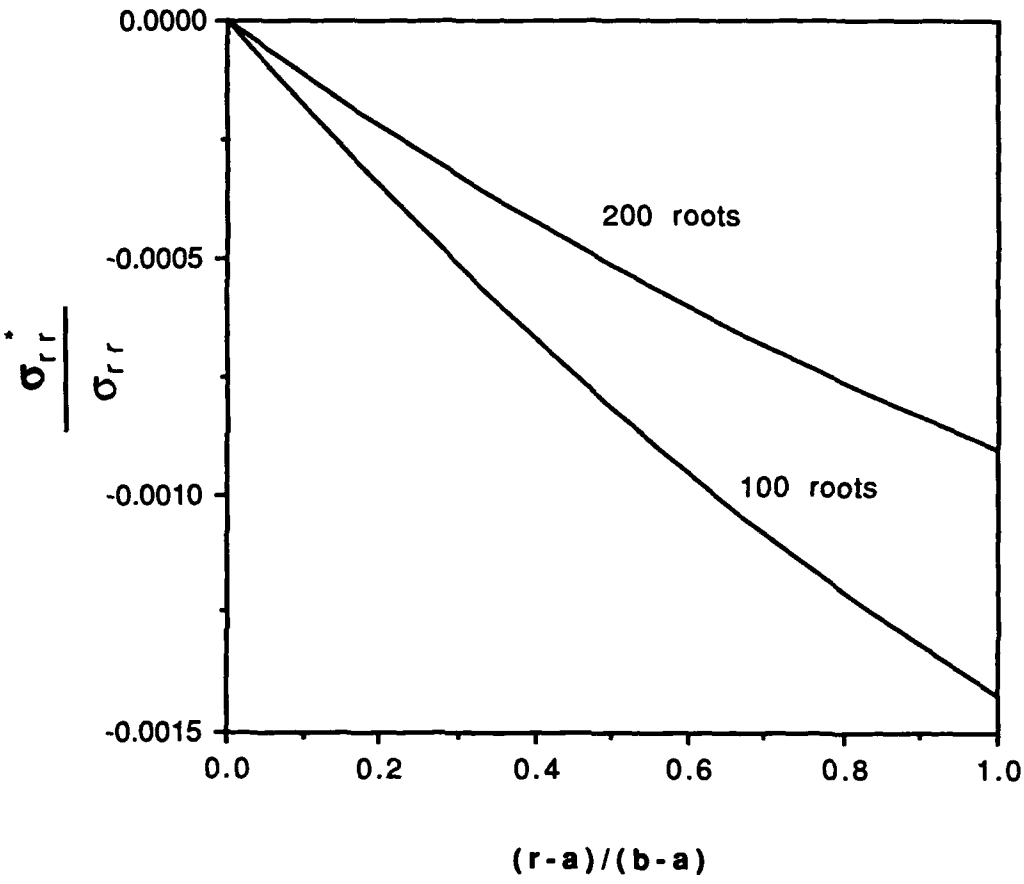

Figure D.1. The ratio of stress σ_{rr} at z=0, $\theta=\pi/4$ vs (r-a)/(b-a) for periodic fibers model where $v_1=0.34$, $v_2=0.22$,$\mu_2/\mu_1=16.67$, a/b=0.55 and a/h=0.05

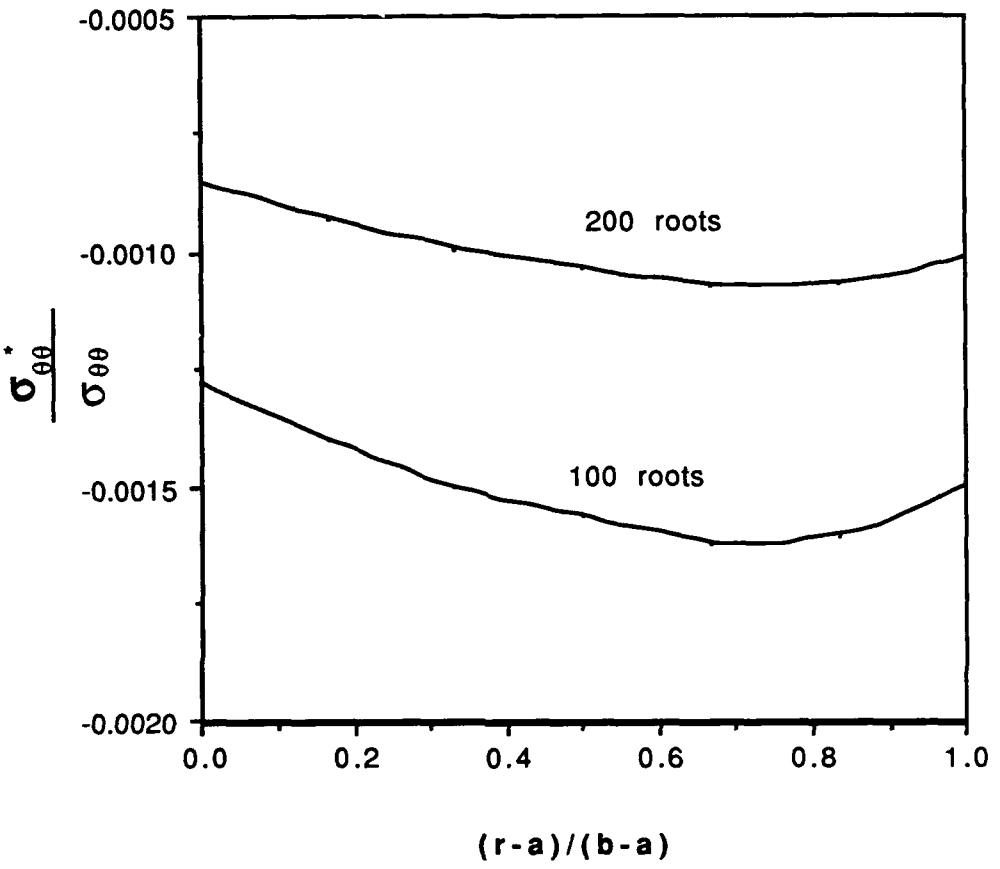

Figure D.2. The ratio of stress $\sigma_{\theta\theta}$ at z=0, $\theta=\pi/4$ vs (r-a)/(b-a) for periodic fibers model where v_1=0.34, v_2=0.22,μ_2/μ_1=16.67, a/b=0.55 and a/h=0.05

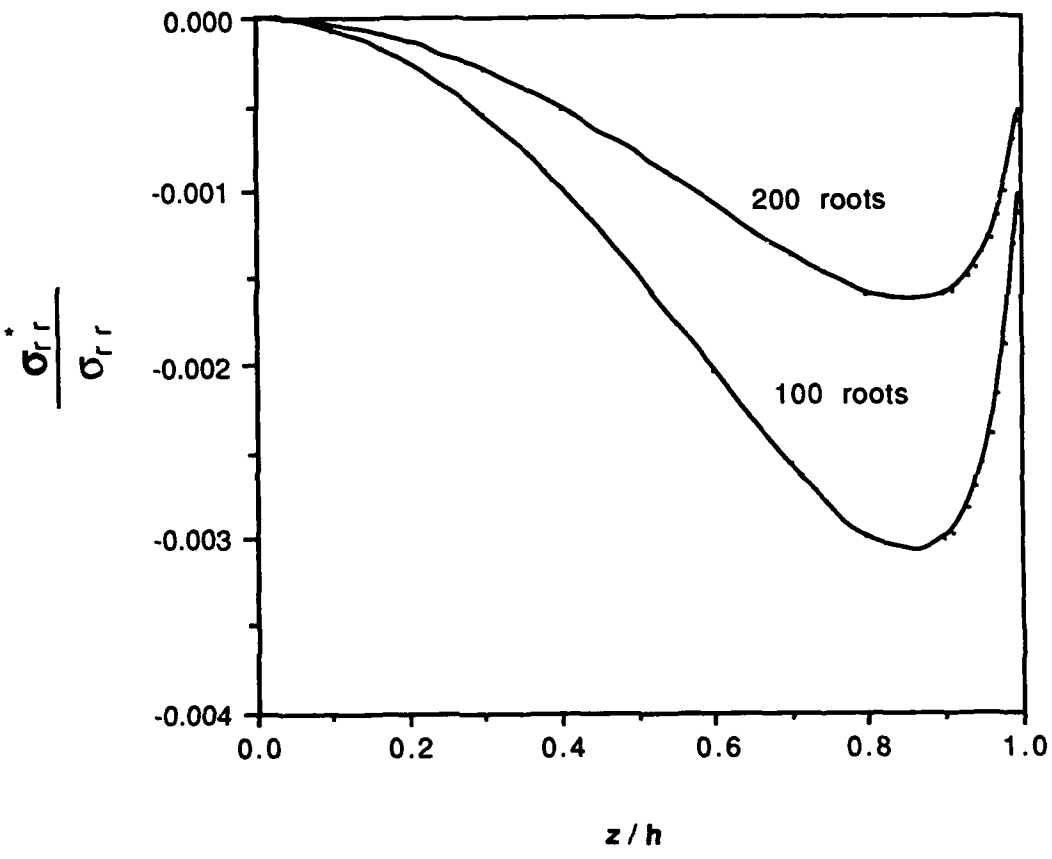

Figure D.3. The ratio of stress σ_{rr} at r=a, $\theta=\pi/4$ vs z/h for periodic fibers model where $v_1=0.34$, $v_2=0.22$,$\mu_2/\mu_1=16.67$, a/b=0.55 and a/h=0.05

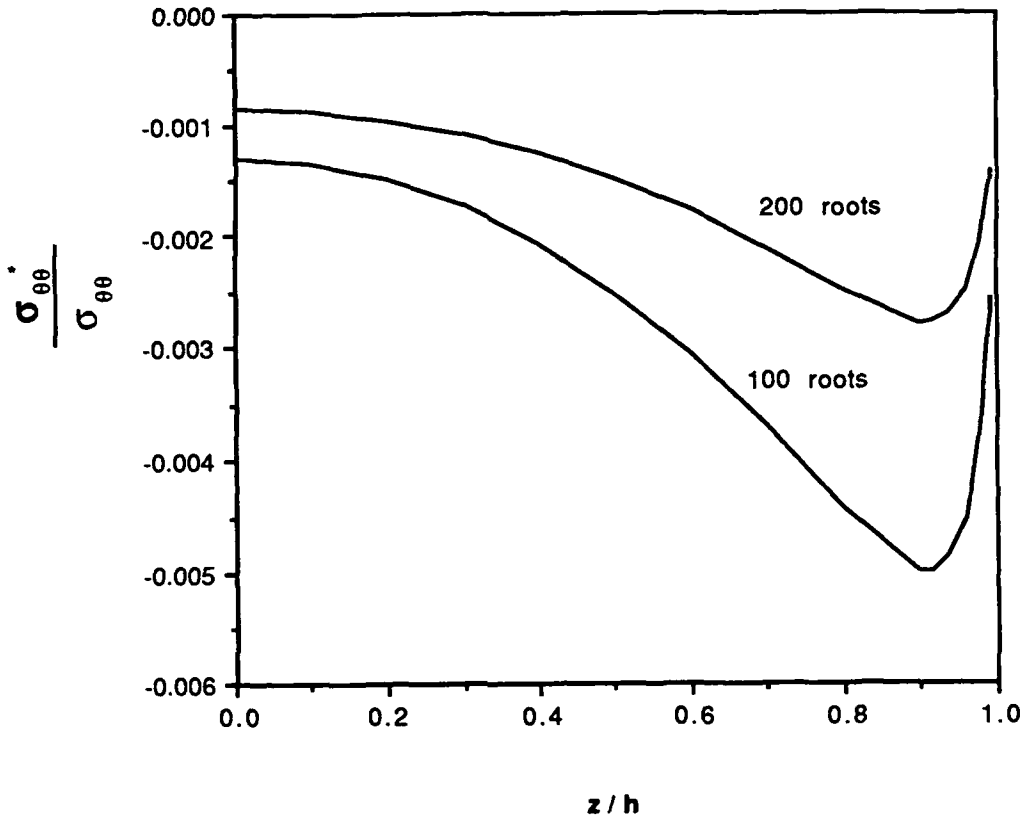

Figure D.4. The ratio of stress $\sigma_{\theta\theta}$ at r=a, $\theta=\pi/4$ vs z/h for periodic fibers model where $v_1=0.34$, $v_2=0.22$,$\mu_2/\mu_1=16.67$, a/b=0.55 and a/h=0.05

REFERENCES

1. E. Reissner, 'On the Calculation of 3-D Corrections for the 2-D Theory of Plane Stress', in *Proceedings of the Fifteenth Semi-Annual Eastern Photoelasticity Conference* (1942).

2. A.E. Green, '3-D Stress Systems in Isotropic Plates, I', *Transactions of the Royal Society of London, London, England, Series A* 240 (1948) 561-570.

3. A.E. Green, 'The Elastic Equilibrium of Isotropic Plates and Cylinders', in *Proceedings of the Royal Society of London, London,England, Series A* 195 (1949) 533-546.

4. J.B. Alblas, 'Theorie Van de Driedimensionale Spanning Stoestand in een Doorboorde plaat', *Doctoral Dissertation, Technische Hogeschool Delft, H.J.Paris, Amsterdam, The metherlands* (1957).

5. E.L. Reiss and S. Locks, 'On the Theory of Plane Stress', *Quarterly of Applied Mathematics* 19 (1961) 195-204.

6. C.K. Yourgdahl and E. Sternberg, '3-D Stress Concentration Around a Cylindrical Hole in a Semi-Infinite Elastic Body', *Journal of Applied Mechanics* 33 (1966) 855-865.

7. E.S. Folias, 'On the Three Dimensional Theory of Cracked Plates', *Journal of Applied Mechanics.* 42 (1975) 663-674.

8. J.J. Wang and E.S. Folias, 'On the Three Dimensional Stress Field Around a Circular Hole in a Plate of Arbitrary Thickness', in *Proceedings of the 19th Midwestern Mechanics Conference, Columbus, Ohio* (1985).

9. E.S. Folias, 'The 3-D Stress Field at the intersection of a Hole and a Free Surface', *International Journal of Fracture* 35 (1987) 187-194.

10. F.E. Penado and E.S. Folias, 'The 3-D Stress Field Around a Cylindrical inclusion in a Plate of Arbitrary Thickness', *International Journal of Fracture* 39 (1989) 129-146.

11. E.S. Folias, 'On the Stress Singularities at the intersection of a Cylindrical Inclusion with the Free Surface of a Plate', *International Journal of Fracture* 39 (1989) 25-34.

12. E.S. Folias and J.H. Liu, 'On the 3D Modeling of a Fiber/Matrix Interface', (in press).

13. F.H. Zhong and E.S. Folias, 'The three-Dimensional Stress Field of a Fiber Embedded into a Matrix and Subjected to an Axial Load', *Ph.D Thesis, University of Utah* (1991).

14. J.G. Goree, 'In-Plane Loading in an Elastic Matrix Containing Two Cylindrical Inclusions', *Journal of Composite Materials* 1 (1967) 404-412.

15. J.M. Hedgpeth, 'Local Stress Concentrations in Imperfect Filamentary Composite Materials', *Journal of Composite Materials* 1 (1967) 294-309.

16. D.F. Adams, 'Longitudinal Shear of a Unidirectional Composite', *Journal of Composite Materials* 1 (1967) 4-17.

17. D.F. Adams, 'Transverse Normal Loading of a Unidirectional Composite', *Journal of Composite Materials* 1 (1967) 152-164.

18. J. Haener, 'Three-Dimensional Stress Distribution in a Unidirectional Composite', *Journal of Composite Materials* 1 (1967) 54-63.

19. R.H. Marloff and I.M. Daniel, 'Three-Dimensional Photoelastic Analysis of a Fiber-Reinforced Composite Model', *Experimental Mechanics*, 9 (1969) 156-167.

20. L.M. Keer, et al., 'Separation of a Smooth Circular Inclusion from a Matrix', *International Journal of Engineering Science* 11 (1973) 1221-1233.

21. G.P. Sendeckyj, 'Elastic Inclusion Problems in Plane Elastostatic', *International Journal of Solids and Structure* 6 (1970) 1535-1543.

22. I.W. Yu and G.P. Sendeckyj, 'Multiple Circular Inclusion Problems in Plane Elastostatics', *Journal of Applied Mechanics* 41 (1974) 215-221.

23. D.F. Adams and D.A. Crane, 'Combined Loading Micro-Mechanical Analysis of a Unidirectional Composite', *Composite* 15 (1984) 181-191.

24. Anthony G. Evans, et al., 'The Mechanics of Matrix Cracking in Brittle-Matrix Fiber Composites', *Journal of American Ceramic Society* 73, No.6 (1985) 1691-1699.

25. M. Isida, in *Private Communication* (1990).

26. E.S. Folias and J.H. Liu, 'On the Three-Dimensional Stress Field of a Periodic Array of Fibers Embedded into a Plate Matrix', (in press).

27. E.S. Folias and J.H. Liu, 'A 3D Model for the Stress Field in a Composite Plate Subjected to a Longitudinal Loading', (in press).

28. O.H. Griffin, 'Three-Dimensional Curing Stresses in Symmetric Cross-Ply Laminates with Temperature-Dependent Properties', *Journal of Composite Materials* 17 (1983) 449-463.

29. O.H. Griffin and J.C. Roberts, 'Numerical/Experimental Correlation of Three-Dimensional Thermal Stress Distributions in Graphite/Epoxy Laminates', *Journal of Composite Materials* 17 (1983) 539-548.

30. D.E. Bowles, 'Effect of Microcracks on the Thermal Expansion of Composite Laminates', *Journal of Composite Materials* 17 (1984) 173-187.

31. Anthony G. Evans, et al., 'High-Temperature Mechanical Properties of a Ceramic Matrix Composite', *Journal of American Ceramic Society* 70, No.7 (1987) 466-469.

32. A.C. Garg, 'Effect of Moisture and Temperature on Fracture Behavior of Graphite-Epoxy Laminates', *Engineering Fracture Mechanics* 29 (1988) 127-149.

33. G.P. Fang, 'Thermally-Induced Fracture in Composites', *Engineering Fracture Mechanics* 33 (1989) 619-632.

34. Y. Mikata and M. Taya, 'Stress Field in a coated Continuous Fiber Composite Subjected to Thermo-Mechanical Loadings', *Journal of Composite Materials*, 19 (1985) 554-578.

35. D.E. Bowles and S.S. Tompkins, 'Prediction of Coefficients of Thermal Expansion for Unidirectional Composites', *Journal of Composite Materials*, 23 (1988) 370-387.

36. F. Delale, 'Critical Fiber Size for Microcrack Suppression in Ceramic-Fiber/Ceramic-Matrix Composites', *Engineering Fracture Mechanics* 31 (1988) 145-155.

37. Anthony G. Evans, et al., 'Debonding Properties of Residually Stressed Brittle-Matrix Composites', *Journal of American Ceramic Society* 72, No.5 (1989) 746-753.

38. Anthony G. Evans, et al., 'Effect of Interfaces on the Properties of Fiber-Reinforced Ceramics', *Journal of American Ceramic Society* 73, No.6 (1990) 1691-1699.

PART VI

THE 3D STRESS FIELD OF A FIBER EMBEDDED INTO A MATRIX AND SUBJECTED TO AN AXIAL LOAD

by

F. H. Zhong and E. S. Folias

The Department of Mechaniacl Engineering
The University of Utah
Salt Lake City, UT 84112

Revised in August, 1991

ABSTRACT

This paper presents several topics related to the 3D mechanics study of a single fiber embedded into a matrix and subjected to axial loadings. Both the perfect bonding model and the imperfect bonding model are formulated and numerically solved by a method developed by Folias (1975, 1990). The numerical results show that the geometric ratio a/h (fiber radius to plate half thickness) and shear moduli ratio μ_2/μ_1 (fiber to matrix) have great effect on the stress field. The failure mechanisms corresponding to these different models are found in the paper. In addition, comparisons with the experimental results are also made.

INTRODUCTION

The problem of determining the stress distribution induced by inclusions under load has been a hot topic for about half a century. Two-dimensional solutions (plane stress and plane strain) for plates with perfectly bonded circular inclusions can be found in the papers of Sendeckyj (1970) and of Yu and Sendeckyj (1974). A general representation of the solution of the elastic curvilinear inclusion problem is presented by Sendeckyj. As an example, the elliptical shape of inclusion is discussed. The discussion is limited to the case of an infinite matrix. Later, the problem of an unbounded elastic matrix containing any number of elastic inclusions is solved by Yu et al.. Both of these use the complex variable formulation. A more practical model for the mechanical behavior of unidirectional fiber-reinforced materials subjected to axial loading is examined by Bloom (1967), where a hexagonal array of perfectly bonded filaments is assumed. While these approaches are well understood in two dimensions, they are less so in three. Since these solutions are based on two-dimensional considerations, the effect of the thickness of the plate on the stress distributions could not be examined.

Three dimensional solutions to similar problems are not fully investigated due to the mathematical difficulties involved. Muki and Sternberg in 1970 investigated the diffusion of an axial load from a bar of arbitrary uniform cross-section that is immersed in, up to a finite depth, and bounded to a semi-infinite solid of distinct elastic properties. Their approximate method requires the radius of the rod to be small in comparison to its length. Luk and Keer in 1979 investigated a very similar problem. The rod bar at this time is assumed to be rigid. Many plots of the stresses based on numerical calculation are given. The authors have also examined what effect different parameters of the problem have on the stress field. It is important to note that all of the above works deal with one perfect isolated

inclusion. On the other hand, in a fiber-reinforced composite thousands of fibers can be used to construct one layer of the laminate. Similar to the geometry of the problem examined by Bloom (1967), a three-dimensional solution is achieved by using Boussinesq-Papkovitch potentials by Haener (1967). However, only few numerical results are presented in the paper. Perhaps the reason for this is the numerical complexity encountered because of the double summation. Folias in 1975 examined a method for constructing solutions to some three-dimensional mixed boundary-value problems and applied it to the problem of a uniform extension of an infinite plate containing a through the thickness line crack. Subsequently the general solution is used to investigate some related problems. In Penado and Folias (1989), the stress field around a cylindrical inclusion in a plate of arbitrary thickness is investigated, where a uniform tension is applied in the plane of the plate at points far remote from the inclusion. Since the thickness of the plate is no longer assumed to be infinite or semi-infinite, the results allow the examination of very thick and very thin plates and bridge the gap in between.

While all above discussions are restricted to the case of a perfect bonding condition at the interface, there are few analytical models which deal with the imperfect bonding problem. The first model assumes that the inclusion and the plate are connected by an elastic spring at the interface. Tractions and displacements u and v are continuous across the interface, but the vertical displacement w may not be continuous and the difference Δw is assumed to be proportional to the shear stress τ_{rz} at the interface. Papers by Lawrence (1972) and Banbaji (1988) approach the problem based on shear lag analysis and the results are, therefore, approximate. Most recent work done by Steif and Hoysan (1986) approaches the problem based on 2D considerations and the case in which the fiber and the matrix have identical elastic properties is solved. Numerical solutions for cases in which the fiber and the matrix have different elastic properties are obtained by a finite element method. The second model

developed by Dollar and Steif (1988) assumes that the transfer of load at the interface is described by Coulomb friction. The mathematical models for stick, slip and separation conditions are given and the residual stress σ_{rr} is introduced into the discussion. These two models have their deficiency which will be seen later. Haritos and Keer (1985) considered the problem of a finite, rigid insert partially embedded in and adhesively bonded to an elastic half plane. The problem is then formulated in terms of a singular integral equation which is solved numerically. The fiber/matrix debonding problem is solved by Gao et al. (1988) based on the fracture energy balance. The friction at the debonded interface and the Poisson contraction of the fiber are included. Interfacial friction is shown to have a significant effect on the debonded load. A similar work is also carried out later by Penn and Lee (1989). Shear lag models are used both in these two papers to calculate the stress and the displacement fields.

A boundary layer effect is expected to prevail in the neighborhood of the intersection of the interface and of the plate surface. This matter has recently been investigated by Folias (1989) based on 3D consideration, where by assuming a certain form of the solution he was able to use an asymptotic expansion developed by Williams (1959) and to extract the explicit displacement and stress fields. The stress field is shown to be proportional to $\rho^{-\alpha}$ where α is a weak singularity which depends on the material properties and the angle of intersection of the fiber with the free surface.

On the other hand, the experiments focusing on the interfacial strength have also been a hot topic for quite a while. Experiments on a two dimensional model of an aluminium alloy fiber in an Araldite resin are carried out by Tyson and Davies (1965), the interfacial shear stress is obtained by photoelastic method. Experiments conducted by Chua and Piggott (1985) have measured several important parameters, such as interfacial yield strength and

an interfacial work of fracture. The stress transfer and fracture in single fiber/epoxy composites have been investigated by DiBenedetto et al. (1986) and Bascom et al. (1986). Their main efforts is to find the cumulative distribution of critical fiber lengths, which can be used to calculate the interfacial shear strength.

The purpose of this analysis is to consider a similar problem as that of Penado et al. (1989), but the plate is now subjected to a uniform tensile load along the axis of the cylindrical inclusion. As far as the authors know, no analytical work for the problem under consideration has ever been carried out. The method which will be used in this analysis is the same as that of Folias (1975, 1990). The problem will subsequently be extended to two other cases: first the plate surface will also be allowed to carry a portion of the load and second the interface will be assumed to be imperfectly bonded. A fracture mechanics approach is beyond the scope of current analysis. It is expected, however, that the current analysis will lead to the calculation of strain energy more accurately in the future. In order to simplify the mathematical complexities of our problem, the following assumptions will be made:

(1). Both the plate and the inclusion are made of isotropic, homogeneous and linearly elastic materials.

(2). As a first step, only one isolated inclusion is assumed to be embedded into the plate.

FORMULATION OF THE PROBLEMS

Perfect Bonding model 1

we consider a body which occupies the space $|x|<\infty$, $|y|<\infty$, $|z|\le h$ and contains two regions with different elastic properties. The inclusion is a cylinder of radius $r=a$ through the thickness (see Fig.1). For convenience, the region $r>a$ (plate) and the region $r<a$ (inclusion) are denoted by superscripts (1) and (2), respectively. Uniformly distributed tensile stress σ_0 is applied both on the bottom and the top of the inclusion and all other boundaries are assumed free of stress.

In the absence of body forces, the governing equation (Navier's equation) for the displacements $u^{(i)}$, $v^{(i)}$, $w^{(i)}$ (i=1,2) is

$$\frac{m_i}{m_i-2}\frac{\partial e^{(i)}}{\partial x_k}+\nabla^2 u_k^{(i)}=0; \quad (k=1,2,3) \tag{2.1}$$

where ∇^2 is the 3D Laplacian operator, $m_i=1/\nu_i$, ν_i is Poisson's ratio and

$$e^{(i)}=\frac{\partial u_k^{(i)}}{\partial x_k}; \quad k=1,2,3 \tag{2.2}$$

The stress-displacement relations are given by Hooke's law as:

$$\sigma_{kl}^{(i)}=2\mu_i\{\frac{1}{m_i-2}e_{jj}^{(i)}\delta_{lk}+e_{lk}^{(i)}\}; \; k,l=1,2,3 \tag{2.3}$$

where μ_i are the respective shear moduli.

As to the boundary conditions one must require that

as $r \to \infty$;

$$\sigma_{xx}^{(1)}=\sigma_{yy}^{(1)}=\sigma_{zz}^{(1)}=0 \tag{2.4}$$

$$\tau_{xy}^{(1)}=\tau_{yz}^{(1)}=\tau_{xz}^{(1)}=0 \tag{2.5}$$

at $z=|h|$;

$$\tau_{xz}^{(1)}=\tau_{yz}^{(1)}=\sigma_{zz}^{(1)}=0 \tag{2.6}$$

$$\tau_{xz}^{(2)}=\tau_{yz}^{(2)}=0 \tag{2.7}$$

$$\sigma_{zz}^{(2)}=\sigma_0 \tag{2.8}$$

at $r=a$;

$$\sigma_{rr}^{(1)} - \sigma_{rr}^{(2)} = \tau_{r\theta}^{(1)} - \tau_{r\theta}^{(2)} = \tau_{rz}^{(1)} - \tau_{rz}^{(2)} = 0 \tag{2.9}$$

$$u_{rr}^{(1)} - u_{rr}^{(2)} = u_{\theta\theta}^{(1)} - u_{\theta\theta}^{(2)} = u_{zz}^{(1)} - u_{zz}^{(2)} = 0 \tag{2.10}$$

also the following continuity condition must hold

at $r=0$; all stresses and displacements for

the inclusion must be bounded (2.11)

Our approach is to seek a solution in the form:

$$u^{(i)}=u^{(p)(i)} + u^{(c)(i)} \tag{2.12}$$

$$v^{(i)}=v^{(p)(i)} + v^{(c)(i)} \tag{2.13}$$

$$w^{(i)}=w^{(p)(i)} + w^{(c)(i)} \tag{2.14}$$

where the component with the superscript (p) represents the particular solution, and the component with the superscript (c) represents the complementary solution.

In general, the particular solution is relatively easy to obtain. It must satisfy the governing equation (2.1) as well as the boundary condition far away from the inclusion. For the problem under consideration, the particular solution in cylindrical coordinates is:

(1) for the plate:

$$u_{rr}^{(p)(1)}=u_{\theta\theta}^{(p)(1)}=u_{zz}^{(p)(1)}=0 \tag{2.15}$$

$$\sigma_{rr}^{(p)(1)}=\sigma_{\theta\theta}^{(p)(1)}=\sigma_{zz}^{(p)(1)}=0 \tag{2.16}$$

$$\tau_{r\theta}^{(p)(1)}=\tau_{rz}^{(p)(1)}=\tau_{\theta z}^{(p)(1)}=0 \tag{2.17}$$

(2) for the inclusion:

$$u_{rr}^{(p)(2)}=C_1 r \tag{2.18}$$

$$u_{\theta\theta}^{(p)(2)}=0 \tag{2.19}$$

$$u_{zz}^{(p)(2)}=\left[\frac{\sigma_0}{2\mu_2}\frac{1-2\nu_2}{1-\nu_2}-\frac{2\nu_2}{1-\nu_2}C_1\right]z \tag{2.20}$$

$$\sigma_{rr}^{(p)(2)}=\sigma_{\theta\theta}^{(p)(1)}=\sigma_0\frac{\nu_2}{1-\nu_2}+2\mu_2\frac{1+\nu_2}{1-\nu_2}C_1 \tag{2.21}$$

$$\sigma_{zz}^{(p)(2)}=\sigma_0 \tag{2.22}$$

$$\tau_{r\theta}^{(p)(2)}=\tau_{rz}^{(p)(2)}=\tau_{\theta z}^{(p)(2)}=0 \tag{2.23}$$

where C_1 is a constant to be determined later from the boundary conditions of the complementary problem.

In view of the particular solution, one needs to find six complementary displacements $u^{(i)}$, $v^{(i)}$, $w^{(i)}$ (i=1, 2), such that they satisfy both the governing equation and the boundary conditions:

at $|z|=h$; $\tau_{xz}^{(c)(i)}=\tau_{yz}^{(c)(i)}=\sigma_{zz}^{(c)(i)}=0$ (2.24)

at $r=a$; $\sigma_{rr}^{(c)(1)}-\sigma_{rr}^{(c)(2)}=-\sigma_{rr}^{(p)(1)}+\sigma_{rr}^{(p)(2)}$ (2.25)

$$\tau_{r\theta}^{(c)(1)}-\tau_{r\theta}^{(c)(2)}=-\tau_{r\theta}^{(p)(1)}+\tau_{r\theta}^{(p)(2)} \quad (2.26)$$

$$\tau_{rz}^{(c)(1)}-\tau_{rz}^{(c)(2)}=\tau_{rz}^{(p)(1)}-\tau_{rz}^{(p)(2)} \quad (2.27)$$

$$u_{r}^{(c)(1)}-u_{r}^{(c)(2)}=-u_{r}^{(p)(1)}+u_{r}^{(p)(2)} \quad (2.28)$$

$$u_{\theta\theta}^{(c)(1)}-u_{\theta\theta}^{(c)(2)}=-u_{\theta\theta}^{(p)(1)}+u_{\theta\theta}^{(p)(2)} \quad (2.29)$$

$$u_{zz}^{(c)(1)}-u_{zz}^{(c)(2)}=-u_{zz}^{(p)(1)}+u_{zz}^{(p)(2)} \quad (2.30)$$

It may be appropriate at this stage to point out that a uniform tensile stress σ_0 assumed in Fig.1 has neglected the stress concentration effect existing at the edge region. Such a stress concentration effect could be taken into account if one considers a non-uniform tensile stress acting on the fiber surface as shown in Fig. 2. It will be shown later that the error brought on by such a simplification is very localized (about one fiber diameter from the fiber end). A follow-up paper on this matter is under preparation.

Perfect bonding model 2

The above discussions are based on the fact that only the inclusion is subject to an axial load while the plate is free of any external loads. Such a model is often used to illustrate how the load is being transferred from the fiber to the matrix, as we have reviewed in the Introduction. But in reality in composites, both the fiber and the matrix carry portions of the external load provided that the shear modulus μ_1 of the matrix is not negligible. For this reason in Fig. 3 we consider a modified model which allows the plate to carry an axial load σ_i. The magnitude of σ_i may be different from that of σ_0 and in our subsequent numerical calculations, the ratio σ_i/σ_0 will be considered.

Most of the formulas developed for perfect bonding model 1 still hold except some modifications need to be made for expressions (2.15-2.17).

$$u_r^{(p)(1)} = -\frac{\sigma_i}{2\mu_1(m_1+1)} r \tag{2.31}$$

$$u_{\theta\theta}^{(p)(1)} = 0 \tag{2.32}$$

$$u_{zz}^{(p)(1)} = \frac{m_1\sigma_i}{2\mu_1(m_1+1)} z \tag{2.33}$$

$$\sigma_r^{(p)(1)} = \sigma_{\theta\theta}^{(p)(1)} = 0 \tag{2.34}$$

$$\sigma_{zz}^{(p)(1)} = \sigma_i \tag{2.35}$$

$$\tau_{r\theta}^{(p)(1)} = \tau_{rz}^{(p)(1)} = \tau_{\theta z}^{(p)(1)} = 0 \tag{2.36}$$

On the other hand, the particular solution for the inclusion is the same as that given in (2.18-2.23).

Imperfect Bonding Model

Perfect bonding conditions require that the displacements and the stresses be continuous at the interface throughout the thickness. Since both of the above models satisfy (2.9) to (2.10), we define them as perfect bonding cases. As it was previously noted, imperfect bonding models which have been examined based on 2D consideration are basically of two types: in the first type the transfer of load across the interface is described by Coulomb friction, while in the second the transfer of load across the interface is described by a continuous elastic spring connecting the fiber and the matrix. In this analysis we choose the latter for it is more suitable to the structure of our complementary solution given in the subsequent analysis.

This model is shown schematically in Fig. 4. Crucial to the problem of interest is the bonding between the fiber and the matrix at r=a where the relevant stresses as well as the

displacements u and v must be continuous. The vertical displacement w, however, is allowed to be discontinuous but its jump must be proportional to the shear stress. i.e., along r=a:

$$u_{zz}^{(1)}-u_{zz}^{(2)}=K_s\ \tau_{rz}^{(i)};\qquad (i=1 \text{ or } 2) \tag{2.37}$$

where $1/K_s$ is the interface shear stiffness.

A boundary condition of the type (2.37) is inappropriate for the edge region (near z=h) for the displacement field is non-singular while the stress field is singular (Folias, 1989). However, except in the boundary layer region, the results are expected to be valid.

In view of this consideration, the last boundary condition in (2.14) becomes

$$u_{zz}^{(1)}-u_{zz}^{(2)}=K_s\ \tau_{rz}^{(i)};\qquad (i=1 \text{ or } 2) \tag{2.38}$$

All other boundary conditions remain the same. Finally in terms of the complementary and particular solutions, the boundary condition (2.38) becomes

$$u_{zz}^{(c)(1)}-u_{zz}^{(c)(2)}=-u_{zz}^{(p)(1)}+u_{zz}^{(p)(2)}+K_s\ \tau_{rz}^{(i)} \tag{2.39}$$

All other boundary conditions are given by eq. (2.24-2.30).

It remains, therefore, for us to find a complementary solution such that it satisfies Navier's equations and the appropriate boundary conditions.

METHOD OF SOLUTION

The general method for constructing solutions to some 3D mixed boundary-value problems has been developed by Folias (1975, 1990). The solution may be written in the following more convenient form by considering θ-independence of the problem:

$$u^{(c)(i)}=\frac{1}{m_i-2}\sum_{\nu=1}^{\infty}\frac{\partial^2 H_\nu^{(i)}}{\partial x^2}\{2(m_i-1)f_1(\beta_\nu z)+m_i f_2(\beta_\nu z)\}$$
$$+\lambda_1^{(i)}-y\frac{\partial\lambda_3^{(i)}}{\partial x}+\frac{1}{m_i+1}z^2\frac{\partial^2\lambda_3^{(i)}}{\partial x\partial y} \qquad (3.1)$$

$$v^{(c)(i)}=\frac{1}{m_i-2}\sum_{\nu=1}^{\infty}\frac{\partial^2 H_\nu^{(i)}}{\partial x\partial y}\{2(m_i-1)f_1(\beta_\nu z)+m_i f_2(\beta_\nu z)\}$$
$$+\frac{3m_i-1}{m_i+1}\lambda_3^{(i)}+\lambda_2^{(i)}-y\frac{\partial\lambda_3^{(i)}}{\partial y}-\frac{1}{m_i+1}z^2\frac{\partial^2\lambda_3^{(i)}}{\partial x^2} \qquad (3.2)$$

$$w^{(c)(i)}=\frac{1}{m_i-2}\sum_{\nu=1}^{\infty}\frac{\partial H_\nu^{(i)}}{\partial x}\{(m_i-2)f_3(\beta_\nu z)-m_i f_4(\beta_\nu z)\}-\frac{2}{m_i+1}z\frac{\partial\lambda_3^{(i)}}{\partial x} \qquad (3.3)$$

Furthermore the stresses are given by the Hooke's law:

$$\frac{1}{2\mu_i}\sigma_{xx}^{(c)(i)}=\frac{1}{m_i-2}\sum_{\nu=1}^{\infty}\{2\beta_\nu^2\frac{\partial H_\nu^{(i)}}{\partial x}f_1(\beta_\nu z)+\frac{\partial^3 H_\nu^{(i)}}{\partial x^3}[2(m_i-1)f_1(\beta_\nu z)+m_i f_2(\beta_\nu z)]\}$$
$$+\frac{\partial\lambda_1^{(i)}}{\partial x}-y\frac{\partial^2\lambda_3^{(i)}}{\partial x^2}+\frac{2}{m_i+1}\frac{\partial\lambda_3^{(i)}}{\partial y}+\frac{1}{m_i+1}z^2\frac{\partial^3\lambda_3^{(i)}}{\partial x^2\partial y} \qquad (3.4)$$

$$\frac{1}{2\mu_i}\sigma_{yy}^{(c)(i)}=\frac{1}{m_i-2}\sum_{\nu=1}^{\infty}\{2\beta_\nu^2\frac{\partial H_n^{(i)}}{\partial x}f_1(\beta_\nu z)-(\frac{\partial^3 H_\nu^{(i)}}{\partial x^3}-\beta_\nu^2\frac{\partial H_\nu^{(i)}}{\partial x})[2(m_i-1)f_1(\beta_\nu z)+m_i f_2(\beta_\nu z)]\}$$

$$-\frac{\partial\lambda_1^{(i)}}{\partial x}+y\frac{\partial^2\lambda_3^{(i)}}{\partial x^2}+\frac{2m_i}{m_i+1}\frac{\partial\lambda_3^{(i)}}{\partial x}-\frac{1}{m_i+1}z^2\frac{\partial^3\lambda_3^{(i)}}{\partial x^2\partial y} \tag{3.5}$$

$$\frac{1}{2\mu_i}\sigma_{zz}^{(c)(i)}=-\frac{m_i}{m_i-2}\sum_{\nu=1}^{\infty}\frac{\partial H_\nu^{(i)}}{\partial x}\beta_\nu^2 f_2(\beta_\nu z) \tag{3.6}$$

$$\frac{1}{2\mu_i}\tau_{xy}^{(c)(i)}=\frac{1}{m_i-2}\sum_{\nu=1}^{\infty}\frac{\partial^3 H_\nu^{(i)}}{\partial x^2\partial y}\{2(m_i-1)f_1(\beta_\nu z)+m_i f_2(\beta_\nu z)\}$$
$$+\frac{\partial\lambda_2^{(i)}}{\partial x}+y\frac{\partial^2\lambda_3^{(i)}}{\partial x\partial y}+\frac{m_i-1}{m_i+1}\frac{\partial\lambda_3^{(i)}}{\partial x}-\frac{1}{m_i+1}z^2\frac{\partial^3\lambda_3^{(i)}}{\partial x^3} \tag{3.7}$$

$$\frac{1}{2\mu_i}\tau_{yz}^{(c)(i)}=-\frac{m_i}{m_i-2}\sum_{\nu=1}^{\infty}\frac{\partial^2 H_\nu^{(i)}}{\partial x\partial y}\beta_\nu\{f_3(\beta_\nu z)+f_4(\beta_\nu z)\} \tag{3.8}$$

$$\frac{1}{2\mu_i}\tau_{xz}^{(c)(i)}=-\frac{m_i}{m_i-2}\sum_{\nu=1}^{\infty}\frac{\partial^2 H_\nu^{(i)}}{\partial x^2}\beta_\nu\{f_3(\beta_\nu z)+f_4(\beta_\nu z)\} \tag{3.9}$$

where

$$\alpha_n=\frac{n\pi}{h},\quad n=1,2,3,..., \tag{3.10}$$

β_ν are the roots of the equation

$$\sin(2\beta_\nu h)=-2\beta_\nu h \tag{3.11}$$

$H_\nu^{(i)}$ (i=1, 2) are functions of x and y which satisfy the reduced wave equation:

$$\left(\frac{\partial^2}{\partial x^2}+\frac{\partial^2}{\partial y^2}-\beta_\nu^2\right)H_\nu^{(i)}=0 \tag{3.12}$$

$\lambda_1^{(i)}$, $\lambda_2^{(i)}$ and $\lambda_3^{(i)}$ are two dimensional harmonic functions, and

$$f_1(\beta_\nu z)=\cos(\beta_\nu h)\cos(\beta_\nu z) \tag{3.13}$$

$$f_2(\beta_\nu z)=\beta_\nu h\sin(\beta_\nu h)\cos(\beta_\nu z)-\beta_\nu z\cos(\beta_\nu h)\sin(\beta_\nu z) \tag{3.14}$$

$$f_3(\beta_v z)=\cos(\beta_v h)\sin(\beta_v z) \tag{3.15}$$

$$f_4(\beta_v z)=\beta_v h\sin(\beta_v h)\sin(\beta_v z) + \beta_v z\cos(\beta_v h)\cos(\beta_v z) \tag{3.16}$$

The reader may notice that the above complementary solution automatically satisfies the boundary conditions at |z|=h and that it only remains to satisfy the remaining boundary conditions at the interface r=a.

In the case of perfect bonding (model 1 and model 2), we transform the complementary solution into cylindrical coordinates in order to take advantage of the symmetry. Thus, equations (2.25-2.30) may be written in the following form:

$$\sin^2\theta(\sigma_{xx}^{(c)(1)} - \sigma_{xx}^{(c)(2)}) + \cos^2\theta\,(\sigma_{yy}^{(c)(1)} - \sigma_{yy}^{(c)(2)}) + \sin(2\theta)(\tau_{xy}^{(c)(1)} - \tau_{xy}^{(c)(2)})$$

$$= \sigma_0 \frac{\nu_2}{1-\nu_2} + 2\mu_2 \frac{1+\nu_2}{1-\nu_2} C_1 \tag{3.17}$$

$$\frac{1}{2}\sin 2\theta(\sigma_{xx}^{(c)(1)} - \sigma_{xx}^{(c)(2)}) - \frac{1}{2}\sin 2\theta\,(\sigma_{yy}^{(c)(1)} - \sigma_{yy}^{(c)(2)}) + \cos(2\theta)(\tau_{xy}^{(c)(1)} - \tau_{xy}^{(c)(2)}) = 0 \tag{3.18}$$

$$\sin\theta(\tau_{xz}^{(c)(1)} - \tau_{xz}^{(c)(2)}) + \cos\theta(\tau_{yz}^{(c)(1)} - \tau_{yz}^{(c)(2)}) = 0 \tag{3.19}$$

$$\sin\theta(u^{(c)(1)} - u^{(c)(2)}) + \cos\theta(v^{(c)(1)} - v^{(c)(2)}) = C_1 a + \frac{\sigma_i}{2\mu_1(m_1+1)} a \tag{3.20}$$

$$\cos\theta(u^{(c)(1)} - u^{(c)(2)}) - \sin\theta(v^{(c)(1)} - v^{(c)(2)}) = 0 \tag{3.21}$$

$$w^{(c)(1)} - w^{(c)(2)} = \left[\frac{\sigma_0}{2\mu_2}\frac{1-2\nu_2}{1-\nu_2} - \frac{2\nu_2}{1-\nu_2} C_1\right] z - \frac{m_1\sigma_i}{2\mu_1(m_1+1)} z \tag{3.22}$$

In as much as model 1 is a special case of model 2 wth σ_i=0, from here on we will concentrate on the recovery of the solution to model 2.

Taking into account the symmetry of the problem (θ independence), we let

$$\frac{\partial H_\nu^{(1)}}{\partial x} = C_{1\nu} K_0(\beta_\nu r) \tag{3.24}$$

$$\frac{\partial H_\nu^{(2)}}{\partial x} = C_{2\nu} I_0(\beta_\nu r) \tag{3.25}$$

and all λ=0 except

$$\lambda_1^{(1)} = \frac{A}{r}\sin\theta \tag{3.26}$$

$$\lambda_2^{(1)} = \frac{A}{r}\cos\theta \tag{3.27}$$

where I_0 and K_0 are, respectively, the modified Bessel functions of the first and second kind of order zero; $C_{1\nu}$ and $C_{2\nu}$ are complex constants. The constants A and C_1 are to be determined in such a way that all remaining conditions are satisfied.

In the case of imperfect bonding, the boundary condition corresponding to (3.22) becomes

$$w^{(c)(1)} - w^{(c)(2)} = K_s \tau_{rz}^{(i)} + \left[\frac{\sigma_0}{2\mu_2}\frac{1-2\nu_2}{1-\nu_2} - \frac{2\nu_2}{1-\nu_2} C_1\right] z - \frac{m_1 \sigma_i}{2\mu_1(m_1+1)} z \tag{3.28}$$

while all other boundary conditions are obtained from (3.17-3.21) by letting σ_i =0.

RESULTS AND DISCUSSIONS

Perfect Bonding Model 1

In as much as the interface is of greatest practical interest, plots at r=a are given for the displacements and stresses as functions of z. The case of perfect bonding (model 1) will be taken as the basis of our first discussion. Two different shear moduli ratios are chosen: these are $\mu_2/\mu_1=2$ and $\mu_2/\mu_1=17$ corresponding to (a) and (b) respectively in each Figure. The purpose of these plots is to examine how the shear moduli ratio affects the displacement and the stress fields. Each plot consists of several curves which corresponds to different a/h ratios. Superscripts are used to distinguish whether the stress or displacement is in the fiber or in the matrix as they have been defined early in the Figure 1. However the superscripts are omitted if the stress or displacement is same for the fiber and the matrix at the interface.

Stress σ_{rr} (Fig.5 (a) (b)) increases with z/h. At the center region, the Figure shows only a slight change of the magnitude of the stress. However, it jumps suddenly to a large value near the plate surface, suggesting, therefore, the presence of a singularity (Folias, 1989). It is interesting to note that in the cases of small a/h ratios, σ_{rr} is slightly negative over a wide span of the center region. This suggests, therefore, that small compression exists at the interface between the fiber and the matrix at this region. In the cases of large a/h ratios, however, the positive value of σ_{rr} suggests that small tension exists at the interface. Our analysis shows that the shear stress τ_{rz} (see Fig. 6 (a) (b)) starts from zero at z=0 and then increases in absolute value along the interface. A sudden jump of the stress near the points z=h is observed and may very well explain why a crack is most likely to initiate at this region. The sign for the shear stress is negative because the shear stress will always be opposing the direction of the external stress σ_0 applied at the face of the fiber. The variation of the magnitude of the shear stress τ_{rz} seems more complicated in the cases with $\mu_2/\mu_1=17$

than in the cases with $\mu_2/\mu_1=2$ because the former one (Fig. 6 (b)) shows the shear stress to return as a/h increases after it reaches a maximum absolute value at a certain a/h value. It appears that both "very thick" and "very thin" plates will induce very small shear stress at the center region. The matrix tensile stress $\sigma_{zz}^{(2)}$ at the interface is plotted in Fig. 7(a) (b), the stress increases as ratio a/h increases. A extremely high stress in the vicinity of fiber end may cause the matrix to break at this region. For most cases, the stress $\sigma_{zz}^{(2)}$ shown in Fig. 8 (a) (b) decays as z/h moves from the fiber end (z=h) to the fiber center (z=0). But for the cases with a/h=1.0, the result shows that the stress bounces back slightly when it reaches the fiber center. It is also noted that the tensile stress at the matrix will decrease as μ_2/μ_1 increases by comparing Fig. 7(b) with Fig. 7(a) while the tensile stress at the fiber will increase by comparing Fig. 8(b) with Fig. 8(a). This suggests that the load diffusion from the fiber to the matrix will decrease when the fiber is stiffer.

The displacement u_{zz} at z=h vs the radial direction is given in Fig. 9. It shows that a softer fiber ($\mu_2/\mu_1=2$) gives a smoother connection of the displacement at r=a while a stiffer fiber ($\mu_2/\mu_1=17$) gives a sharper connection of the displacement at the interface.

Perfect Bonding Model 2

In as much as, in practice, the matrix also carries a small portion of the applied load it is desirable now to extend our model to the case where the matrix also carries part of the load in the direction of the fiber length. Thus, perfect bonding model 2 allows us to examine how the load is being transferred from the fiber to the matrix and vice versa. As it was previously noted, the perfect bonding model 1 is taken as the basis of our discussion. To obtain the effect of σ_i (recall Fig.3), the shear moduli ratio is chosen as $\mu_2/\mu_1=17$ and the geometric parameter a/h is fixed at a/h=0.05. Three curves are plotted in each figure, which corresponds to $\sigma_i/\sigma_0=0.0$, 0.05 and 0.1, respectively. It is worth pointing out that ratio

σ_i/σ_0 is not an independent parameter. Actually this ratio will depend on the shear moduli ratio μ_2/μ_1 if a uniform strain is assumed on the surface of fiber and matrix. Thus, for the parameters chosen, a realistic ratio of σ_i/σ_0 must be around 1/17.

Stress σ_{rr} shown in Fig. 10 will not be greatly influenced in the center region as σ_i/σ_0 increases. However it may jump to the negative direction when σ_i/σ_0 passes a certain critical value. The numerical calculations appears suggesting that the stresses (including other stresses which will be discussed later) will change the direction of the singularity when $\sigma_i/\sigma_0 > \mu_1/\mu_2$. Such a change indicates that the debonding in the edge region becomes less possible because of the negative value of the radial stress. Fig. 11 shows the shear stress τ_{rz} vs z/h. Identical to σ_{rr}, an increase of σ_i/σ_0 beyond a certain value will also change the sign of τ_{rz}, which implies that the shear stress now will be in the same direction of external tensile stress. Moreover, this figure suggests the presence of a negligible shear stress at the interface when σ_i/σ_0, μ_2/μ_1 and a/h are properly chosen. Fig. 12 shows $\sigma_{zz}^{(2)}$ at the interface. Notice that the magnitude of the stress dramatically increases as the ratio of σ_i/σ_0 increases (see the curve with $\sigma_i/\sigma_0=0.1$). This figure also indicates that the stress value at the center (z=0) may be the maximum value.

Imperfect Bonding Case

When the interface is allowed to slip, the magnitude of the stresses in the matrix will be expected to decrease while in the fiber they are expected to increase slightly. In order to show the effect of stiffness of the interface, two parameters are fixed: they are a/h=0.05 and $\mu_2/\mu_1=17$. Three curves, which corresponds to the reciprocal of the spring constants K_e=0,0, 0.1 and 1.0, are plotted.

The radial stress σ_{rr} shown in Fig. 13 increases slightly as the interface becomes softer (note K_e=0,0 corresponds to perfect bonding case, or, the rigid interface). This indicates that the softer interface will increase the chance of interfacial debonding. The shear stress τ_{rz} shown in Fig. 14, on the other hand, shows a dramatic decrease of the stress along the interface. It appears that the interface is somehow relaxed by a softer interface. The fiber tensile stress $\sigma^{(2)}_{zz}$ (Fig. 15) increases as slippage is allowed to increase. This suggests that less load will be transferred from the fiber to the matrix if the interface is softer, which also substantiates our initial assumption.

The spring constant can be calculated by the equations given by Stief and Hoysan (1986), where the coated fiber model and the interfacial crack model are considered. As pointed out by them, a significant change of stress field can only happen when the coating material is very soft. This means that the stress field calculated from the practical parameters may be quite close to that calculated from the perfect bonding model.

COMPARISONS AND CONCLUSIONS

Our present results are consistent with the previous observations based on 1D and 2D considerations (Lawrence, 1972 and Banbaji, 1988) that τ_{rz} and $\sigma_{zz}^{(2)}$ will attain their maximum values at the loaded end of the fiber. Although, our present model differs from previous 3D models (Muki et al. 1970, Luk et al. 1979, Haener et al. 1967), the stress profiles obtained are similar. For example, comparing the result of Haener (1965) to that of our perfect bonding model 1, one finds that the stresses $\sigma_{zz}^{(i)}$ and $\sigma_{rr}^{(i)}$ obtained in these two different models both show a flat behavior in the center region (actually the value is rather small in this region for σ_{rr}) and then a sudden jump to a larger value near the surface. In addition, our present numerical results do confirm the presence of a stress singularity.

The qualitative explanation of fiber multiple crack phenomenon found in the Dogbone test samples (DiBenedetto et al., 1986 and Bascom et al., 1986) can be made by investigating the fiber tensile stress along its length. Fig. 16 shows two curves corresponding to two different geometric ratios a/h=0.01 and a/h=0.05, where $[\sigma]$ denotes the tensile strength of the fiber. As we can see, the tensile strength in longer fiber (a/h=0.01) has passed the dash line and hence will break while the shorter fiber (a/h=0.05) will not break because the maximum tensile stress is below the dash line. However, if σ_i increases, the dash line will move lower provided that the tensile strength of the fiber is independent of the ratio a/h. This may lead to the breakage of shorter fiber. It becomes clear that the fiber tends to relax itself by having shorter length. Another interesting phenomenon is that the non-dimensionalized tensile stress at the fiber center for the case a/h=0.01 is about 17, which is equal to the shear moduli ratio of the current problem. Cox (1952) has predicted that the maximum tensile stress of the fiber under this model will occur at the fiber center and the value will be $E_2\sigma_i/E_1$. This will yield $17\sigma_i$ assuming the Poisson ratio is same for the fiber

and the matrix in our current problem. The prediction, however, becomes inaccurate when the fiber length decreases. This indicates that the $E_2\sigma_f/E_1$ can only be taken as a uplimit of the fiber tensile stress.

A quantitative comparison of our current results with the experimental results obtained by Tyson and Davies (1965) is given in Fig. 17. The parameters of their 2D experimental model are taken to fit our current 3D model. The diameter of the fiber is taken as 4mm and the half thickness of the plate h is determined by photoelastic method by measuring the distance from the fiber end to the isotropic point. All other parameters are given in the paper and can be used directly. As seen from the Figure, our result predicts the interfacial shear stress quite satisfactorily throughout the interface. A deviation starts at x=4mm, one fiber diameter from the fiber end. The authors are aware that this deviation may be caused by neglecting the stress concentration effect at the edge region as discussed previously. On the other hand, it also indicates that the influence of such a stress concentration effect is extremely localized. In addition, the result calculated from the shear lag analysis greatly underestimates the interfacial shear stress especially in the vicinity of the fiber.

In view of the numerical results, one may conclude that:

(1) The thickness as well as the material properties, play a fundamental role on the failure mechanism of a plate with a cylindrical inclusion. More specifically, the geometric parameter a/h and the shear moduli ratio μ_2/μ_1 are two important ratios which greatly affect the displacement and stress fields.

(2) A boundary layer effect is shown to exist in the vicinity of z=h where the presence of a stress singularity (Folias, 1989) may result to crack initiation.

(3) The shear lag analysis may underestimate the interfacial shear stress and may overestimate the fiber tensile stress.

(4) When $\sigma_i/\sigma_0<\mu_1/\mu_2$, the interfacial debonding, slippage and fiber breakage will most likely initiate at the edge region.

(5) When $\sigma_i/\sigma_0>\mu_1/\mu_2$, the interfacial slippage will initiate at the edge region while the interfacial debonding and fiber breakage may initiate at the center region.

(6) Taking a uniform tensile stress at the the plate surface by neglecting the stress concentration effect at the edge region may slightly underestimate the interfacial shear stress near the fiber end. However, such a error reduces quickly as the distance from the fiber end increases.

(7) The substitution of the "interphase" with an elastic spring may give inaccurate information of the stress at the edge region because one of the boundary conditions breaks down at the region.

References

[1] Sendeckyj, G. P. "Elastic Inclusion Problems in Plane Elastostatic", International Journal of Solids and Structures 6 (1970) 1535-1543.

[2] Yu, I. W. and G. P. Sendeckyj, "Multiple Circular Inclusion Problems in Plane Elastostatic", Journal of Applied Mechanics 41 (1974) 215-221.

[3] Bloom, Joseph M., "Axial Loading of a Unidirectional Composite",Journal of composite materials1 (1967) 268-277.

[4] Muki, R. and E. Sternberg, "Elastostatic Load-Transfer to a Half-Space from a Partially Embedded Axially Loaded Rod", International Journal of Solids and Structures 6 (1970) 69-90.

[5] Luk, V. K. and L. M. Keer, "Stress Analysis for an Elastic Half Space Containing an Axially-Loaded Rigid Cylindrical Rod". International Journal of Solids and Structures 15 (1979) 805-827.

[6] Haener, Juan and Noel Ashbaugh, "Three-Dimensional Stress Distribution In a Unidirectional Composite", Journal of Composite materials 1 (1967) 54-63.

[7] Folias, E. S., "On the Three Dimensional Theory of Cracked Plates", Journal of Applied Mechanics (1975) 663-673

[8] Penado, F. E. and E. S. Folias, "the Three Dimensional Stress Field around a Cylindrical Inclusion in a plate of Arbitrary Thickness",International Journal of Fracture 39 (1989) 129-145.

[9] Lawrence, p., "Some Theoretical Considerations of Fiber Pull-out from an Elastic Matrix", Journal of Materials Science 7 (1972) 1-6.

[10] Banbaji, J., "On a More Generalized Theory of the Pull-out Test from an Elastic Matrix", Composites Science and Technology 32 (1988) 183-193.

[11] Steif, Paul S. and Steven F. Hoysan, "On Load Transfer between Imperfectly Bonded Interface", Mechanics of Materials 5 (1986) 375-382.

[12] Dollar, Anna and Paul S. Steif, "Load Transfer in Composites with a Coulum Friction Interface", International Tournal of Solids and Structures 24 (1988) 789-803.

[13] Haritos, G. K. and L. M. Keer, "Pullout of a Rigid Insert Adhesively Bonded to an Elastic Half Plane" Journal of Adhesion 18 (1985) 131-150.

[14] Gao, Yu-Chen, Yiu-Wing Mai and Brian Cotterell, "Fracture of Fiber-Reinforced Materials", ZAMP 39 (1988), 550-572.

[15] Penn, Lynn S. and Shaw M. Lee, "Interpretation of Experimental Results in the Single Pull-Out Filament Test", Journal of Composites Technology & Research 11 (1989), 23-30.

[16] Folias, E. S., "On the Stress Singularities at the Intersection of a Cylindrical Inclusion with the Free Surface of a Plate", International Journal of Fracture 39 (1989) 25.

[17] Williams, M. L., "Stress Singularities Resulting from Various Boundary Conditions in Angular Corners of Plates in Extension", Journal of Applied Mechanics 74 (1952), 526.

[18] Folias, E. S. and W. G. Reuter, "On the Equilibrium of a Linear Elastic Layer", Computational Mechanics 5 (1990) 459-468.

[19] Tyson and G. J. Davies, " A Photoelastic Study of the Shear Stress Associated with the Transfer of Stress During Fiber Reinforcement", British Journal of Applied Physics 16 (1965) 199-205.

[20] Chua, P. S. and M. R. Piggott, "The Glass Fiber-Polymer Interface: II - Work of Fracture and Shear Stress", Composites Science and Technology 22 (1985) 107-119.

[21] DiBenedetto, A. T., L. Nocolais, L. Ambrosio and J. Groeger, "Stress Transfer and Fracture in Single Fiber/Epoxy Composites", Proceeding of the First International Conference on Composite Interface (1986), 47-54.

[22] Bascom, W. D. and R. M. Jensen, " Stress Transfer in Single Fiber/Resin Tensile Tests", Journal of Adehesion 19 (1986), 219-239.

[23] Cox, H. L., "The Elasticity and Strength of Papers and Other Fiberous Materials", British Journal of Apllied Physics 3 (1952) 72-79.

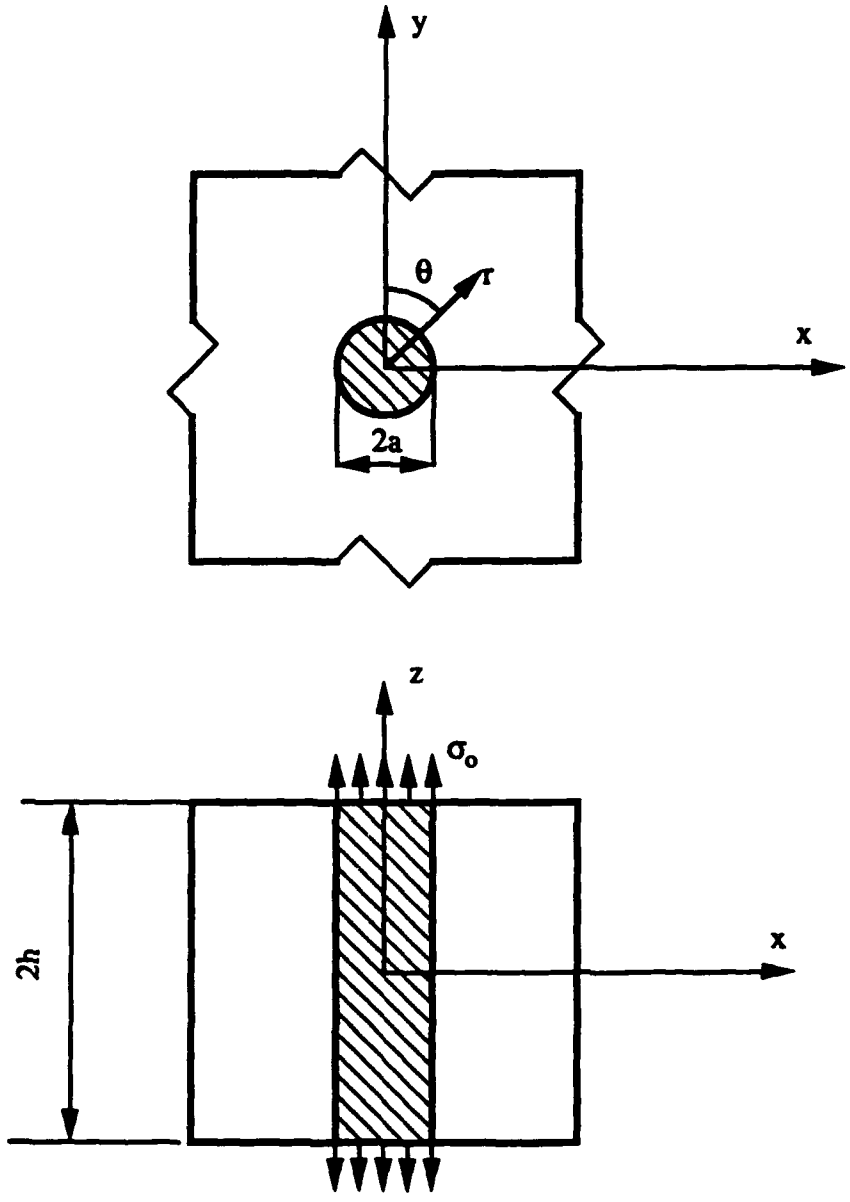

Fig. 1 Perfect bonding Model 1: only fiber is subjected to an axial load

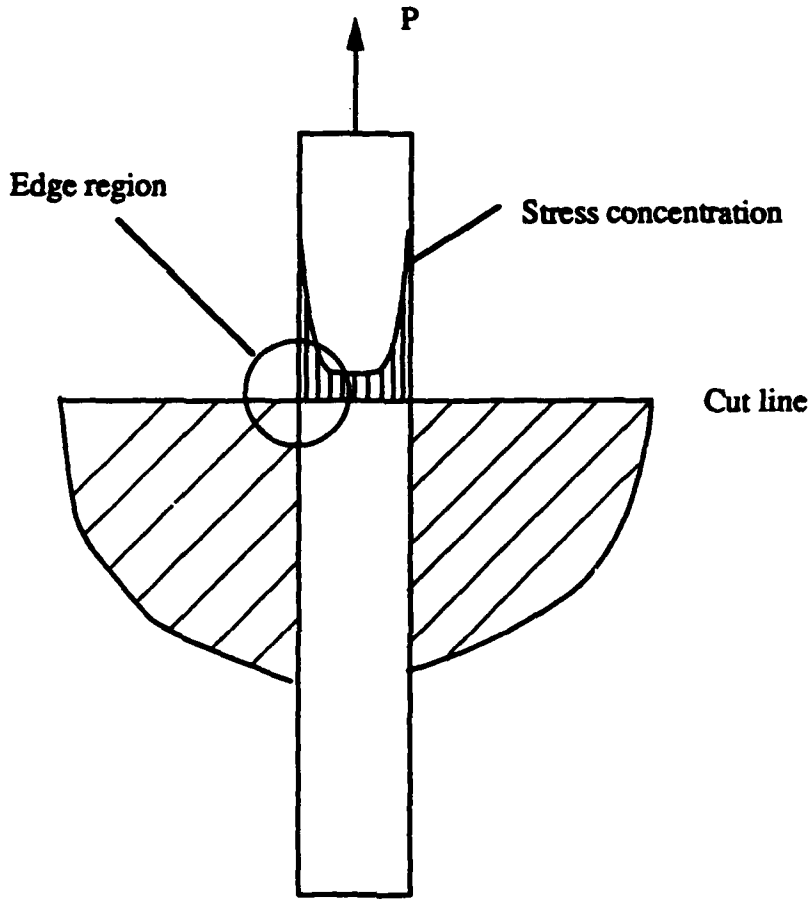

Fig. 2 Perfect bonding model 1 with stress concentration effect at edge region

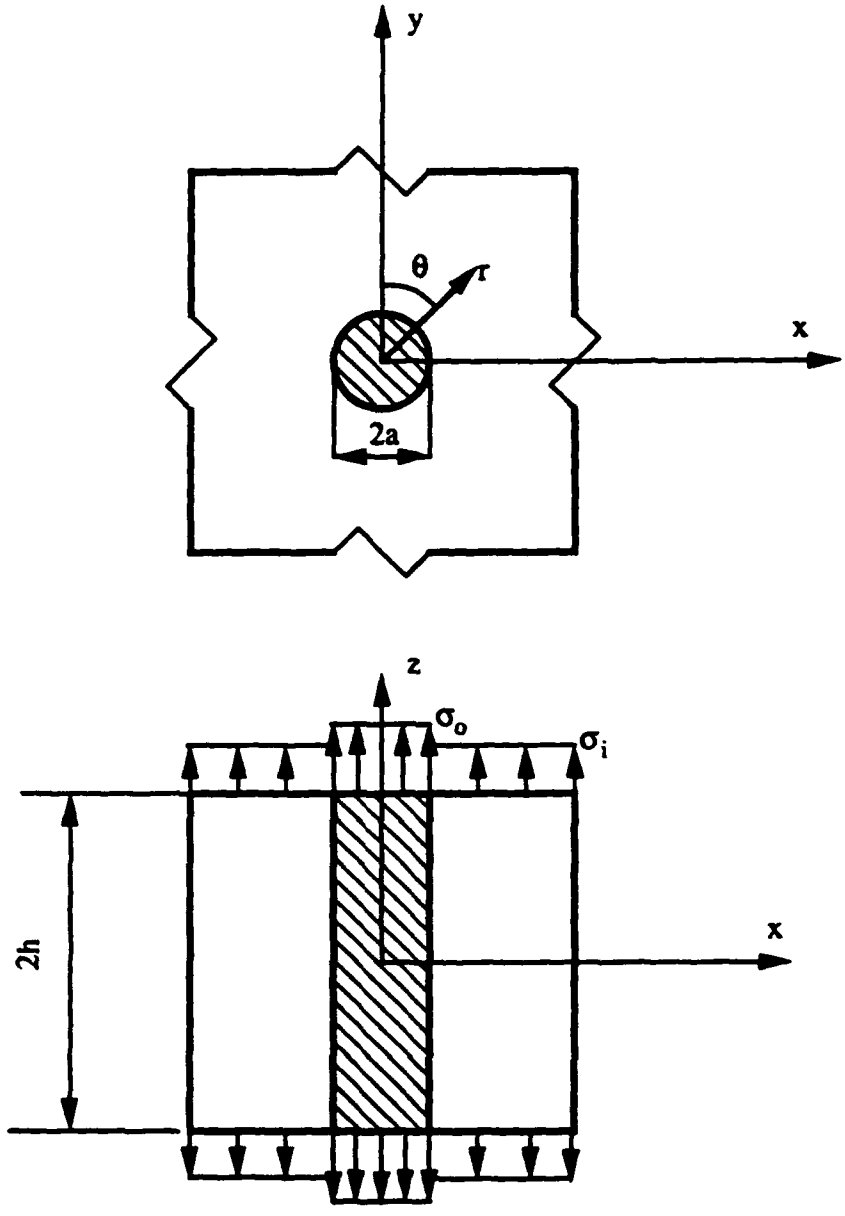

Fig. 3 Perfect bonding Model 2: both fiber and matrix are subjected to axial loads

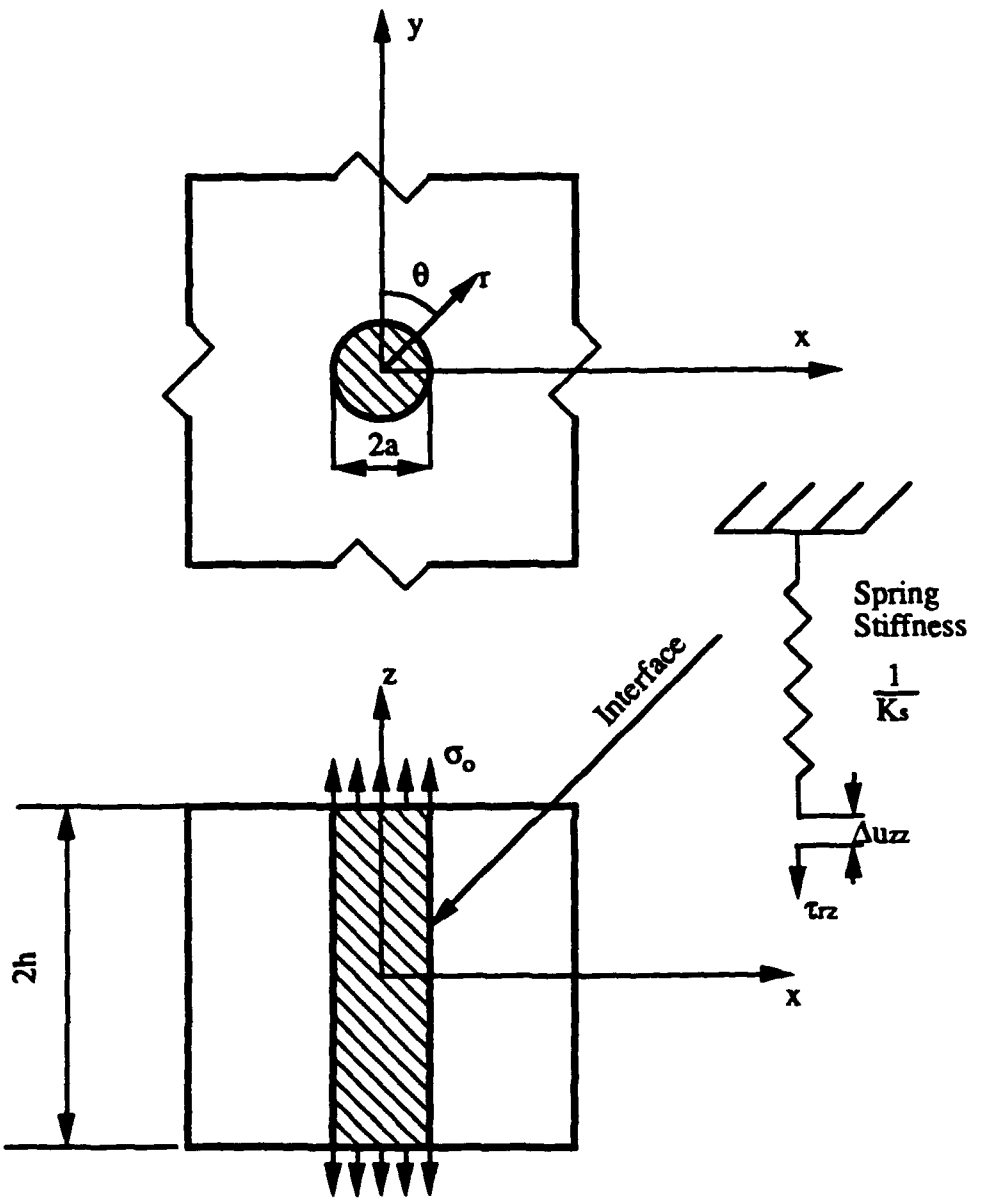

Fig. 4 Imperfect bonding Model: elastic spring exists at the interface

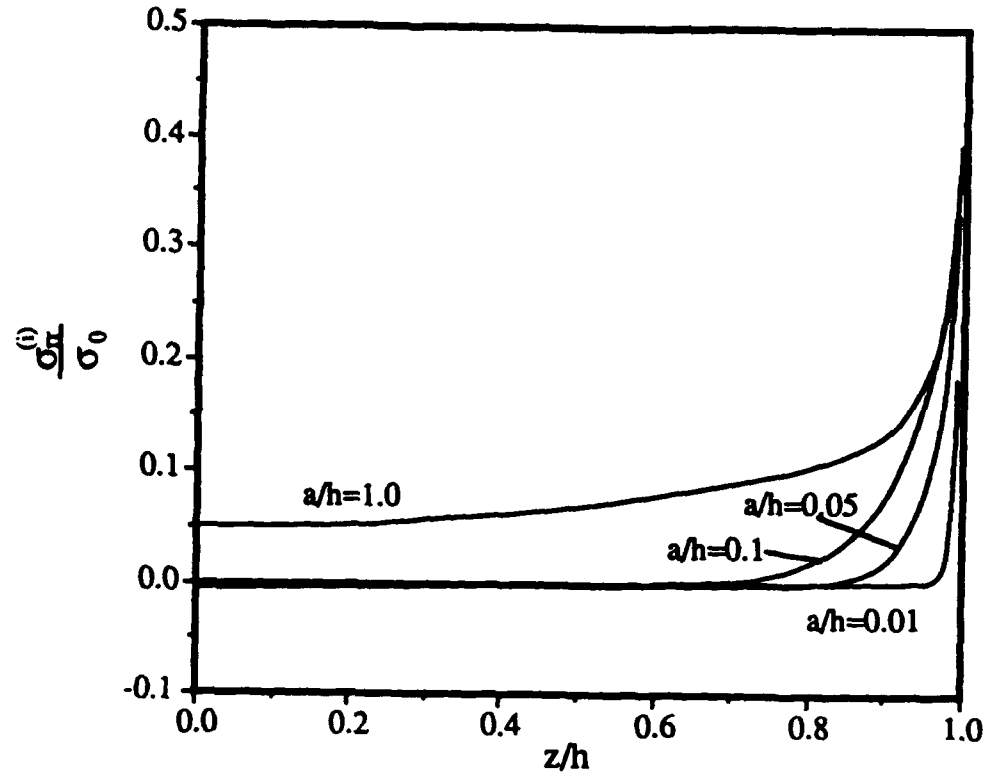

(a) $\mu_2/\mu_1=2$ and $\nu_1=\nu_2=0.33$

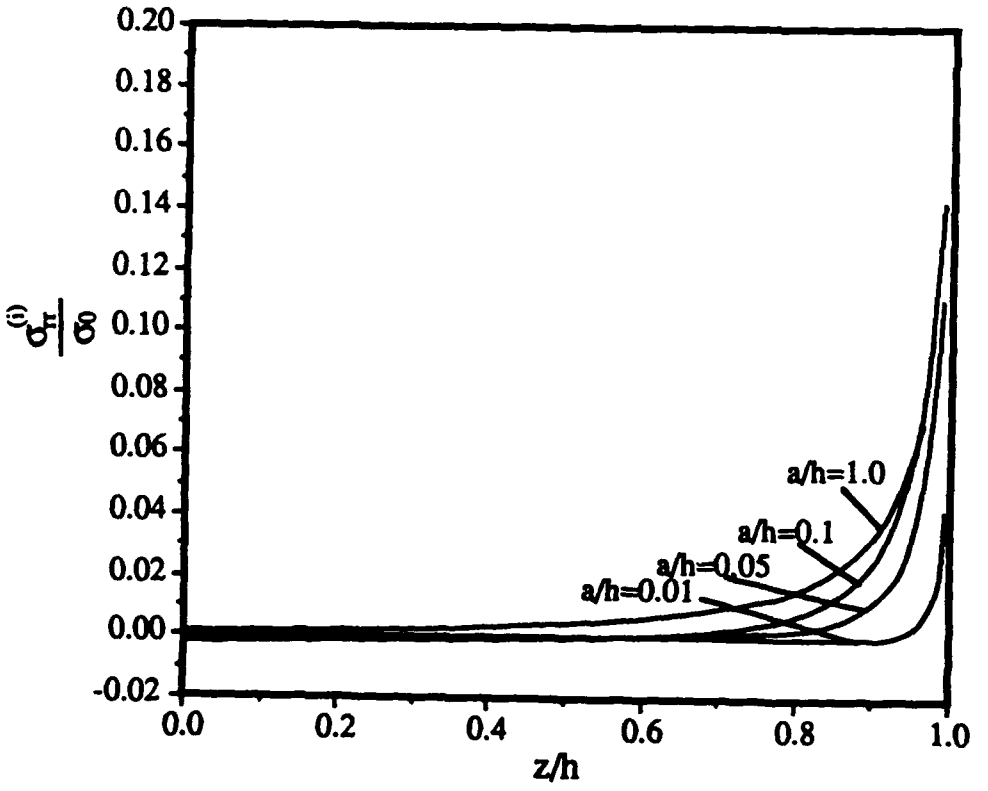

(b) $\mu_2/\mu_1=17$ and $\nu_1=\nu_2=0.33$

Fig. 5 Stress σ_{rr} vs z/h for perfect bonding Model 1

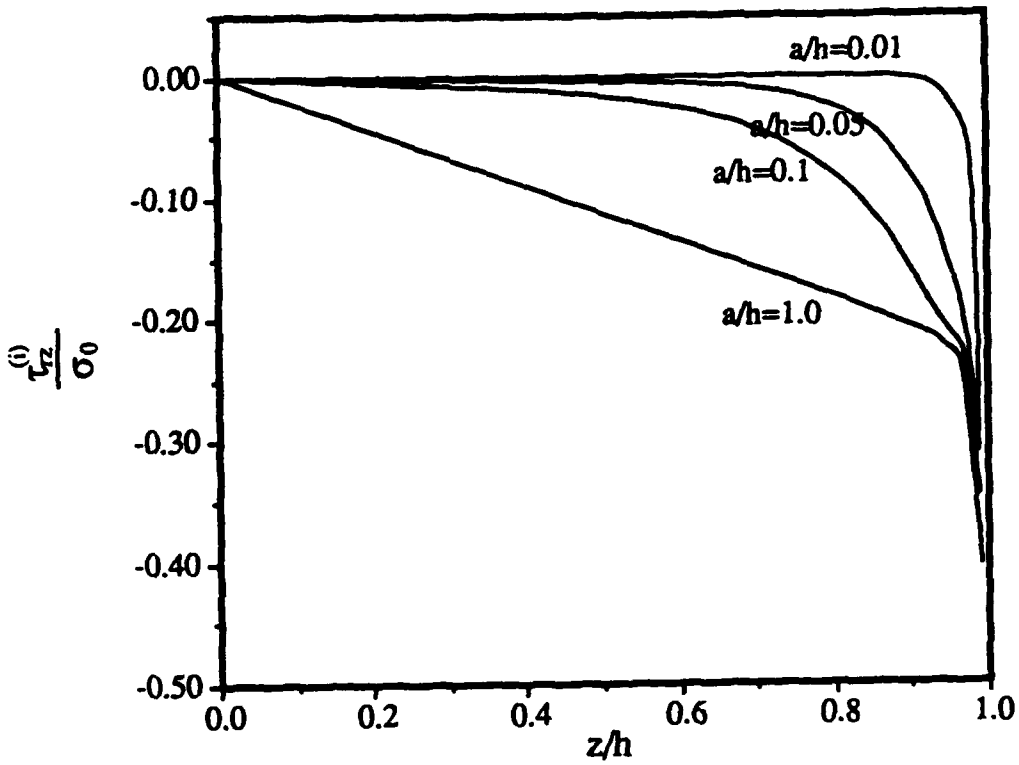

(a) $\mu_2/\mu_1=2$ and $\nu_1=\nu_2=0.33$

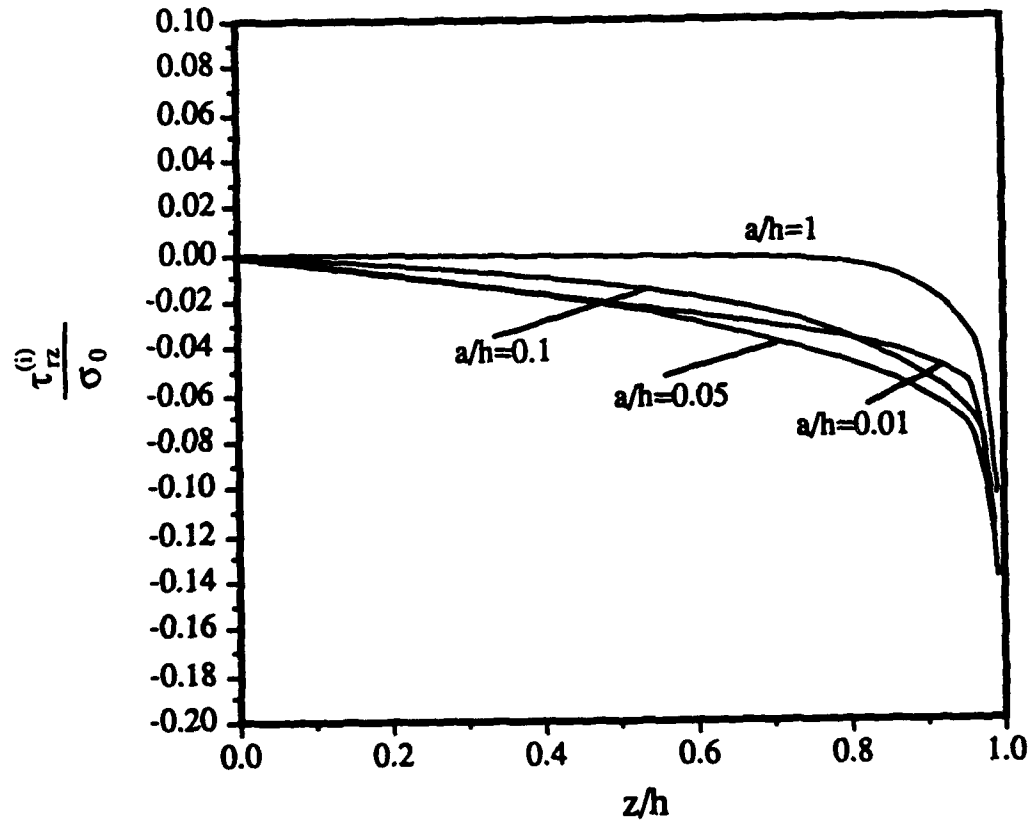

(b) $\mu_2/\mu_1=17$ and $\nu_1=\nu_2=0.33$

Fig.6 Stress τ_{rz} vs z/h for perfect bonding Model 1

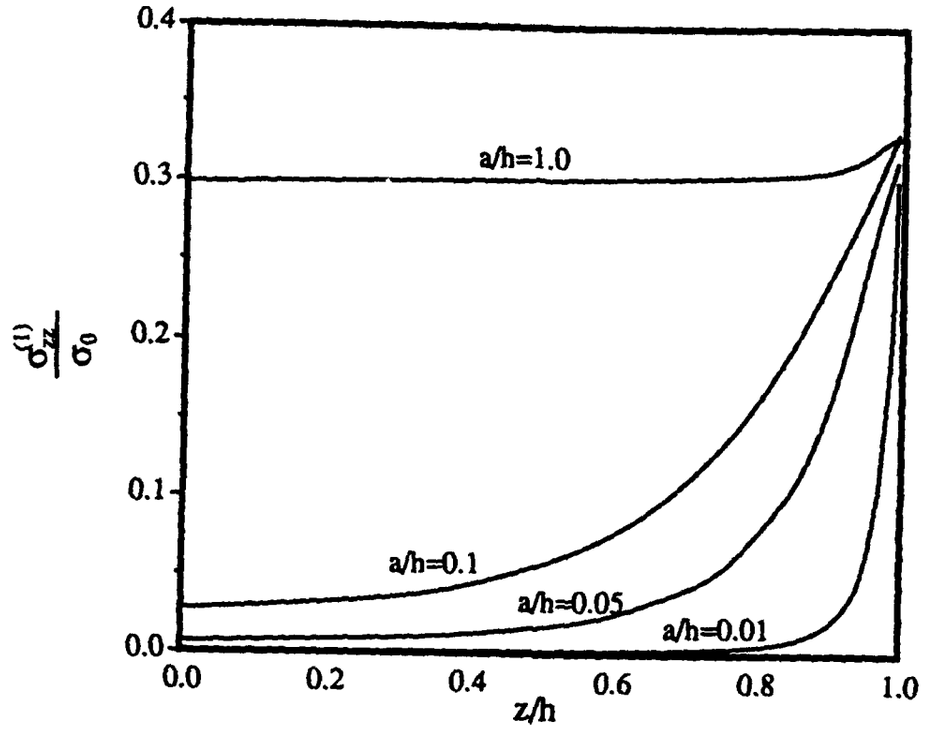

(a) $\mu_2/\mu_1=2$ and $\nu_1=\nu_2=0.33$

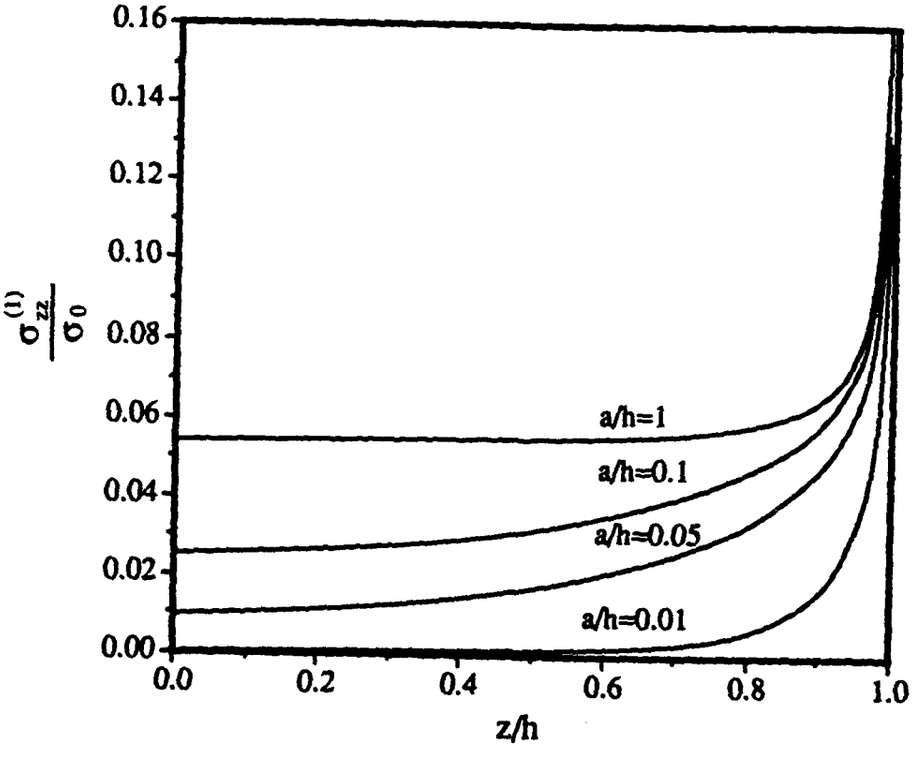

(b) $\mu_2/\mu_1=17$ and $\nu_1=\nu_2=0.33$

Fig.7 Stress $\sigma_{zz}^{(1)}$ vs z/h for perfect bonding Model 1

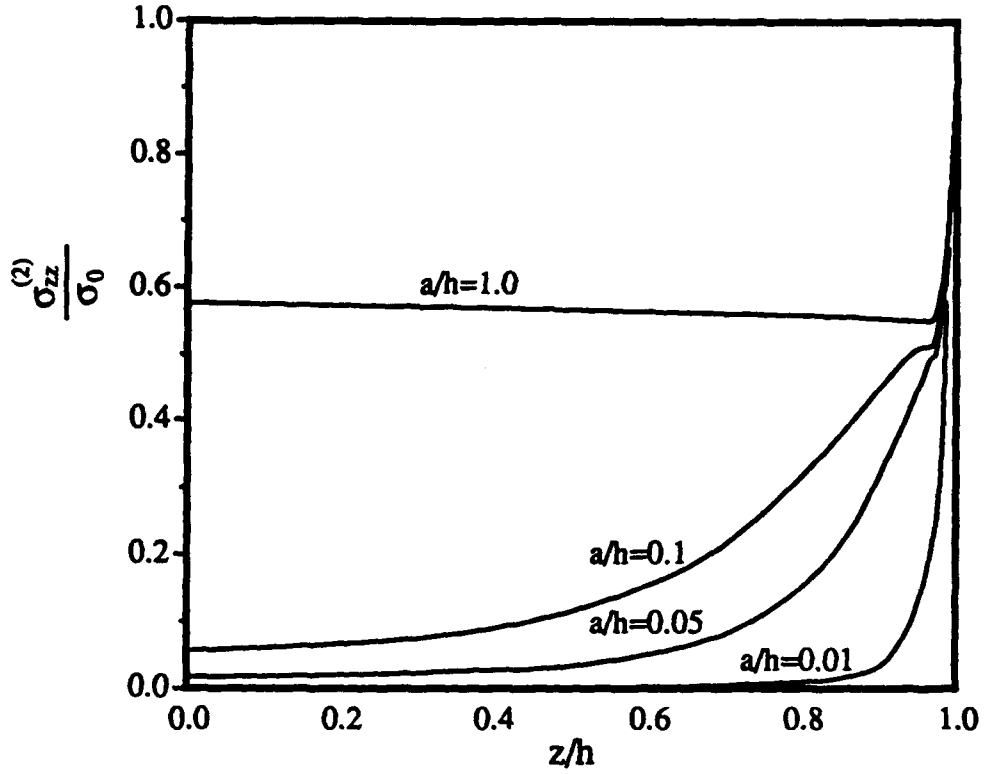

(a) $\mu_2/\mu_1=2$ and $\nu_1=\nu_2=0.33$

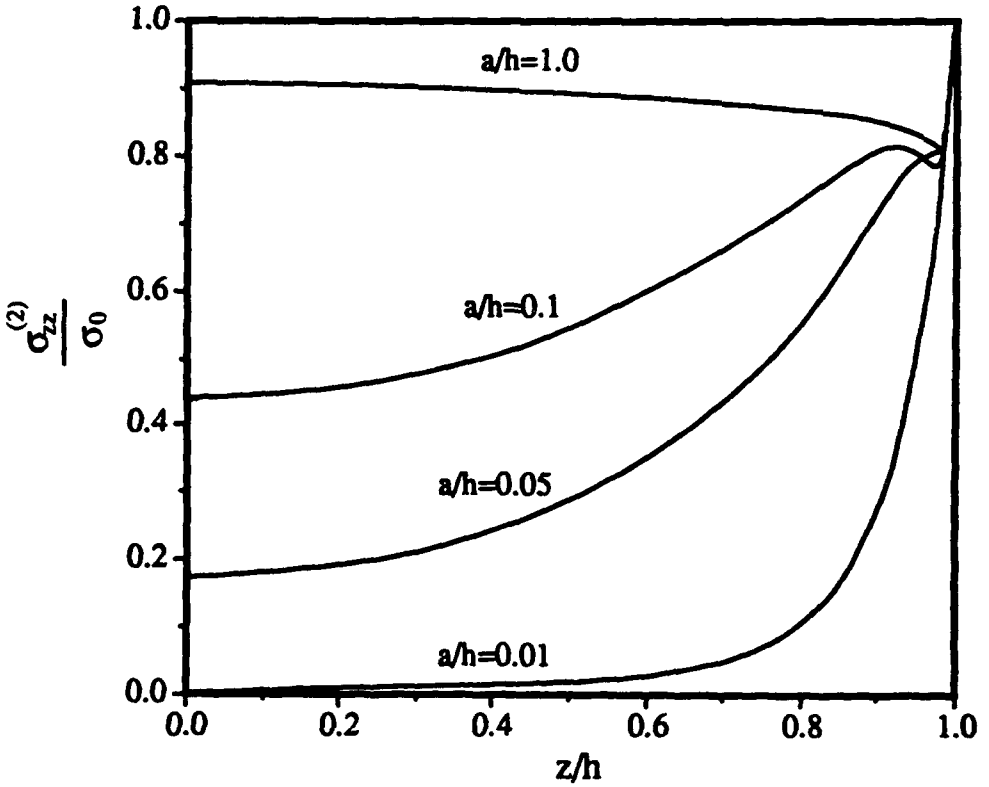

(b) $\mu_2/\mu_1=17$ and $\nu_1=\nu_2=0.33$

Fig. 8 Stress $\sigma_{zz}^{(2)}$ vs z/h for perfect bonding Model 1

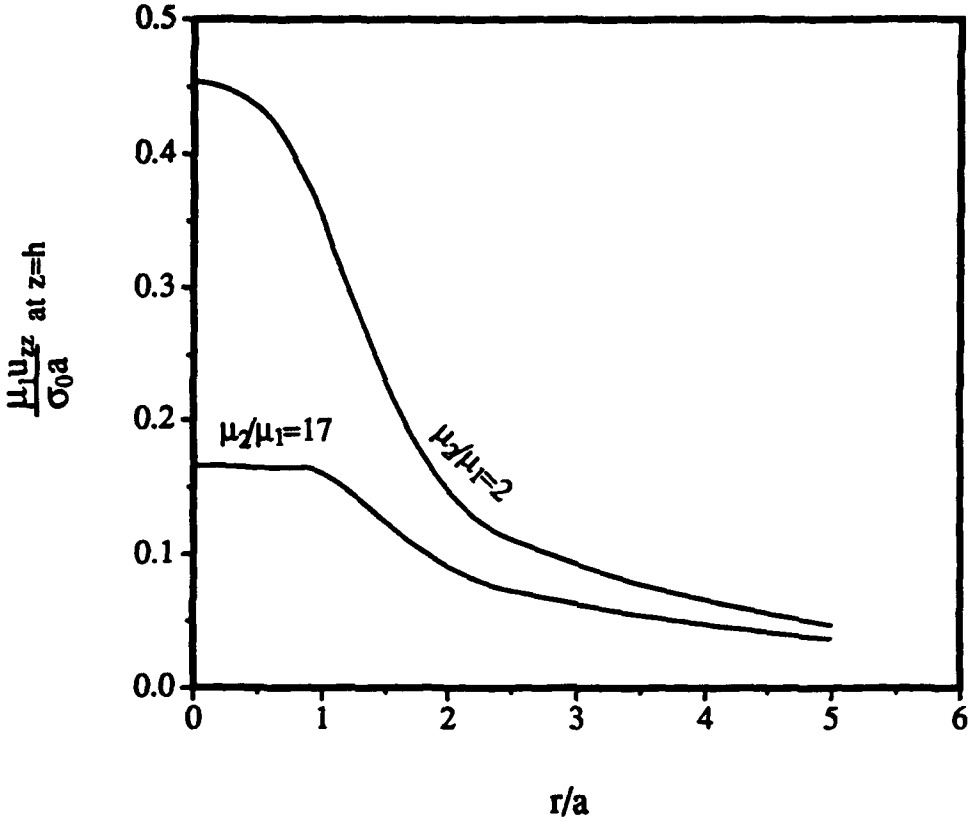

Fig. 9 Displacement u_{zz} at z=h vs r/a for perfect bonding model 1 where $\nu_1=\nu_2=0.33$ and a/h=0.05

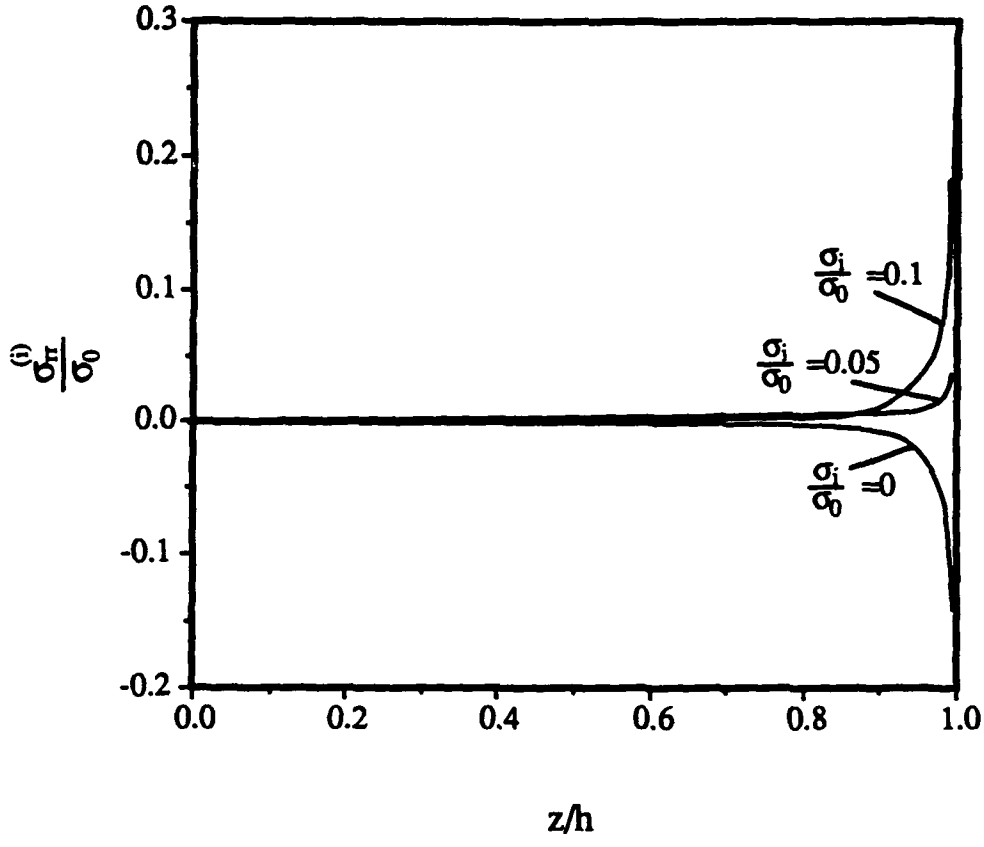

Fig.10 Stress σ_{rr} vs z/h for perfect bonding Model 2
where $\nu_1=\nu_2=0.33$; $\mu_2/\mu_1=17$ and a/h=0.05

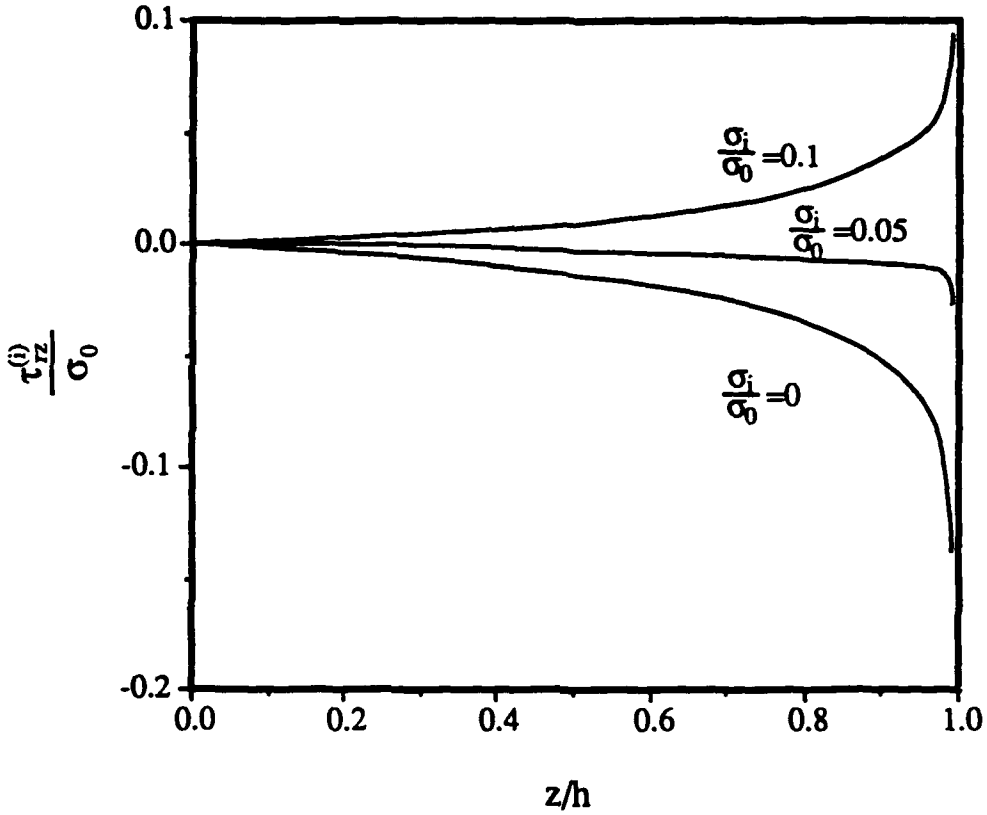

Fig.11 Stress τ_{rz} vs z/h for perfect bonding Model 2
where $\nu_1=\nu_2=0.33$; $\mu_2/\mu_1=17$ and a/h=0.05

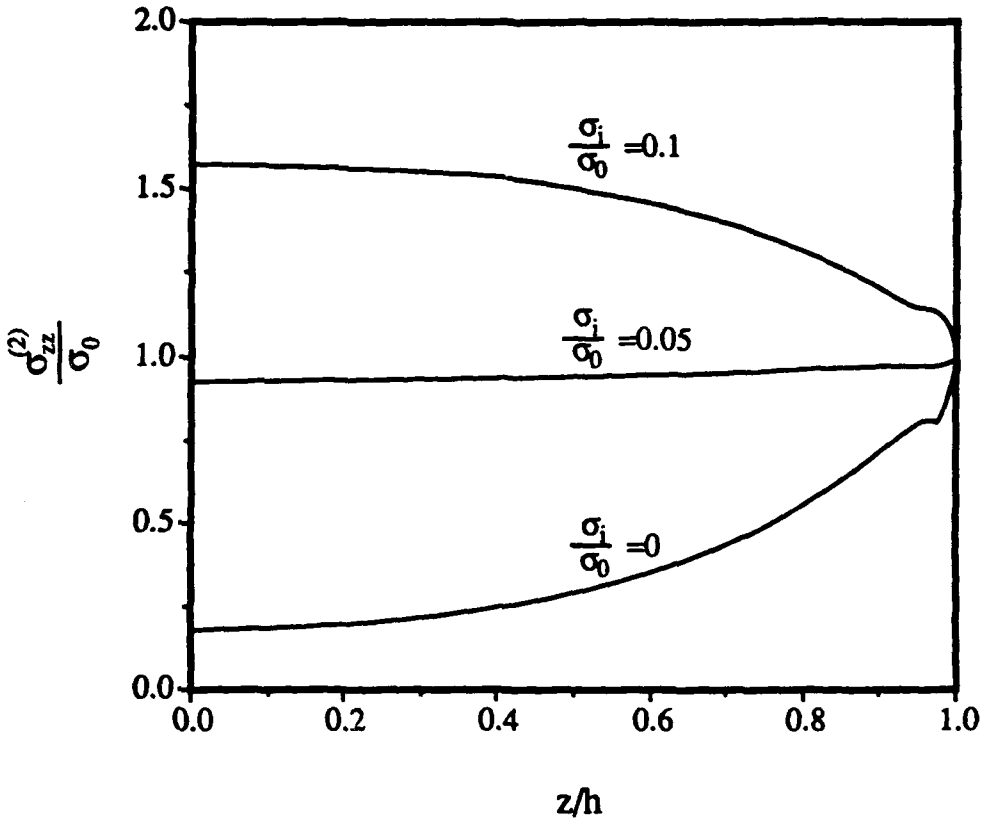

Fig.12 Stress $\sigma_{zz}^{(2)}$ vs z/h for perfect bonding Model 2
where $\nu_1=\nu_2=0.33$; $\mu_2/\mu_1=17$ and a/h=0.05

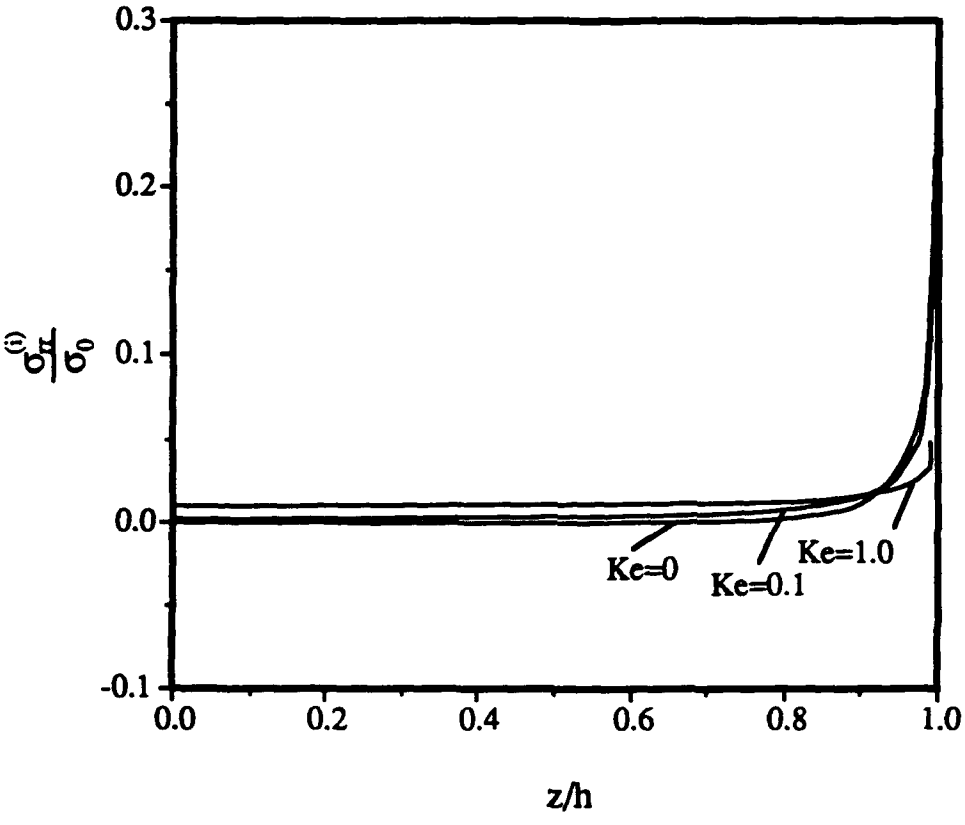

Fig.13 Stress σ_{rr} vs z/h for imperfect bonding case where $\nu_1=\nu_2=0.33$; $\mu_2/\mu_1=17$ and $a/h=0.05$

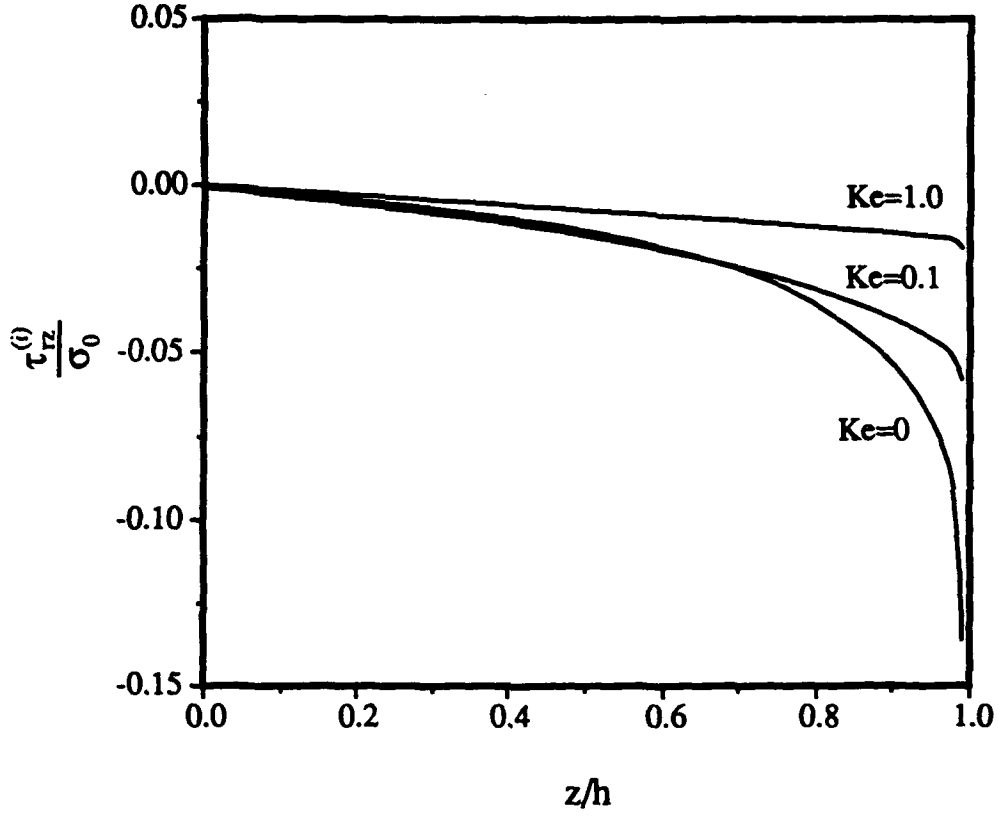

Fig.14 Stress τ_{rz} vs z/h for imperfect bonding case where $\nu_1=\nu_2=0.33$; $\mu_2/\mu_1=17$ and $a/h=0.05$

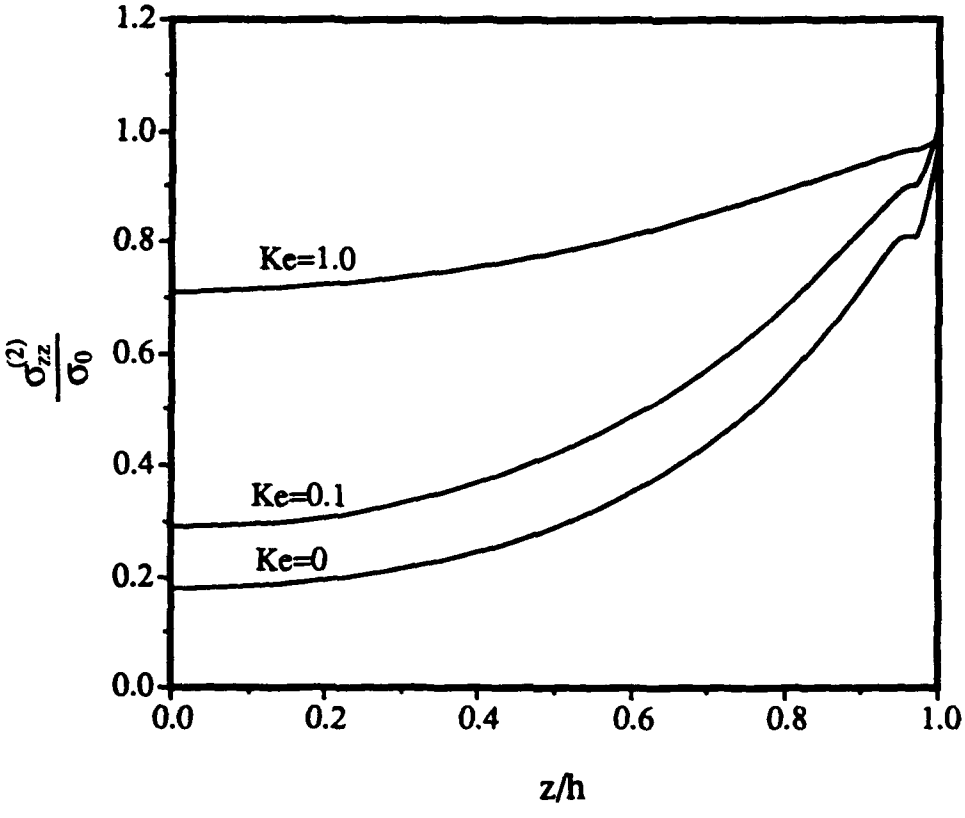

Fig.15 Stress $\sigma_{zz}^{(2)}$ vs z/h for imperfect bonding case where $\nu_1=\nu_2=0.33$; $\mu_2/\mu_1=17$ and a/h=0.05

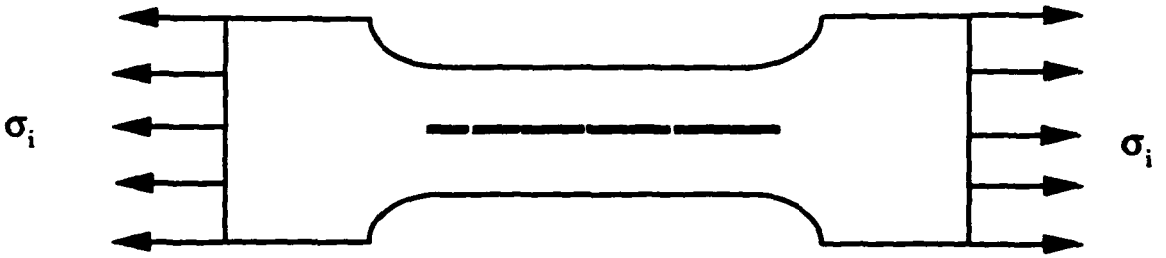

"Dogbone" test sample

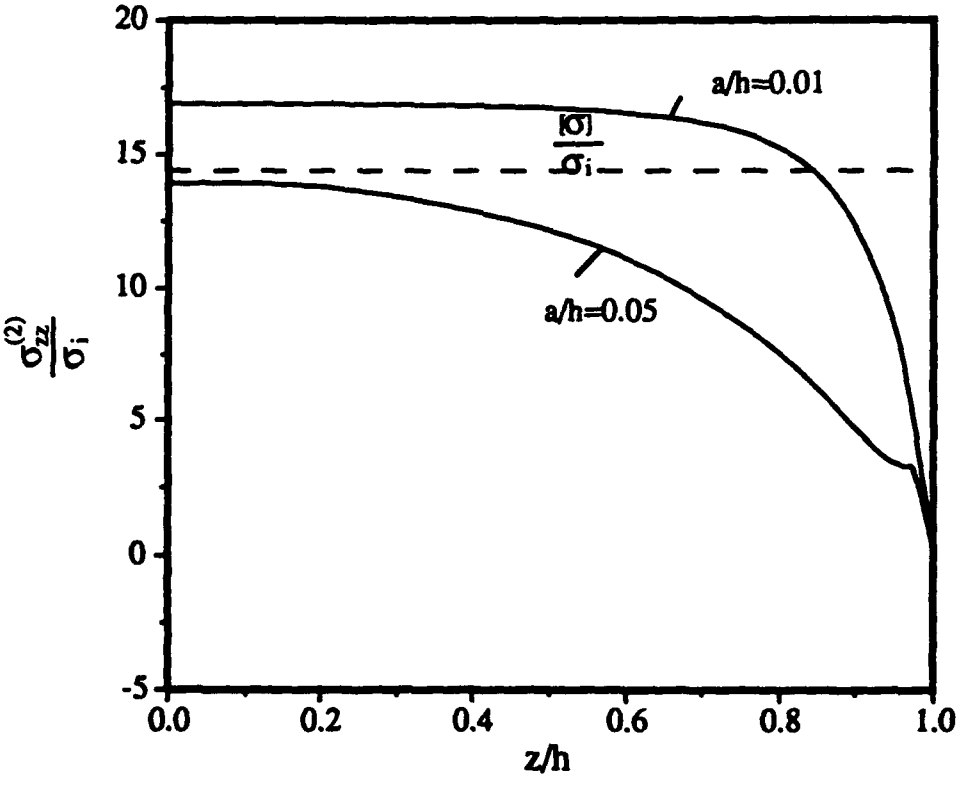

Fig. 16 Stress $\sigma_{zz}^{(2)}$ vs z/h for short fiber model where $\nu_1=\nu_2=0.33$; $\mu_2/\mu_1=17$

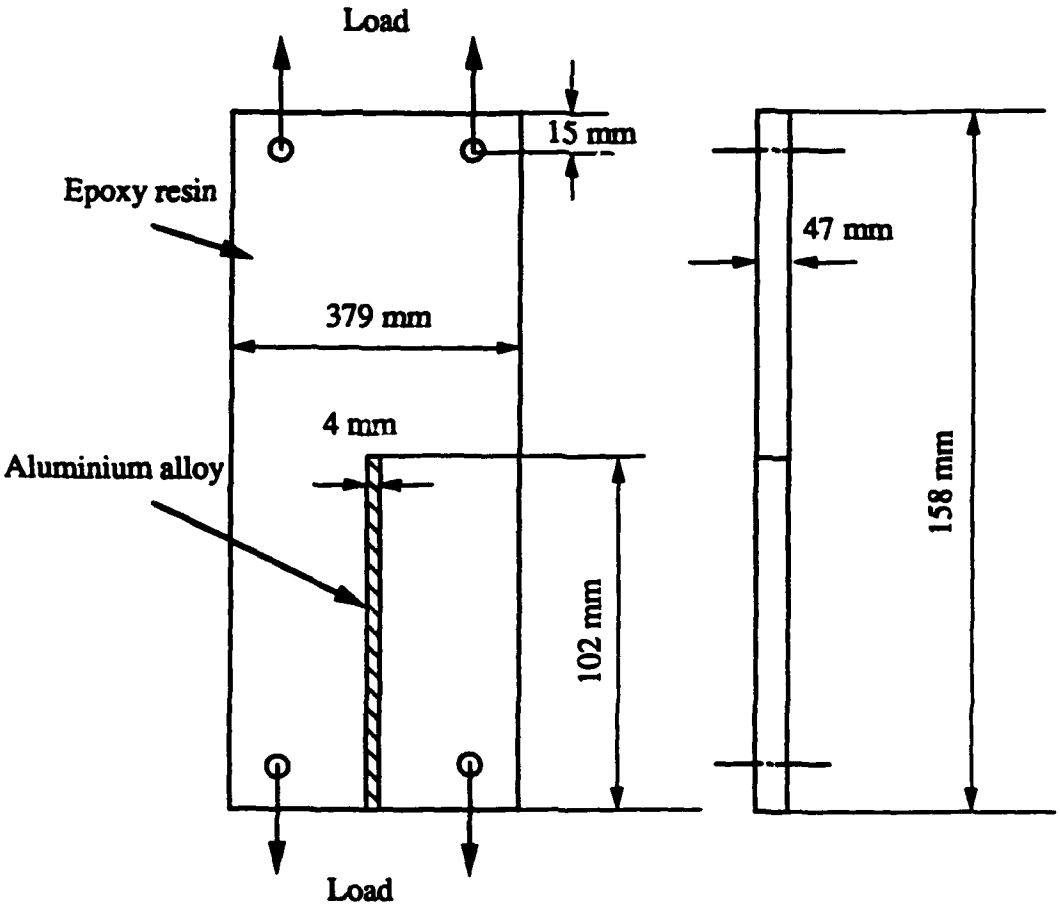

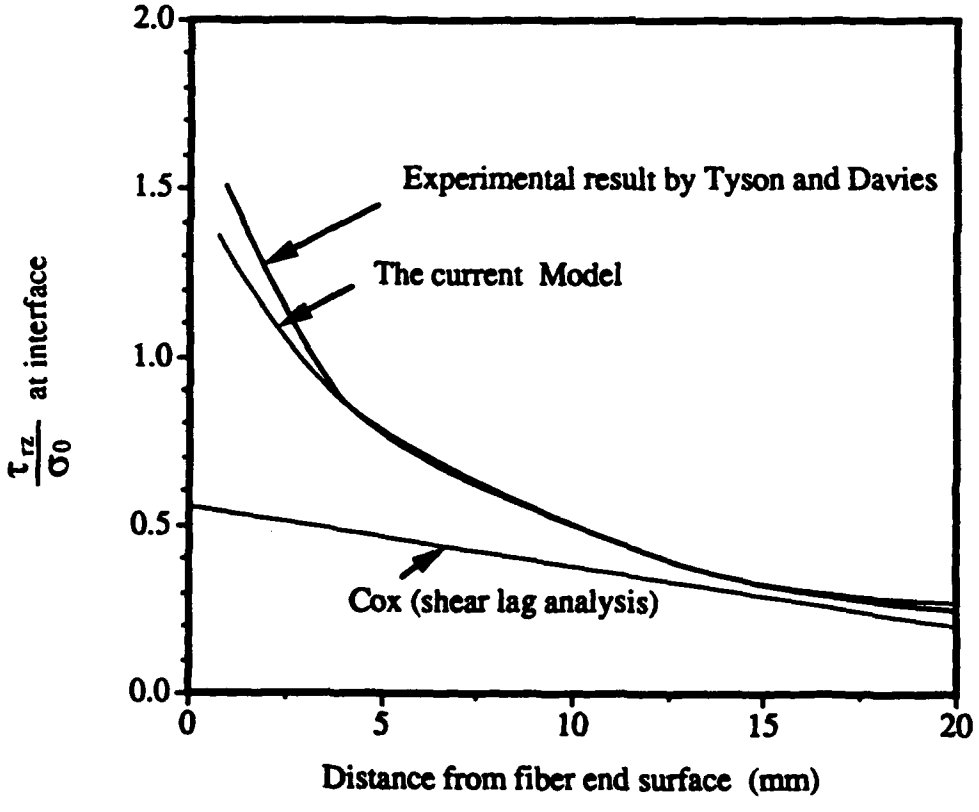

Fig. 17 Comparison with the experimental results abtained by Tyson and Davies

PART VII

THE 3D STRESS FIELD IN A COMPOSITE SYSTEM UNDER THE ACTION OF A UNIFORM LOAD IN THE FIBER DIRECTION

by

E. S. Folias and J. H. Liu

University of Utah
Department of Mechanical Engineering
Salt Lake City, Utah, 84112

The previous analysis may now be extended to the the case of a periodic array of fibers embedded into a matrix plate and under the action of a uniform load in a direction parralel to the fiber axis (see figs 1 and 2). Without going into the mathematical details, which are similar to the previous parts, the results are given in figures 3 through 11. From these figures it becomes evident that the load transfer characteristics from the fibers to the matrix are gaverned by the material properties, the fiber radious to fiber lentgh ratio, the fiber volume fraction, and finally the load ratio matrix and fibers.

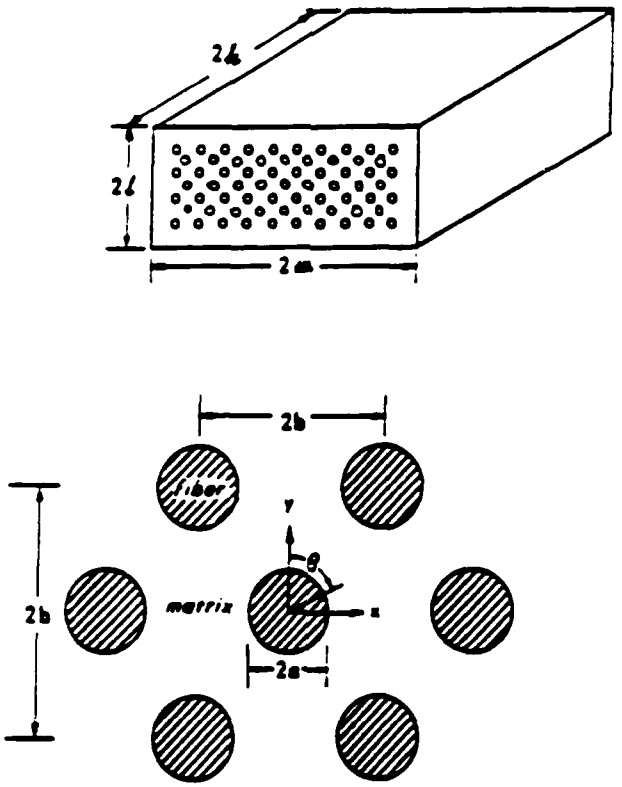

Fig. 1. Geometrical configuration

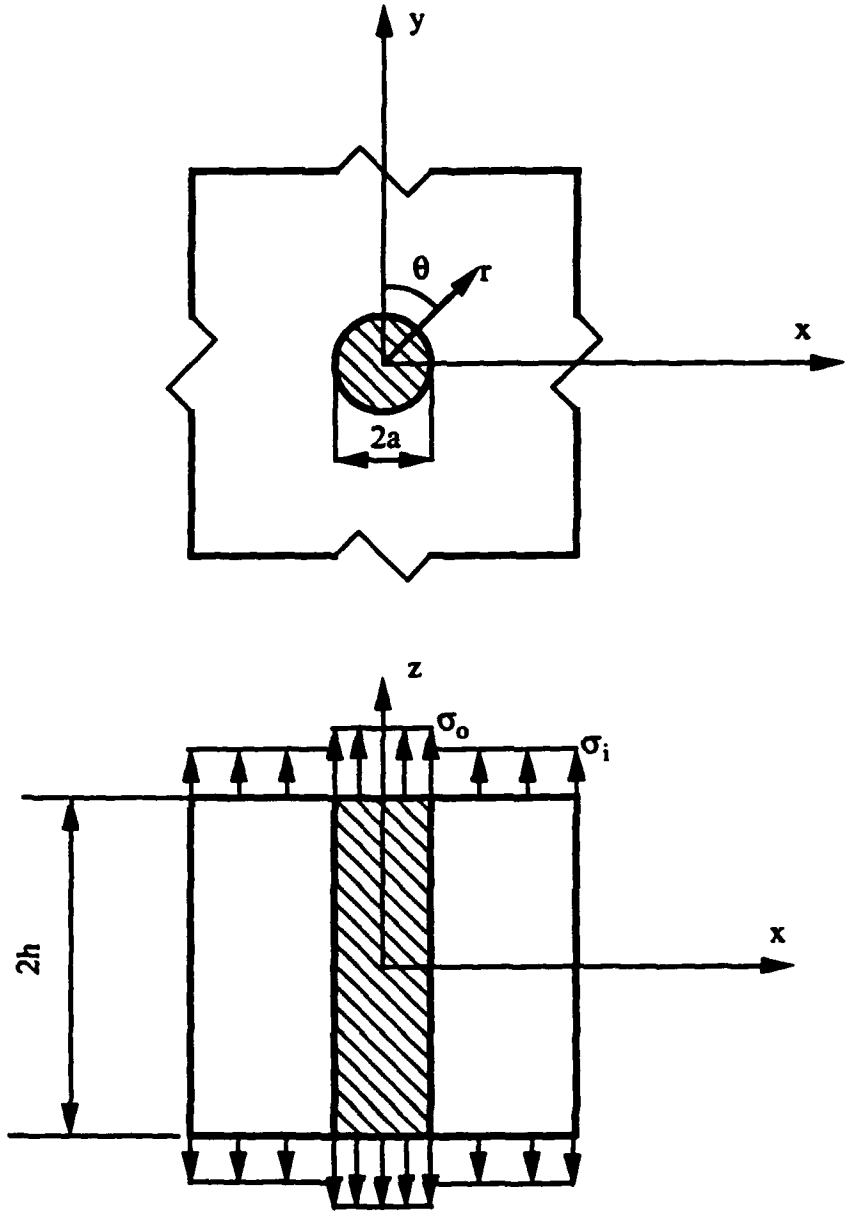

Fig. 9. Perfect bonding Model both fiber and matrix are subjected to axial loads

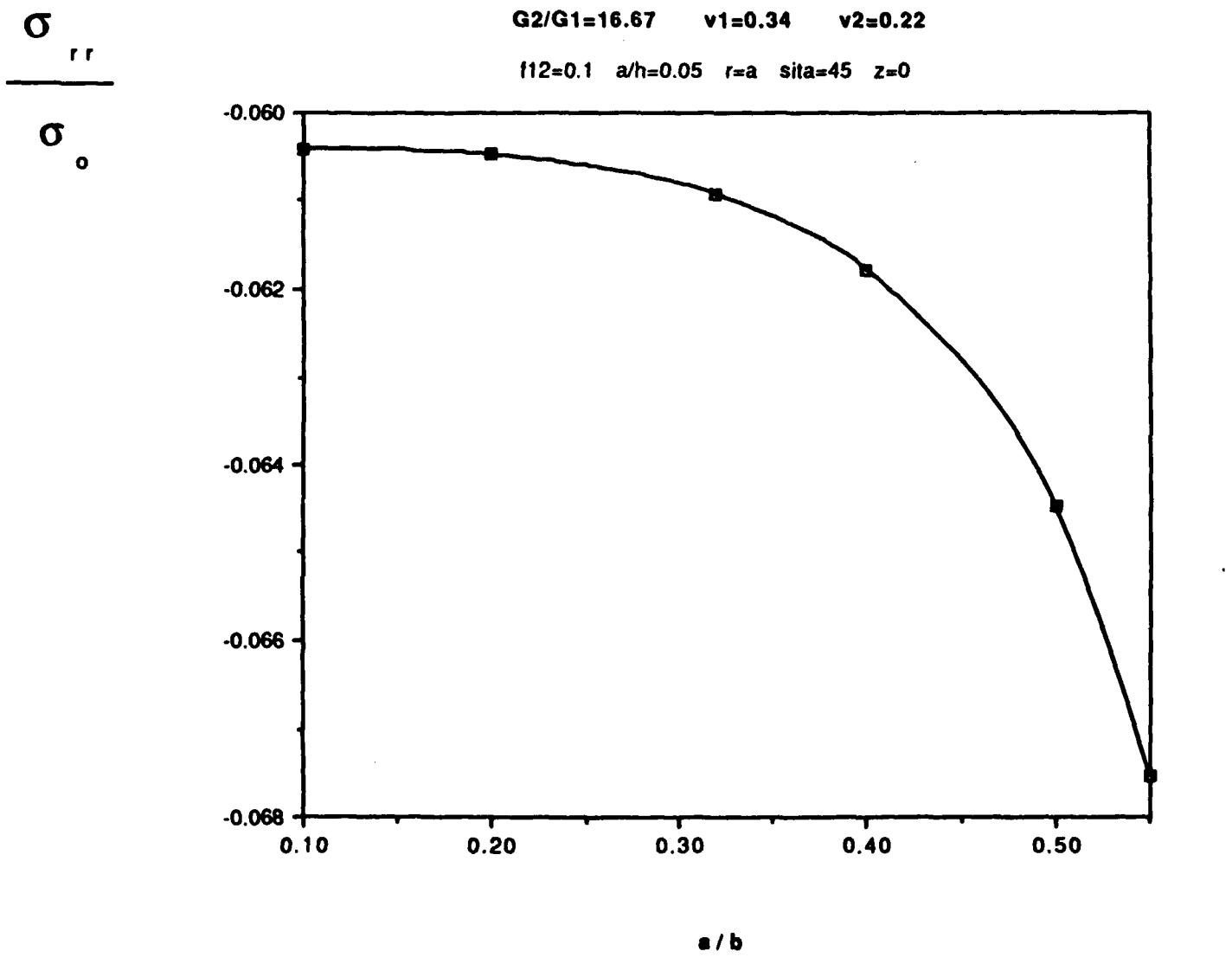

Fig. 3 The radial stress σ_{rr} at the interface versus a/b at z=0 , θ=45 and f12= σ_i/σ_0=0.1.

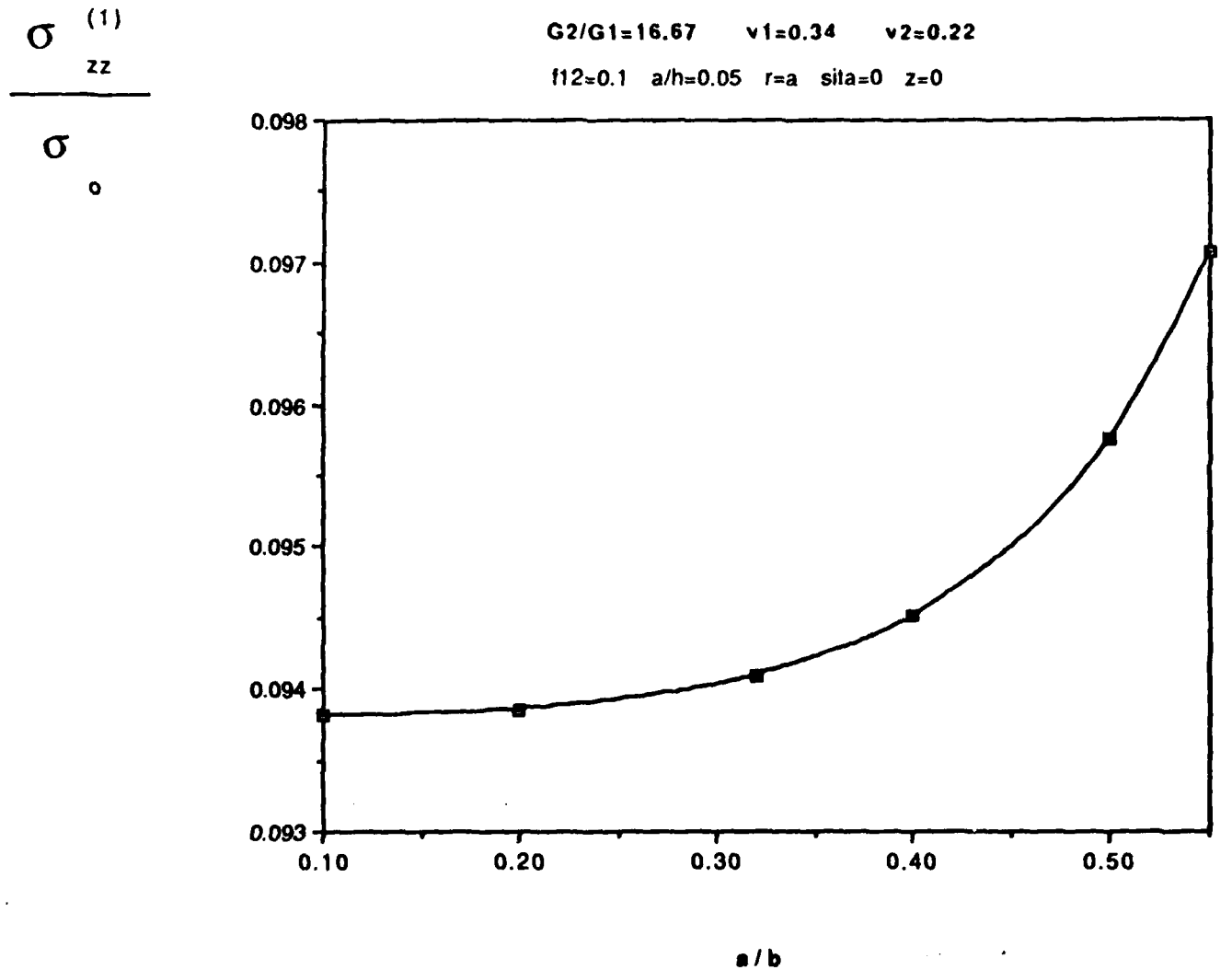

Fig. 4 The stress $\sigma_{zz}^{(1)}$ at the interface versus a/b at z=0 , θ=0 and f12= σ_j/σ_0=0.1.

$\frac{\sigma_{zz}^{(1)}}{\sigma_0}$

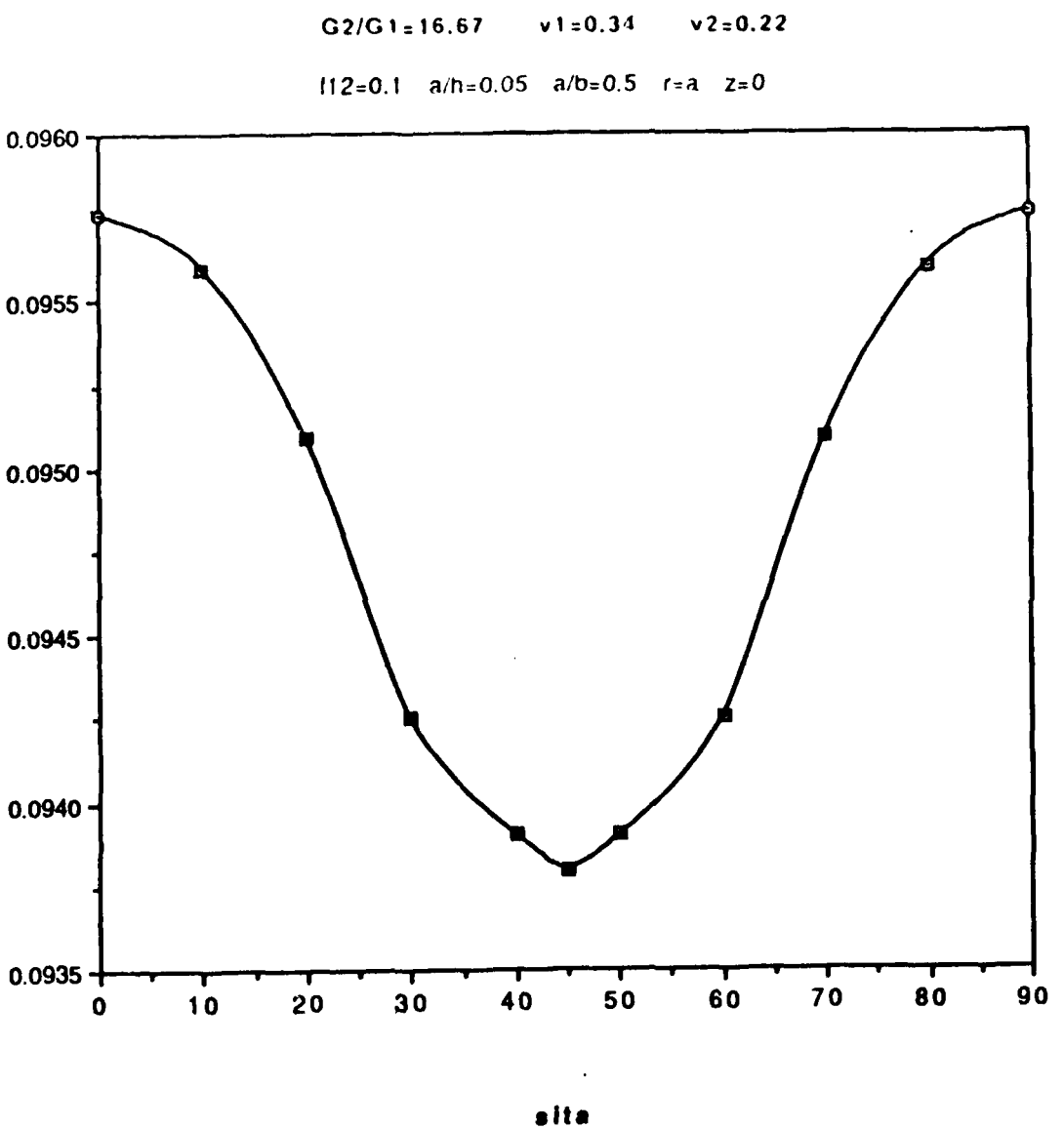

Fig. 5 The stress $\sigma_{zz}^{(1)}$ at the interface versus θ at z=0 and f12= σ_i/σ_0=0.1.

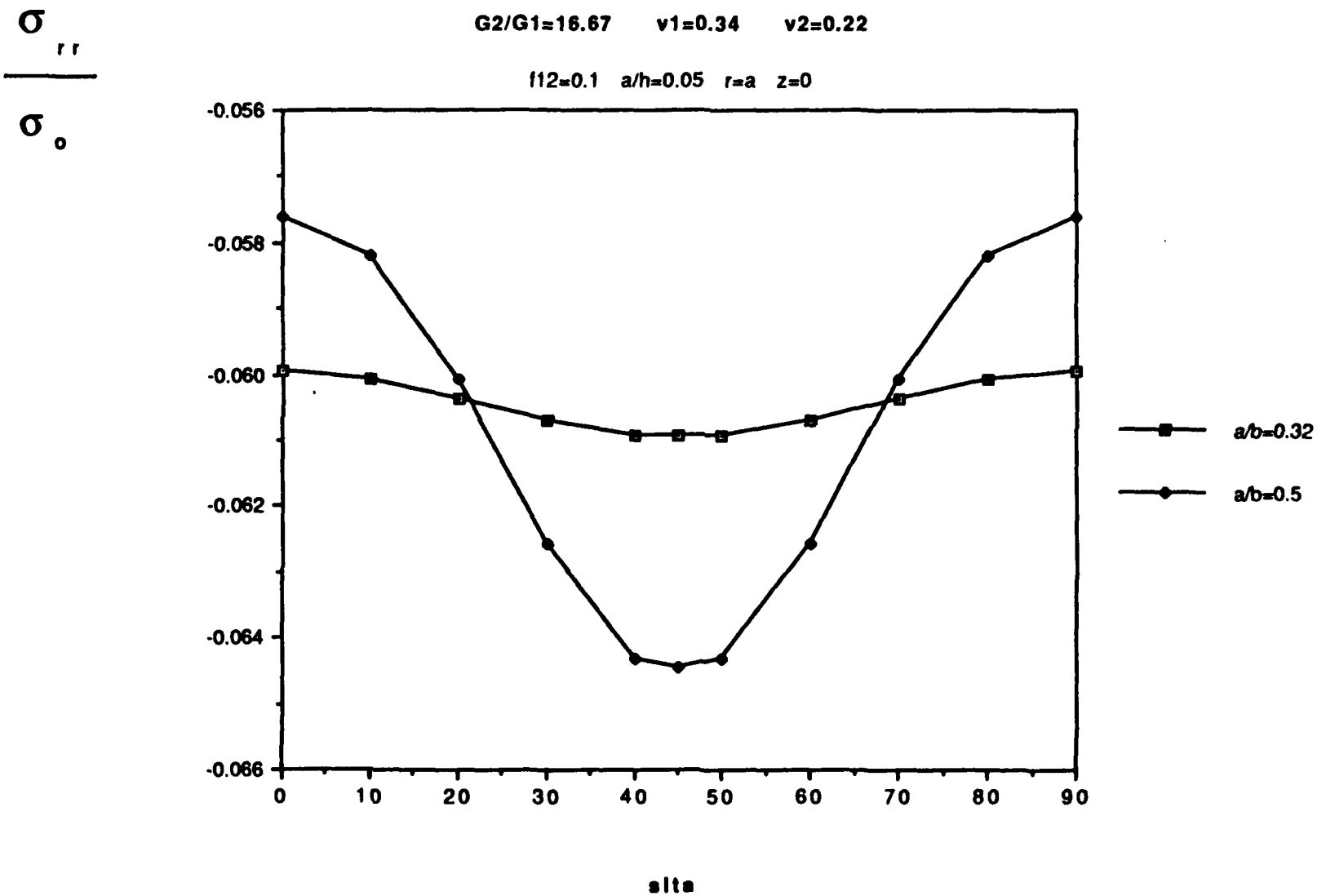

Fig. 6 The stress σ_{rr} at the interface versus θ at z=0 and f12= σ_i/σ_0=0.1.

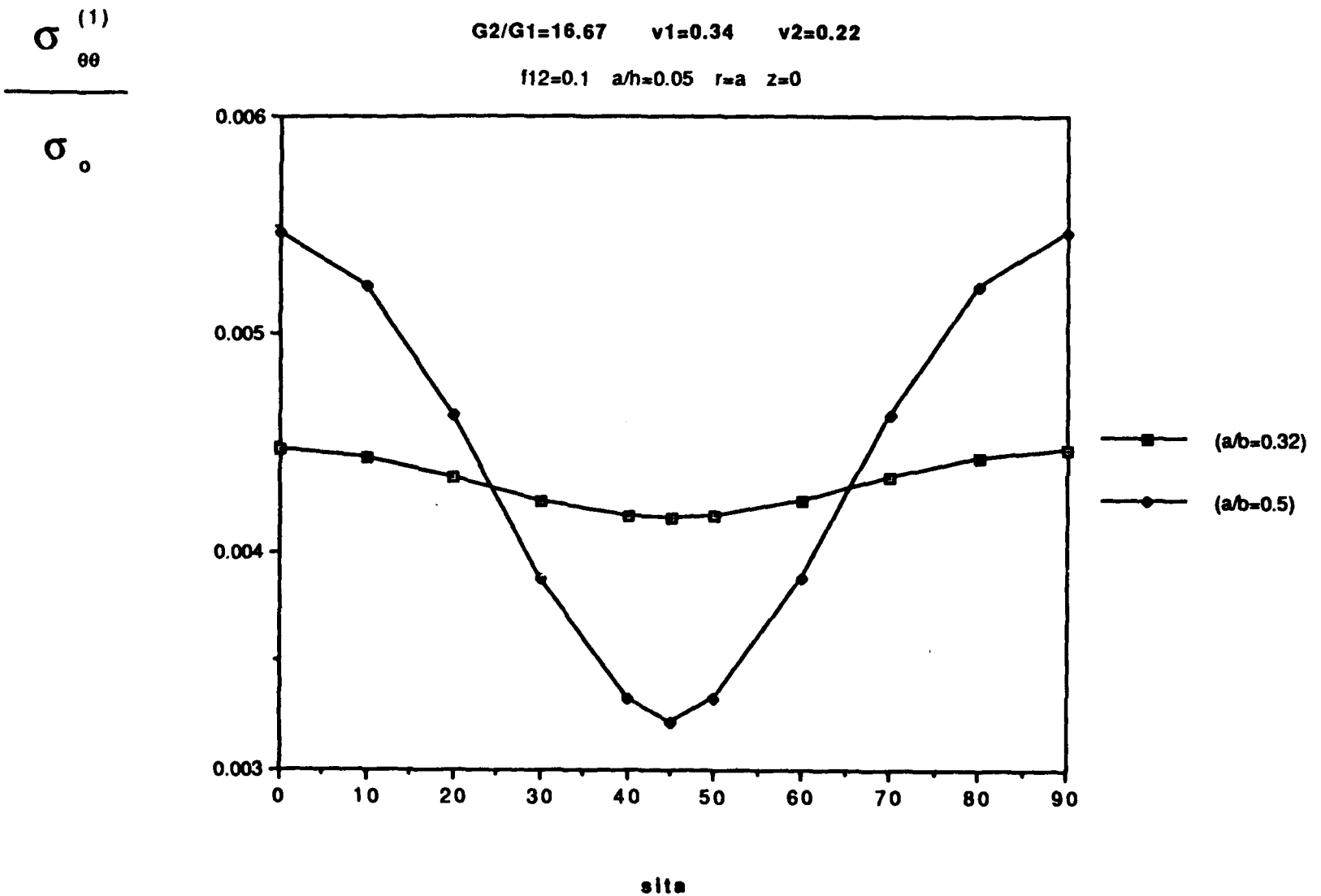

Fig. 7 The stress $\sigma_{\theta\theta}^{(1)}$ at the interface versus θ at z=0 and f12= σ_1/σ_0=0.1.

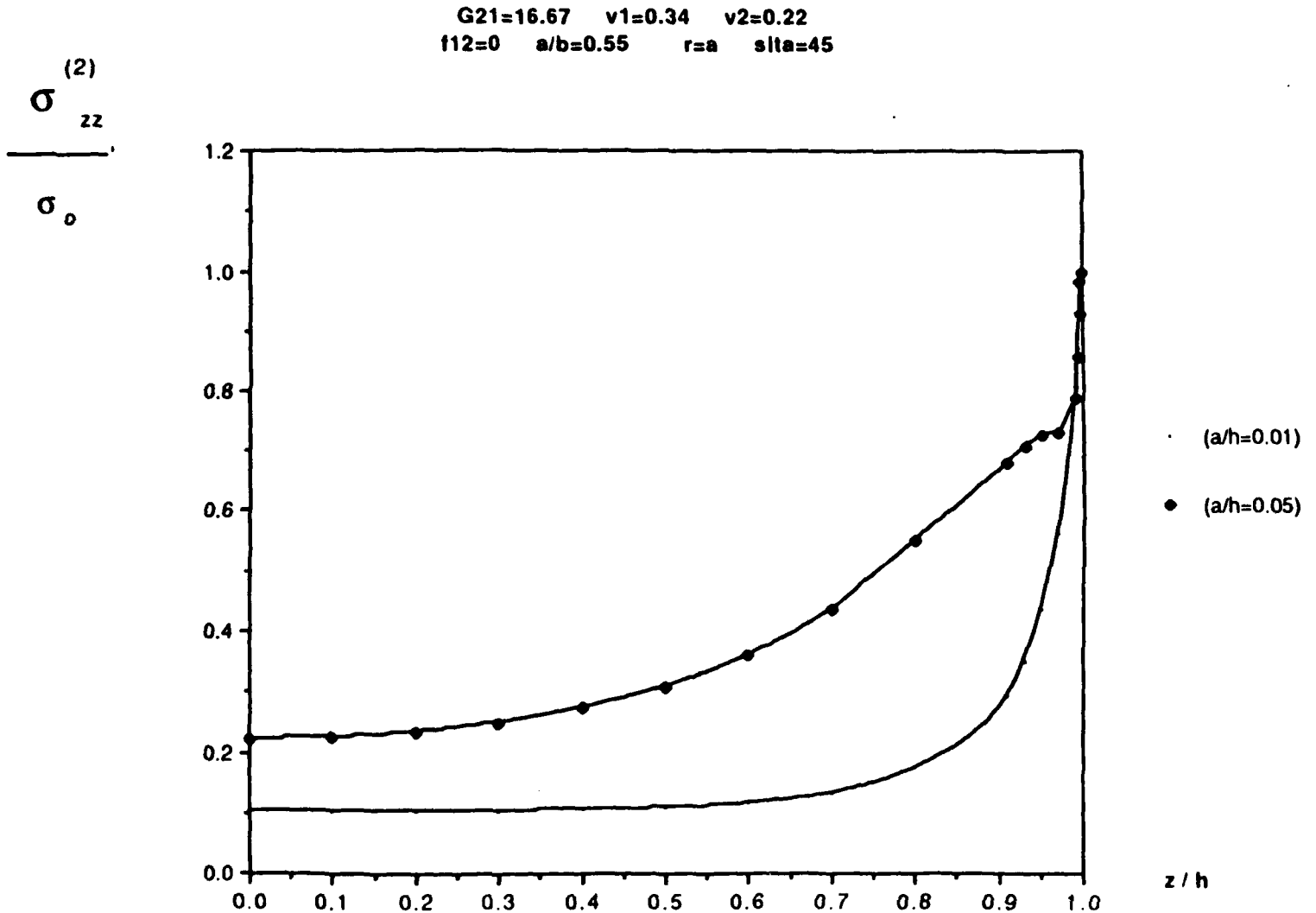

Fig. 8 The stress $\sigma_{zz}^{(2)}$ at the interface versus z=h at θ= 45 and f12= σ_i/σ_0=0.

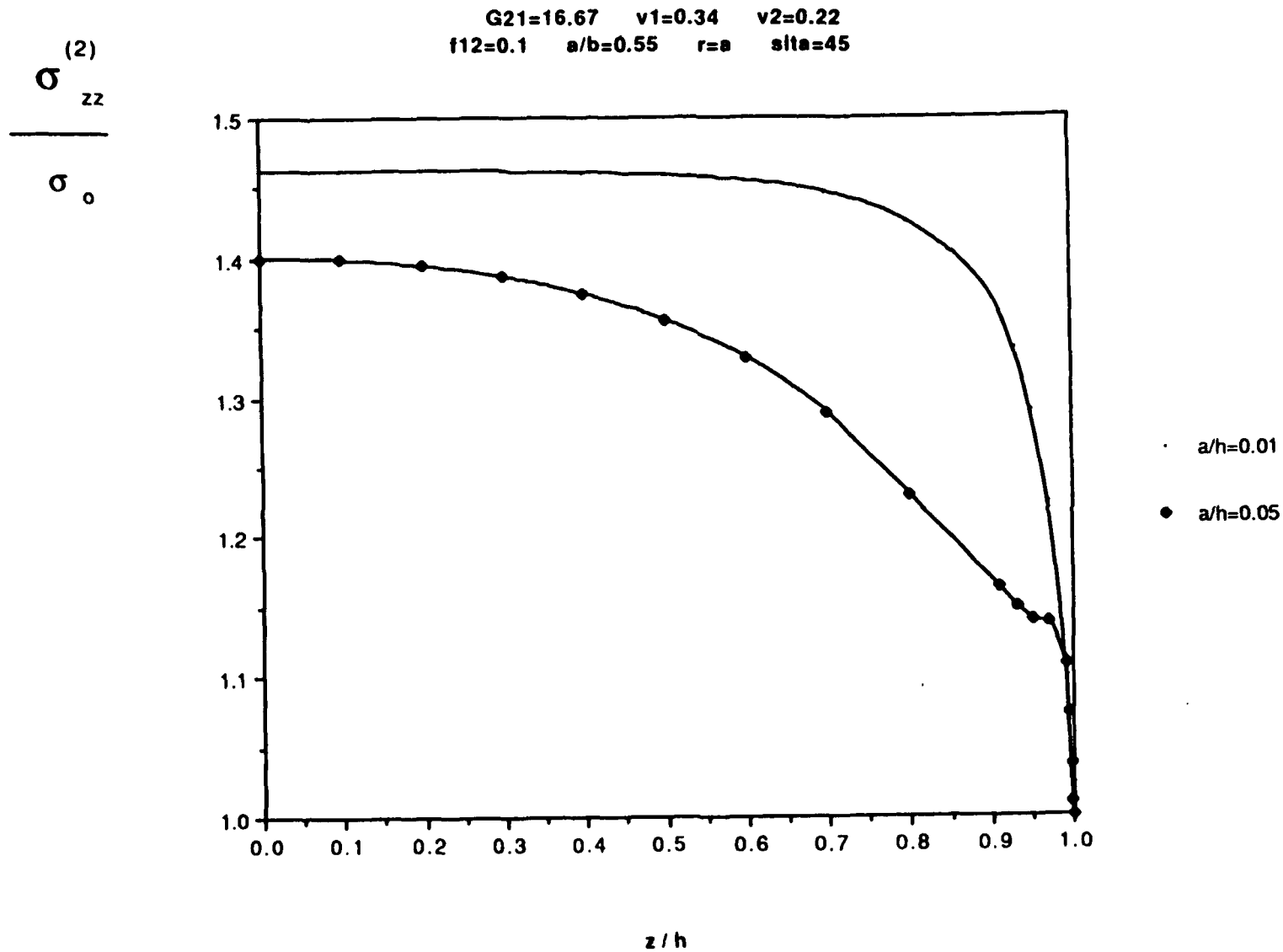

Fig. 9 The stress σ_{zz} at the interface versus z=h at θ= 45 and f12= σ_i/σ_0=0.1 and for various a/h ratios.

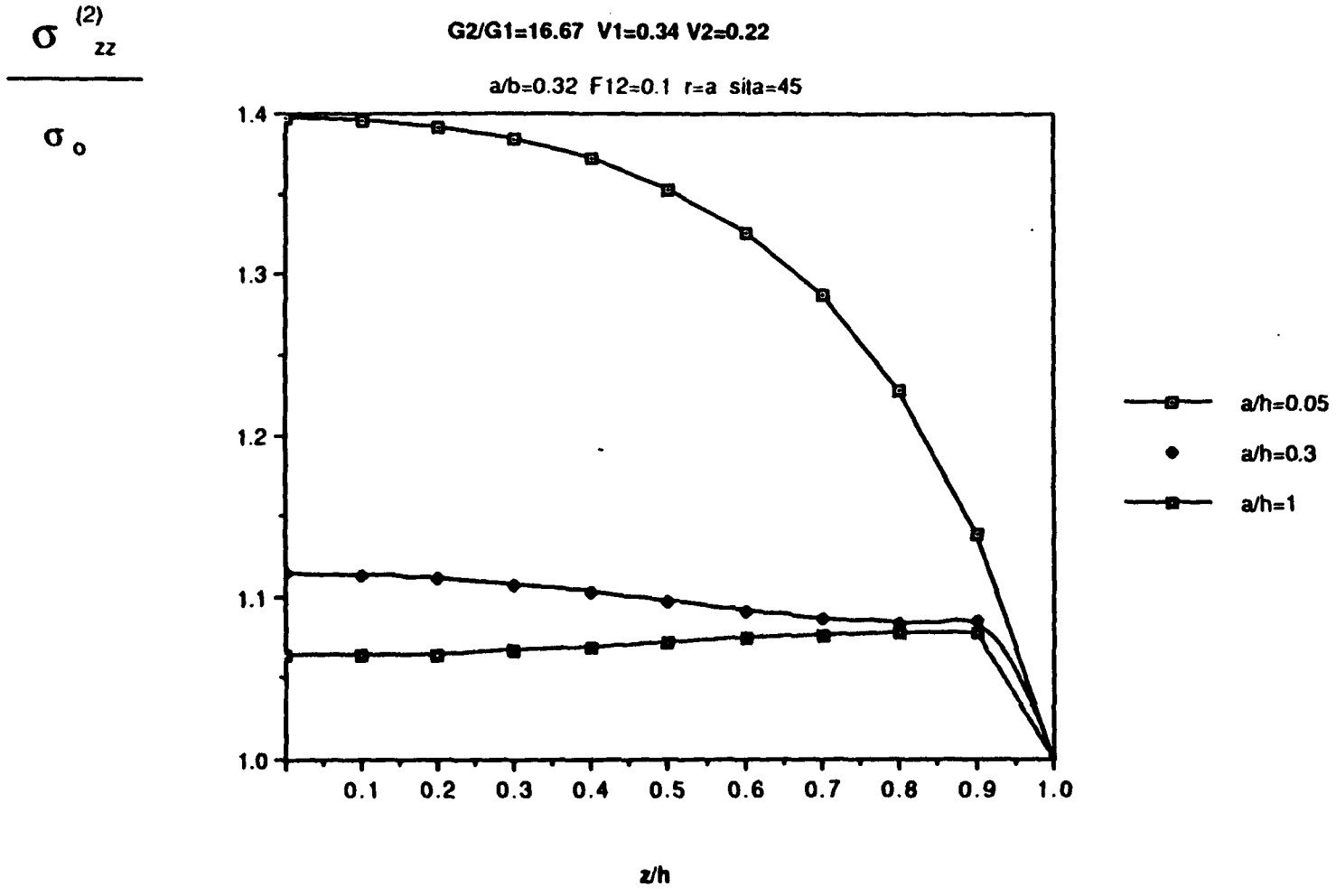

Fig. 10 The stress σ_{zz} at the interface versus z=h at θ= 45 and f12= σ_i/σ_0=0.1 and various a/h ratios.

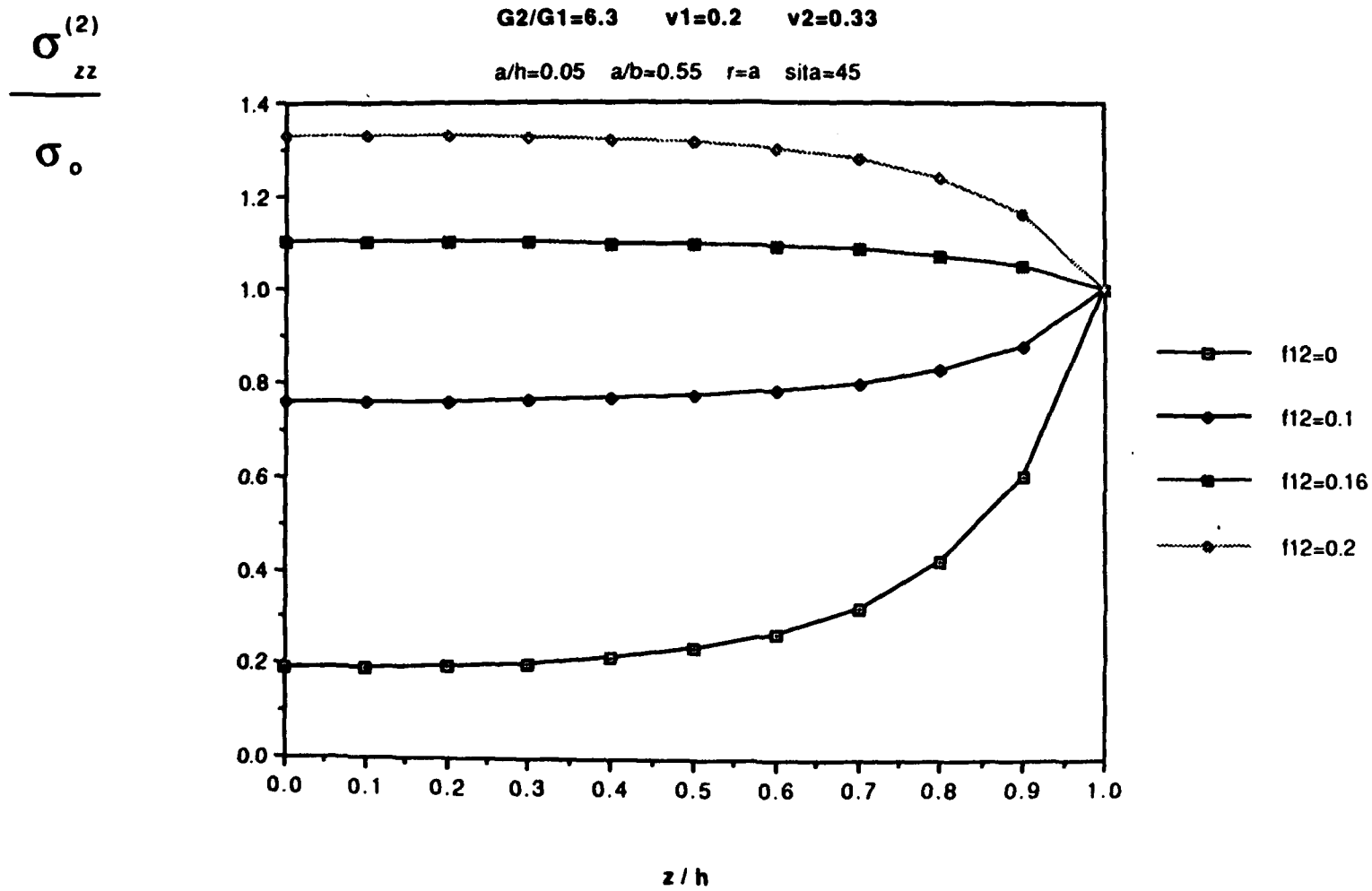

Fig. 11 The stress $\sigma_{zz}^{(2)}$ at the interface versus z=h at θ= 45 and various ratios of f12= σ_i/σ_0.

PART VIII

STRESS ANALYSIS OF AN ADHESIVE BUTT JOINT UNDER TENSION

by

Liu, Y. C., Folias, E. S., Liu, J. H.

Department of Mechanical Engineering
The University of Utah
Salt Lake City, UT84112

ABSTRACT

The adhesive butt joint has been solved by using the theory of linear elasticity under the assumption of plane strain conditions. Both the adherend and the adhesive layer are assumed to be homogeneous and isotropic materials with different material properties. Perfect bonding is also assumed to prevail at the interface.

The numerical results show that under a tension load the interface plane does not remain plane and that the normal stress possesses a weak singularity near the free surface z/h=1. It is also found that there is significant variation in the normal and shear stress profiles across the adhesive thickness especially near the free surface and that the stress distribution is very sensitive to the value of the adhesive thickness to width ratio (a/h) particularly when this is less than 1. An examination of the octahedral shear stress shows that a crack is most likely to initiate at the corner of the adhesive layer. Finally, the numerical results show a good agreement with the results obtained by finite element method (FEM).

INTRODUCTION

In recent years, there has been a continuing increase in the use of adhesives as an alternate method for assembling the structures. From the definitions of ASTM (1982), an adhesive is a substance capable of holding materials together by surface attachment, an

adherend is a body that is held to another body by an adhesive and adhesive joint is the location at which two adherends are held together with a layer of adhesive. Figure 1 shows some adhesive joints that are commonly found in engineering practice.

The single-lap joint is one of the most commonly found joint configurations in engineering practice (see Figure 1). There are numerous papers in the literature that deal with the problem of a lap joint from a theoretical as well as a finite element point of view. However, very few analyses have been done on adhesive butt joints. Adhesive butt joints are usually designed with rectangular or circular cross-section. The mechanical properties of adhesive in bulk form are different from those in thin-film form, so the adhesive butt joint has been widely used as a testing specimen to obtain the thin-film mechanical properties of adhesive. Gent et al. (1970) have analyzed the incompressible adhesive (i.e., its Poison's ratio is 0.5) in tension or compression between rigid adherends. Lindsey (1966) has calculated the stress distribution of the adhesive butt joint in tension with the assumptions that adherends are rigid and stresses are constant across the adhesive layer. Two-dimensional plane stress finite element analysis has been done by Harrison et al. (1972) who use the same assumptions as Lindsey (1966) and maximum shear stress is found near the free surface., Alwar et al. (1976) and Adams et al. (1978) have used the finite element method to analyze plane stress and axisymmetric adhesive butt joint. Both analyses assume that the adherends are nonrigid materials and their numerical results show

that there is significant variation in normal and shear stress profiles across the adhesive thickness. A similar conclusion is obtained by Sawa et al. (1989) who analyze the axisymmetric adhesive butt joint under tension by using the Michell's stress function from the three-dimensional theory of elasticity.

In this paper, a plane strain adhesive butt joint loaded in tension has been analyzed using the general solution derived by Folias (1975, 1990). Both the adherend and the adhesive layer are assumed to be homogeneous and isotropic materials with different material properties. Perfect bonding (i.e., continuity of displacements at the interface between adhesive and adherend) is assumed to prevail at the interface. The stress distribution of adhesive layer with respect to different values of geometric ratio (a/h; adhesive thickness/ adhesive width) and material property ratio (G_2/G_1; adhesive shear modulus/ adherend shear modulus) have been investigated and these results give further understanding of the adhesive butt joint problem in the presence of a tensile load.

FORMULATION OF THE PROBLEM

Consider two adherends of thickness 2h bonded together in a butt joint configuration by an adhesive layer, as shown in Figure 2. The adherends occupy the space $a \leq |x| < \infty$, $|y| < \infty$, $|z| \leq h$ and the adhesive layer occupies the space $|x| \leq a$, $|y| < \infty$ and $|z| \leq h$. Let the joint be subjected to a uniform tensile load σ_o along the x-axis and

parallel to the bonding planes. The shear modulus G_2 and Poisson's ratio ν_2 represent the material constants of the adhesive layer. In order to simplify this adhesive butt joint into a symmetrical problem, one may assume that these two adherends are homogeneous, isotropic and linearly elastic materials with the same shear modulus, G_1, and Poisson's ratio, ν_1, respectively. Since this adhesive butt joint has been simplified to a symmetrical problem, one needs only to consider the one quarter part of this joint with displacement u equal to zero along the line x = 0 and displacement w equal to zero along the line z = 0. According to Figure 2, this adhesive butt joint has a very large dimension in the y direction and it is reasonable to analyze it as a two-dimensional plane strain problem.

For this type of problem, it is convenient to separate the solution in two parts, the particular and complementary solution

$$u^{(i)} = u^{(p)(i)} + u^{(c)(i)} \tag{1}$$

$$w^{(i)} = w^{(p)(i)} + w^{(c)(i)} \tag{2}$$

i=1,2, where i=1 represents the adherend and i=2 represents the adhesive layer. Superscript (p) represents the particular solution and superscript (c) represents the complementary solution.

The particular part must satisfy the Navier's equations and the loading conditions which without the presence of the adhesive

bonding interface, and the complementary part takes care of the adhesive bonding interface with no contribution far away from the interface. The particular solution of this problem can be constructed as:

$$u^{(p)(i)} = \frac{m_i - 1}{m_i} \frac{\sigma_o}{2G_i} x \tag{3}$$

$$v^{(p)(i)} = 0 \tag{4}$$

$$w^{(p)(i)} = - \frac{1}{m_i} \frac{\sigma_o}{2G_i} z \tag{5}$$

$$\sigma_{xx}^{(p)(i)} = \sigma_o \tag{6}$$

$$\tau_{xz}^{(p)(i)} = 0 \tag{7}$$

$$\sigma_{zz}^{(p)(i)} = 0 \tag{8}$$

Assuming that a particular solution has been constructed, one then needs to find four complementary displacement functions $u^{(c)(1)}(x,z)$, $w^{(c)(1)}(x,z)$, $u^{(c)(2)}(x,z)$ and $w^{(c)(2)}(x,z)$ in order to satisfy the Navier's equations and the required boundary conditions which are:

$$|x| \to \infty, \quad \tau_{xz}^{(c)(1)} = \sigma_{xx}^{(c)(1)} = 0 \tag{9}$$

$$|z| = h, \quad \sigma_{zz}^{(c)(1)} = \tau_{xz}^{(c)(1)} = 0 \tag{10}$$

$$\sigma_{zz}^{(c)(2)} = \tau_{xz}^{(c)(2)} = 0 \tag{11}$$

$$|x| = a, \qquad \sigma_{xx}^{(p)(1)} + \sigma_{xx}^{(c)(1)} = \sigma_{xx}^{(p)(2)} + \sigma_{xx}^{(c)(2)} \tag{12}$$

$$\tau_{xz}^{(p)(1)} + \tau_{xz}^{(c)(1)} = \tau_{xz}^{(p)(2)} + \tau_{xz}^{(c)(2)} \tag{13}$$

$$w^{(p)(1)} + w^{(c)(1)} = w^{(p)(2)} + w^{(c)(2)} \tag{14}$$

$$u^{(p)(1)} + u^{(c)(1)} = u^{(p)(2)} + u^{(c)(2)} \tag{15}$$

Since the adherend is a semi-infinite strip, the complementary displacements and stresses of the adherend must vanish as x tends to infinity. On the other hand, the complementary displacements and stresses of the adhesive layer must also be bounded at x=a.

METHOD OF SOLUTION

A general three-dimensional solution to Navier's equation for plates of uniform thickness, 2h, and with plate faces free of stress has been constructed by Folias (1975) and applied to the problem of a plate of finite thickness containing a finite, through the thickness, line crack. Later, Folias et al. (1990) applied the solution to the problem of a finite thickness plate that has been weakened by a cylindrical hole. Without going into the mathematical details, the general form of solution obtained by Folias et al. (1990) is:

$$u^{(c)} = \frac{1}{m-2} \sum_{v=1}^{\infty} \tilde{A}_v \frac{\partial H_v}{\partial x} \{ [\, 2(m-1) \cos(\beta_v h) + m\beta_v h \sin(\beta_v h) \,] \cos(\beta_v z) - m\beta_v z \cos(\beta_v h) \sin(\beta_v z) \} + \sum_{n=1}^{\infty} B_n \frac{\partial H_n}{\partial y} \cos(\alpha_n h) \cos(\alpha_n z) + I_1 - y \frac{\partial I_3}{\partial x} + \frac{1}{m+1} z^2 \frac{\partial^2 I_3}{\partial x \partial y} \tag{16}$$

$$v^{(c)} = \frac{1}{m-2} \sum_{v=1}^{\infty} \tilde{A}_v \frac{\partial H_v}{\partial y} \{ [\, 2(m-1) \cos(\beta_v h) + m\beta_v h \sin(\beta_v h) \,] \cos(\beta_v z) - m\beta_v z \cos(\beta_v h) \sin(\beta_v z) \} - \sum_{n=1}^{\infty} B_n \frac{\partial H_n}{\partial x} \cos(\alpha_n h) \cos(\alpha_n z) + \frac{3m-1}{m+1} I_3 + I_2 - y \frac{\partial I_3}{\partial y} + \frac{1}{m+1} z^2 \frac{\partial^2 I_3}{\partial x^2} \tag{17}$$

$$w^{(c)} = \frac{1}{m-2} \sum_{v=1}^{\infty} \tilde{A}_v H_v \beta_v \{ [\, (m-2) \cos(\beta_v h) - m\beta_v h \sin(\beta_v h) \,] \sin(\beta_v z) - m\beta_v z \cos(\beta_v h) \cos(\beta_v z) \} - \frac{2}{m+1} z \frac{\partial I_3}{\partial y} \tag{18}$$

Since the adhesive butt joint considered here is a two-dimensional plane strain problem, one may simplify the complementary displacements as:

$$u^{(c)(l)} = \frac{1}{m_l-2} \sum_{v=1}^{\infty} \tilde{A}_v^{(l)} \frac{\partial H_v^{(l)}}{\partial x} \{ [\, 2(m_l-1) \cos(\beta_v h) + m_l \beta_v h \sin(\beta_v h) \,] \cos(\beta_v z) - m_l \beta_v z \cos(\beta_v h) \sin(\beta_v z) \} + I_1^{(l)} \tag{19}$$

$$w^{(c)(i)} = \frac{1}{m_i-2} \sum_{\nu=1}^{\infty} A_\nu^{(i)} H_\nu^{(i)} \beta_\nu \{ [(m_i-2) \cos(\beta_\nu h) - m_i \beta_\nu h \sin(\beta_\nu h)] \sin(\beta_\nu z) - m_i \beta_\nu z \cos(\beta_\nu h) \cos(\beta_\nu z) \} \quad (20)$$

By using the Hooke's law, one may find the corresponding complementary stresses as:

$$\sigma_{xx}^{(c)(i)} = \frac{2G_i m_i}{m_i-2} \sum_{\nu=1}^{\infty} \tilde{A}_\nu^{(i)} H_\nu^{(i)} \beta_\nu^2 \{ [2 \cos(\beta_\nu h) + \beta_\nu h \sin(\beta_\nu h)] \cos(\beta_\nu z) - \beta_\nu z \cos(\beta_\nu h) \sin(\beta_\nu z) \} \quad (21)$$

$$\tau_{xz}^{(c)(i)} = - \frac{2G_i m_i}{m_i-2} \sum_{\nu=1}^{\infty} \tilde{A}_\nu^{(i)} \frac{\partial H_\nu^{(i)}}{\partial x} \beta_\nu \{ [\cos(\beta_\nu h) + \beta_\nu h \sin(\beta_\nu h)] \sin(\beta_\nu z) + \beta_\nu z \cos(\beta_\nu h) \cos(\beta_\nu z) \} \quad (22)$$

$$\sigma_{zz}^{(c)(i)} = \frac{2G_i m_i}{m_i-2} \sum_{\nu=1}^{\infty} \tilde{A}_\nu^{(i)} H_\nu^{(i)} \beta_\nu^2 \{ - \beta_\nu h \sin(\beta_\nu h) \cos(\beta_\nu z) + \beta_\nu z \cos(\beta_\nu h) \sin(\beta_\nu z) \} \quad (23)$$

where $i = 1, 2$, $I_1^{(2)} = 0$, and β_ν are the roots of the transcendental equation

$$\sin (2\beta_\nu h) = - (2\beta_\nu h), \quad (24)$$

It is easy to assure that the complementary stresses, i.e., $\tau_{xz}^{(c)(i)}$ and $\sigma_{zz}^{(c)(i)}$, vanish at the plate faces $|z|=h$.

Substituting equations (19) and (20) into the Navier's equations , one can show that the complementary displacement field does indeed satisfy Navier's equations, provided that the function $H_\nu^{(i)}$ satisfies the following equations:

$$\frac{\partial^2 H_\nu^{(i)}(x)}{\partial x^2} - \beta_\nu^2 H_\nu^{(i)}(x) = 0 \qquad (25)$$

The proper type of functions $H_\nu^{(1)}$ and $H_\nu^{(2)}$ for this problem is:

$$H_\nu^{(1)}(x) = e^{-(\beta_\nu x)} \qquad (26)$$

$$H_\nu^{(2)}(x) = \cosh(\beta_\nu x) \qquad (27)$$

By substitution the particular and complementary solutions into the guided boumdary conditions (12)-(15), one may conclude that the governing boundary conditions become respectively:

$$\sum_{\nu=1}^{\infty} [\, m_1 A_\nu^{(1)} - m_2 \frac{G_2}{G_1} A_\nu^{(2)} \,] \beta_\nu$$

$$\{[2\cos(\beta_\nu h) + \beta_\nu h \sin(\beta_\nu h)]\cos(\beta_\nu z) - \beta_\nu z \cos(\beta_\nu h)\sin(\beta_\nu z)\}$$

$$= 0 \qquad ; |z| \le h \qquad (28)$$

$$\sum_{\nu=1}^{\infty} [\, m_1 A_\nu^{(1)} + m_2 \frac{G_2}{G_1} \tanh(\beta_\nu a) A_\nu^{(2)} \,] \beta_\nu$$

$$\{[\cos(\beta_\nu h) + \beta_\nu h \sin(\beta_\nu h)]\sin(\beta_\nu z) + \beta_\nu z \cos(\beta_\nu h)\cos(\beta_\nu z)\}$$

$$= 0 \qquad ; |z| \le h \qquad (29)$$

$$\sum_{\nu=1}^{\infty} A_\nu^{(1)} \{[(m_1-2)\cos(\beta_\nu h) - m_1\beta_\nu h \sin(\beta_\nu h)]\sin(\beta_\nu z)$$

$$- m_1\beta_\nu z \cos(\beta_\nu h)\cos(\beta_\nu z)\}$$

$$- \sum_{\nu=1}^{\infty} A_\nu^{(2)} \{[(m_2-2)\cos(\beta_\nu h) - m_2\beta_\nu h \sin(\beta_\nu h)]\sin(\beta_\nu z)$$

$$- m_2\beta_\nu z \cos(\beta_\nu h)\cos(\beta_\nu z)\}$$

$$= -\frac{1}{2}\left(\frac{1}{m_2}\frac{G_1}{G_2} - \frac{1}{m_1}\right)\left(\frac{z}{a}\right) \qquad ; |z| \le h \qquad (30)$$

$$\sum_{\nu=1}^{\infty} A_\nu^{(1)} \{[2(m_1-1)\cos(\beta_\nu h) + m_1\beta_\nu h \sin(\beta_\nu h)]\cos(\beta_\nu z)$$

$$- m_1\beta_\nu z \cos(\beta_\nu h)\sin(\beta_\nu z)\}$$

$$+ \sum_{\nu=1}^{\infty} \tanh(\beta_\nu a) A_\nu^{(2)} \{[2(m_2-1)\cos(\beta_\nu h) + m_2\beta_\nu h \sin(\beta_\nu h)]\cos(\beta_\nu z)$$

$$- m_2\beta_\nu z \cos(\beta_\nu h)\sin(\beta_\nu z)\}$$

$$= \frac{m_1-1}{2m_1} - \frac{m_2-1}{2m_2}\frac{G_1}{G_2} + I_1^{(1)} \qquad ; |z| \le h \qquad (31)$$

where $A_\nu^{(1)}$ and $A_\nu^{(2)}$ are the normalized coefficients, with the definitions of:

$$A_\nu^{(1)} = \frac{1}{m_1 - 2} \frac{\beta_\nu G_1}{\sigma_o a} e^{-(\beta_\nu a)} \tilde{A}_\nu^{(1)} \tag{32}$$

$$A_\nu^{(2)} = \frac{1}{m_2 - 2} \frac{\beta_\nu G_1}{\sigma_o a} \cosh(\beta_\nu a) \tilde{A}_\nu^{(2)} \tag{33}$$

Examination of equations (28)-(33) shows that the coefficients $A_\nu^{(1)}$ and $A_\nu^{(2)}$ are functions of β_ν , the dimensionless ratio a/h, the shear modulus ratio G_2/G_1 and the Poisson's ratio ν_1/ν_2. Since the roots β_2, β_4, β_6,..... are the complex conjugates of β_1, β_3, β_5,....., one concludes that the unknown complex coefficients $A_2^{(i)}$, $A_4^{(i)}$, $A_6^{(i)}$,..... are also the complex conjugates of $A_1^{(i)}$, $A_3^{(i)}$, $A_5^{(i)}$,..... (where i = 1, 2).

The unknown complex coefficients $A_\nu^{(1)}$ and $A_\nu^{(2)}$ are to be determined from the system of linear equations (28)-(31), by using the method discussed in Kantorovich and Krylov (1964, p.54-56). The system, equations (28)-(31), is very sensitive to even small changes of the coefficients, so the methods of "collocation" and "least squares" lead to a nonconvergent solution. However, the method, which was discussed by Kantorovich and Krylov (1964), shows the complex coefficients to converge as the number of roots taken increases.

Once the unknown complex coefficients have been determined, the displacement and stress fields may then be computed at any point in the adhesive layer.

The displacement field in the adhesive layer becomes:

$$\left(\frac{G_1}{\sigma_o a}\right) u^{(2)} = \frac{m_2-1}{2m_2}\frac{G_1}{G_2}\frac{x}{a} + \sum_{v=1}^{\infty}\frac{\sinh(\beta_v x)}{\cosh(\beta_v a)}A_v^{(2)}\{[2(m_2-1)\cos(\beta_v h) + m_2\beta_v h\sin(\beta_v h)]\cos(\beta_v z) - m_2\beta_v z\cos(\beta_v h)\sin(\beta_v z)\} \tag{34}$$

$$\left(\frac{G_1}{\sigma_o a}\right) w^{(2)} = -\frac{1}{2m_2}\frac{G_1}{G_2}\frac{z}{a} + \sum_{v=1}^{\infty}\frac{\cosh(\beta_v x)}{\cosh(\beta_v a)}A_v^{(2)}\{[(m_2-2)\cos(\beta_v h) - m_2\beta_v h\sin(\beta_v h)]\sin(\beta_v z) - m_2\beta_v z\cos(\beta_v h)\cos(\beta_v z)\} \tag{35}$$

Similarly, the stress field of the adhesive layer becomes:

$$\frac{\sigma_{xx}^{(2)}}{\sigma_o} = 1 + 2m_2\left(\frac{a}{h}\right)\left(\frac{G_2}{G_1}\right)\sum_{v=1}^{\infty}\beta_v h\frac{\cosh(\beta_v x)}{\cosh(\beta_v a)}A_v^{(2)}\{[2\cos(\beta_v h) + \beta_v h\sin(\beta_v h)]\cos(\beta_v z) - \beta_v z\cos(\beta_v h)\sin(\beta_v z)\} \tag{36}$$

$$\frac{\tau_{xz}^{(2)}}{\sigma_o} = -2m_2\left(\frac{a}{h}\right)\left(\frac{G_2}{G_1}\right)\sum_{v=1}^{\infty}\beta_v h\frac{\sinh(\beta_v x)}{\cosh(\beta_v a)}A_v^{(2)}\{[\cos(\beta_v h) + \beta_v h\sin(\beta_v h)]\sin(\beta_v z) + \beta_v z\cos(\beta_v h)\cos(\beta_v z)\} \tag{37}$$

$$\frac{\sigma_{zz}^{(2)}}{\sigma_o} = 2m_2\left(\frac{a}{h}\right)\left(\frac{G_2}{G_1}\right)\sum_{v=1}^{\infty}\beta_v h\,\frac{\cosh(\beta_v x)}{\cosh(\beta_v a)}A_v^{(2)}$$

$$\{ -\beta_v h\,\sin(\beta_v h)\,\cos(\beta_v z) + \beta_v z\,\cos(\beta_v h)\,\sin(\beta_v z)\} \qquad (38)$$

NUMERICAL RESULTS AND DISCUSSION

In the present analysis, we let the $a/h = 0.1$, $G_2/G_1 = 0.05$, $\nu_1 = 0.3$ and $\nu_2 = 0.33$. After determining the complex coefficients $A_v^{(1)}$ and $A_v^{(2)}$, one needs to substitute these complex coefficients into equations (28) - (31) to examine how well the complex coefficients satisfy the original boundary equations (28) - (31). Figure 3 shows how the error of equation (28) improves as one increases the number of roots from 100 to 200. The numerical study shows that the errors of these boundary equations improve only 3% if one increases the root number v from 200 to 220 and it is reasonable to set 200 roots throughout this present analysis. If further accuracy is required, then more sophisticated algorithms must be used for the solution of the matrix system.

By substituting the complex coefficients $A_v^{(2)}$ into equations (34) - (38), one obtains the displacement and stress fields in the adhesive layer. The numerical study indicates the interface does not remain plane under load, although the shear modulus of adherends is 20 times as stiff as that of adhesive. The variation of displacement $u^{(2)}$ along the interface implies that the stresses are not uniform along the

interface (see Figure 4). Along the interface, the effect of dissimilar material properties (i.e., $G_2/G_1 < 1$) between adherend and adhesive causes the normal stress to possess a weak singularity (Folias 1989) near the free surface $z/h=1$. On the other hand, there will be no stress singularity present when the material properties of the adherends are the same as that of the adhesive (i.e., a uniform plate).

In the central region (see Figure 4), the normal stress is uniformly distributed and is slightly higher than the average applied stress, and the shear stress almost equals zero except in the region close to the free surface. On the mid-plane of the adhesive, the normal stress decreases to a low value near the free surface, and the shear stress is always zero since this is a symmetrical problem. It is also noted from Figure 4 that there is a significant variation in the normal and shear stresses across the adhesive thickness especially near the free surface $z/h = 1$ (see Figure 5). Near the free surface, $z/h= 0.99$, the interface normal and shear stress increases as the a/h value increases (see Figure 6), but it does not change after the a/h value is greater than 1. It is also observed from Figure 6 that the stress values decreases as the G_2/G_1 value increases.

In the present analysis, the theory of linear elasticity has been used to evaluate the stress field in the adhesive layer. In order to examine the possible failure mode of this adhesive joint, one may choose the octahedral shear stress, τ_{oct}, as a suitable parameter. The numerical results show that the region around the point of intersection between the free surface and the joint interface is

subjected to higher stress values. Thus yielding is most likely to initiate first in this region. Figure 7 shows the yielding zone at the corner of the adhesive joint with respect for different values of the applied load. It is observed that, when the load is small (ie., $\sigma_o=0.75\sigma_Y$), the initial yielding is along the interface. As the load increases further (ie., $\sigma_o=0.85\sigma_Y$), this yielding area is not extending along the interface but with an angle of approximately 60° from the interface. Thus, a crack will initiate at the corner and propagate along the interface up to a certain distance beyond which it will curve into the adhesive layer due to the mixed-mode (normal and shear) stress field around the crack tip.

Figure 8 and 9 show the comparison of the analytical results obtained by this study (plane stress case) with the results obtained by the Finite Element Method (Alwar et al. 1976) with respect to the stress distributions at the interface. In this comparison, the a/h value is 0.1, the G_2/G_1 value is 0.01, the Poisson's ratio ν_1 = 0.3 and ν_2 = 0.33 and both results are in fairly good agreement. Except in the vicinity of the corner point z=h where a boundary layer region is present.

CONCLUSIONS AND RECOMMENDATIONS

From the above study of adhesive butt joints, the following conclusions can be made:

(1) The interface does not remain plane under a tension load due to the dissimilarity of the material properties between adherend and adhesive, and this displacement variation results in the presence of a stress singularity at the interface and close to the free surface. Along the interface, the normal stress attains its maximum at the free surface while the shear stress attains its maximum very very close to the free surface. Furthermore, it is also observed that there is significant variation in the normal and shear stress profiles across the adhesive thickness especially near the free surface.

(2) The maximum normal and shear stress increases as one decreases the shear modulus of the adhesive layer or increases the a/h value, but the stresses do not change very much when the a/h value is greater than 1.

(3) An examination of the octahedral shear stress shows that a crack is most likely to initiate at the corner and propagate along the interface up to a certain distance beyond which it will curve into the adhesive layer.

(4) The analytical results from this study show a good agreement with the results obtained by Finite Element Method.

In this paper, the plane strain case of adhesive butt joint under tension has been solved, but the similar procedures can be applied to the problem of axisymmetric butt joint under tension or torsion, if one transforms the general solution (16)-(18) from rectangular to

cylindrical coordinates. Furthermore, the single-lap and bevel joints can also be solved by the application of the general solution used in this analysis. Identical and isotropic adherends are considered in this present analysis. Therefore, stress analysis of adhesive joint with nonidentical or anisotropic adherends is an important extension of this work. Finally, perfect bonding is assumed in the present analysis, but partial debonding (flaw) is often found at joint interface in practical situations. Another important extension of this work is to analyze an adhesive joint which contains flaw at the interface by relaxing the assumption of perfect bonding.

REFERENCES

Adams, R. D., Coppendale, J., and Peppiatt, N. A., 1978, "Stress analysis of axisymmetric butt joint loaded in torsion and tension," *J. Strain Analysis*, Vol. 13, No. 1, pp. 1-10.

Allman, D. J., 1977, "A theory for elastic stresses in adhesive bonded lap joints," *Q. J. Mech. Appl. Math.*, Vol. 30, pp. 415-436.

Alwar, R. S., and Nagaraja, Y. R., 1976, "Elastic analysis of adhesive butt joints," *J. Adhesion*, Vol. 7, pp. 279-287.

Chen, D., and Cheng, S., 1983, "An analysis of adhesive-bonded single-lap joints," *J. Appl. Mech.*, Vol. 50, pp. 109-115.

Delale, F., Erdogan, F., and Aydinoglu, M. N., 1981, "Stresses in adhesively bonded joints : a closed-form solution," *J. Composite Mat.*, Vol. 15, pp. 249-271.

Folias, E. S., 1989, "On the stress singularities at the intersection of a cylindrical inclusion with the free surface of a plate," *Int. J. Fracture*, Vol. 39, pp. 25-34.

Folias, E. S., 1975, "On the three-dimensional theory of cracked plates," *J. Appl. Mech.*, Vol. 42, pp. 663-674.

Folias, E. S., and Wang, J. J., 1990, "On the three-dimensional stress field around a circular hole in a plate of arbitrary thickness," *Computational Mech.*, Vol. 6, pp. 379-391.

Gent, A. N., and Meinecke, E. A., 1970, "Compression, bending and shear of bonded rubber blocks," *Polymer Eng. Sci.*, Vol. 10, No. 1, pp. 48-53.

Goland, M., and Reissner, E., 1944 "Stress in cement joints," *J. Appl. Mech. Trans. ASME*, Vol. 11, pp. A17-A27.

Harrison, N. L., and Harrison, W. J., 1972, "The stresses in an adhesive layer," *J. Adhesion*, Vol. 3, pp. 195-212.

Kantrovich, L. V., and Krylov, V. I., 1964, *Approximate methods of higher analysis*, Noordhoff, Holland, pp. 54-56.

Lindsey, G. H., 1966, "Hydrostatic tensile fracture of a polyurethane elastomer," *Aerospace Research Lab. Report* ARL 66-0029.

McLaren, A. S., and MacInnes, I., 1958, "The influence on the stress distribution in an adhesive lap joint of bending of the adhering sheets," *British J Appl. Physics*, Vol. 9, pp. 72-77.

Ojalvo, I. U., and Eidinoff, H. L., 1978, "Bond thickness effects upon stresses in single-lap adhesive joints," *AIAA J.*, Vol. 16, No. 3, pp. 204-211.

Renton, W. J., and Vinson, J. R., 1977, "Analysis of adhesively bonded joints between panels of composite materials," *J. Appl. Mech.*, Vol. 9, pp. 101-106.

Sawa, T., Temma, K., and Ishikawa, H., 1989, "Three-dimensional stress analysis of adhesive butt joints of solid cylinders subjected to external tensile loads," *J. Adhesion*, Vol. 31, pp. 33-43.

Volkersen, O., 1938, "Die Nietkrafrverteilung in Zugbeanspruchten Nietverbindungen mit Konstanten Laschenquerschnitten," *Luftfarhtforschung*, Vol. 15, pp. 41-47.

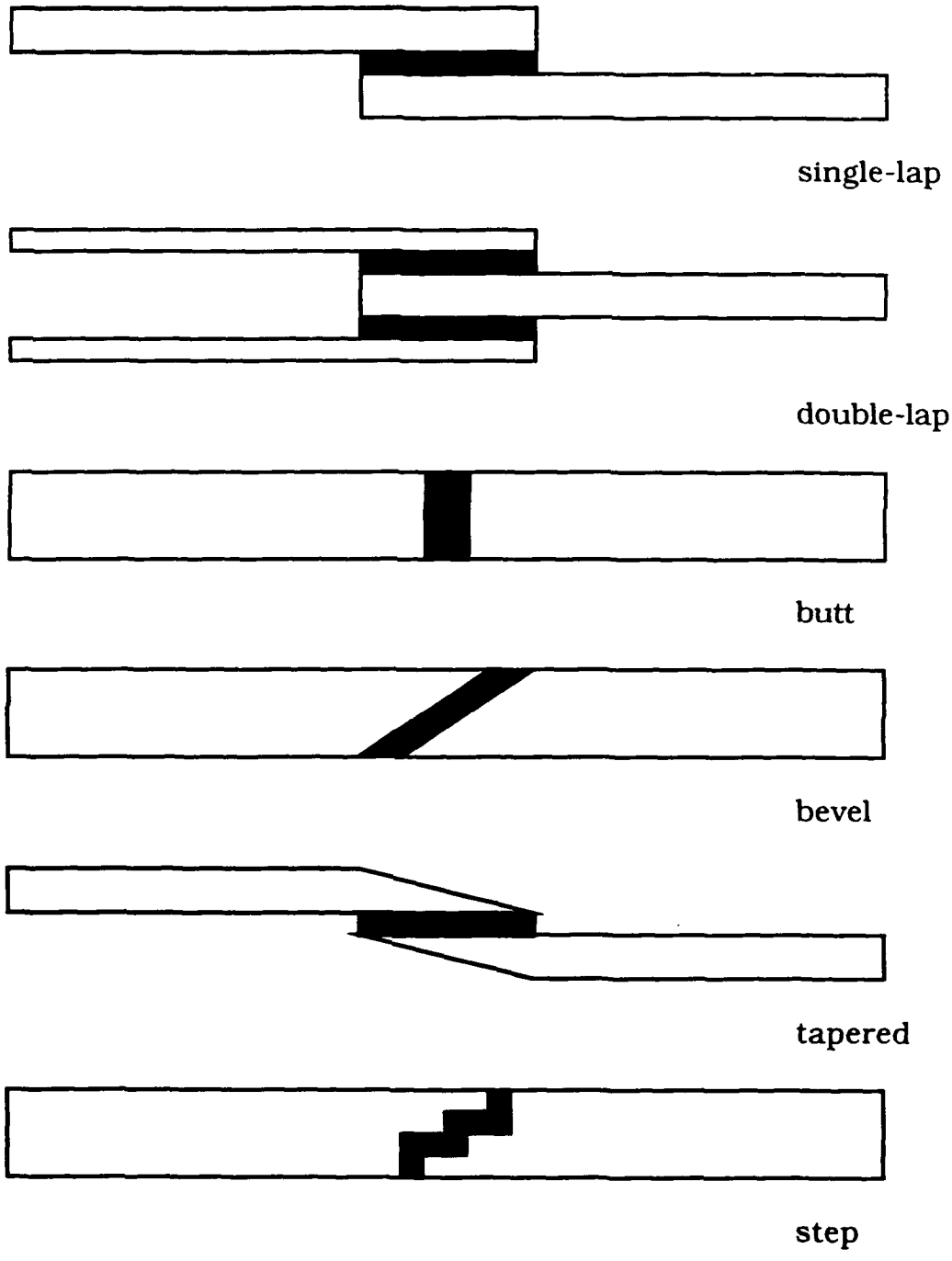

Figure 1 Some common engineering adhesive joints.

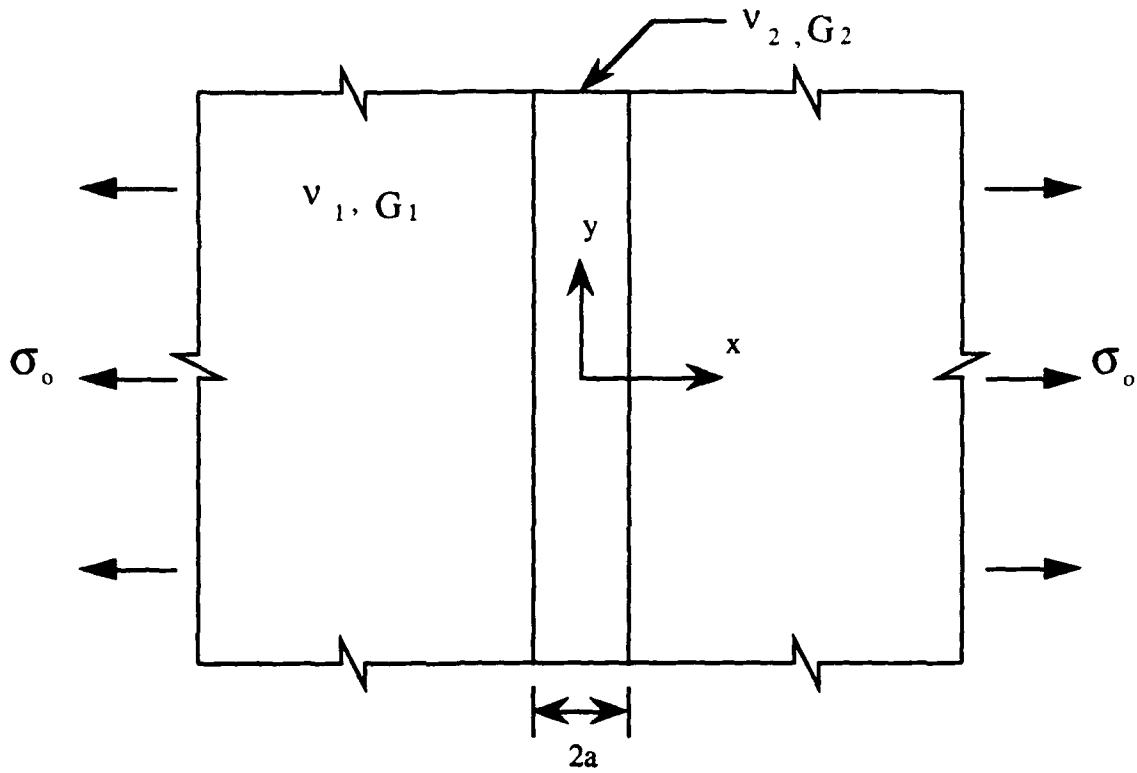

(a) Top View

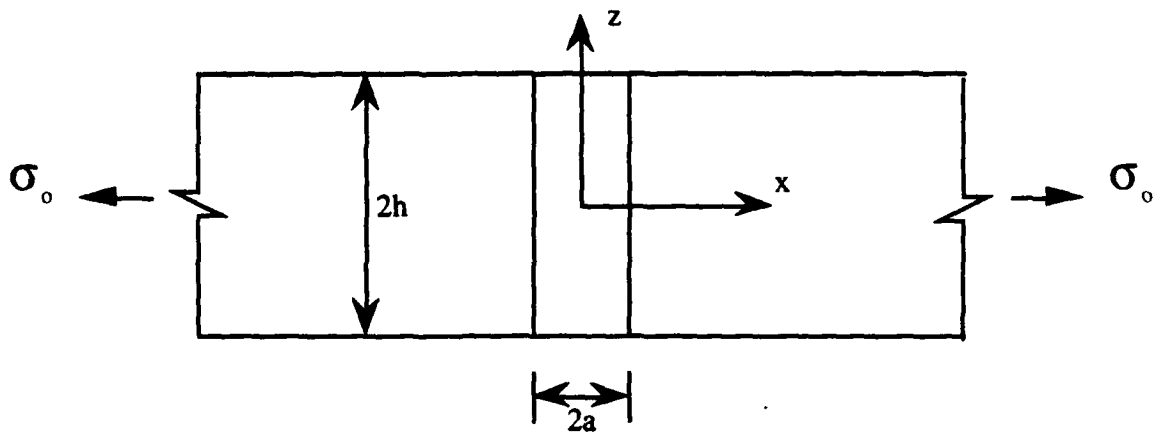

(b) Side View

Figure 2 Adhesive butt joint with finite thickness subject to an in-plane tensile load.

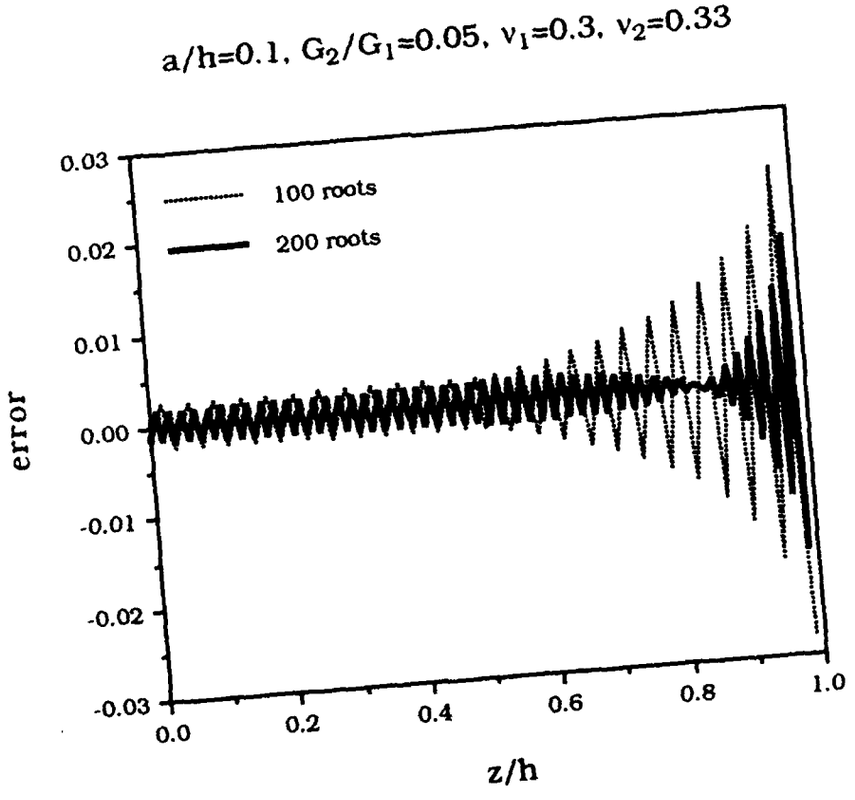

Figure 3 Numerical error for equation (28) for a/h=0.1, G_2/G_1= 0.05, ν_1=0.3, ν_2=0.33 and different number of roots.

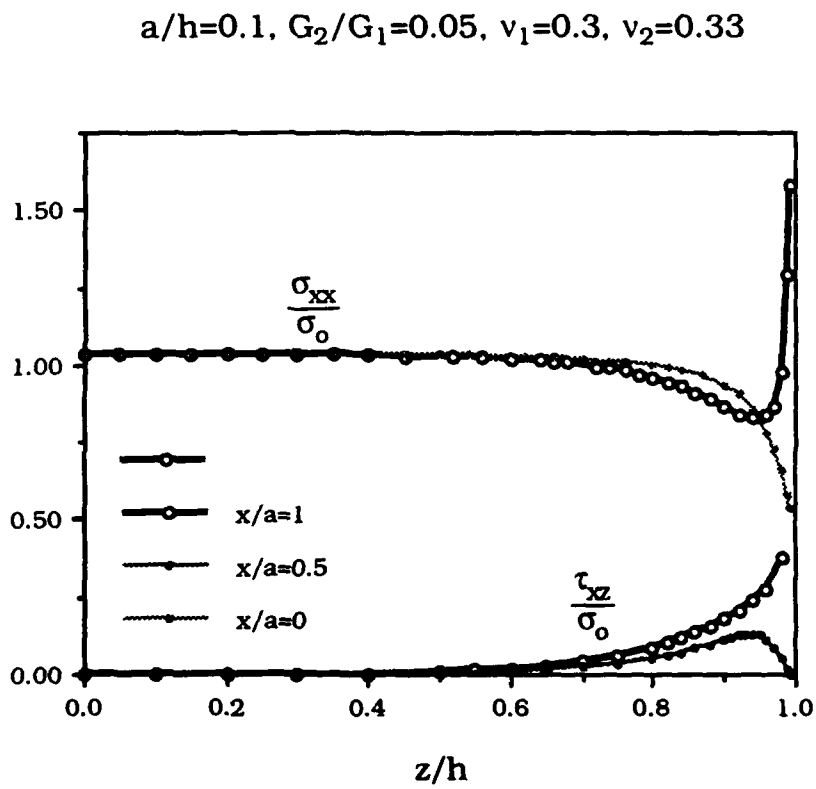

Figure 4 Stress σ_{xx} and τ_{xz} for the adhesive layer at the interface and mid-plane for a/h=0.1, G_2/G_1=0.05, ν_1=0.3 and ν_2=0.33.

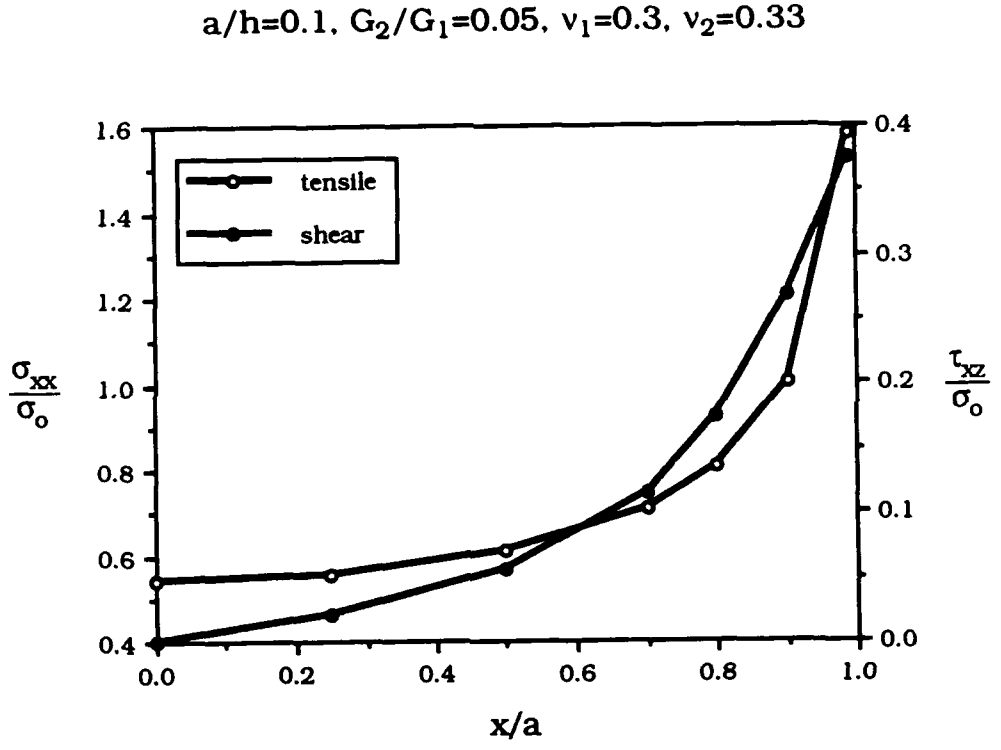

Figure 5 Stress σ_{xx} and τ_{xz} for the adhesive layer across the thickness at z/h= 0.98 for a/h=0.1, G_2/G_1=0.05, ν_1=0.3 and ν_2=0.33.

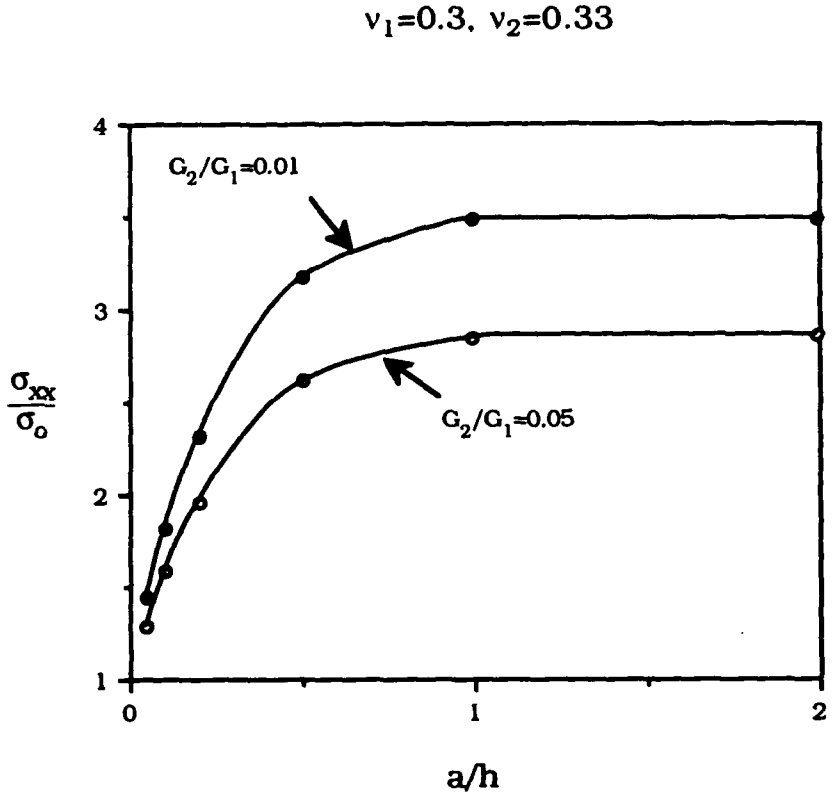

Figure 6 Stress σ_{xx} for the adhesive layer with respect to the different a/h values at z/h=0.99, x/a=1 for ν_1=0.3 and ν_2=0.33.

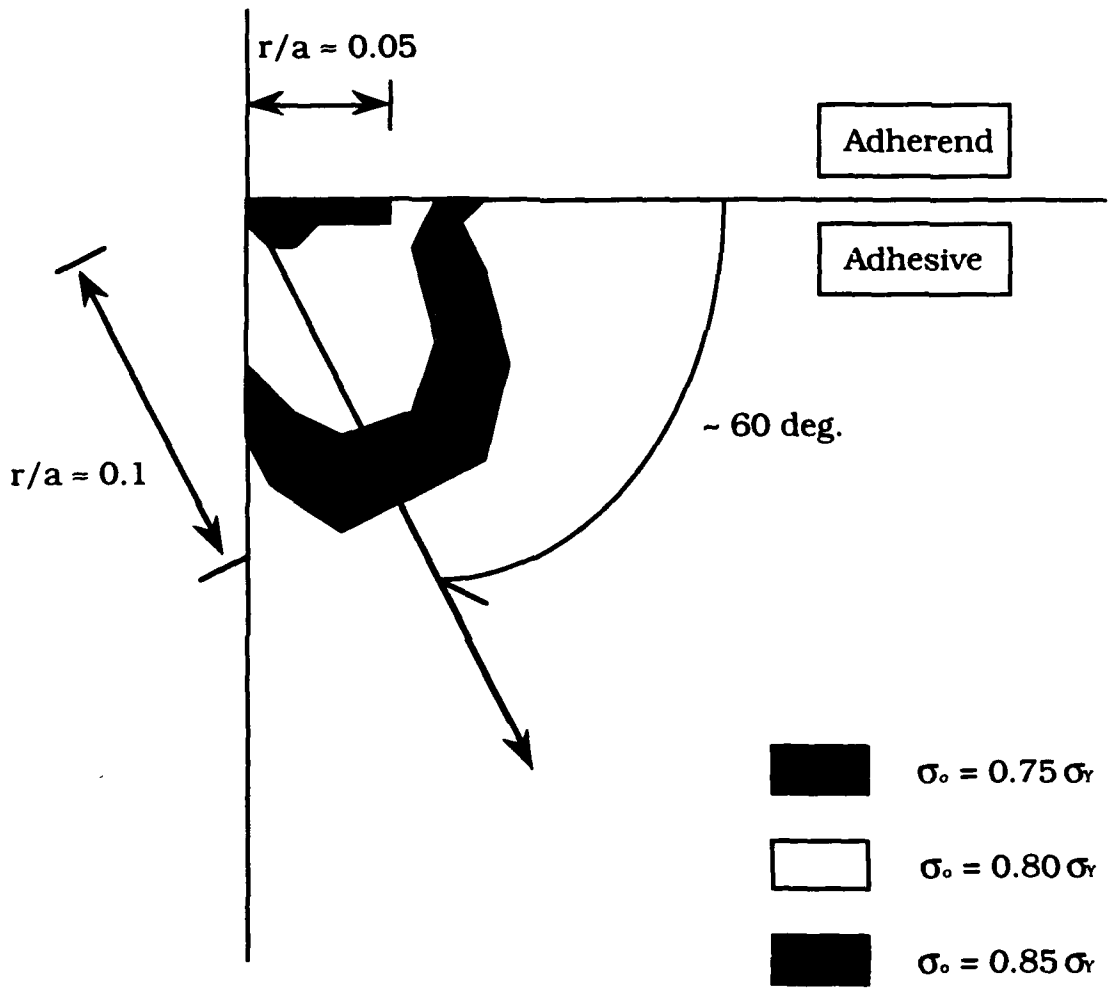

Figure 7 The yielding zone at the corner of the adhesive joint with respect to different values of the applied load.

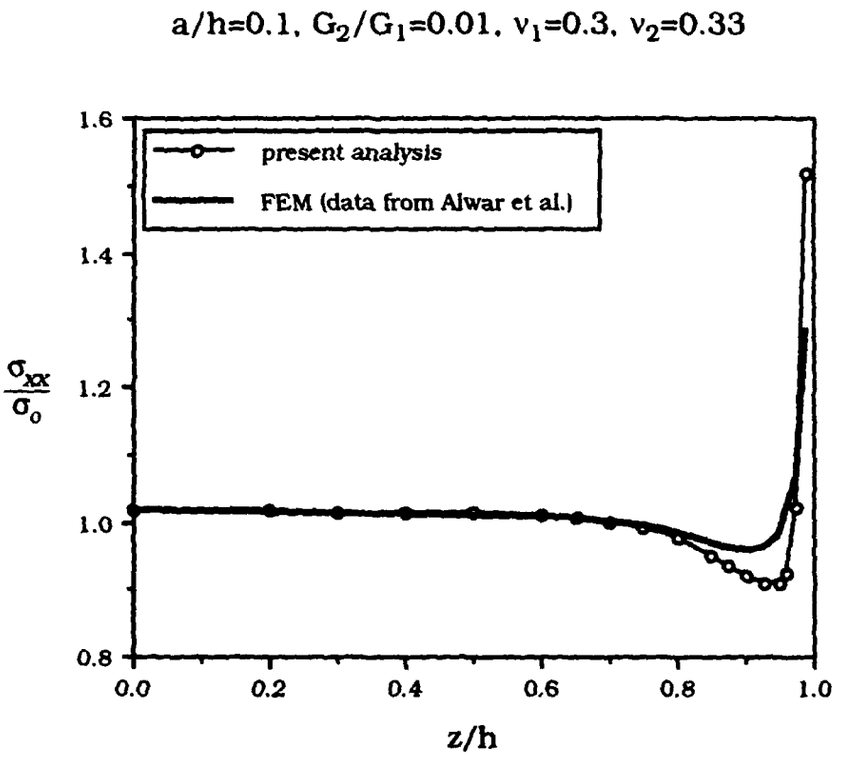

Figure 8 Comparison of the stress σ_{xx} at the interface with result of FEM (data from Alwar et al.) for a/h=0.1, G_2/G_1=0.01, ν_1=0.3 and ν_2=0.33.

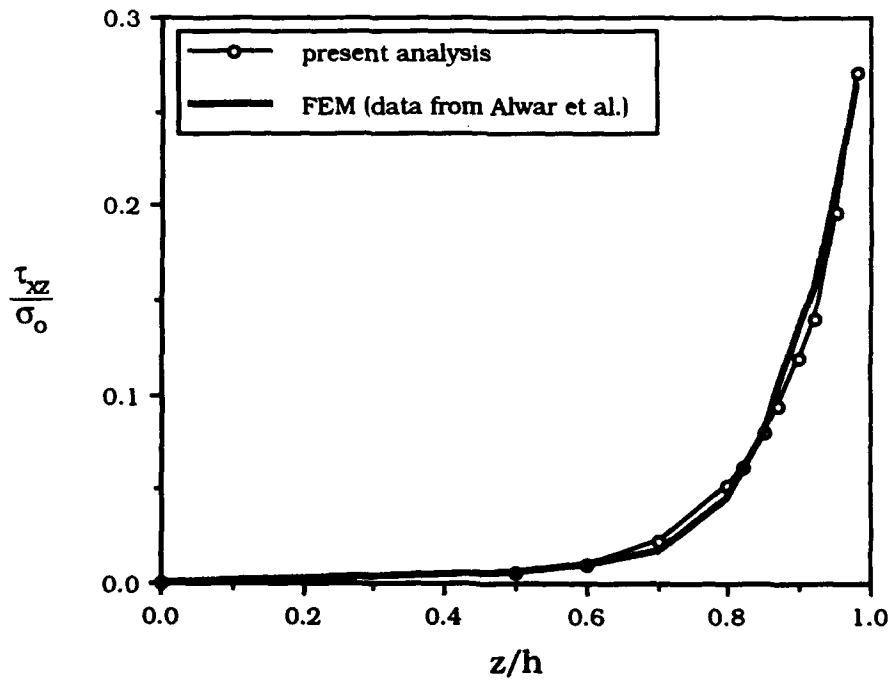

Figure 9 Comparison of the stress τ_{xz} at the interface with result of FEM (data from Alwar et al.) for a/h=0.1, G_2/G_1=0.01, ν_1=0.3 and ν_2=0.33.

SECURITY CLASSIFICATION OF THIS PAGE (When Data Entered)

REPORT DOCUMENTATION PAGE

READ INSTRUCTIONS BEFORE COMPLETING FORM

1 REPORT NUMBER	2 GOVT ACCESSION NO. / 3 RECIPIENT'S CATALOG NUMBER
4 TITLE and Subtitle: FAILURE CONSIDERATIONS IN COMPOSITE SYSTEMS BASED ON 3D MICROMECHANICAL STRESS FIELDS : PART A	5 TYPE OF REPORT & PERIOD COVERED: Final Technical Report / 6 PERFORMING ORG. REPORT NUMBER
7 AUTHOR(s): E. S. Folias	8 CONTRACT OR GRANT NUMBER(s): AFOSR 90-0351
9 PERFORMING ORGANIZATION NAME AND ADDRESS: Department of Mathematics, University of Utah, Salt Lake City, Utah, 84112	10 PROGRAM ELEMENT, PROJECT, TASK AREA & WORK UNIT NUMBERS
11 CONTROLLING OFFICE NAME AND ADDRESS: Air Force Office of Scientific Research, Bolling A.F.B., Washington, D.C. 20332	12 REPORT DATE: Dec. 1992 / 13 NUMBER OF PAGES
14 MONITORING AGENCY NAME & ADDRESS (if different from Controlling Office)	15 SECURITY CLASS. (of this report): Unclassified / 15a DECLASSIFICATION DOWNGRADING SCHEDULE

16 DISTRIBUTION STATEMENT (of this Report)

Unlimited

17 DISTRIBUTION STATEMENT (of the abstract entered in Block 20, if different from Report)

Approved for public release; distribution unlimited

18 SUPPLEMENTARY NOTES

19 KEY WORDS (Continue on reverse side if necessary and identify by block number)

3D stress fields, composites, micromechanics, residual stresses, transverse strength, longitudinal strength, thermal expansion mismatch, fiber/matrix interface

20 ABSTRACT (Continue on reverse side if necessary and identify by block number)

In this investigation, a systematic 3D micromechanics approach is used to model a composite. The fibers are assumed to be cylindrical inclusions which are periodically embedded into a matrix plate. A three dimensional analysis is used in order to capture any edge effects which may be present. A set of fundamental key problems has been identified

DD FORM 1 JAN 73 1473 EDITION OF 1 NOV 65 IS OBSOLETE

Unclassified

SECURITY CLASSIFICATION OF THIS PAGE (When Data Entered)

and their respective solutions for the displacement and stress fields are then used in order to provide us with some answers to the following fundamental questions: transverse strength, longitudinal strength, residual stresses due to thermal expansion mismatch, modeling of fiber matrix interface, edge effects.

The 3D results are then used to first identify critical locations where failure, due to fracture, is most likely to initiate and second to derive fracture criteria for crack initiation at the local level. The criteria reveal the dependance of the composite strength on the material properties, the local cell geometry, the ratio of the fiber volume fraction, the ratio of fiber radius to fiber length and finally the applied mechanical and or thermal loads.